Degenerate Polar Molecules with Controlled Interactions and Reactivity

by

William Gray Tobias

A.B., Harvard University, 2016

M.S., University of Colorado, Boulder, 2019

A thesis submitted to the

Faculty of the Graduate School of the

University of Colorado in partial fulfillment

of the requirements for the degree of

Doctor of Philosophy

Department of Physics

2022

Committee Members:

Jun Ye, Chair

Ana Maria Rey

John Bohn

Cindy Regal

Carl Lineberger

Tobias, William Gray (Ph.D., Physics)

Degenerate Polar Molecules with Controlled Interactions and Reactivity

Thesis directed by Prof. Jun Ye

Ultracold polar molecules, which have complex internal structures and dipole moments tunable with external electric fields, are a promising system for studying many-body physics. Producing degenerate molecules and observing quantum effects has been a long-standing goal. Technical barriers that have prevented reaching degeneracy include inelastic loss of molecules from chemical reactions and relatively high temperatures, since standard methods of cooling atomic gases are not effective for molecules.

This thesis documents the creation of degenerate potassium-rubidium (KRb) molecules and the control of intermolecular interactions using electric fields. In three dimensions, molecules are produced by pairing in a degenerate atomic mixture and reach thermal equilibrium through elastic collisions with unpaired atoms. We probe the fermionic statistics of the degenerate molecules by measuring reduced number fluctuations in the momentum state occupation, a direct consequence of the Pauli exclusion principle. In two dimensions, we apply an external electric field to induce repulsive dipolar interactions, suppressing inelastic collisions and enabling direct evaporation to degeneracy. At particular electric fields, pairs of rotational states can be tuned into resonance, generating strongly attractive or repulsive intermolecular potentials and modifying the chemical reaction rate by orders of magnitude. We also develop the capability to address the molecule distribution with nanometer-scale precision using electric field gradients, enabling sub-wavelength field sensing and microscopic control of interacting ultracold molecules.

Dedication

For Mom, Dad, Jim, and Cecilia.

Acknowledgements

My years at JILA have been some of the happiest of my life, and I owe that to the following people. Thanks to my advisor, Jun, and my wonderful colleagues, who made even the difficult months enjoyable: Kyle, Junru, Luigi, Giacomo, Cal, Annie, and Jake. We were lucky to work with brilliant theorists and experimentalists at JILA and elsewhere, including Ana Maria, John, Eric, Thomas, Reuben, Peiru, Jose, and many others. Thanks as well to all of the Ye Group members and other scientists at JILA who lent us equipment, gave us advice, and were great friends.

Our work would not have been possible without the help of JILA staff members in the electronics and instrument shops, supply office, computing group, and administration: Terry, Carl, James, Felix, Hans, James, J.R., Jim, Dan, Corey, Amy, Beth, Krista, Jason, Kim, Brian, Jen, Randall, Dan, and Karen.

I feel very lucky to have been able to work every day with my friends on complicated physics problems, with access to the resources and support that JILA provides. Thanks most of all to my family and friends, new and old, for being there for me.

Contents

Chapter

1 Introduction **1**

1.1 Properties of Polar Molecules 2

1.1.1 Producing Ultracold Molecules 2

1.1.2 Chemical Reactions 3

1.1.3 Quantum Statistics 6

1.1.4 Dipolar Interactions 6

1.1.5 Confinement Geometry 7

1.2 Contents 9

2 Ultracold Molecule Apparatus **11**

2.1 Experiment Overview 11

2.2 Gray Molasses Cooling 13

2.2.1 Rubidium 16

2.2.2 Potassium 18

2.3 Tunable STIRAP 22

2.3.1 "Accidental Resonance" at 4.5 kV/cm 24

2.3.2 Fiber EOMs 26

2.3.3 Excited State Spectroscopy 32

2.4 State-Resolved Imaging 33

2.4.1 Stern-Gerlach Imaging 34
2.4.2 *In Situ* Imaging 37

3 Electric Field Control **39**
3.1 KRb Structure 39
3.1.1 Hyperfine Structure 42
3.2 Electrode Geometry and Field Simulations 44
3.3 High Voltage Stabilization 48
3.3.1 Grounding 50
3.3.2 Voltage Reference 50
3.3.3 Output Filter 52
3.3.4 AC Noise Characterization 56
3.4 Aligning Molecules to the Electrodes 61
3.4.1 Moving the Molecules 62
3.4.2 Gradient Spectroscopy of Vertical Position 64
3.4.3 Single-Rod Gradient Measurement 65

4 Reaching Degeneracy in Three Dimensions **67**
4.1 Introduction 67
4.2 Molecule Association 68
4.3 Feshbach Molecule Thermalization 73
4.3.1 K-KRb* Scattering Length 74
4.4 Two-Body Loss 78
4.4.1 Temperature Dependence 80
4.4.2 Suppressed Loss Below T_F 81

5 Density Fluctuations in a Degenerate Fermi Gas **83**
5.1 Introduction 83

5.2 Density Fluctuations in Degenerate Gases 84
5.3 Imaging Number Fluctuations 86
5.3.1 Saturation Intensity 87
5.3.2 Correcting the Optical Density Variance 88
5.3.3 Image Binning and Resolution 91
5.4 Fluctuation Measurements 93
5.4.1 Degenerate KRb and Non-Degenerate K 94
5.4.2 Degenerate K, KRb*, and KRb 95
5.5 Effects of STIRAP 95
5.5.1 Association 97
5.5.2 Dissociation 98

6 Direct Evaporation in Two Dimensions **101**
6.1 Introduction 101
6.2 Counting Layers 102
6.2.1 Matter Wave Focusing 104
6.3 Sample Preparation 107
6.3.1 Large-Spacing Lattice 108
6.4 Dipolar Suppression of Two-Body Loss 108
6.5 Cross-Dimensional Thermalization 111
6.6 Direct Evaporation to Degeneracy 113
6.6.1 Combined Electro-Optical Trap Potential 113
6.6.2 Results 115

7 Resonant Shielding of Collisions **118**
7.1 Introduction 118
7.2 Shielding Resonance 119
7.2.1 Simple Model for Resonant Shielding 122

7.3 Two-Body Loss . . . 123
7.4 Dipolar Elastic Collisions . . . 125
7.4.1 Cross-Dimensional Thermalization . . . 126
7.4.2 Density Correction . . . 128
7.4.3 Bootstrap Fitting . . . 129
7.5 Evaporative Cooling in 3D . . . 130

8 Dipolar Exchange **133**
8.1 Introduction . . . 133
8.2 Layer Selection . . . 134
8.2.1 Phase Stabilization . . . 135
8.2.2 Lattice Tilt Angle . . . 137
8.2.3 Results . . . 140
8.3 State Preparation and Electric Field Microscopy . . . 142
8.4 Rotational Coherence in a Single Layer . . . 145
8.4.1 Optimizing Magic Angle . . . 147
8.4.2 Measuring Single-Layer Coherence . . . 148
8.4.3 Modeling Coherence Time . . . 149
8.5 Spin Exchange . . . 152
8.5.1 Density and State Dependence on Resonance . . . 155
8.5.2 Detuning Dependence . . . 155
8.5.3 Theory Results . . . 158

9 Conclusion **161**
9.1 Outlook . . . 162

Bibliography **164**

Appendix

A High Voltage Noise Floor **178**

A.1 Noise Sources 178

A.2 Voltage Reference and DAC 180

A.3 High Voltage Divider and Loop Filter 182

A.4 Real Values and Outlook 184

A.4.1 AC Noise (> 0.1 Hz) 184

A.4.2 Long-Term Drift 188

B WKB Approximation for Two-Body Loss Temperature Dependence **191**

Tables

Table

4.1 Atom conditions for molecule association 69

A.1 High voltage reference and feedback circuit component values 185

A.2 Summary of sources contributing to high voltage noise 185

A.3 Specified and measured noise for circuit components 186

A.4 Temperature coefficients of ICs in the control loop. 189

Figures

Figure

1.1 Interacting polar molecules 4

2.1 Overview of molecule formation 12

2.2 Atom and molecule conditions during the experimental sequence 14

2.3 Schematic picture of gray molasses cooling 15

2.4 Rb gray molasses level diagram 17

2.5 K gray molasses level diagram 19

2.6 K D1 gray molasses optics layout 20

2.7 K D1 detuning parameters 22

2.8 STIRAP association level diagram 23

2.9 Excited state shift between 0-4.5 kV/cm 25

2.10 EOM cavity locking schematic 26

2.11 Up leg sideband powers 29

2.12 STIRAP optics layout 30

2.13 Frequency offset of STIRAP from the optical cavity 32

2.14 STIRAP excited state Stark shift 33

2.15 Stern-Gerlach imaging schematic 35

2.16 Stern-Gerlach imaging experimental results 36

3.1 State mixing of $|0, 0\rangle$ vs. electric field 41

3.2 Rotational state energy and dipole moment vs. electric field 43
3.3 $|1,0\rangle$ hyperfine structure and loss 45
3.4 Electrode assembly 46
3.5 Electric field curvature vs. angle 48
3.6 Electric field control loop 49
3.7 Long-term drift of the LTC6655 reference 51
3.8 Low-pass filter on the HV output 53
3.9 HV servo bandwidth 54
3.10 AC noise spectrum on high voltage electrodes 56
3.11 Phase noise measurements with Ramsey interferometry 58
3.12 Aligning the molecules using imaging 61
3.13 Mapping the electric field using molecules 63
3.14 Measuring the molecule position using applied gradients 64
3.15 Single-rod gradient alignment 65

4.1 Atom conditions for molecule association 69
4.2 Momentum profile of degenerate KRb 72
4.3 Feshbach molecule thermalization with K atoms 74
4.4 Using STIRAP to excite molecule oscillations 75
4.5 Elastic collisions between K atoms and KRb* molecules 76
4.6 K-KRb* and Rb-KRb* scattering lengths 77
4.7 Molecule degeneracy vs. Feshbach ramp rate 78
4.8 Temperature dependence of two-body loss 80
4.9 Dependence of two-body loss on temperature and T/T_F 81

5.1 Momentum state occupation in degenerate Fermi gases 85
5.2 Density fluctuations in 3D 86
5.3 Photon number statistics 89

5.4 Subtracting imaging noise from number fluctuations 90
5.5 Number fluctuations vs. bin width 92
5.6 Number fluctuations for thermal and degenerate particles 94
5.7 Spatial distribution of number fluctuations in degenerate K, KRb*, and KRb 96
5.8 Modifying T/T_F to account for STIRAP 98

6.1 Matter wave focusing for layer counting 105
6.2 Experimental configuration and LSL loading 107
6.3 Intermolecular potential curves with an induced dipole moment 109
6.4 Two-body loss suppression and 2D/3D crossover 110
6.5 Cross-dimensional thermalization in quasi-2D 112
6.6 Lowering the trap potential using electric field curvature 114
6.7 Evaporation trajectory 115
6.8 Evaporation results in quasi-2D 117

7.1 Resonant shielding in KRb 120
7.2 Dependence of resonant shielding potentials on orientation and field 121
7.3 Electric field dependence of two-body loss in 3D 124
7.4 Cross-dimensional thermalization in 3D. 127
7.5 Two-body loss vs. dipole angle 128
7.6 Bootstrap fitting of cross-dimensional thermalization 129
7.7 Direct evaporation in 3D 131

8.1 Phase stabilization diagram 135
8.2 Lattice phase shift and displacement 136
8.3 Spectroscopic measurement of lattice tilt angle 139
8.4 Measuring molecule distribution with layer selection 141
8.5 Optimizing layer selection pulse width 142

8.6 Experimental configuration for layer selection and spin exchange 143

8.7 Pulse sequence for layer selection 144

8.8 Trilayer selection and electric field microscopy 146

8.9 Locating the electric field "magic angle" 148

8.10 Increasing single-layer coherence 150

8.11 Simulating decoherence from differential polarizability 151

8.12 Interaction and loss dynamics for molecules in 2D 153

8.13 Rotational state and density dependence of spin exchange 154

8.14 Dependence of spin exchange rate on detuning, rotational state, and temperature . . 157

8.15 Two-body model of spin exchange 160

A.1 Voltage reference and DAC circuit diagram 180

A.2 High voltage feedback circuit diagram 182

B.1 WKB approximation of two-body loss temperature dependence 194

Chapter 1

Introduction

Ultracold polar molecules, which have complex internal structures and dipole moments tunable with external electric fields, are a promising system for studying open problems in physics and chemistry. Present and future applications include wide-ranging topics such as quantum simulation of condensed matter models, measurements of fundamental symmetries, ultracold chemistry, and quantum information science [1, 2, 3, 4, 5, 6].

The unfortunate reality is that ultracold molecules behave differently in the laboratory than on paper. At the temperatures where molecules are formed, thermal energy and disorder predominate over interactions and wash out the delicate signatures of quantum many-body effects. Reactive loss limits the lifetime of trapped molecules and increases the entropy over the time needed to manipulate the molecules with sequences of applied electric fields and microwave pulses.

This thesis describes our work to realize the full potential of ultracold potassium-rubidium (KRb) molecules, with the end goal of producing a stable, low-temperature molecular gas with strong dipolar interactions in varying geometries. We spent the first two years making a degenerate atomic mixture and optimizing molecule association, resulting in the production of degenerate polar molecules. In our subsequent experiments, we used electric fields to control dipolar interactions and probe molecular gases on microscopic scales. The two guiding themes of our research, which will frequently reappear together in the following chapters, are suppressing loss and enhancing interactions.

1.1 Properties of Polar Molecules

This section describes the properties of ultracold molecules that played important roles in our explorations, with some historical context included for scale. These are: molecule association at ultracold temperatures, interactions between molecules, quantum statistical effects, and optical trapping and dimensionality.

1.1.1 Producing Ultracold Molecules

Many quantum phenomena are primarily observable in low entropy ensembles. Two main approaches have been used to produce ultracold polar molecules. First, high-temperature molecules can be directly laser cooled using standard techniques from atomic physics such as Doppler and gray molasses cooling [7, 8, 9, 10]. Compared to atoms, molecules have additional rotational and vibrational degrees of freedom and more complicated electronic and hyperfine structure. Consequently, establishing a closed cycling transition typically requires many lasers and techniques such as polarization or magnetic field switching to avoid accumulating population in dark states. Related methods have recently been extended to polyatomic molecules, demonstrating that the group of laser-coolable molecules is rapidly expanding [11]. While temperatures as low as 1 μK have been achieved [12], phase space densities remain far from quantum degeneracy.

An alternative method is to coherently associate molecules from ultracold atoms. The upside of this approach is that the molecules inherit the low temperature and high density of the atoms; the downside is that a relatively small set of atoms can be cooled to degeneracy, only a subset of which can be associated into molecules. Alkali atoms, which have single unpaired electrons that allow laser cooling and magnetic tuning of interatomic scattering lengths, were particularly promising candidates for forming heteronuclear molecules [13]. In 2008, an earlier generation of the KRb experiment created the first ultracold polar molecules using a two-step process of magnetoassociation and coherent optical transfer [14]. In the years following, many other species of bialkali molecules were produced near quantum degeneracy in the rovibrational ground state by similar techniques

[15, 16, 17, 18, 19, 20]. In the experiments described in this thesis, we use the same method to associate KRb molecules and we study the role of atom degeneracy and atom-molecule collisions in the molecule association process.

1.1.2 Chemical Reactions

KRb molecules in the lowest vibrational and rotational energy level have an energetically allowed reaction pathway at ultracold temperatures: $\mathrm{KRb} + \mathrm{KRb} \rightarrow \mathrm{K_2} + \mathrm{Rb_2}$ (illustrated in Fig. 1.1a). This reaction releases 10 cm^{-1} of energy, equal to a frequency of approximately 300 GHz or a temperature of 14 K. The product energies are about six orders of magnitude larger than typical trapping potentials, so molecules undergoing reactions are ejected from the trap.

Collisions between KRb molecules were observed in 2010, soon after they were first produced [21]. Reactions between identical molecules were found to be two orders of magnitude slower than between distinguishable molecules, and to exhibit linear scaling with temperature. Theoretical work reproduced these results by separating the long-range and short-range intermolecular potentials [22, 23]. The short-range potential is difficult to treat analytically since reactions progress through a complicated potential energy surface involving several intermediate complexes [24]. As an approximation to the true dynamics theorists used "quantum defect" theory, where a single parameter quantifies the loss probability at short range inside the long-range barrier.

By comparison, the long-range interactions can be simply described and involve only a few parameters. For fermionic molecules such as KRb, the lowest allowed angular momentum partial wave has a p-wave centrifugal barrier preventing molecules from reaching short range. The temperature dependence of two-body loss arises from the energy-dependent tunneling probability through the p-wave barrier. Distinguishable molecules instead collide in the s-wave channel, leading to the enhancement of loss. Other long-range potentials include the attractive van der Waals force and dipolar interactions, which depend on orientation. The loss rates measured for KRb were consistent with near-universal loss, meaning molecules at short range are lost with high probability.

While ultracold chemistry is an interesting topic of study in its own right, reactions are gen-

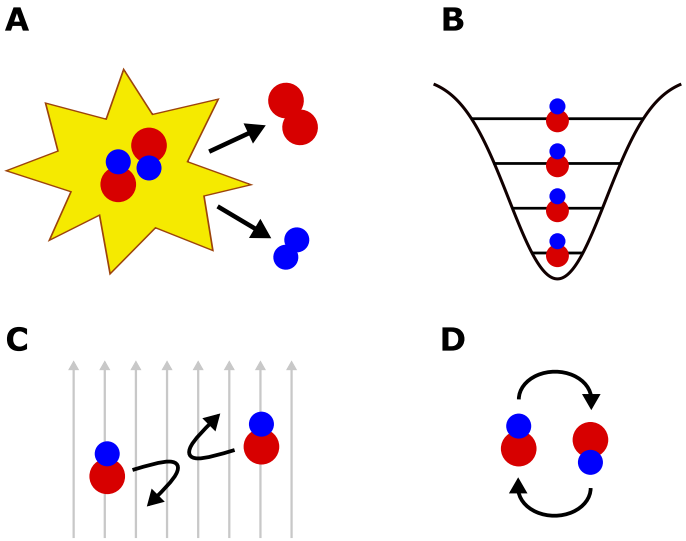

Figure 1.1: Interacting polar molecules. **(a)** At short range, pairs of KRb molecules undergo chemical reactions and form K_2 and Rb_2 molecules. **(b)** Quantum degenerate fermions singly occupy energy levels in an optical trap due to Pauli exclusion. **(c)** Dipole moments induced by an external electric field create attractive or repulsive long-range interactions depending on the molecule orientations. **(d)** Degeneracies between rotational states lead to resonant exchange interactions and can strongly modify the intermolecular potential.

erally unwelcome in quantum gas experiments since they cause particle loss and heating. Following studies of reactions in KRb, several bialkali species with only endothermic reaction pathways were identified, including RbCs and NaK [25]. Calculations showed that these molecules would have larger dipole moments than KRb [26], allowing for the realization of chemically stable quantum gases with strong dipolar interactions.

Unfortunately, when nominally non-reactive molecules were first synthesized, they also exhibited near-universal loss [15, 27, 28], even in direct comparisons of endothermic and exothermic pathways in the same molecule [29]. One mechanism proposed to explain the loss was collisions of molecules with long-lived four-body complexes formed by two colliding molecules, resulting in the loss of all three molecules [30]; however, subsequent investigation found only two-body loss with a lower rate than predicted by this model [31]. Following these results, a new model was developed proposing the loss of complexes by photoexcitation from optical trapping light [32, 33]. Experimental tests of this model used various methods to reduce the average light intensity, such as chopping the trapping beams and using repulsive blue-detuned traps. Results were mixed: for RbCs, in which sub-universal loss had been previously measured [31, 34], the loss scaled strongly with the intensity. In one experiment on KRb where the K_2Rb_2 complex could be directly probed, the inferred complex lifetime was similar to predictions [35]. However, for NaRb and both bosonic and fermionic NaK, universal loss was still observed at low intensity [36, 37]. Theoretical and experimental investigation into these observations continues [38].

Atom-exchange reactions and photoexcitation should produce identical loss behavior in our experiment: both mechanisms lead to universal two-body loss and the rate of molecules reaching short range is determined predominantly by the long-range potentials. In this thesis, I describe our efforts to reduce the reactive loss—independent of loss mechanism—by modifying the dipolar interactions, statistical properties, and confinement geometry. Though we do not probe the short-range dynamics, the open questions in ultracold chemistry revealed by the study of polar molecules show that they are controllable model systems and yet can still produce surprising results.

1.1.3 Quantum Statistics

Even for non-interacting particles, at low temperatures quantum statistics strongly modify the thermodynamic properties measured in experiment. These effects have been well-studied in degenerate bosonic [39] and fermionic [40] atomic gases, which were first created decades prior.

For fermions such as KRb molecules, the statistical properties are determined by the Pauli exclusion principle, which prevents two particles from occupying the same quantum state [41]. Our experiments primarily involve identical KRb molecules in a single internal state, meaning that each molecule must occupy a different harmonic mode of the optical trap. At very low temperatures exactly one molecule occupies each mode up to the Fermi energy (Fig. 1.1b), a quantity determined by the particle number and trapping potential. Compared to Bose-Einstein condensates, where particles accumulate in the lowest energy state, the average energy of degenerate fermions saturates at a large fraction of the Fermi energy.

As discussed above, ultracold fermions collide in the p-wave channel, which has a large repulsive barrier preventing molecules from colliding at short range. This reduces the collision cross section at low temperatures, which has been measured for elastic collisions of atoms [42]. Elastic collisions are necessary for thermalization during evaporation, so different strategies were historically used to evaporate fermions to degeneracy. These included preparing distinguishable fermions in multiple internal states [40, 43], between which s-wave collisions can occur, and using magnetic atoms with dipole-mediated elastic collisions [44]. The former technique does not work with reactive molecules because inelastic collisions are also enhanced between distinguishable molecules, but we later demonstrate dipolar evaporation in experiments in both 2D and 3D.

1.1.4 Dipolar Interactions

Dipolar interactions are central to proposals for exploring many-body physics using molecules. The expression for the potential energy of two dipoles, which will reappear in various forms through-

out this thesis, is

$$V_{dd}(\mathbf{r}) = \frac{1}{4\pi\epsilon_0}\frac{\mathbf{d}_1 \cdot \mathbf{d}_2 - 3(\mathbf{d}_1 \cdot \hat{r})(\mathbf{d}_2 \cdot \hat{r})}{|\mathbf{r}|^3} \tag{1.1}$$

where $\mathbf{d}_1$ and $\mathbf{d}_2$ are the dipole moments of the two particles and $\mathbf{r}$ is the vector connecting them. Compared to contact interactions in ultracold atoms, which are spatially isotropic and occur at short range, dipolar molecules have long-ranged and anisotropic interactions. Stable, degenerate gases of atoms with magnetic dipole moments can also be produced [45], although the interaction strength between magnetic atoms is much smaller than between polar molecules[1] .

Polar molecules develop induced dipole moments in external electric fields, which strongly modify the dynamics. In previous experiments, the inelastic loss rate of molecules was found to increase rapidly with dipole moment, a behavior attributed to the attractive region of the dipolar potential reducing the p-wave barrier [46, 47]. By eliminating the attractive interactions using confinement to 2D, the reactive collisions were instead suppressed and the elastic collisions were enhanced ([48], Fig. 1.1c). In this thesis, we build on these results in 2D by working at larger dipole moments and using dipolar collisions to directly evaporate molecules.

Polar molecules can also be used to study resonant dipolar interactions, where multiple internal states are coupled. Even at zero field, where the induced dipole moment is zero, these interactions can lead to rotational state exchange (Fig. 1.1d). In this work, we measure two types of resonant interactions. First, we study controlled rotational state exchange in layered systems of molecules near zero field, building on the work of Ref. [49]. Second, we measure a new (though previously predicted) phenomenon where coupling between pairs of rotational states at high electric fields induces strong attractive or repulsive potentials.

1.1.5 Confinement Geometry

The accessible physics in experiments on polar molecules depends strongly on dimensionality, defined as the number of dimensions along which the thermal energy exceeds the harmonic frequency

[1] The conversion between magnetic and electric dipoles is given by $\left(\frac{d_e^2}{4\pi\epsilon_0}/\frac{\mu_0\mu_B^2}{4\pi}\right)^{1/2} \approx 108$, for $d_e = 1$ D. The largest magnetic dipole moment in a neutral atom is 10 μ_B for bosonic Dy, compared to the permanent electric dipole moment of KRb of 0.57 D.

of the confining potential. Optical dipole traps can be designed to confine atoms and molecules in specified geometries: for example, high-intensity optical lattices can be used to freeze out motion along one or more trap axes [50]. Because of the anisotropy of the dipolar potential, the sign and strength of interactions between molecules can be varied by controlling their density and motion relative to the orientation of the dipoles and the intermolecular axis.

Ultracold molecules were first formed in three-dimensional optical traps [14], where interactions between molecules such as reactive collisions typically depend on thermal energy [21]. In order to eliminate reactions, molecules were later pinned in 3D optical lattices. For sufficiently deep lattices, tunneling between sites does not occur and the molecule lifetime could be be extended past tens of seconds [51]. In lattices, where interactions occur at long range and with a quantized distribution of energies due to the fixed distances between particles and orientations of dipolar potentials [49], polar molecules could be used to study phenomena including superfluidity [52], spin-orbit coupling [53], and many-body localization [54]. An exciting recent experiment demonstrated microscopy of single molecules in an optical lattice [55]; combined with techniques demonstrated on KRb for increasing the lattice filling by associating molecules from atomic insulators [56], long-sought models of quantum magnetism may be realized in the near future.

A parallel technique for confining molecules to eliminate reactions involves trapping in optical tweezers, tightly focused laser beams that hold single molecules and can be arranged dynamically. Excited state molecules were recently formed in tweezers [57] and later produced in their ground state [58] and in configurable arrays of multiple tweezers [59, 60]. Tweezers are promising platforms for creating non-rectangular geometries such as triangular or kagome lattices and for studying few-body dynamics such as collisions [28].

The experiments described in this thesis involve molecules trapped in 3D and 2D. In 2D, where molecules occupy planes of a 1D optical lattice, the interactions combine features of both higher- and lower-dimensional systems since thermal motion is allowed within each plane but only long-range dipolar interactions occur between planes.

1.2 Contents

The dynamics of ultracold polar molecules arise from the complicated interdependence of the properties described above. For example, by manipulating the long-range intermolecular potentials using direct and resonant dipolar interactions, we can suppress or enhance the chemical reaction rate. In this work, I describe our progress in reaching quantum degeneracy with KRb and controlling interactions. The following chapters contain these topics, approximately in the order we conducted the experiments:

(2) Overview of the experimental procedure and recent modifications to the apparatus and methods, including gray molasses cooling of K and Rb, tunable lasers for associating atoms into molecules at non-zero electric fields, and rotational state-resolved imaging of KRb molecules.

(3) Electric field control system, including the high voltage electrodes and control loop and the procedures for measuring electric fields directly using molecules.

(4) Creation of degenerate KRb molecules in 3D using association in a degenerate atomic mixture and thermalization between Feshbach molecules and K atoms. We measure suppressed chemical reactivity at degeneracy, a phenomenon that still lacks theoretical explanation. Based on Refs. [61, 62].

(5) Suppressed density fluctuations in the degenerate molecular gas due to Pauli exclusion. This technique provides an alternative measurement of degeneracy and directly shows the role of quantum statistics in the momentum state distribution of the gas. Based on Ref. [62].

(6) Direct dipolar interactions between molecules in two dimensions. We reduced the reactive loss and were able to directly evaporate below the Fermi temperature in 2D using elastic collisions between molecules. Based on Ref. [63].

(7) Resonant dipolar interactions from couplings between KRb rotational states at particular

electric fields. We use this property to tune chemical reaction rates over several orders of magnitude and to evaporatively cool the molecules in 3D. Based on Refs. [64, 65].

(8) Rotational state-changing interactions between 2D layers of molecules, where the layers are addressed using precision electric field control and lattice stabilization. Based on Ref. [66].

(9) Summary of the present work and an outlook for short-term and long-term experiments with ultracold polar molecules.

In addition, this thesis contains the following two appendices:

(A) Analysis of electric field noise sources and outlook for improving the noise performance.

(B) Semiclassical calculation of the temperature dependence of two-body loss.

Chapter 2

Ultracold Molecule Apparatus

The KRb experiment is comprised of optical and electrical subsystems that have been described in previous group theses [67, 68, 69, 70, 71, 72]. In this chapter, I will briefly describe the general experimental procedure, and then highlight several recent additions and improvements to the apparatus: gray molasses cooling of both K and Rb, dynamic frequency tuning of STIRAP lasers for forming molecules at non-zero electric fields, and rotational state-resolved imaging of molecules.

2.1 Experiment Overview

Our experiment begins in the MOT chamber (Fig. 2.1), where K and Rb dispensers release high-temperature atomic gases. We cool and trap the atoms using magneto-optical trapping, with a quadrupole field generated by a pair of coils in the anti-Helmholtz configuration. The atoms are further cooled using gray molasses, described in detail in the next section. Next, we optically pump K into the hyperfine state $|F, m_F\rangle = |9/2, 9/2\rangle$ and Rb into $|2, 2\rangle$, and load the atoms into a deep quadrupole trap. To move the trapped atoms from the MOT chamber to the lower-pressure science cell, we translate the coils on a mechanical stage along the **z**-axis, transferring about 35% of the initial number at a temperature of 120 μK.

In the science cell, we perform plugged magnetic evaporation in the quadrupole trap down to 4 μK and load the atoms into a crossed optical dipole trap (ODT) formed by a pair of beams oriented along the **x**- and **z**-axes. By lowering the optical trap depth, we evaporate the atoms to

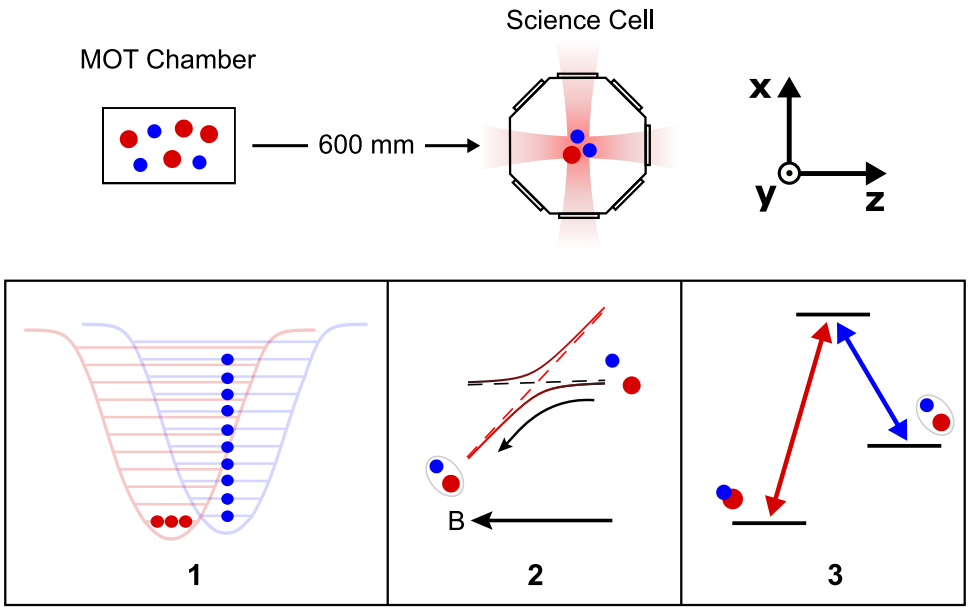

Figure 2.1: Experiment overview. The atoms are cooled in the MOT chamber, and loaded into a quadrupole trap and translated to the science cell. There they are evaporated to degeneracy (1), paired into Feshbach molecules using magnetoassociation (2), and transferred to the rovibrational ground state using STIRAP (3). The coordinate system shown is used throughout this thesis. Adapted from Ref. [61].

1 μK, and transfer K and Rb to states $|9/2, -9/2\rangle$ and $|1, 1\rangle$ using microwave adiabatic rapid passage at a magnetic field of 30 G. Further optical evaporation is performed to approximately 200 nK, creating a degenerate Fermi gas (DFG) of K and a Bose-Einstein condensate (BEC) of Rb (labeled (1) on Fig. 2.1), and the magnetic field is increased to 556 G. Weakly-bound Feshbach molecules are produced adiabatically by ramping the magnetic field through a Feshbach resonance at 546.6 G (2) [73, 74]. Using stimulated Raman adiabatic passage (STIRAP), in which the Feshbach state and a tightly-bound molecular state are connected through an excited state using two phase-coherent lasers (3), we associate molecules. KRb is formed in the rovibrational ground state $|N, m_N\rangle = |0, 0\rangle$ [14, 75], where N is the rotational angular momentum and m_N its projection onto the quantization axis. Figure 2.2 summarizes the number and temperature of the atoms and molecules throughout the experimental sequence [61].

At this stage, depending on the experiment, the molecules may be additionally trapped in optical lattices with 540 nm and 8 μm spacing, both with **y** as the axis of tight confinement. We generate electric fields and microwaves for manipulating the molecules using a set of six in-vacuum electrodes (Chapter 3), to which we apply voltages via feedthroughs on the outside of the vacuum chamber. To image the molecules after an experimental sequence, we reverse the STIRAP process and directly image the Feshbach molecules, which have an imaging cross section of 70% relative to K atoms. We have the capability to image the atoms and molecules along any of the **x**-, **y**-, and **z**-axes.

2.2 Gray Molasses Cooling

We use gray molasses cooling (GMC) on both atomic species to lower the temperature below the Doppler limit prior to loading into the quadrupole trap. This technique has been successfully demonstrated with a number of atomic and molecular species [76, 77, 78, 10]. GMC involves both bright and dark atomic states (hence "gray") [79, 80], in contrast to normal Sisyphus cooling [81]. Though many hyperfine sublevels are involved in the cooling of K and Rb, the basic principles of gray molasses cooling can be understood using a three-level system, illustrated in Fig. 2.3a. We

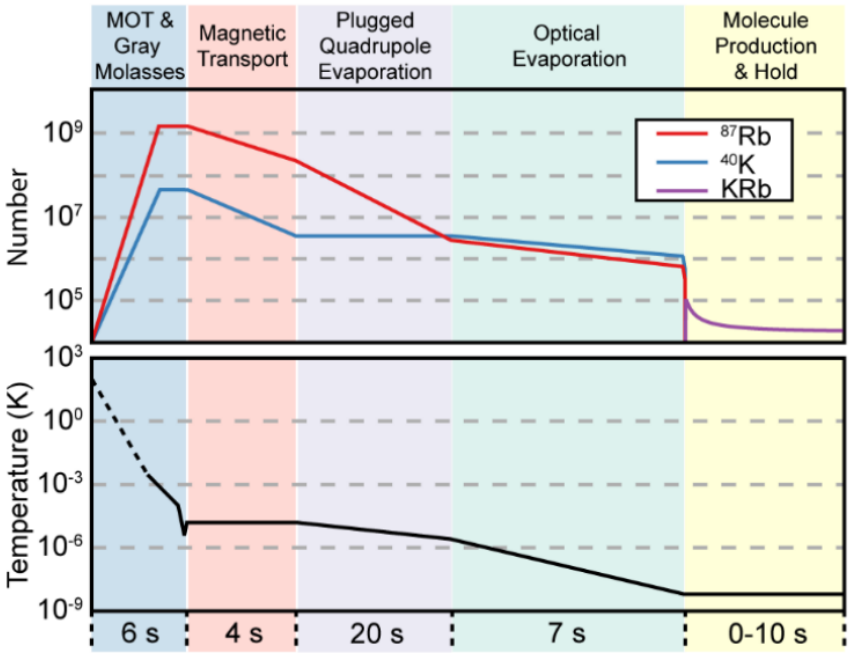

Figure 2.2: Atom and molecule conditions during the experimental sequence. This graphic is reproduced from Ref. [61] and describes the conditions for that work, which is the subject of Chapter 4.

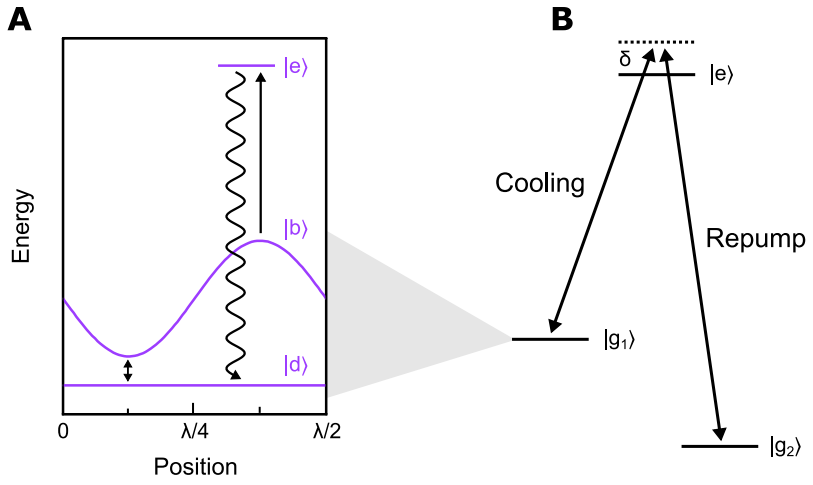

Figure 2.3: Schematic picture of Λ-enhanced gray molasses cooling (GMC). **(a)** GMC within a single hyperfine manifold. Atoms in the bright state $|b\rangle$ move along a potential landscape due to the spatial variation in light polarization and are pumped into the dark state $|d\rangle$ through the excited state $|e\rangle$. $|b\rangle$ and $|d\rangle$ are coupled near the potential minima by the motion of the atoms. **(b)** Λ-enhancement of GMC. In addition to the dark state structure of manifolds $|g_1\rangle$ and $|e\rangle$, connected by the cooling laser, forming a Λ system by adding a phase-coherent repump on $|g_2\rangle \rightarrow |e\rangle$ leads to additional cooling. $|b\rangle$ and $|d\rangle$ are hyperfine components of $|g_1\rangle$.

refer to the states shown as the "bright," "dark," and "excited" states ($|b\rangle$, $|d\rangle$, and $|e\rangle$).

GMC is performed using counterpropagating laser beams that form a polarization gradient. We consider the case of perpendicular linear polarizations (lin⊥lin) which create a spatially-varying polarization that rotates between σ^+ and σ^- circular polarizations. Gray molasses cooling is performed on transitions with $F \rightarrow F' = F$ or $F \rightarrow F' = F - 1$, where F and F' are the total angular momenta of the ground and excited states, respectively. For this structure, polarization-dependent linear combinations of hyperfine sublevels (with quantum number m_F) can always be constructed to form a dark state that is not coupled to the excited state. For example, if the local polarization is purely σ^+, the state with $m_F = F$ is dark. The bright states experience a spatially-varying potential because of the polarization gradient, and are higher in energy than the dark states because the light is blue-detuned of the transition to the excited state [50].

Consider an atom in state $|b\rangle$ starting in a potential minimum. As the atom moves away from the minimum, it loses kinetic energy and is eventually pumped to $|d\rangle$ through the excited state $|e\rangle$.

At very low velocities, the atom will remain in $|d\rangle$. However, at higher velocities, the atom may make a non-adiabatic transition back to the bright manifold $|b\rangle$, which occurs preferentially at the potential minima where the energy difference between $|b\rangle$ and $|d\rangle$ is minimized.

Additional cooling can be achieved using Λ-enhancement [82]. The GMC described so far occurs between the ground hyperfine manifold $|g_1\rangle$ and excited manifold $|e\rangle$ (Fig. 2.3b). A Λ system is formed by adding a phase-coherent laser to address $|g_2\rangle$, a second ground hyperfine manifold. We refer to these as the "cooling" and "repump" lasers, respectively. In the case where the cooling intensity is much larger than the repump intensity and when the Raman (two-photon) resonance condition is met, as shown in Fig. 2.3b, dark states are formed with primarily $|g_2\rangle$ character. Atomic motion detunes the lasers from two-photon resonance, so cold atoms accumulate in $|g_2\rangle$ while hot atoms are pumped into the cooling cycle on $|g_1\rangle$ (Fig. 2.3a), akin to velocity-selective coherent population trapping [83]. The lasers are blue-detuned from the excited state by the one-photon detuning δ, a parameter that affects the final atomic temperatures achieved.

2.2.1 Rubidium

We perform GMC on ^{87}Rb on the D_2 line ($5^2S_{1/2} \rightarrow 5^2P_{3/2}$) [78, 84]. Since this is the same line used for imaging and MOT cooling, no additional lasers are needed. The imaging transition is $F = 2 \rightarrow F' = 3$ (Fig. 2.4); during gray molasses, we tune this laser instead to $F = 2 \rightarrow F' = 2$. The ability to dynamically change the frequency of this laser is an existing capability of the experiment [67, 71]: the Rb probe laser is offset locked to a second Rb laser (which itself is locked to an atomic vapor cell), allowing fast frequency changes over hundreds of MHz. To generate a phase-coherent repump tone on the $F = 1 \rightarrow F' = 2$ transition, separated by 6.834 GHz from the trap light, we use a custom Newport free-space electro-optic modulator (EOM, model 4851). This modulation is added prior to the tapered amplifier (TA) used for amplifying the MOT light, so the GMC light follows the same path as the MOT light in the experiment [71]. Driving the EOM with 2 W of RF power yields a cooling/repump optical power ratio of about 4. The lowest temperature measured immediately after the gray molasses stage of cooling is 7(2) μK, and adding gray molasses improves

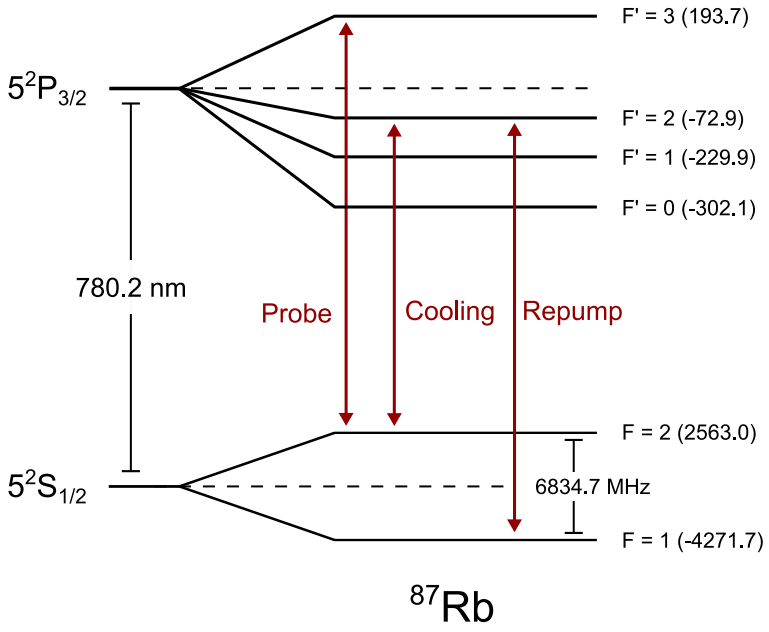

Figure 2.4: Level diagram of Rb D2 line. The imaging probe addressing $F = 2 \rightarrow F' = 3$ is tuned to the $F = 2 \rightarrow F' = 2$ transition for GMC and a repump tone is added using an EOM. Frequencies in parentheses represent detuning in MHz from the dashed lines, and are from Daniel Steck's excellent ^{87}Rb reference [84].

the Rb number after magnetic evaporation by about 20%.

2.2.2 Potassium

Performing GMC on ^{40}K is more complicated due to the atomic structure: the hyperfine splitting of the D_2 line ($4^2S_{1/2} \rightarrow 4^2P_{3/2}$) is relatively small compared to the linewidths, making it impractical to address individual F' levels. Instead, we use the D_1 line ($4^2S_{1/2} \rightarrow 4^2P_{1/2}$) for GMC, necessitating an additional laser system at 770 nm. Figure 2.5 shows the level structure of the D1 lines of ^{39}K and ^{40}K. The natural abundance of ^{40}K is only 0.012%, compared to 93% for ^{39}K; this means that if we want to use an unenriched vapor cell to provide an atomic frequency reference, we need to lock the laser to ^{39}K. The cooling and repump transitions in ^{40}K are $F = 9/2 \rightarrow F' = 7/2$ and $F = 7/2 \rightarrow F' = 7/2$, respectively, separated by the ground state splitting of 1285.8 MHz plus the two-photon detuning Δ. Both laser frequencies are tuned to the blue side of $F' = 7/2$ by the one-photon detuning δ. We chose to use the $F = 1 \rightarrow F' = 2$ transition for spectroscopy, which is the closest in frequency to $F = 9/2 \rightarrow F' = 7/2$. The frequency difference between these two transitions is 474 MHz, a gap we bridge using acousto-optic modulators (AOMs).

Figure 2.6 shows the optical layout of the D1 laser system. We use a custom distributed Bragg reflector (DBR) laser manufactured by Photodigm (model PH770DBR080T8). This is the same type of laser that we use for the K and Rb MOT and imaging systems. The DBR architecture consists of a gain region abutting a Bragg reflector, which is a periodic grating that reflects only a single longitudinal mode. Compared to an external cavity diode laser (ECDL), which has an external reflector to provide feedback, DBRs are monolithic and more robust to temperature and vibration, at the cost of broader linewidths due to the shorter cavity length. Another benefit of DBRs is that they can provide high output powers (>100 mW), which is sufficient for seeding tapered amplifiers (TAs) and providing light for imaging and optical pumping using only a single laser.

We use two AOMs to connect the spectroscopy and cooling transitions. On Fig. 2.6, AO1 provides a positive frequency shift f_{AO1} and AO2, which is in a double-pass configuration, provides

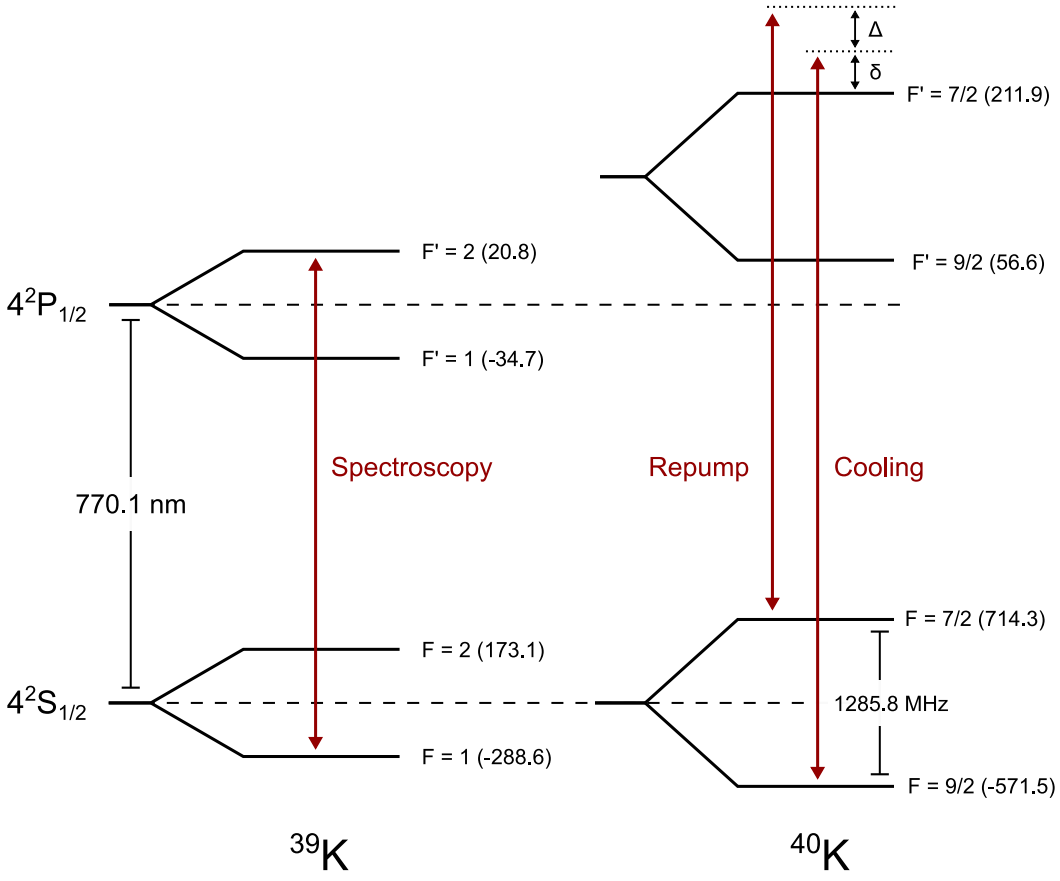

Figure 2.5: Level diagram of the ^{39}K and ^{40}K D1 lines. The D1 laser is locked to ^{39}K and AOMs are used to shift the laser frequency for GMC cooling on ^{40}K. Frequencies in parentheses represent detuning in MHz from the dashed lines, and are from Tobias Tiecke's invaluable K reference [85].

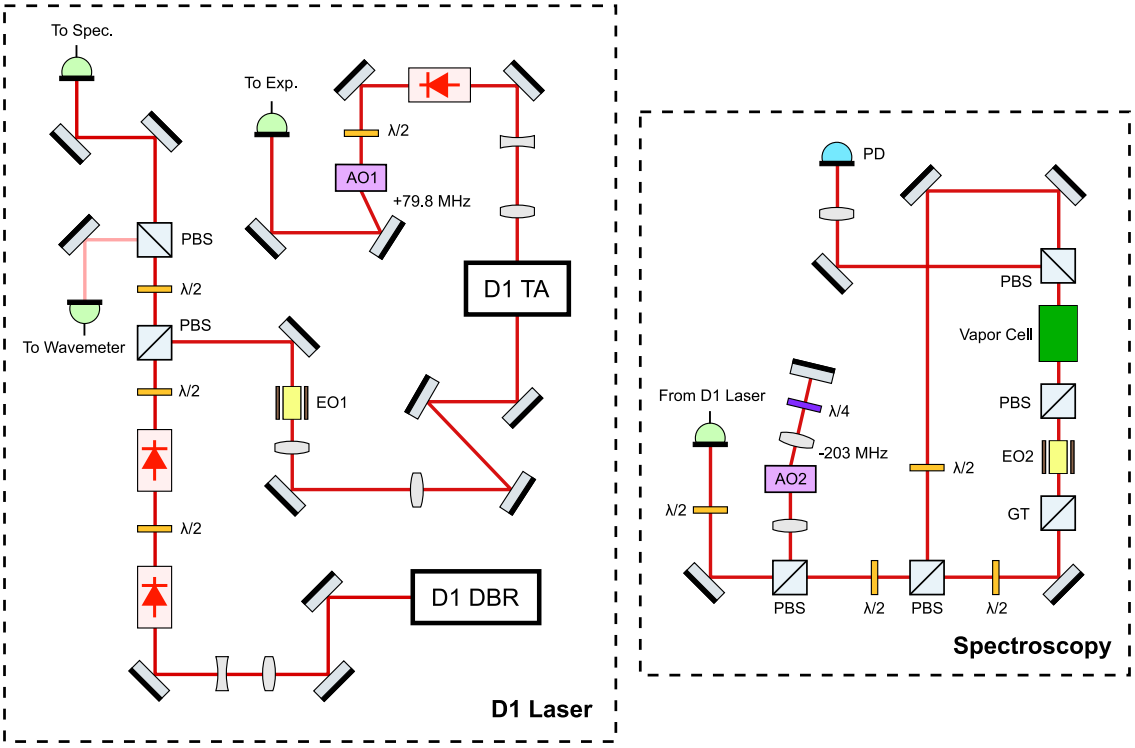

Figure 2.6: Optical layout for K D1 gray molasses. The output light from a DBR at 770.1 nm is split between the tapered amplifier (TA) going to the experiment and the vapor cell spectroscopy using half-waveplates ($\lambda/2$) and polarizing beamsplitters (PBS). The frequency of the light going to the experiment is shifted relative to the atomic reference by acousto-optic modulators (AO1 and AO2). The repump for GMC is generated by an electro-optic modulator (EO1) resonant with the ground hyperfine splitting of 1285.8 MHz. The vapor cell lock is achieved using standard frequency modulation spectroscopy [86], with 20 MHz sidebands added to the probe beam prior to the vapor cell using EO2 (Thorlabs model EO-PM-R-20-C1).

a negative frequency shift f_{AO2}. The frequency of the light going to the experiment f_{exp} is

$$f_{\mathrm{exp}} = f_{\mathrm{spec}} + f_{\mathrm{AO1}} + 2f_{\mathrm{AO2}} \tag{2.1}$$

where f_{spec} is the frequency of the spectroscopic $F = 1 \rightarrow F' = 2$ transition. Considering the 474 MHz difference between the relevant transitions in ^{39}K and ^{40}K, the one-photon detuning δ is

$$\delta = f_{\mathrm{exp}} - f_{\mathrm{spec}} - (474\ \mathrm{MHz}) \tag{2.2}$$

For our experimental parameters $f_{\mathrm{AO1}} = 79.8$ MHz and $f_{\mathrm{AO2}} = 203$ MHz, $\delta = 11.8\ \mathrm{MHz} \approx 2\Gamma$, where $\Gamma = 5.96$ MHz is the natural linewidth of the excited state of the ^{40}K D1 line [85]. The two-photon detuning Δ is the difference between the frequency of EO1, which generates the repump tone, and the ground hyperfine splitting of 1285.8 MHz. Similarly to Rb, we use a Newport free-space EOM (model 4421) to generate sidebands with about 30% of the carrier power.

The cooling performance depends strongly on δ and Δ [76]. We first scan δ and measure the K number after loading into the quadrupole trap in the MOT region of the experiment (Fig. 2.7a). δ increases with $2f_{\mathrm{AO2}}$, and since AO2 is in a double-pass configuration its frequency can be changed by about ± 10 MHz without significantly reducing the diffraction efficiency. Atom heating occurs if δ is nearly resonant with $F' = 7/2$ and appears as atom loss because the quadrupole trap has a finite trap depth. The atom number is essentially flat with δ over 6Γ, but drops sharply near resonance (gray line).

Δ shows a similar dependence (Fig. 2.7b). We vary Δ using EO1 (Fig. 2.6), where increasing the modulation frequency decreases Δ since the repump beam is derived from the negative EOM sideband. The K number peaks on two-photon resonance ($\Delta = 0$, gray line) and remains high for relatively large detunings on the red side of resonance ($\Delta < 0$). For $\Delta > 0$, however, the atoms are strongly heated and lost from the trap, in qualitative agreement with simulations of Λ-enhanced gray molasses in ^{6}Li [82]. We operate with $\Delta = -0.1$ MHz, very near two-photon resonance. Introducing GMC for K lowered the temperature after molasses to 10(2) μK and improved the number after magnetic evaporation by a factor of five, to about 8×10^6 at most.

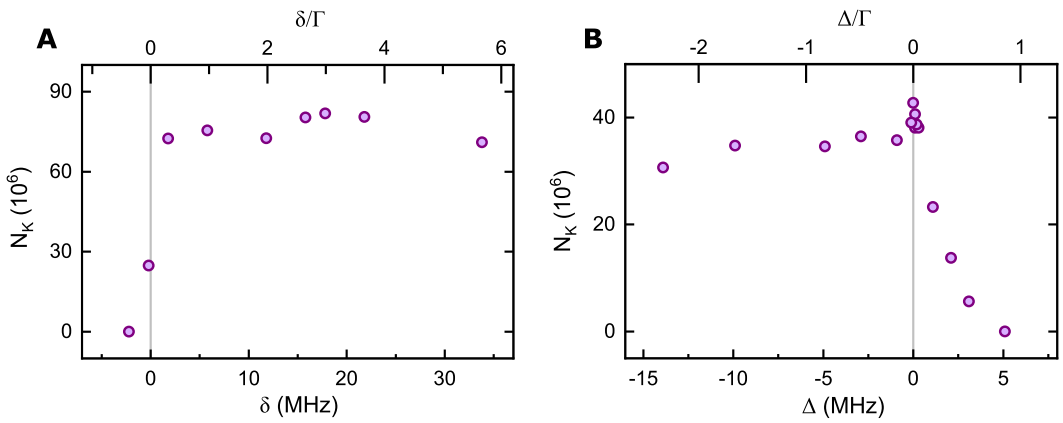

Figure 2.7: K gray molasses parameters, in units of MHz and Γ. **(a)** One-photon detuning δ. The atom number drops sharply near resonance with $F = 9/2 \rightarrow F' = 7/2$. **(b)** Two-photon detuning Δ. The number peaks on resonance, and drops on the blue side of resonance. This data is taken prior to optical pumping and loading into the quadrupole trap, so the imaged atom number is lower than (a).

2.3 Tunable STIRAP

The properties of polar molecules vary with electric field, as we explore in subsequent chapters. For instance, we directly evaporated KRb at 6.5 kV/cm, where the induced dipole is large [63], we used rotational state resonances to shield KRb against chemical reactions at 12.72 kV/cm [64, 65], and we associated atoms into degenerate molecules at 0 kV/cm [61]. Chapter 3 describes our methods for stabilizing large electric fields.

In previous works, STIRAP has only been used at or near zero field [14]. In order to study molecules at higher fields, the molecules would first be associated at zero field and then the field ramped up and allowed to settle, a process that takes up to 100 ms. If there are field gradients or curvatures present, changing the field distorts the molecular cloud. Additionally, dwelling in a large electric field can result in reduced molecule number because of chemical reactions enhanced by attractive dipolar interactions [65, 46].

The solution is to associate the molecules directly at different electric fields. The level diagram for STIRAP is shown in Fig. 2.8 and is described in detail in Refs. [14, 68]. Using magnetoassociation, K and Rb atoms are weakly paired together into Feshbach molecules ($|f\rangle$), which have

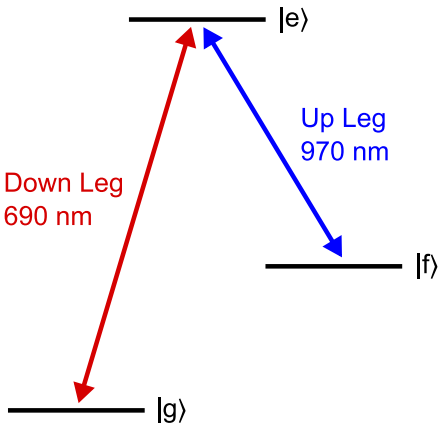

Figure 2.8: STIRAP association. The Feshbach $|f\rangle$ and ground $|g\rangle$ molecular states are coherently connected by two lasers through an intermediate excited molecular state $|e\rangle$. The energy difference between $|f\rangle$ and $|g\rangle$ is 125.3 THz [14].

magnetic field-dependent binding energies of about 500 kHz and internuclear separations of 100 a_0 [73]. Using STIRAP, the molecules are transferred to the ground rovibrational state $|g\rangle$ via lasers resonant with the intermediate excited state $|e\rangle$. We refer to the laser connecting $|f\rangle \rightarrow |e\rangle$ at 970 nm as the "up leg" and to the laser connecting $|g\rangle \rightarrow |e\rangle$ at 690 nm as the "down leg." Due to the large internuclear separation of the Feshbach molecules, which behave much like their constituent K and Rb atoms (see Chapter 4), $|f\rangle$ has essentially zero dipole moment [87]. By contrast, $|g\rangle$ has a permanent electric dipole moment of 0.57 D and $|e\rangle$ can also have a non-zero dipole moment. This means that both STIRAP laser frequencies must be adjusted in order to associate molecules at non-zero electric fields.

The STIRAP lasers are locked to a stable optical cavity, which establishes a fixed frequency reference. In the previous iteration of the STIRAP laser system, the frequencies addressing the molecules were offset from the cavity frequency by AOMs [71]. Since the deflection angle of the diffracted beam from an AOM varies with frequency, the STIRAP frequencies could only be varied by several MHz without substantial realignment. Considering that the energy of $|g\rangle$ changes by nearly 1 GHz between 0 and 10 kV/cm, a different approach was needed. In this section, I describe two approaches we used for associating molecules at non-zero electric fields: first, we took advantage

of an avoided crossing in the excited state to associate molecules at 4.5 kV/cm, and second, we added fiber EOMs to offset the STIRAP lasers from the cavity by variable frequencies without realignment.

2.3.1 "Accidental Resonance" at 4.5 kV/cm

Ideally, we could associate molecules at any non-zero electric field. A close second best, however, would be the ability to associate the molecules at any single large electric field. Here, the induced dipole moments would be large enough to see strong interactions between molecules, and we would bypass the "forest" of avoided crossings in $|1,0\rangle$ below 500 V/cm (Fig. 3.3). We decided to look for an excited state at non-zero electric field with the same energy difference as $|f\rangle \rightarrow |e\rangle$ at zero field; in other words, a state and electric field for which we would not have to change the up leg detuning.

The advantage of this approach is that we would only need to change one set of fixed AOMs to adjust the down leg frequency. Since the Stark shift of $|g\rangle$ is known, we should be able to calculate the correct frequencies. The disadvantage is that we did not know whether such a state existed at an accessible electric field, and whether the properties of such a state (angular momentum, Franck-Condon factors, etc.) would allow STIRAP to the ground state. Prior spectroscopy on KRb identified three states within 2 GHz of $|e\rangle$ at zero field [14].

Our spectroscopy method was very simple: we prepared molecules in the Feshbach state $|f\rangle$ at zero electric field, ramped the field to a non-zero value, and applied a strong pulse from the up leg laser locked at the zero-field STIRAP frequency. The signal that would indicate a candidate state was the depletion of Feshbach molecules. To our great surprise, we found that $|f\rangle$ was depleted at 4.5 kV/cm (Fig. 2.9a). Besides the resonances at 0 and 4.5 kV/cm, we didn't identify any other resonances at the zero-field frequency.

To better understand the behavior of the excited state, we tracked the resonant state from 4.5 kV/cm back to 0 kV/cm. Since we anticipated that the Stark shift would be larger than our tuning range using the up leg AOMs, we used a different method for addressing this state:

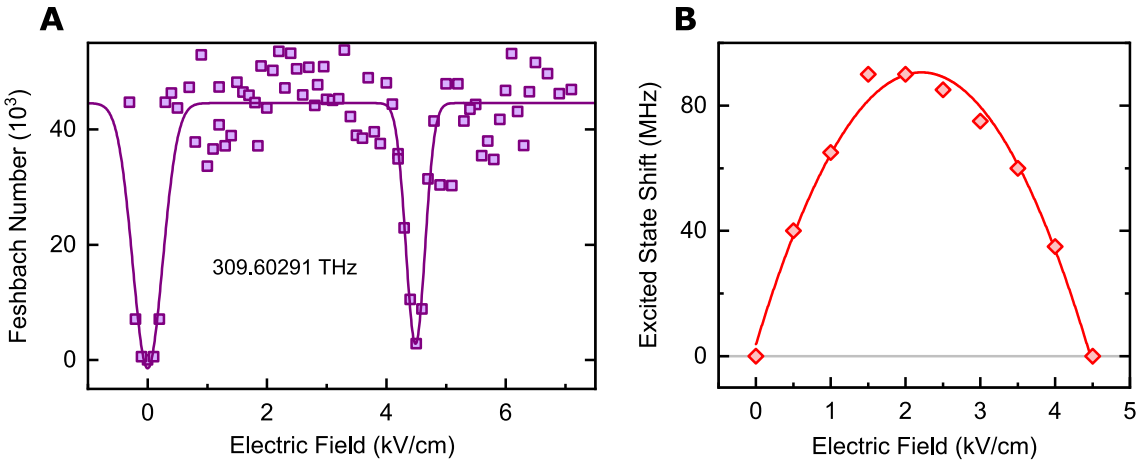

Figure 2.9: Searching for $|f\rangle \rightarrow |e\rangle$ resonances at non-zero electric field. **(a)** Scanning the electric field with the up leg frequency fixed to 309.60291 THz. We identify resonances at 0 and 4.5 kV/cm. **(b)** The high-field resonance connects to the zero-field resonance. The solid line is a guide to the eye.

we unlocked the up leg from the cavity, allowing continuous tuning of the frequency using the diode current, and measured the frequency using a wavemeter. The frequency resolution of the wavemeter is coarse ($\pm$10 MHz) and humidity and temperature changes lead to day-to-day offsets in its reading, but it enabled us to quickly measure relative frequency shifts without changing the frequency locking setup.

We found that the state at 4.5 kV/cm connected to the state at 0 kV/cm, shifting up in energy by about 85 MHz before apparently undergoing an avoided crossing with a higher-energy state with a Stark shift of opposite sign (Fig. 2.9b). We therefore expected that STIRAP would still connect to the ground state using the original STIRAP polarizations. Relative to 0 kV/cm, the required down leg frequency increases by 239 MHz. Previously, there was a -77 MHz AOM on the output of the down leg; by replacing this with a $+162$ MHz AOM, we corrected the down leg frequency to operate at 4.5 kV/cm and successfully associated ground state molecules.

The induced dipole moment of the ground state $|0, 0\rangle$ at 4.5 kV/cm is 0.2 D, or about one-third the permanent dipole moment. This made it a good starting point for measuring dipole-dipole interactions in the 2D lattice [63], as described in Chapter 6, particularly since the ratio of elastic to

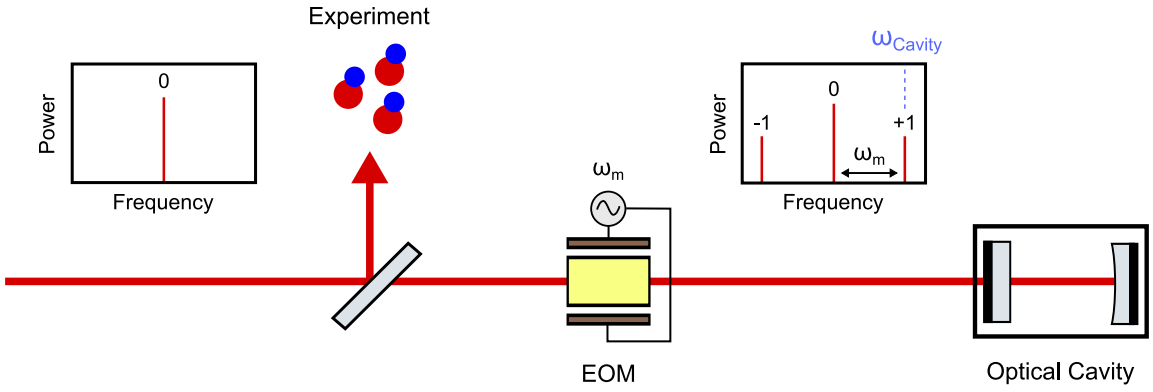

Figure 2.10: Dynamic laser frequency tuning using an EOM. The 0th order laser frequency addresses the molecules and also passes through an EOM, where frequency sidebands are added at frequency offset ω_m. One of the 1st order sidebands is locked to an optical cavity. By varying ω_m, the frequency of the carrier relative to the cavity can be adjusted.

inelastic collisions is predicted to be maximized near this dipole moment in quasi-2D confinement [88]. In addition, for our later studies of chemical reactions between $|1,0\rangle$ molecules (Refs. [64, 65] and Chapter 7), associating molecules at 4.5 kV/cm and then ramping to the target field allowed us to avoid the $|1,0\rangle$ hyperfine state crossings at low field. The primary disadvantage of using fixed AOMs to shift the STIRAP frequency relative to the optical cavity is inflexibility; in order to conduct experiments at zero field (where the molecules interact most strongly via spin exchange, for example) we would need to replace the output AOM again and realign the lasers.

2.3.2 Fiber EOMs

To compensate for the ground and excited state Stark shifts and perform STIRAP at arbitrary electric field, we need a method for dynamically changing the laser frequencies without realigning the laser system. The frequency reference for the STIRAP system is a stable optical cavity, with a free spectral range (FSR) of 1.3 GHz and a linewidth of 30 kHz, described in Ref. [71]. In order to change the STIRAP frequency, we change the offset frequency between the cavity and the lasers.

We use a fiber electro-optic modulator (EOM) for this purpose. The basic principle is illustrated in Fig. 2.10. The unmodulated STIRAP frequency (also called the "carrier" or "0th

order" frequency) is split into two paths, the first addressing the molecules and the second passing through an EOM. EOMs consists of a crystalline waveguide (often $LiNbO_3$, as for the EOMs we use) between two electrodes. Due to the Pockels effect, the refractive index of $LiNbO_3$ depends on the electric field. By applying a voltage to the electrodes, light propagating through the waveguide picks up a variable phase, linear in the applied voltage and crystal length. If a time-varying voltage is applied, as shown in Fig. 2.10, the frequency spectrum of the output light changes. Denoting the carrier frequency ω, the electric field prior to entering the EOM is

$$\vec{E} = \vec{E}_0 e^{i\omega t} \tag{2.3}$$

After the EOM, the field is shifted by a sinusoidal phase with amplitude ϕ and frequency ω_m:

$$\vec{E}_{\text{mod}} = \vec{E}_0 e^{i\omega t + i\phi \sin \omega_m t} \tag{2.4}$$

This can be expanded as [86]:

$$\vec{E}_{\text{mod}} = \vec{E}_0 \sum_{n=-\infty}^{\infty} J_n(\phi) e^{i(\omega + n\omega_m)t} \tag{2.5}$$

where $J_n(\phi)$ are Bessel functions of the first kind. Therefore, the effect of sinusoidal modulation is to add sidebands offset from the carrier frequency by integer multiples of the modulation frequency ω_m. The nth sideband (with frequency $\omega + n\omega_m$) has power $|J_n(\phi)|^2$, so the power in each sideband can be varied by changing the modulation depth (often represented $|\phi/\pi|$). Most EOMs specify V_π, or the voltage across the electrodes such that $\phi = \pi$. Relating the modulation depth, V_π, and the applied peak voltage V_p, we have:

$$\frac{V_p}{V_\pi} = \frac{\phi}{\pi} \tag{2.6}$$

Compared to an AOM, where the angle of diffraction depends on the modulation frequency, the EOM does not change the light propagation direction.

After the EOM, the light contains frequency sidebands at integer multiples of ω_m (Fig. 2.10). Only the 1st order sidebands are shown, since we generally operate with small modulation depths. We lock one of the 1st order sidebands to the cavity by the PDH technique [89]. In terms of the

cavity frequency ω_{cavity}, which we take to be fixed, the laser frequency ω addressing the molecules is $\omega = \omega_{\text{cavity}} \pm \omega_m$, where the sign depends on the sideband used for locking.

We use both free space and fiber EOMs in our experiment. In general, EOMs trade off between V_π and insertion loss, or the fraction of optical power lost propagating through the EOM. The free space modulators in the experiment have crystal sizes with cross sections of about 1 mm and can handle intensities greater than 1 W/mm^2 with only 10% power loss; the downside is that $V_\pi \approx 30$ V, necessitating watts of RF power to achieve the needed sideband depth. Most of the free space modulators we use incorporate the crystal and electrodes as the capacitor in a resonant LC circuit, reducing V_π but also limiting the frequency tunability. For EO1 in Fig. 2.6, which adds the repump tone for gray molasses, these characteristics are acceptable because the drive frequency is fixed at 1285.8 MHz, the 1st order (repump) power only needs to be about 30% of the carrier (cooling) power, and low insertion loss is essential for seeding the TA.

For fiber modulators, the crystal forms a single-mode optical waveguide with a core size of only a few μm. This means that the electric field can be much higher than for a free space modulator for an equivalent applied voltage. Another benefit to the small crystal size is electric field homogeneity. The wavelength of 10 GHz radiation in glass is 2 cm, which leads to substantial inhomogeneity across mm-size crystals and reduces the modulation efficiency. For fiber EOMs, by contrast, the small crystal size allows modulation frequencies greater than 40 GHz, a common frequency for telecommunications applications. Fiber modulators typically have higher insertion loss, reaching as high as 6 dB (75% power lost) for short wavelengths. One contributor to insertion loss is photorefraction due to light absorption by impurities in $LiNbO_3$ below 700 nm [90]. This effect generally worsens with higher optical power, limiting the power handling capability of EOMs at the down leg wavelength of 690 nm.

Our primary requirements are sufficient sideband power for PDH locking, meaning that the product of the input power, the insertion loss, and the sideband fraction at maximum drive power exceeds a few 100 μW, and broadband frequency tuning over the cavity FSR of 1.3 GHz. We chose to use fiber EOMs made by Jenoptik (models PM690 and PM970). The insertion loss of these

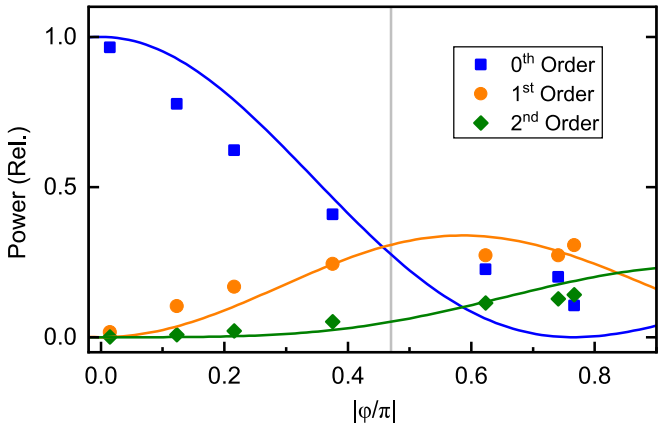

Figure 2.11: Up leg sideband power vs. modulation depth at 125 MHz modulation. The power in the 1st and 2nd sidebands is measured interferometrically (points) and compared to theory (lines, Eq. 2.5). The measured powers are averages of positive and negative orders, which should be identical. The theory curves are calculated using the specified $V_\pi = 4.9$ V. We operate at $|\phi/\pi| \approx 0.47$ (gray line), which corresponds to a drive power of about 17 dBm.

EOMs is specified to be 4 dB, though in practice it is somewhat higher due to mode-matching inefficiencies between the down and up leg laser modes and the fiber. The maximum optical input power is 20 mW; assuming worst-case 8 dB insertion loss and 30% sideband power, this leaves 1 mW available for PDH locking.

V_π for these EOMs is specified to be between 3.5-9 V for broadband modulation between DC and 3 GHz, depending on the wavelength and modulation frequency. We measure the up leg sideband powers interferometrically by frequency-shifting unmodulated light and beating it against the modulated light (Fig. 2.10). This allows us to measure the relative powers of the carrier and sideband tones (Fig. 2.11). Modulating at 125 MHz and assuming $V_\pi = 4.9$ V, as specified for low-frequency modulation, we find good agreement with the predicted carrier and 1st and 2nd sideband powers (Eq. 2.5) up to a modulation depth of $|\phi/\pi| = 0.75$. The 1st order sideband power is maximized at $|\phi/\pi| = 0.6$, but we choose to operate at $|\phi/\pi| = 0.47$ to reduce the 2nd order sideband power. This corresponds to an RF drive power of only 17 dBm.

Figure 2.12 shows the optics layout for the STIRAP laser system, redesigned in order to accommodate the fiber EOMs. The down leg and up leg systems are similar: a "primary" ECDL

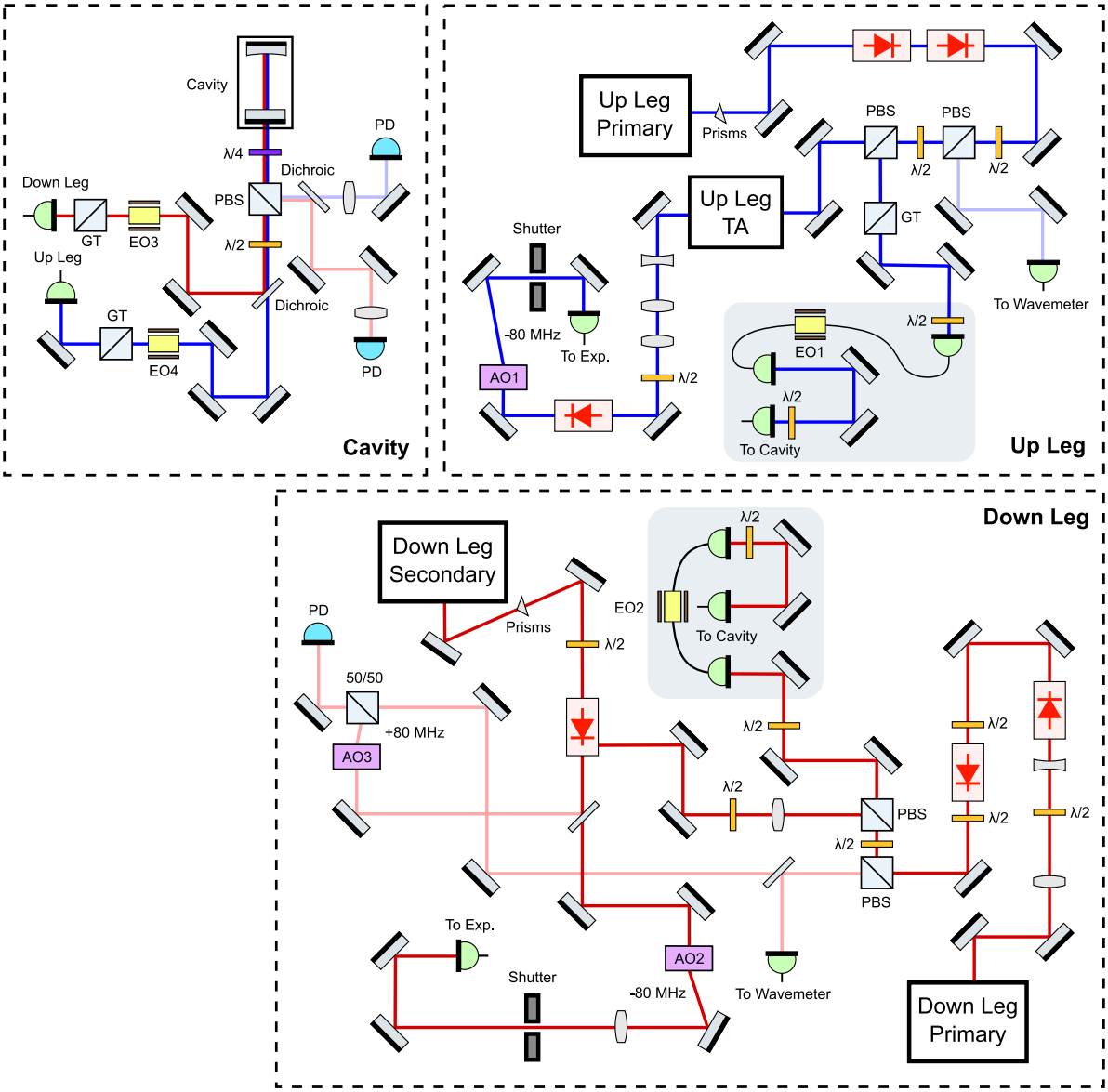

Figure 2.12: Optical layout for STIRAP lasers. Up leg and down leg primary lasers are ECDLs that seed a TA and secondary laser diode, respectively, to generate sufficient power for STIRAP. Both beams have sidebands added using fiber EOMs (EO1 and EO2, gray squares), and the 1st order sidebands are locked to a stable optical cavity. By varying the sideband frequency, the carrier frequency going to the experiment shifts correspondingly.

generates light that is split between two paths, similarly to the schematic picture (Fig. 2.10). One path goes through the fiber EOM (highlighted in gray) and then to the optical cavity, and the second path is amplified and goes to the experiment. To amplify the up leg we use a tapered amplifier (TA) and to amplify the down leg we use a "secondary" high-power laser diode, seeded using primary light coupled backwards through the rejection port of an optical isolator. Previously, the down leg secondary was seeded using light transmitted through the cavity, which had a very clean optical mode and frequency spectrum. We compared the STIRAP efficiency seeding the secondary with the cavity transmission and the primary light and found they were nearly identical. To monitor the seeding of the secondary diode, which depends sensitively on alignment and diode current, we interfere primary and secondary light and measure the power of the beat signal.

One additional change we made to the STIRAP system was replacing the output shutter for the down leg. Even with the AOM used for switching the output (AO2, Fig. 2.12) disabled, a few μW of scattered light is coupled through the fiber to the molecules. This can strongly affect the measured lifetime by depleting the ground state; at zero electric field, we measured an effective doubling of the two-body loss rate due to the down leg. We replaced the preexisting shutter with a high speed shutter from Stanford Research Systems (model SR476), which reduced the shutter closing time from 5 ms to 0.5 ms.

The STIRAP frequency offsets from the cavity depend on the frequency and order of both the fiber EOMs and fixed AOMs on the outputs (AO1 and AO2, Fig.2.12). Figure 2.13 summarizes the frequency offset of the STIRAP lasers from the optical cavity. The energy difference between $|f\rangle$ and $|e\rangle$ decreases with electric field (see the following section) and the energy difference between $|e\rangle$ and $|g\rangle$ increases with electric field (see Chapter 3), so the frequencies of the up and down leg must move different directions. We use the -1st order to lock the down leg, meaning the STIRAP frequency increases as the fiber EOM frequency increases, and the $+1$st order to lock the up leg. To dynamically change the STIRAP frequencies during the experiment, we drive the fiber EOMs using a programmable source that can ramp smoothly between frequencies. Since the frequency step size is small compared to the cavity linewidth (30 kHz, per Ref. [71]) and the ramp rate is small

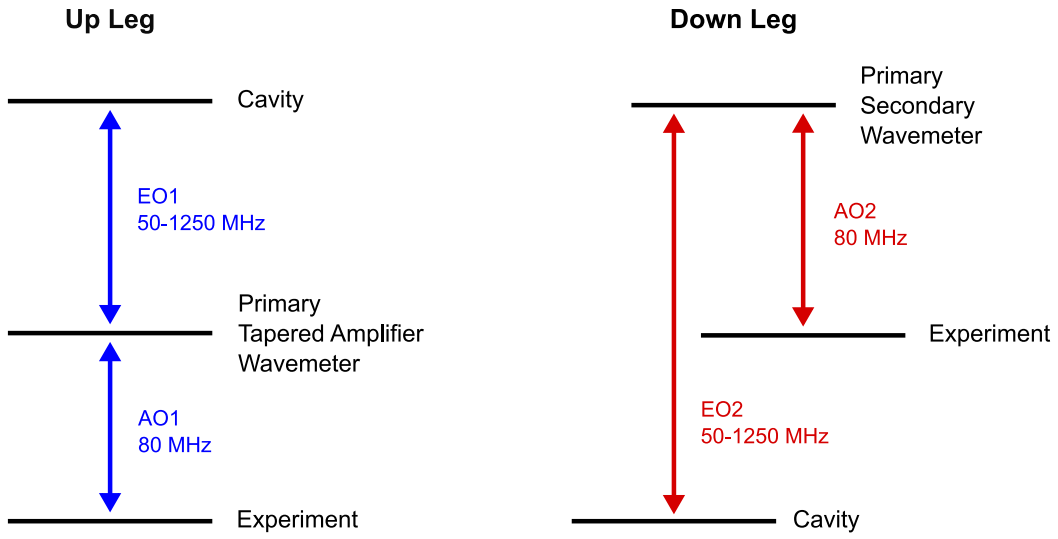

Figure 2.13: STIRAP frequency detunings vs. AOM and EOM frequencies. Labels refer to Fig. 2.12.

relative to the PDH lock bandwidth (> 1 MHz), the EOM frequency can be changed dynamically over hundreds of MHz.

2.3.3 Excited State Spectroscopy

Using these tools, we measure the Stark shift of the excited state. We measure this frequency shift using the up leg alone, on the assumption that the Feshbach state has a negligible dipole moment. The measurements shown in Fig. 2.14 were taken over months and used multiple methods for varying the up leg frequency. Prior to adding the fiber EOMs, for frequency shifts greater than several tens of MHz, the up leg AOM could not be scanned far enough while remaining locked to the cavity without needing realignment. In this case—similarly to Fig. 2.9b, the data from which is reproduced in Fig. 2.14—we unlocked the up leg from the cavity and measured the frequency using the wavemeter. These points are represented as diamonds. When the laser could be locked to the cavity (that is, for small frequency deviations from the zero-field value prior to adding the EOM, and at any field after adding the EOM), we locked the laser and scanned the frequency using the AOM/EOM. These points are represented as circles. All frequencies are referenced to the zero-field up leg frequency of approximately 309602.91 GHz, although our wavemeter is uncalibrated and

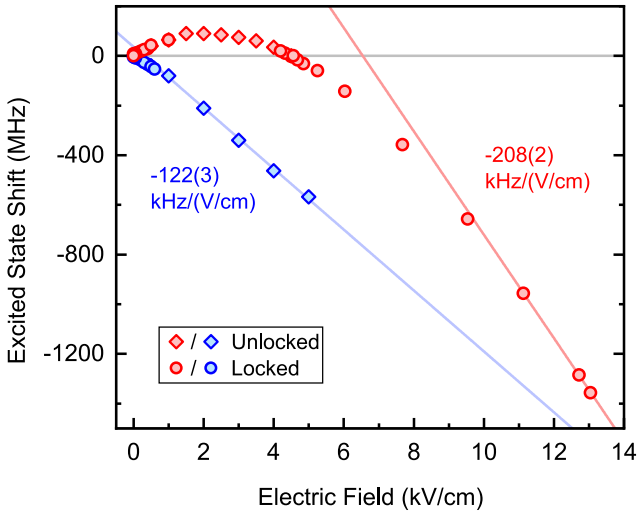

Figure 2.14: Stark shift of the intermediate state used for STIRAP. We identify an upper and lower state, and use the upper state for molecule formation at non-zero electric fields. Diamonds correspond to fields where the laser is unlocked and the frequency is measured using a wavemeter, and circles are fields where the laser is locked and the frequency is scanned using an AOM/EOM.

there may be tens of MHz uncertainty on this reference value.

We observe two states originating near the zero-field frequency, split by about 16 MHz at zero field. At high electric fields, the Stark shift of the upper state is -208(2) kHz/(V/cm). This is equivalent to the slope of the ground state at over 25 kV/cm, corresponding to a dipole moment of 0.41 D. The lower state has a slightly smaller slope, although presumably it approaches the slope of the upper state as they come together at higher electric fields. Using this spectroscopy, we performed STIRAP at 0, 1, 2, 4.5, and 12.72 kV/cm, electric fields we use in the subsequent experiments. The STIRAP efficiency drops from 85-90% at zero field to about 65% at 12.72 kV/cm, possibly due to the changing angular momentum character of the excited state at large electric fields.

2.4 State-Resolved Imaging

In many of the experiments in subsequent chapters we perform spectroscopy on the rotational states of KRb, most frequently addressing the $|0,0\rangle \rightarrow |1,0\rangle$ rotational transition. For example, the most precise way to measure the electric field is to measure the frequency spacing of these states,

which is approximately 2.228 GHz at zero electric field. In order to image molecules, we essentially reverse the molecule formation process. After an experimental sequence, we use STIRAP to convert $|0,0\rangle$ molecules to Feshbach molecules, and then we directly image Feshbach molecules using the K imaging light. Importantly, the STIRAP dissociation is state-selective, meaning that it only converts the state $|0,0\rangle$ back to Feshbach molecules, though it also depletes other rotational states at certain electric fields.

In the presence of total molecule number variation, imaging only one state presents a problem for rotational spectroscopy: how can you differentiate between a 75% efficient pulse on 20,000 molecules and a 50% efficient pulse on 10,000?[1] The solution is to normalize the number in each rotational state against the total molecule number by performing state-resolved imaging, where the numbers in states $|0,0\rangle$ and $|1,0\rangle$ are both counted. In the following subsections I discuss two methods for overcoming the state-selectivity of STIRAP and imaging both states:

(1) "Stern-Gerlach" imaging, where the two rotational states are separated spatially in time of flight using an electric field gradient

(2) *in situ* imaging, our current method, where the states are imaged sequentially while still optically trapped

2.4.1 Stern-Gerlach Imaging

In a series of foundational quantum mechanics experiments, Otto Stern and Walther Gerlach demonstrated the quantization of angular momentum by splitting a beam of silver atoms according to electron spin using an applied magnetic field gradient [91]. This technique and analogues based on differential optical forces [92] are used regularly in experiments on ultracold atoms to measure populations in hyperfine states.

Here we instead use an applied electric field gradient to separate KRb rotational states $|0,0\rangle$ and $|1,0\rangle$ in time of flight, and then perform state transfer only on the $|1,0\rangle$ molecules. Figure 2.15

[1] These number fluctuations may sound exaggerated, but the experiment is capable of much worse when you go out for lunch and leave it up to its own devices.

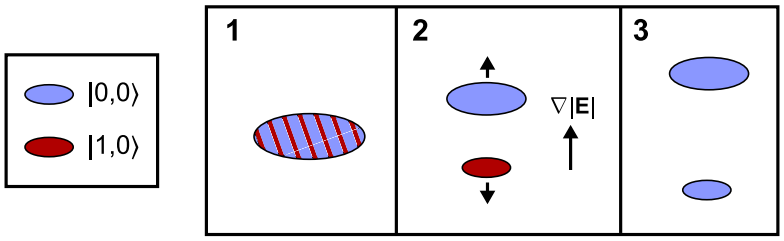

Figure 2.15: Stern-Gerlach imaging procedure. The rotational state mixture (1) is split into rotational components using an electric field gradient (2), and the $|1,0\rangle$ component is transferred to $|0,0\rangle$ prior to imaging (3).

shows the process schematically:

(1) After an experimental sequence involving rotational state transfer, the molecules are in a superposition of states $|0,0\rangle$ and $|1,0\rangle$ in the optical trap. Preparing for the imaging sequence takes several milliseconds and therefore the rotational state superposition completely decoheres prior to imaging.

(2) The molecules are released from the trap and an electric field gradient is applied parallel to gravity. Since $|0,0\rangle$ and $|1,0\rangle$ have different electric dipole moments, the gradient $\partial_y |\mathbf{E}|$ accelerates each state differently. After holding in the gradient, the molecules in each rotational state become separated in space.

(3) In the presence of $\partial_y |\mathbf{E}|$, the electric field varies in space and therefore so does the transition frequency of $|0,0\rangle \rightarrow |1,0\rangle$. Using this property, we address the molecules with a microwave frequency that is only resonant with one of the separated clouds and transfer the molecules from $|1,0\rangle$ to $|0,0\rangle$. In $|0,0\rangle$ the molecules can be imaged as normal and the rotational state distribution corresponds to the spatial distribution.

For Stern-Gerlach imaging we typically used an electric bias field of $|\mathbf{E}| = 1$ kV/cm. To split the rotational states we used a gradient of $\partial_y |\mathbf{E}| = 4$ kV/cm^2, which we reduced to 0.3 kV/cm^2 for rotational state transfer and imaging (step 3, Fig. 2.15). The dipole moments for states $|0,0\rangle$ and $|1,0\rangle$ at 1 kV/cm are $d_0 = 0.05$ D and $d_1 = -0.03$ D, so the two states are accelerated in

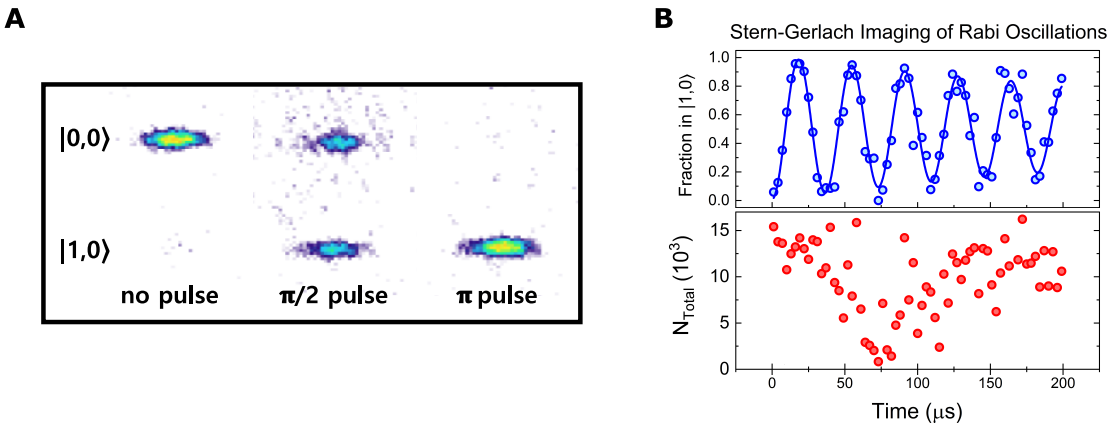

Figure 2.16: Stern-Gerlach imaging of Rabi oscillations. **(a)** Molecule images for pulse areas 0, $\pi/2$, and π. The states $|0,0\rangle$ and $|1,0\rangle$ are widely separated in space. **(b)** Rabi oscillations with number normalization. The fraction in each rotational state shows clear oscillations despite large total number fluctuations.

opposite directions by the field gradient. The frequency splitting $\Delta\nu$ per distance Δy between the two separated clouds is the product of the gradient and differential dipole moment:

$$\Delta\nu = (d_0 - d_1) \cdot \Delta y \cdot \partial_y |\mathbf{E}| \tag{2.7}$$

For our parameters, at $\partial_y |\mathbf{E}| = 0.3$ kV/cm^2, this quantity is $\Delta\nu/\Delta y = 7$ kHz/μm. By separating the clouds by tens of μm, the resultant frequency shifts are easily large enough to address each position individually. In principle, this technique could be used to image any number of rotational states with different dipole moments (for example, populations in ten hyperfine states have been measured simultaneously in ^{87}Sr [93]), but for simplicity we only image two states.

Figure 2.16 shows experimental results for Stern-Gerlach imaging. For these gradients and timings, the separation between the two rotational states far exceeds the width of the clouds along the y-axis (Fig. 2.16a). To demonstrate number normalization using this method, we measure Rabi oscillations on the $|0,0\rangle \rightarrow |1,0\rangle$ transition and plot both the total molecule number and the fraction of molecules in $|1,0\rangle$ (Fig. 2.16b). Despite number fluctuations of almost 100% of the full number (much larger than the usual 10% fluctuations, but useful for this demonstration), we recover a clear Rabi oscillation.

This method has several practical and fundamental limitations. At every electric field, all of the gradients, timings, and frequencies for rotational state splitting and transfer must be re-optimized. This adds significant complexity to the experimental sequence. The molecules can only be imaged in time of flight, which lowers the optical density and makes it difficult to image small numbers of molecules compared to imaging in the trap. Finally, since applying a large gradient to separate the states distorts the spatial distribution of the molecules, measurement of quantities that depend on the size of the cloud (such as temperature) is less reliable. For these reasons, we transitioned to measuring the molecules *in situ* in the optical trap.

2.4.2 *In Situ* Imaging

Imaging both spin states in the optical trap has been previously explored on this experiment [71], but was not adopted at the time. The basic sequence is very simple:

(1) Prepare a superposition of $|0,0\rangle$ and $|1,0\rangle$ during an experiment

(2) Image $|0,0\rangle$ as normal

(3) Transfer the remaining $|1,0\rangle$ molecules to $|0,0\rangle$ and image $|0,0\rangle$ a second time

The primary problem with this sequence is the loss of $|1,0\rangle$ molecules during the imaging of $|0,0\rangle$ due to interactions with the STIRAP light. State $|1,0\rangle$ is approximately 2 GHz detuned from the excited molecular state used for STIRAP, much larger than the natural linewidth of the state and the laser linewidth, but there are many additional excited states (all of which exhibit electric field dependence). It was found in 2013 that applying the down leg for 5 μs at $E = 0$ results in the loss of 25% of $|1,0\rangle$ [71]. We find that the situation at higher electric fields is substantially worse, presumably because some excited states have shifted into resonance: at 1 kV/cm, we fully deplete $|1,0\rangle$ in 2 μs, and lose 75% of $|1,0\rangle$ in 10 μs at 2 kV/cm.

The solution to this problem is to involve a third state, $|2,0\rangle$, that is not lost when the STIRAP beams are applied. Referring back to the procedure described above, we transfer $|1,0\rangle$ to $|2,0\rangle$ prior to step (2), and transfer back to $|1,0\rangle$ prior to step (3). In this way, the molecules

initially in $|1,0\rangle$ are protected against the STIRAP light, at the cost of adding additional RF pulses that reduce the $|1,0\rangle$ molecule number to about 80-90% of the initial number. This procedure is explored in more detail in Chapter 8, where shelving in $|2,0\rangle$ is an essential technique for selecting single 2D layers of molecules.

Chapter 3

Electric Field Control

KRb molecules are polar, meaning their rotational state energies depend on electric field and they experience forces in field gradients and curvatures. A large electric dipole moment is both a blessing and a curse: it enables strong interactions between molecules but also necessitates very precise electric field control.

In this chapter, I will first discuss the internal state structure of KRb in applied electric fields. Second, I will describe our efforts to generate stable electric fields with controllable gradients and curvatures. Finally, I will describe the experimental procedures we employed for aligning the molecules relative to the electrodes, involving direct electric field measurements using the molecules.

3.1 KRb Structure

The energies of polar molecules depend on rotational state and electric field. The rotational Hamiltonian is:

$$H_R = \frac{\mathbf{L}^2}{2I} \tag{3.1}$$

where $\mathbf{L}$ is the orbital angular momentum operator and I is the moment of inertia. The eigenstates of H_R are states $|N, m_N\rangle$, with energies

$$\langle N, m_N|H_R|N, m_N\rangle = BN(N+1) \tag{3.2}$$

where $B = \hbar^2/2I$ is the rotational constant. For KRb, $B = 1.1139$ GHz. B can be simply estimated: if we treat a molecule as a pair of point masses m_1 and m_2 separated by bond length l_0, the moment

of inertia is

$$I = \frac{m_1 m_2}{m_1 + m_2} l_0^2 \tag{3.3}$$

or the reduced mass times the bond length squared. This implies that the smaller the molecular mass, the shorter the bond length, and the more unequal the masses of the constituent atoms, the larger the rotational constant. The bond length of KRb can be estimated as the sum of the covalent radii of K (203 pm) and Rb (220 pm) [94], which gives $l_0 = 423$ pm (8 a_0). Using this value and the ^{40}K and ^{87}Rb masses, we find $B = 1$ GHz, very close to the real value.

The zero-field eigenstates $|N, m_N\rangle$ are the spherical harmonics:

$$\langle \theta, \phi | N, m_N \rangle = Y_N^{m_N}(\theta, \phi) \tag{3.4}$$

Since $Y_N^{m_N}$ have even or odd parity with respect to the internuclear axis, the rotational states have no dipole moment at zero electric field. In an applied electric field, the rotational states mix and a dipole moment is induced. The dipolar Hamiltonian is

$$H_D = -\mathbf{d} \cdot \mathcal{E} \tag{3.5}$$

where $\mathbf{d}$ is the dipole operator and $\mathcal{E}$ is the electric field. The magnitude of $\mathbf{d}$ is the permanent electric dipole moment $d = 0.574$ D [14], which we take as given in calibrating our electric fields.

Using the basis of zero-field rotational eigenstates $|N, m_N\rangle$ and setting the quantization axis parallel to the electric field, the matrix elements of the rotational and dipolar Hamiltonians are:

$$\begin{aligned}
\langle N', m_N' | H_R | N, m_N \rangle &= BN(N+1)\delta_{N,N'}\delta_{m_N,m_N'} \\
\langle N', m_N' | H_D | N, m_N \rangle &= -d\mathcal{E}\sqrt{(2N+1)(2N'+1)} \begin{pmatrix} N & 1 & N' \\ m_N & 0 & -m_N' \end{pmatrix} \begin{pmatrix} N & 1 & N' \\ 0 & 0 & 0 \end{pmatrix}
\end{aligned} \tag{3.6}$$

The bracketed elements are Wigner 3-j symbols, which are zero unless the following conditions are met: $N - 1 \leq N' \leq N + 1$ and $m_N = m_N'$. The second condition implies that only states with the same m_N mix. Diagonalizing this matrix produces the field-dressed eigenstates $|\widetilde{N}, m_N\rangle$ and

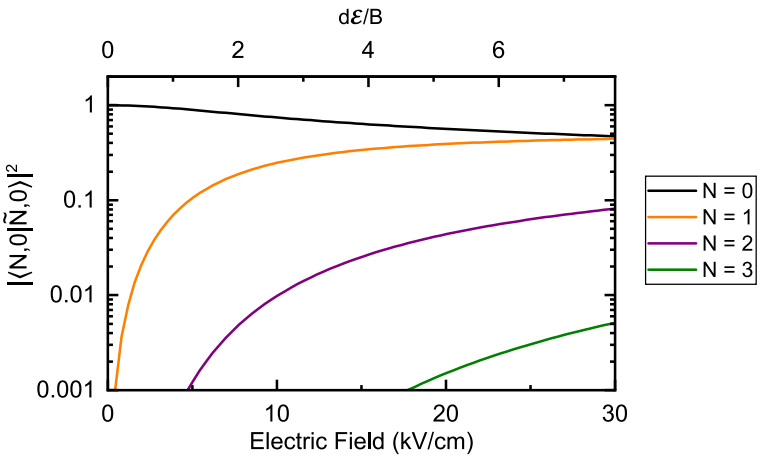

Figure 3.1: Composition of $|\widetilde{0},0\rangle$ in the basis of zero-field rotational eigenstates $|N,0\rangle$, with $|\langle\widetilde{N},0|N,0\rangle|^2 = |\alpha^0_{\widetilde{N},N}|^2$. The upper axis gives electric field $\mathcal{E}$ in terms of the dimensionless quantity $d\mathcal{E}/B$.

energies $E_{\widetilde{N},m_N}$. $|\widetilde{N},m_N\rangle$ is the superposition of zero-field eigenstates

$$|\widetilde{N},m_N\rangle = \sum_N \alpha^{m_N}_{\widetilde{N},N}(\mathcal{E})\,|N,m_N\rangle \tag{3.7}$$

and is defined as the state that adiabatically connects to $|N,m_N\rangle$ at zero field, i.e. $\alpha^{m_N}_{\widetilde{N},N}(0) = \delta_{\widetilde{N},N}$. Figure 3.1 shows the composition of $|\widetilde{0},0\rangle$ in terms of $|N,0\rangle$ as a function of electric field. Since the only two energy scales for ground state bialkali molecules are B and $d\mathcal{E}$ (neglecting additional structure such as vibrational and hyperfine states), the dimensionless quantity $d\mathcal{E}/B$ is frequently used for electric field. For KRb, $B/d = 3.854$ kV/cm. When the energy shift induced by the electric field is small relative to the rotational splitting (i.e. $\mathcal{E} < B/d$), the mixing between rotational states is small (Fig. 3.1). Over the range of electric fields accessible in experiment, below about 30 kV/cm, $|\widetilde{0},0\rangle$ is largely comprised of only $|0,0\rangle$ and $|1,0\rangle$. By convention, for the rest of this work we will use $|N,m_N\rangle$ interchangeably with $|\widetilde{N},m_N\rangle$: at $\mathcal{E} \neq 0$, we are always referring to the field-dressed state.

The diagonal and off-diagonal elements of the dipole operator in the basis of $|N,m_N\rangle$ are referred to as induced and transition dipole moments, respectively. The induced dipole moment

d_{N,m_N} is equal to the derivative of the energy with respect to electric field:

$$d_{N,m_N} = \langle N, m_N | \mathbf{d} | N, m_N \rangle = -\frac{dE_{N,m_N}}{d\mathcal{E}} \tag{3.8}$$

Figure 3.2 shows the energies and dipole moments of the $N = 0, 1, 2$ manifolds of KRb, which are the rotational states studied in the subsequent chapters. For reference, a dipole moment of 1 D corresponds to a Stark shift of -504 kHz/(V/cm). $|0, 0\rangle$ possesses a positive dipole moment and reaches half of $d = 0.574$ D at about 8 kV/cm, while $|1, 0\rangle$ has a negative dipole moment at low field and shifts in the opposite direction. The $N = 1$ and $N = 2$ rotational manifolds are higher than $N = 0$ by 2.23 and 6.68 GHz, respectively.

The transition dipole moments are:

$$d_{N,m_N,N',m'_N} = \langle N', m'_N | \mathbf{d} | N, m_N \rangle \tag{3.9}$$

These quantify the strength of microwave transitions between rotational states and of "spin exchange," or dipolar interactions between molecules that result in the exchange of rotational state (see Chapter 8). Figure 3.2c shows the transition dipole moments for pairs of states with $m_N, m'_N = 0$, which are the primary transitions addressed in the following sections. The maximum transition dipole moment is $d/\sqrt{3} = 0.331$ D; importantly, in contrast to the induced dipole moment, the transition dipole is maximized at $\mathcal{E} = 0$, where it has a magnitude equal to that of the induced dipole at $\mathcal{E} = 12$ kV/cm.

3.1.1 Hyperfine Structure

Most of the physics studied here depends only on the rotational state; however, the hyperfine structure plays a small role. The ground electronic state of KRb is a spin singlet ($^1\Sigma$) with zero electron spin and orbital angular momentum. Therefore, the hyperfine structure arises from the nuclear spin of the constituent atoms, with contributions to the energy coming from spin-spin, spin-rotation, and nuclear quadrupole interactions as well as the nuclear and rotational Zeeman shifts in an applied magnetic field [95].

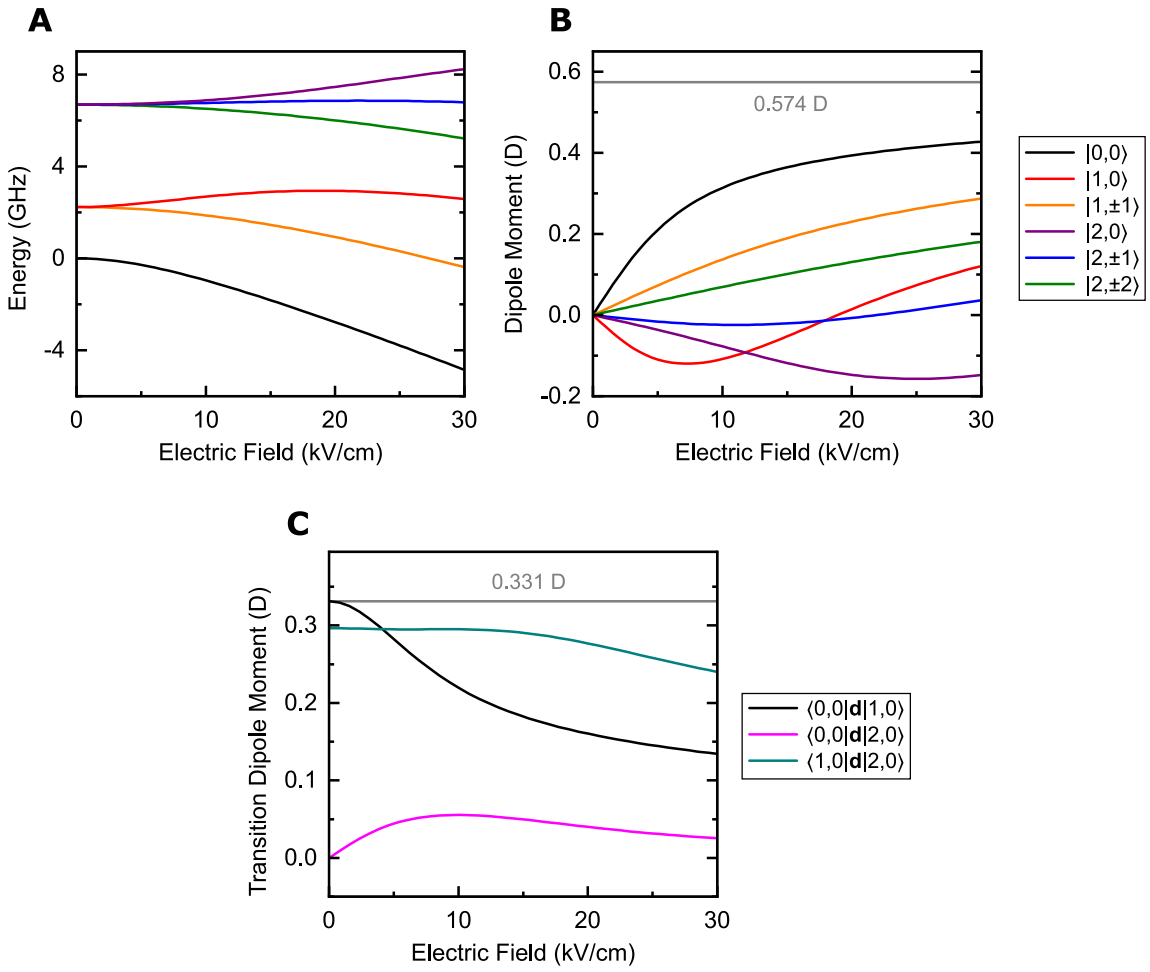

Figure 3.2: Rotational state energy and dipole moments vs. electric field, for $N = 0, 1$ and 2. **(a)** Rotational state energies. The $N = 0, 1, 2$ manifolds are split by 2.23 and 6.68 GHz and shift with field. **(b)** Induced dipole moments. At large field, the dipole moments trend towards the permanent dipole moment $d = 0.574$ D (gray line). **(c)** Transition dipole moments for states with $m_N = 0$. The maximum value, achieved at $\mathcal{E} = 0$, is $d/\sqrt{3} = 0.331$ D (gray line).

The nuclear spins of the atoms are $I^{\mathrm{K}} = 4$ and $I^{\mathrm{Rb}} = 3/2$. At 545.5 G, where STIRAP is performed, the nuclear Zeeman shift far exceeds the spin-spin coupling and therefore we label the hyperfine states according to the atomic nuclear spins. We associate molecules in the state $|N, m_N, m_I^{\mathrm{K}}, m_I^{\mathrm{Rb}}\rangle = |0, 0, -4, 1/2\rangle$, which is approximately 750 kHz higher in energy than the absolute ground state, $|0, 0, -4, 3/2\rangle$ [96]. Though we can transfer the molecules to the absolute ground state, we choose to operate in the state populated by STIRAP since the hyperfine state does not strongly affect the dipolar physics.

At small electric fields, the hyperfine states can strongly modify the rotational state spectrum. In the excited rotational state $|1, 0\rangle$, in the range of electric fields 100-350 V/cm, there are many avoided crossings (Fig. 3.3). To measure the effect of these crossings on the molecule number, we prepare molecules at zero field, ramp the field up to a target electric field in 100 ms, hold for 10 ms, and ramp back in 100 ms. The molecule number decays sharply for fields above 150 V/cm, suggesting that molecules are diabatically transferred into other hyperfine states and then either lost to collisions or not imaged at zero field. These measurements were one of the motivations for performing STIRAP at higher electric fields (Chapter 2).

3.2 Electrode Geometry and Field Simulations

The electrode assembly in our apparatus, developed by Jake Covey [72, 97], is designed to generate homogeneous ("flat") fields oriented at any angle as well as to apply gradients and curvatures to manipulate the molecules. The assembly is comprised of six electrodes: two transparent ITO-coated plates with four tungsten rods inside (Fig. 3.4). The voltage on each electrode is independently controlled. We also apply microwave fields for controlling the molecule rotational state using the rods. DC and microwave voltages are coupled onto each rod from separate vacuum ports through an inductor and capacitor, respectively, forming a "bias tee" structure to prevent crosstalk [72]. There are four primary challenges for addressing the molecules with electric fields that we address individually:

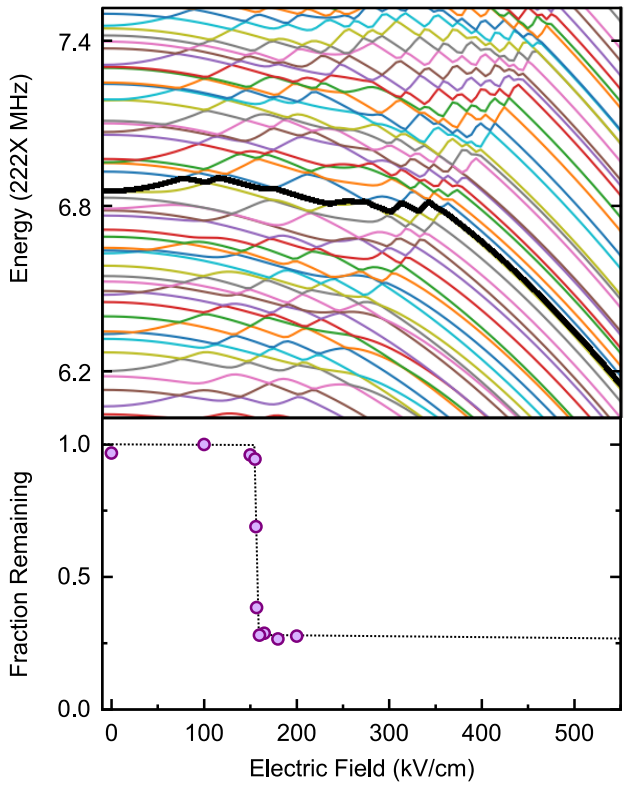

Figure 3.3: Hyperfine structure of $|1,0\rangle$ vs. electric field at a magnetic field of $B = 545.5$ G. Each colored line on the upper panel corresponds to a different hyperfine state. When we ramp the electric field from 0 V/cm to a target electric field, hold, and ramp back, we observe loss of $|1,0\rangle$ molecules that we attribute to avoided crossings with nearby hyperfine states. The black line on the upper panel indicates the hyperfine state populated using STIRAP. The dashed line on the bottom panel is a guide to the eye.

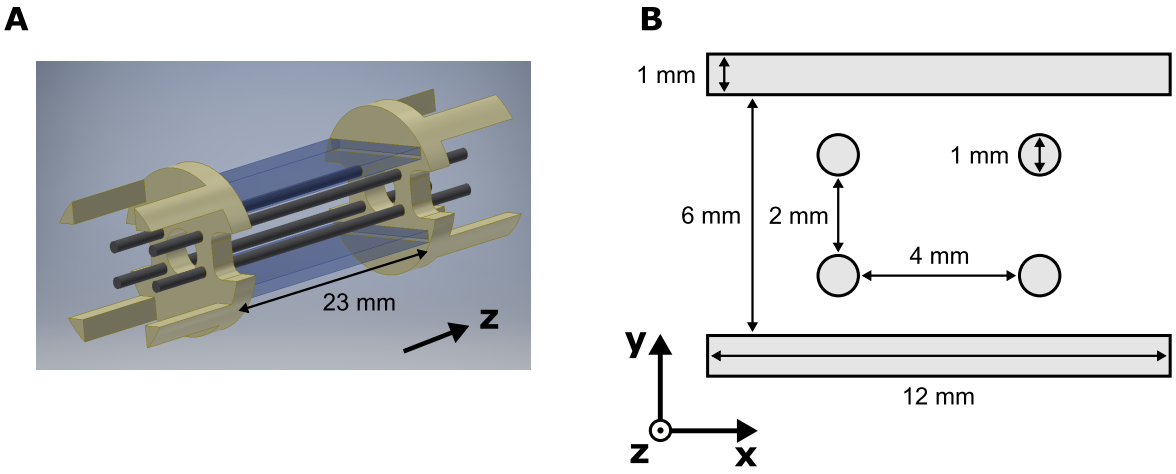

Figure 3.4: Electrode assembly. **(a)** We apply voltages individually to six electrodes: two plates (light blue) and four rods (gray), mounted rigidly using a custom Macor holder (gold). The **z** axis is parallel to the electrodes. **(b)** Electrode dimensions.

(1) Computing the voltages to apply to each electrode in order to generate the desired field configurations, assuming an ideal electrode geometry (i.e. corresponding exactly to Fig. 3.4) and perfectly stable electrode voltages

(2) Generating large, low-noise voltages to realize these field distributions, and optimizing the dynamic response of the voltage feedback control

(3) Measuring the molecule position relative to the electrodes and electric field distribution

(4) Modifying the calculated (ideal geometry) field distribution in order to correct for small imperfections in the electrode geometry

Topics 1-3 will be addressed in this chapter, and topic 4 will be addressed in Chapter 8.

Given the electrode geometry, we calculate the electric field distribution using COMSOL, a finite element analysis software program. It is straightforward to calculate electric fields from known voltages; however, the inverse problem, calculating voltages to apply based on a desired electric field distribution, is more difficult. We make several simplifications to rapidly calculate voltages. First, we reduce the problem from 3D to 2D by approximating the field as being constant

for translations along **z** (Fig. 3.4), which is equivalent to assuming that the electrodes have infinite extent along **z**.

We then used COMSOL to calculate the electric field distribution for unit voltage applied to a single electrode, with the boundary condition of all other electrodes at zero volts: $e_i(x, y)$, for electrode i. By the principle of linear superposition, the total electric field is

$$E(x, y) = \sum_{i=1}^{6} V_i e_i(x, y) \tag{3.10}$$

where V_i is the voltage on the ith electrode. We approximate the field distributions calculated using COMSOL by fitting each $e_i(x, y)$ to a seventh-order polynomial in position coordinates x and y, within a 2 mm square region at the center of the electrodes. This gives

$$e_i(x, y) \approx \sum_{j=0}^{7} \sum_{k=0}^{7} \alpha_{jk} x^j y^k \tag{3.11}$$

where α_{jk} are fit parameters. By approximating the electric field as a sum of polynomials and superposing the field from each electrode, we can rapidly compute electric fields as well as multiple derivatives to obtain gradients and curvatures. When calculating the electric field distribution, $\mathbf{E}(x, y) = [E_x(x, y), E_y(x, y)]$, we specify six scalar parameters: the magnitude of the electric field, $|\mathbf{E}|$; the gradients $\partial_{x,y}|\mathbf{E}|$ and curvatures $\partial^2_{x,y}|\mathbf{E}|$ along each axis; and the electric field angle, $\theta = \tan^{-1}(E_x/E_y)$ [64]. We optimize $\{V_i\}$ to generate a calculated field distribution with the specified parameters at the center of the electrodes, $(x, y) = (0, 0)$.

The symmetry of the electrode geometry imposes fundamental limits on the field distributions that can be produced. For example, consider flat electric fields oriented at 0° (along **y**) and 90° (**x**), as shown in Fig. 3.5. At 0°, parallel to the field generated by the plates alone, all six electrodes contribute to flattening the field near the center. At 90°, by contrast, the plates are fixed at zero voltage by symmetry and the field is generated only by the rods, introducing large curvatures. Though this is an extreme case, it illustrates a general principle: the electrode design constrains the electric field control, especially away from the center of the electrodes or for electric fields oriented at large θ.

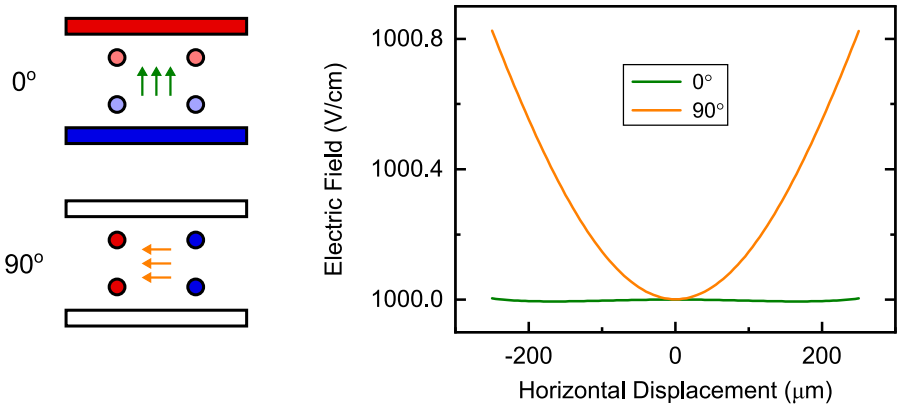

Figure 3.5: Electric field curvature at $|\mathbf{E}| = 1000$ V/cm, with $\theta = 0°$ and 90°. Depending on the angle relative to the electrode orientation, large gradients and curvatures can be introduced.

3.3 High Voltage Stabilization

The interaction strength between KRb molecules separated by 532 nm in an optical lattice is approximately 50 Hz [49]. At an electric field of 1 kV/cm, a field fluctuation of only one part per million (ppm) produces a similar change in the transition frequency between the lowest two rotational states, $|0,0\rangle$ and $|1,0\rangle$. To be able to resolve molecular interactions using rotational spectroscopy, we therefore aim to control the electric field noise and stability at the sub-ppm level. In the following section, I describe our efforts to realize this figure, which included designing a stable voltage reference, characterizing and improving noise sources in and around the control loop, and filtering the output high voltage to reduce the noise on the molecules.

The general architecture for electric field control is shown in Fig. 3.6. Each electrode is connected to a dedicated high voltage amplifier (either model Trek 10/10B or Matsusada AMS/AMT). The amplifiers have control ports, where an input voltage is multiplied to generate the high voltage output. In the absence of active voltage stabilization, the amplifier output is specified to have part-per-thousand peak noise, or 1 V on 1 kV output. This necessitates the use of a feedback loop to correct output noise. In order to reduce the high voltage to compare it with a control voltage, we divide the amplifier output using a 2000:1 precision resistor network.

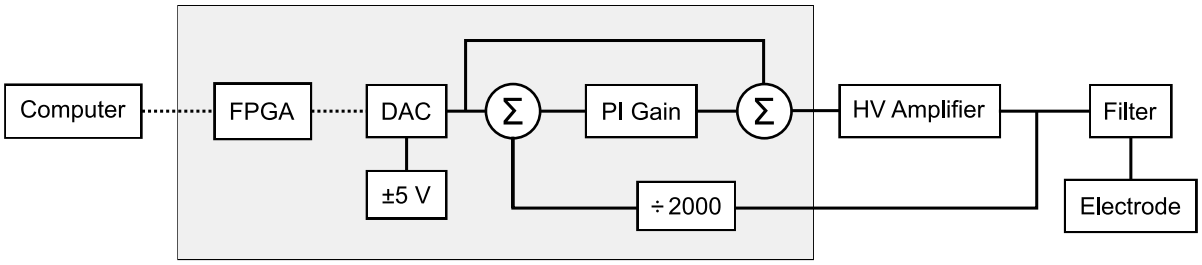

Figure 3.6: Schematic diagram of the electric field control loop. The DAC generates a stable control voltage, which is compared with the output of the high voltage amplifier divided down using a network of resistors. One ±5 V reference and FPGA are shared between six DACs, each controlling one electrode. The gray box represents components that are enclosed, while components outside are external. Analog and digital connections are represented by solid and dashed lines, respectively.

The control voltage is generated using a 20-bit DAC (model AD5791), with ppm accuracy ($2^{20} \approx 10^6$, so 1 LSB = 1 ppm). The time sequence of DAC voltages is programmed into an FPGA prior to each shot of the experiment, which then sends time-synchronized digital codes to the DAC to set the control voltage during the experiment. The analog voltage range of the DAC is set using a precision 5 V reference (model LTC6655) which is inverted to form ±5 V voltage references for each DAC. Each of the six electrodes is controlled by its own DAC (only one is shown in Fig. 3.6), but all six DACs share the same FPGA and voltage reference.

The control voltage and divided HV output are summed to form the error signal, which is amplified in the PI (proportional-integral) gain block. The amplified error is added with the control voltage, which is fed forward to speed up the servo response. The resultant signal enters the control port of the amplifier, where it sets the high voltage output. Finally, there is an output filter between the amplifier and electrode. This filter is formed by a 1 MΩ resistor in series with the amplifier output, with low-pass filtering created by the capacitance of the shield for the cable connecting the amplifier and the electrode feedthrough on the vacuum chamber.

3.3.1 Grounding

The goal of a grounding scheme is to maintain a common ground potential for each subsystem, such as those shown in Fig. 3.6. In our application this is particularly critical, since offsets in the control loop are multiplied by a large factor onto the high voltage. There are two basic approaches to grounding, which are discussed in detail in Ref. [98]: single-point and multipoint grounding. In single-point grounding, also known as "star" grounding, each subsystem has a single return path that connects to a common, low-impedance ground reference. In principle, this scheme eliminates ground loops whereby current flowing in one subsystem offsets the ground voltage in another subsystem, and reduces pickup of electromagnetic interference. However, the complicated interconnections between our equipment (for example, the shared connection to the reference between all six DACs) make this scheme impractical.

We instead use multipoint grounding, where each subsystem is connected to ground and to the other subsystems by many low-impedance paths. This creates a forest of loops, but if the currents and impedances are small, no voltage offsets can develop. In practice, we use large-diameter wires and metal braids to connect all of the equipment chassis, power supplies, and grounding terminals to each other and to an aluminum grounding bar.

In addition to the low-noise analog signals in the circuit, many digital signals are present. These include signals to enable the HV amplifier outputs, signals sent between the FPGA and DACs during the sequence, and USB communication between the computer and FPGA (Fig. 3.6). Digital grounds tend to be noisy due to high-frequency components of digital edges, so digital and analog grounds must be separated to the maximum extent possible. To achieve this, we use a USB groundbreaker and optoisolators to reference the digital signals to the analog ground.

3.3.2 Voltage Reference

To quote an Analog Devices article, "the 20-bit DAC is the easiest part of a 1-ppm-accurate precision voltage source" [99]. The function of the DACs is to subdivide the reference voltages to

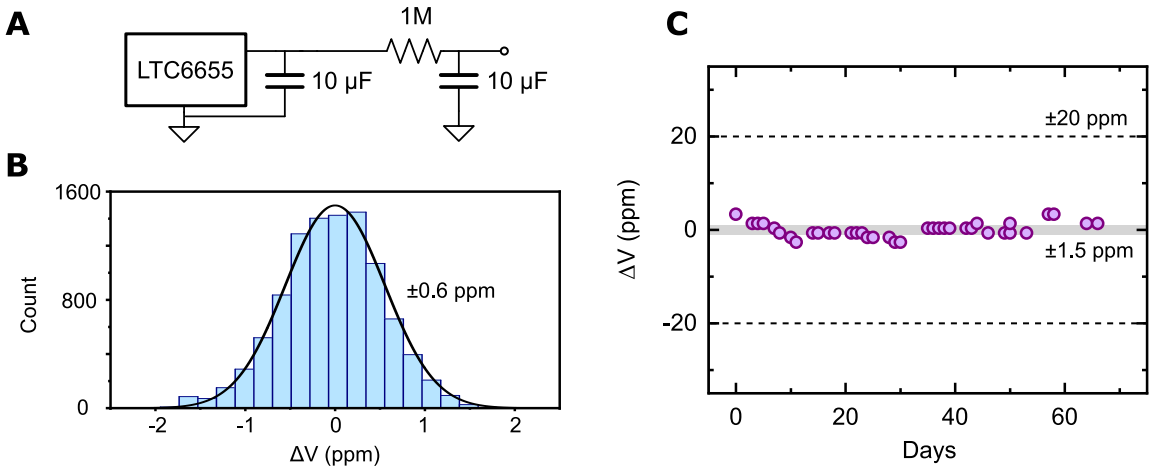

Figure 3.7: Long-term drift of the LTC6655 reference. **(a)** Circuit diagram, showing reference, output capacitor, and low-pass RC filter. **(b)** Stability over 200 s, 10 000 samples with 0.1 NPLC aperture on a Keithley 2002. **(c)** Stability over 66 days, 1 NPLC aperture on a Keithley 2000. For both measurements, the stability is better than the multimeter can measure accurately.

generate the output voltage without adding voltage offsets or noise. This means that the baseline stability and noise spectrum of the high voltage derives originally from the voltage reference, prior to noise added by other electrical components.

We use the LTC6655 5V reference with a two-stage C-RC filter on the output, shown in Fig. 3.7a. This reference has low output noise and low long-term drift, both of which we characterize. With a 10 μF capacitor on the output, the LTC6655 is specified to have lower than 80 nV/$\sqrt{\text{Hz}}$ voltage noise above 10 Hz. Adding a low-pass filter with a corner frequency of 16 mHz, we measure lower than 8 nV/$\sqrt{\text{Hz}}$ in this frequency range, limited by the noise floor of the measurement device. Between 0.1-12 Hz, we measure 0.65 $\mu\text{V}_{\text{p-p}}$ integrated noise, approximately half of the specified typical value. For a detailed discussion of noise sources in the electric field control loop above 0.1 Hz, see Appendix A.

We measure the drift of the reference using a Keithley 2002 multimeter over two time periods: 200 seconds and 66 days. For 10 000 samples taken over 200 s, with an aperture time of 0.1 NPLC, we measure 0.6 ppm noise (Fig. 3.7b). This is well below the specified maximum rms noise of the multimeter on these settings. The LTC6655 has a long-time drift specification of

20 ppm/$\sqrt{\text{kHr}}$. After a burn-in period of several thousand hours, we record the output voltage semi-daily on a Keithley 2000 multimeter and plot the trend (Fig. 3.7c). We measure a standard deviation of 1.5 ppm, with a maximum deviation of ±3 ppm. This is again substantially smaller than the maximum specified 60-day drift of the multimeter, ±20 ppm, which we attribute to the temperature and humidity stability of the laboratory. Typically, the temperature is controlled to within 0.5 °C and the relative humidity to within 5%. In time periods where the relative humidity was uncontrolled and varied by 20-30%, we observed drifts in the measured voltage of up to 20 ppm. The measurements of both the short- and long-term drifts are limited by the multimeters, so the values in Fig. 3.7 should be considered upper bounds.

We take several additional precautions to reduce long-term drift of the reference. The LTC6655 is in a hermetically-sealed package, which has low drift and zero humidity sensitivity. We also cut out slots around the reference on the PCB to reduce voltage changes from stress on the board. The output capacitor is essential for reducing the reference noise, but its insulation resistance forms a voltage divider with the LTC6655 output impedance, which may add additional temperature dependence to the voltage. To eliminate this, we used a polypropylene film capacitor (model WIMA MKP 4), which has an insulation resistance of 3000 MΩ, compared to a typical output impedance of 0.01-1 Ω. Finally, the reference/low-pass circuit is buffered by an amplifier with an input impedance of 10^{12} Ω (model ADA4625) to mitigate the effects of the voltage divider formed with the 1 MΩ low-pass resistor.

3.3.3 Output Filter

The control loop described above reduces the output noise up to a certain frequency, depending on the bandwidth of the loop. If the amplifiers add noise above this bandwidth, that noise will be present on the high voltage. We measure the noise in the frequency band above 500 Hz directly on the amplifier outputs, with the servo loops engaged (Fig. 3.8a). Both amplifiers introduce large amounts of noise—as much as twenty times the baseline at low frequencies—that sum to several millivolts of total noise on the high voltage. The Trek supply primarily adds noise

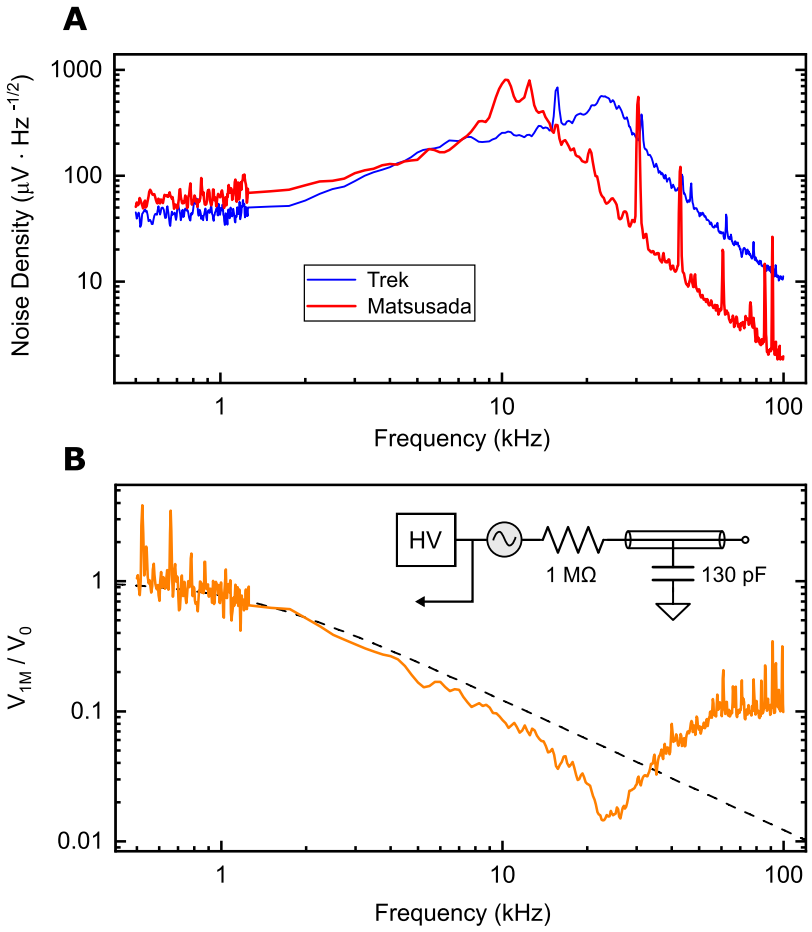

Figure 3.8: Adding a low-pass filter to reduce the high-frequency noise on the high voltage. **(a)** Noise spectra of the Trek and Matsusada power supplies with the servo engaged. Both supplies introduce noise above 10 kHz, which is above the servo bandwidth. **(b)** Adding a 1 MΩ resistor in series with the output forms a low-pass filter with the capacitance of the cable connecting the amplifier and the electrode. The noise is reduced relative to the unfiltered case at high frequencies. The dashed black line shows the expected reduction in noise, assuming a capacitance of 130 pF. **Inset:** Schematic of the amplifier and filter. The noise is measured at the farthest right point, after the filter.

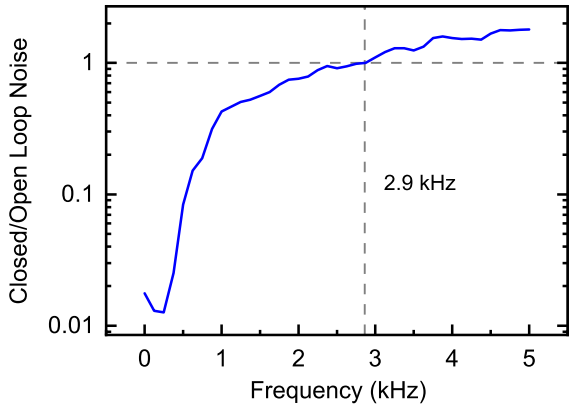

Figure 3.9: HV servo performance. We measure the output spectrum of an HV amplifier with (closed loop) and without (open loop) the servo engaged.

at 25 kHz, while the Matsusada peaks around 10 kHz. The approximate bandwidth of the servo loop, or the frequency at which the noise density doubles relative to the baseline, is 4 kHz. We repeat this measurement using several different amplifiers and servo gain configurations and obtain similar results, confirming that the output noise spectrum is an intrinsic feature of the amplifiers.

We can also make a direct measurement of the servo bandwidth by comparing the output noise spectrum with and without the servo in the loop. We use a battery to generate a stable voltage reference and use this either as the control voltage for the servo ("closed loop," replacing the DAC in Fig. 3.6) or put it directly into the control port of the amplifier ("open loop," replacing everything before the HV amplifier). Figure 3.9 shows the ratio of the output voltage noise between these two conditions. The servo reduces noise below about 3 kHz. The best possible fractional reduction in the noise is limited by the noise floor of the servo, described in detail in Appendix A. In principle, we can configure the servo loop to operate at a bandwidth of higher than 20 kHz [97]. However, for all of the experiments described in this thesis, we typically change the electrode voltages on timescales of milliseconds or longer. For this reason, we kept the servo bandwidth relatively low and removed the high frequency noise using a passive filter rather than using active stabilization. This is represented on Fig. 3.6 by a filter block between the amplifier and electrode.

To filter the noise, we add a resistor in series to the output of the high voltage amplifier

(Fig. 3.8, inset), after the feedback point where the output is divided to generate the error signal. The amplifier and resistor are connected to the electrode feedthrough into the chamber using a homemade assembly of a high-voltage cable (model Judd TV-30, 22 AWG) inside of a metal grounding braid. The entirety of the capacitance of the low-pass filter comes from the cable/braid pair, and we do not add any additional capacitors. We measure the capacitance of the cable by two methods. First, we connect the resistor to a test cable of similar dimensions and directly measure the transfer function. Second, in order to simulate the experimental conditions, we connect the amplifier and engage the servo loop, and measure the time constant of the voltage on the electrode for a voltage step at the amplifier. Both of these methods give a capacitance of approximately 130 pF for a 2 m cable.

We can also estimate the capacitance per length (C/l) of the high voltage cable using

$$\frac{C}{l} = \frac{2\pi\epsilon_p}{\ln\left(r_{\text{out}}/r_{\text{in}}\right)} \tag{3.12}$$

where $\epsilon_p = 2.25\epsilon_0$ is the permittivity of the polyethylene wire insulation in terms of the vacuum permittivity ϵ_0, and $r_{\text{out}} = 0.25$ cm and $r_{\text{in}} = 0.032$ cm are the radii of the grounding shield and cable conductor. This gives $C/l \approx 60$ pF/m, in good agreement with the measured value. In principle, the electrode geometry (Fig. 3.4) contributes a small capacitance, but we calculate that this should be smaller than 1 pF.

On one electrode connected to a Trek power supply, we measure the ratio of the noise above 500 Hz with and without a 1 MΩ resistor in series (Fig. 3.8b). The noise is reduced by more than an order of magnitude past 10 kHz, in the band where the amplifiers add noise. The reduction in noise is approximately consistent with a cable capacitance of 130 pF (dashed black line) below 30 kHz; above this point, there may be a small amount of frequency dependence of the capacitance or resistance that causes deviation from the predicted value. We tested 5 MΩ resistors as well, but found that this made the electrode time constant too long for our experimental sequence timings. It may be possible to construct a second-order LC filter with a steeper roll-off to remove more noise at high frequencies, but large additional capacitors and inductors would be required.

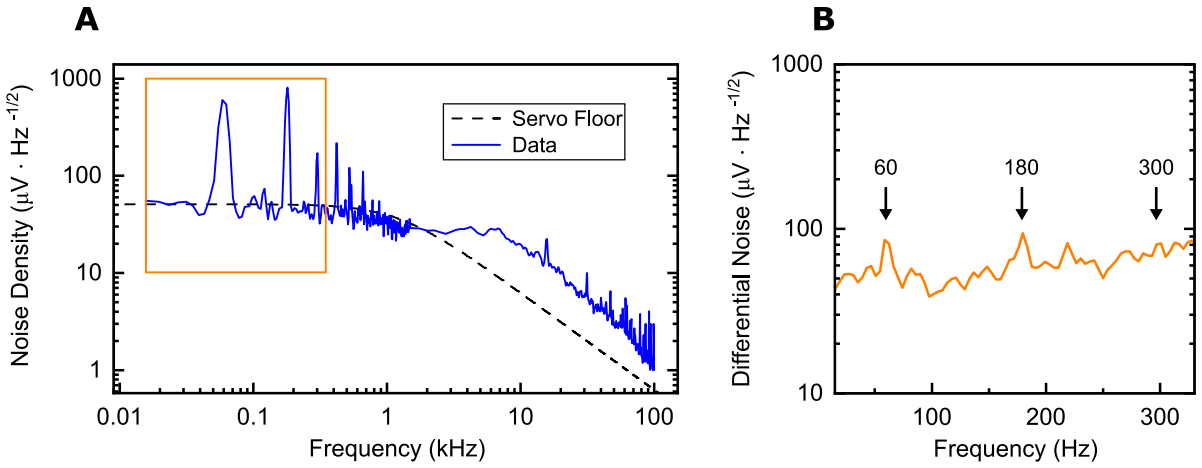

Figure 3.10: AC noise spectrum on high voltage electrodes. **(a)** Noise density on one electrode (solid blue line). The measured noise is similar to the floor (dashed black line) given by the servo noise and the electrode filter, with an increase at high frequencies due to the noise of the HV amplifier (Fig. 3.8). **(b)** Differential noise between two electrodes, corresponding to the orange region marked in (a). Very little noise from the harmonics of 60 Hz is present, in contrast to the single-electrode spectrum.

3.3.4 AC Noise Characterization

Following the addition of the output filter, we measured the electrode noise in the frequency range between 15 Hz and 100 kHz. The following measurements were made after the output filter and before the electrodes. In Appendix A, I calculate the noise floor of high voltage control loop due primarily to Johnson noise and output voltage noise on operational amplifiers. Adding together all of the noise sources, we expect a noise density of about 50 $\mu\text{V}/\sqrt{\text{Hz}}$ above 10 Hz. This noise should be approximately constant ("white noise") below the op-amp and voltage reference bandwidths. The noise floor of our system is given by the product of these noise sources and the low-pass output filter (Fig. 3.10a, dashed black line; see also Fig. 3.8).

The measured noise agrees well with the calculated noise (Fig. 3.10a). Only one electrode is shown in the figure for simplicity, but all six electrodes have similar spectra. The measured noise above 3 kHz is higher than calculated by a factor of three, due to the noise added by the amplifiers (Fig. 3.8). At low frequencies, there are large peaks at the odd harmonics of 60 Hz, the

mains frequency (60 Hz, 180 Hz, 300 Hz, etc.). All of the AC power for the servos and amplifiers is derived from a single electrical breaker, so we suspected the noise at these frequencies was common mode. It is important to differentiate between common-mode and differential noise on the electrodes: if all six electrodes change by the same voltage, the electric field does not change. The random noise from resistors and op-amps gives rise to differential noise on the electrodes, since each electrode has its own servo and amplifier with distinct components generating uncorrelated noise. To find the differential noise, we directly measure the voltage difference between two electrodes in the frequency range 15-350 Hz (Fig 3.10b). To account for the fact that the noise is uncorrelated, we divide the measured value by $\sqrt{2}$. In the region where the harmonics are strongest on a single electrode, there is little differential noise above baseline. This suggests that the 60 Hz harmonics are nearly all common-mode and can be neglected in calculating the electric field fluctuations. We additionally synchronize the experimental sequence to the power line frequency using a line trigger, ensuring that the sequence runs in phase with the 60 Hz noise.

Summing the noise over the entire frequency range, the total rms voltage noise is 3.3 mV. Assuming the electrode voltage noise is uncorrelated (this is not strictly true, due to correlated noise from the voltage reference; see Appendix A), this corresponds to electric field fluctuations with a standard deviation of 6.5×10^{-3} V/cm, independent of electric field magnitude. Put another way, the electric field noise is 6.5 ppm at 1 kV/cm and only 0.5 ppm at 12.67 kV/cm.

3.3.4.1 Molecule-Based Electric Field Spectrum Analyzer

Molecular rotational energies are strongly coupled to electric fields; even small amounts of field noise will affect spectroscopic measurements. We use a dynamical decoupling technique to measure the electric field noise spectrum using the molecules, similarly to previous measurements of environmental noise [100] and laser frequency noise [101]. The equations reproduced here are due to work by our neighbors in the Strontium Clock Group at JILA [102].

The basic experimental sequence, shown in Fig. 3.11a, is Ramsey interferometry with fixed total evolution time T and n echo pulses. We work in the basis $\{+z, -z\} = \{|0,0\rangle, |1,0\rangle\}$, two

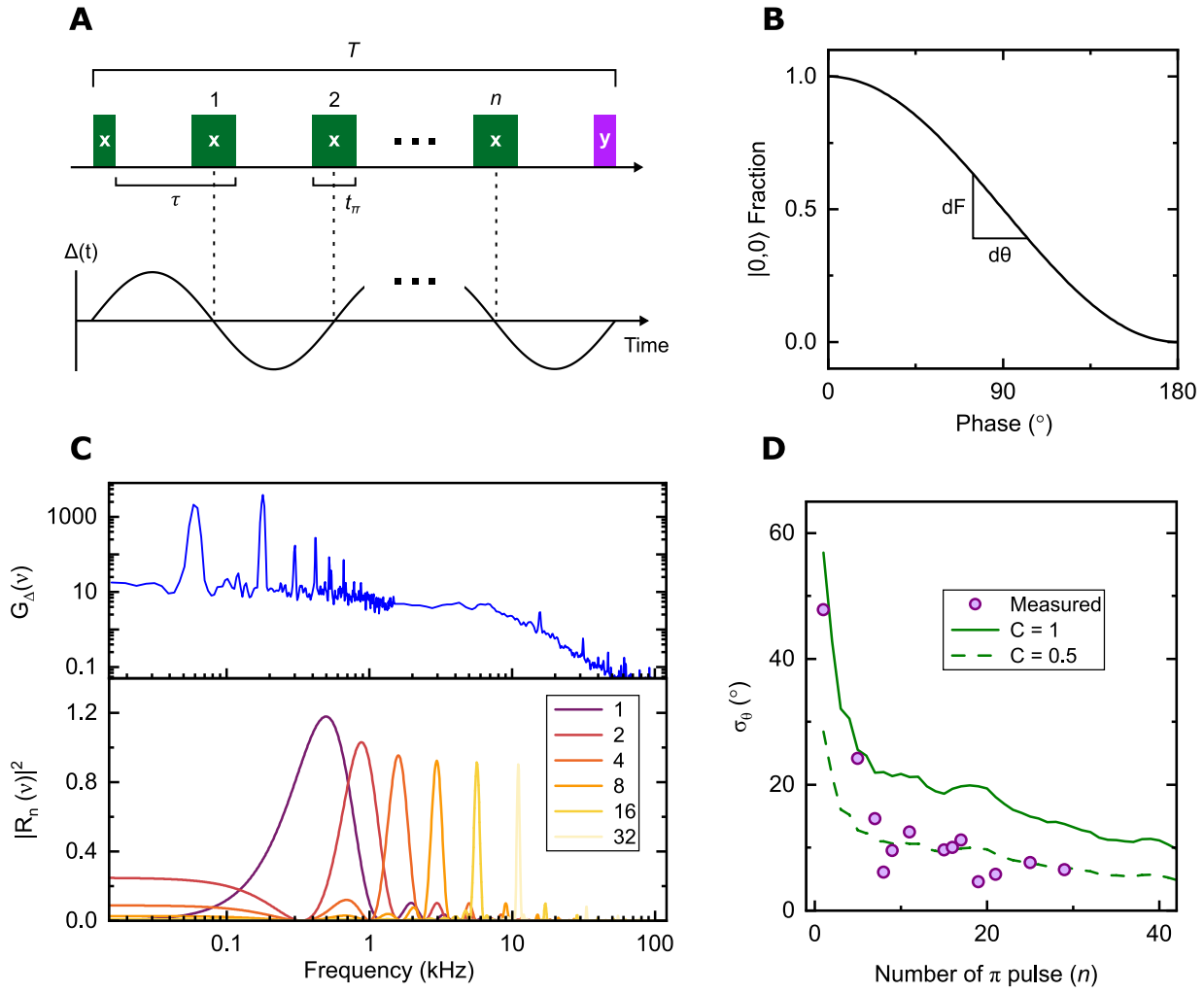

Figure 3.11: Measuring phase noise using Ramsey interferometry. **(a)** Ramsey interferometry is performed with fixed evolution time and a variable number of echo pulses. The sensitivity to frequency noise depends on the number of echoes. **(b)** The accumulated phase shift can be inferred from the fraction in each rotational state. **(c)** Changing the number of echo pulses samples noise from different frequency bands of the electric field noise spectrum. $G_\Delta(\nu)$ is the power spectral density of the transition frequency detuning Δ and $|R_n(\nu)|^2$ is the sensitivity of θ to noise at each frequency. **(d)** The measured σ_θ suggests that the electric field noise is reduced below the calculated value due to partial correlations on the noise among the six electrodes.

rotational states of KRb. All axes referenced in this paragraph are on the Bloch sphere, representing the phase relationship between rotational states rather than physical spatial orientations. The duration of the echo pulses is t_π, and the sum of t_π and the time between pulses, which is the sequence repeated periodically during the evolution time, is denoted $\tau = T/(n+1)$. The frequency of the pulses is resonant with the $|0,0\rangle \rightarrow |1,0\rangle$ transition, at approximately 2.25 GHz at a bias electric field of 1 kV/cm. The sequence begins with a $\pi/2$-pulse around $\hat{x}$, which rotates the molecules from $\hat{z}$ to $\hat{y}$. After the evolution time T and n π-pulses around $\hat{x}$, a second $\pi/2$-pulse is applied around $\hat{y}$ (oriented at 90° relative to the preceding pulses). If the spin vector has precessed away from $\hat{y}$ during the evolution time by an angle θ, the final pulse will rotate the vector out of the $\hat{x}$-$\hat{y}$ plane, changing the measured fraction in the $\hat{z}$ basis (or, the relative populations of the two rotational states). θ can be inferred from F, the fraction of the total population in $|0,0\rangle$, using

$$\theta = \frac{180^\circ}{\pi} \cos^{-1}(2F - 1) \tag{3.13}$$

as shown in Fig. 3.11b.

During the evolution time, the molecules accumulate phase proportional to $\Delta(t)$, the time-dependent detuning of the microwave frequency from resonance. The electric field $E(t)$ is the primary source of detuning. Varying the number of echo pulses changes the sensitivity of Ramsey interferometry to frequency noise in different bands; for example, a single spin echo pulse ($n = 1$) eliminates sensitivity to constant detuning [103]. In the case where $\Delta(t)$ varies with frequency $\nu = 1/2\tau$, as shown in the lower half of Fig. 3.11a, the mean of $\Delta(t)$ changes sign between each echo pulse and the phase continues to accumulate rather than cancel over the evolution time. Using this frequency selectivity, we can vary the pulse number n in order to probe the frequency spectrum of $\Delta(t)$ and thus $E(t)$.

We perform this interferometry sequence and make repeated measurements of F for fixed n, and use Eq. 3.13 to compute σ_θ, the standard deviation of θ. References [101] and [102] give the following expression for σ_θ:

$$\sigma_\theta^2 = (2\pi)^2 \int_0^\infty G_\Delta(\nu)\, |R_n(\nu)|^2 d\nu \tag{3.14}$$

$G_\Delta(\nu)$ is the power spectral density of $\Delta(t)$ and $|R_n(\nu)|^2$ is a function that expresses the frequency sensitivity of θ for Ramsey interferometry with n echo pulses. In terms of τ and T, Refs. [101] and [102] give

$$\begin{aligned} |R_n(\nu)|^2 = &\frac{\Omega}{(\pi\nu\Omega^2 - 4(\pi\nu)^3)^2}\left(2\pi\nu\cos(\pi\nu\tau) + \Omega\sin\left[\pi\nu\left(\tau - \frac{\pi}{\Omega}\right)\right]\right)^2 \\ &\times\left(\frac{\sin(\frac{\pi}{2}(n+1)(1+2\nu\tau))}{\cos(\pi\nu\tau)}\right)^2 \end{aligned} \tag{3.15}$$

where Ω is the Rabi frequency of the microwave pulses:

$$\Omega = \frac{\pi}{t_\pi} \tag{3.16}$$

To calculate $G_\Delta(\nu)$, we convert the voltage noise density on each electrode ($\sigma_{V_i}(\nu)$; shown on Fig. 3.10a for one electrode) into units of transition frequency. First, we convert $\sigma_{V_i}(\nu)$ into electric field noise $\sigma_E(\nu)$ by calculating the derivative of the electric field with respect to voltage on the ith electrode ($\partial E/\partial V_i$) and summing over the voltage noise on each electrode:

$$\sigma_E^2(\nu) = \sum_{i=1}^{6}\left(C\cdot\frac{\partial E}{\partial V_i}\right)^2\sigma_{V_i}^2(\nu) \tag{3.17}$$

The factor C parameterizes correlations in the voltage changes among the six electrodes. If the noise is completely correlated (that is, the voltage noise is in-phase on each electrode), the electric field does not change and $C = 0$; if instead the noise is completely uncorrelated, $C = 1$. Though we treat C as constant here, in general it depends on frequency and electrode configuration. We can then convert σ_E^2 to frequency noise using the electric field sensitivity of the $|0,0\rangle \rightarrow |1,0\rangle$ transition:

$$G_\Delta(\nu) = \left(\frac{\mathrm{d}\Delta}{\mathrm{d}E}\right)^2\sigma_E^2(\nu) \tag{3.18}$$

where $\mathrm{d}\Delta/\mathrm{d}E \approx 40$ kHz/(V/cm) at 1 kV/cm. Figure 3.11c shows $G_\Delta(\nu)$ and $|R_n(\nu)|^2$ for n ranging from 1 to 32, with $T = 1.5$ ms and $t_\pi = 4.8$ μs. For simplicity, since the measured noise on each electrode is so similar, we use a single $\sigma_{V_i}(\nu)$ for all electrodes. The measured phase noise, σ_θ, agrees well with the noise calculated using Eq. 3.14 for correlations between $C = 0.5$-1 (Fig. 3.11d). $C < 1$ agrees with our expectations, since noise at the 60 Hz harmonics is correlated (Fig. 3.10b) and high-frequency noise is partially correlated due to the shared voltage reference. These results

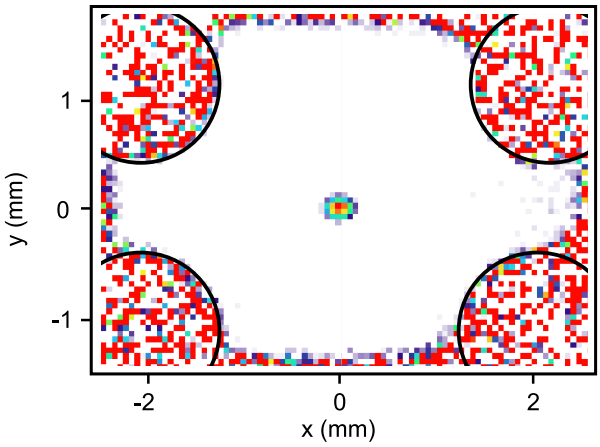

Figure 3.12: Aligning the molecules relative to the rods using low-magnification imaging along **z**. The approximate positions of the rods are indicated with black circles.

suggest there are no major sources of electric field noise that we have not accounted for by measuring the voltage noise spectrum on the electrodes.

3.4 Aligning Molecules to the Electrodes

Away from the exact center of the electrode assembly, gradients and curvatures of the electric field are unavoidable. To correctly apply the electric fields that we calculate, we must center the molecules on the electrodes. In this section, I discuss our strategies for using measurements on the molecules to infer and correct their position relative to the electrodes.

For coarse alignment, we can image the rods and the atoms simultaneously using a large probe beam oriented along **z** (Fig. 3.12). This method is not very precise, since the angle of the probe relative to the rods is not known exactly. However, it allows alignment of the molecules to within about 200 μm of the electrode center along both **x** and **y**. For more precise alignment, we use electric fields.

3.4.1 Moving the Molecules

Since the rotational energies of KRb have a known sensitivity to electric fields, the electric field at the position of the molecules can be measured by performing rotational spectroscopy. By translating the molecules using the optical traps and imaging the position of the molecules, the spatial distribution of the electric field relative to the imaging system can be mapped out with high precision. Based on this measured field profile and using the calculated distribution, the position of the molecules relative to the electrodes can be inferred.

We measure the converse effect: when the molecules are relatively close to the center of the electrodes, measuring the field distribution gives information about the electrode voltages. When we first connected the electrodes and began applying fields, we measured rotational splittings corresponding to about 85% of the calculated field. In addition, turning on the electrodes caused the molecules to slosh in the optical trap, and the Rabi oscillations of rotational transitions decohered very quickly. These measurements suggested that there was a large field gradient present, even though the calculated field was very homogeneous over 100s of μm around the electrode center.

To understand these effects, we translated the optical traps vertically and measured the electric field using rotational spectroscopy on the $|0,0\rangle \rightarrow |1,0\rangle$ transition. The measured field distribution showed a large curvature, very different than the calculated "flat field" (Fig. 3.13b). Based on this measurement, we discovered that the rods were connected incorrectly, with the connections to the top right and bottom left rods interchanged (Fig. 3.13a). The calculated field distribution for this orientation matched the measured field. Though the entire field could be mapped using this method, it is time-consuming to measure a full lineshape at every position. We developed the methods of the following sections to infer the molecule position relative to the electrodes more easily.

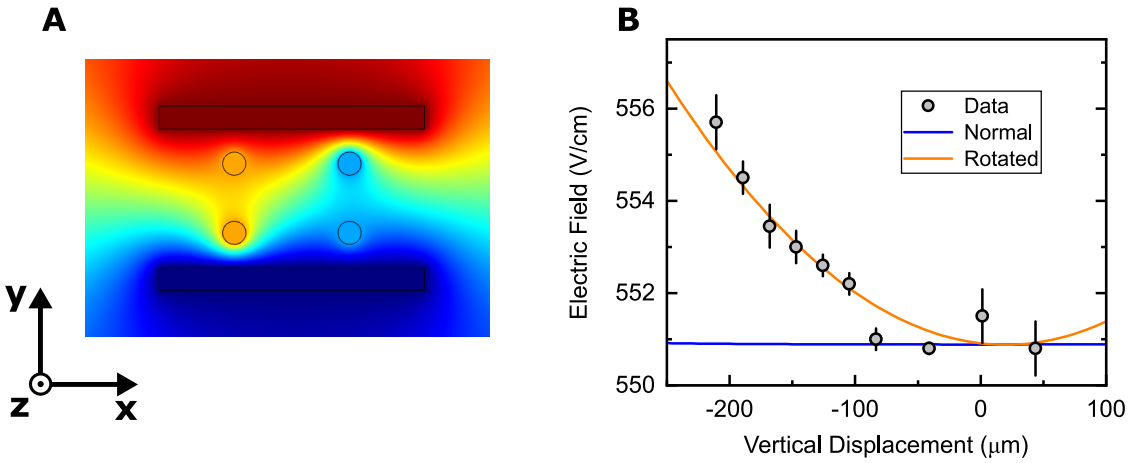

Figure 3.13: Mapping the spatial distribution of the electric field using molecule spectroscopy. **(a)** Simulated electric potential distribution (with red corresponding to positive voltage and blue corresponding to negative voltage) for the rod connections accidentally rotated. **(b)** We translate the molecules along **y** and measure the frequency of the $|0,0\rangle \rightarrow |1,0\rangle$ rotational transition, which we convert to electric field. The simulated field distribution for the "rotated rod" configuration (orange line) fits the data well, in contrast to the "flat field" configuration (blue line).

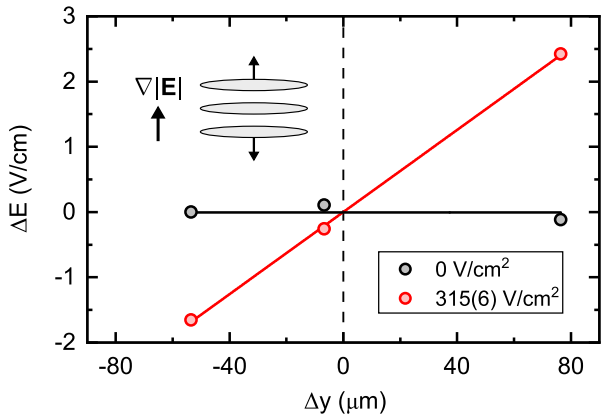

Figure 3.14: Measuring the molecule position relative to the center of the electrodes using an applied gradient. Molecules pinned in an optical lattice are translated along **y** (inset), and the transition frequency is measured at each position. At the center position, the frequency with a gradient (red line) should not shift relative to the case with zero applied gradient (black line).

3.4.2 Gradient Spectroscopy of Vertical Position

With the rods now connected correctly, we use applied gradients along **y** to measure the displacement from the center. Due to the symmetry of the rods, when the molecules are centered between the electrodes adding a gradient should not change the magnitude of the electric field. Therefore, for a known gradient, measuring the frequency shift from the electric field directly gives the displacement from the center. We pin the molecules along **y** in an optical lattice, so applying gradients does not change their position (Fig. 3.14, inset), and measure the $|0,0\rangle \rightarrow |1,0\rangle$ transition frequency in calculated gradients of $\partial_y|\mathbf{E}| = 0$ and 320 V/cm^2. By repeating this measurement at different positions, where the position is determined by imaging the molecules, we can identify the place where the transition frequency does not shift. We fit a gradient of 315(6) V/cm^2, consistent with the calculated value.

In large gradients, this method can be used to localize the cloud with precision better than 1 μm. For example, at a field of 4.5 kV/cm, the sensitivity of the rotational transitions to changes in electric field is 150 kHz/(V/cm). In a gradient of 10 kV/cm^2, this corresponds to a position sensitivity of 150 kHz/μm, large relative to our typical rotational spectroscopy linewidths. In

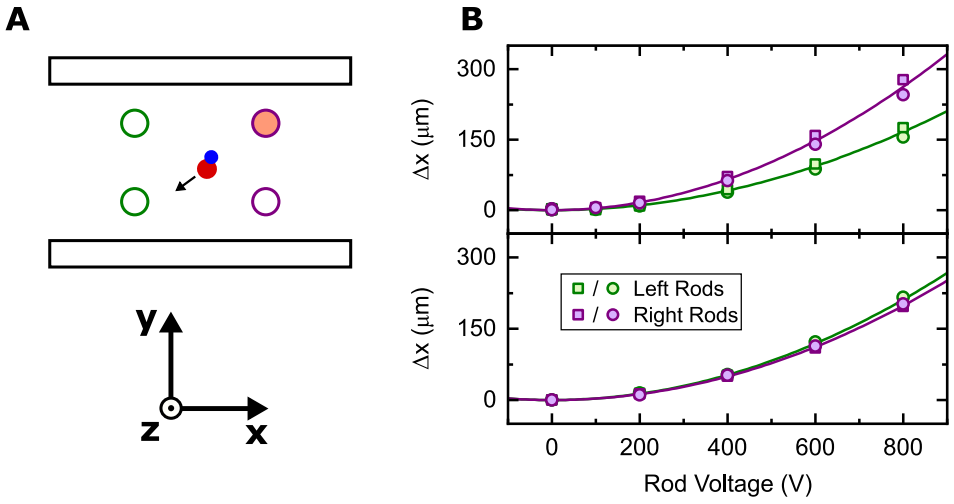

Figure 3.15: Aligning the molecules using gradients generated by single rods in time of flight. **(a)** Voltage is applied to a single rod (shown in red), which accelerates the molecules in **x**. **(b)** Depending on the horizontal position, the molecules will be affected differently by the pair of rods on the left (green) and the pair on the right (purple). The lower panel is about 200 μm closer to the center of the electrodes than the upper panel.

Chapter 6 we use a related technique to count the occupied lattice layers, and in Chapter 8 we measure displacements on the order of ten nanometers with this method.

3.4.3 Single-Rod Gradient Measurement

In principle, the displacement from the electrode center along the **x** axis could also be measured by adding a static gradient. However, since the radial confinement in the optical traps is several hundred times weaker than the confinement along **x** in the lattice, horizontal gradients shift the equilibrium position of molecules in the trap and can cause loss for large enough gradients. We use an alternative method for centering the molecules in this axis.

We let the molecules fall under gravity in time of flight and apply voltage to only one rod, while grounding the other rods and plates (Fig. 3.15a). This creates a large electric field gradient at the position of the molecules, accelerating them along **x**. We then fit the displacement as a function of rod voltage to a parabola and extract the quadratic coefficient. The field gradient decreases with distance from each rod; if the molecules are closer to the left pair of rods than the right pair, the

magnitude of acceleration will be different. At two different horizontal positions separated by about 200 μm, the left and right pairs of rods have visibly different effects (Fig. 3.15b). We are able to align the molecules to within 20 μm of the electrode center using this method.

Chapter 4

Reaching Degeneracy in Three Dimensions

In this chapter, I describe our work on associating degenerate polar molecules from a mixture of degenerate atoms. We reported degenerate molecules in Ref. [61] on the basis of observing a non-classical momentum distribution. At the time, we did not fully understand the mechanism by which the molecules inherited the low atomic phase space density. In the follow-up study Ref. [62], we measured the elastic scattering cross section between K atoms and KRb* Feshbach molecules, and concluded that the molecules thermalized by collisions with the remaining atoms during magnetoassociation. One enduring mystery, part of our evidence for degeneracy, is the suppressed two-body loss rate for degenerate molecules.

4.1 Introduction

Reaching degeneracy with polar molecules, where quantum statistics affect the momentum distribution and interaction energies are comparable to the thermal energy, has been a long-standing goal. 3D gases with dipolar interactions are predicted to exhibit collective behaviors such as Fermi surface deformation [104] and superfluidity [105]. Prior to this work, KRb had been produced near degeneracy by coherent association of degenerate atomic gases [14]. One experimental challenge for reaching higher phase space densities is rapid molecular loss, which occurs not only for molecular species with exothermic reaction pathways [21] but also nominally non-reactive molecules [18]. In a 3D optical lattice, where molecules are prevented from colliding, a low-entropy sample was prepared by overlapping atomic insulators [56]; however, degeneracy in bulk gases had not been achieved.

Atomic gases can be cooled to degeneracy by direct methods such as evaporation, which relies on elastic collisions between particles to redistribute energy and maintain thermal equilibrium. Multiple factors hinder efficient evaporation of ground-state molecules, including inelastic loss [96, 30] and weak elastic interactions in the absence of an applied electric field [106]. Directly laser cooled molecules remain far from quantum degeneracy, despite rapid recent progress in the area [10, 107, 9]. The atomic association process is therefore critically important for creating degenerate ground-state molecules. In the years following this work, we demonstrated direct evaporation using dipolar interactions between molecules at non-zero electric field [63, 65], and another group demonstrated sympathetic cooling using atoms [108]. In this chapter, I describe our measurements of the interactions between K and Rb atoms and KRb* Feshbach molecules during Feshbach association, and of the properties of the first degenerate gas of polar molecules.

4.2 Molecule Association

We associate molecules from an atomic mixture using the techniques described in Chapter 2. For Ref. [61], where we demonstrated degenerate polar molecules, the atoms were held in an optical dipole trap with a 45° crossing angle between the two beams, forming an ellipsoidal trap with trap frequencies for K of $(\omega_x, \omega_y, \omega_z) = 2\pi \times (45, 250, 80)$ Hz. In Ref. [62], our follow-up study on the thermalization and quantum statistical properties of degenerate molecules, the beams were rotated to a 90° crossing angle (as shown in Fig. 2.1), creating a trap with frequencies $(\omega_x, \omega_y, \omega_z) = 2\pi \times (60, 240, 60)$ Hz. The trap frequencies are scaled by factors of 0.72, 0.83, and 0.79 for Rb, KRb*, and KRb, respectively, due to differences in their masses and polarizabilities. For both Refs. [61] and [62], we used zero applied electric field.

The molecule conditions depend sensitively on the initial atomic numbers and temperatures. By varying the power of the MOT light in the initial cooling stage and the final trap depth after optical evaporation, we can control the molecule number and temperature. Figure 4.1 shows three representative atomic density distributions prior to association and the resultant molecule conditions. Table 4.1 lists the corresponding numbers and temperatures. At high temperatures, where

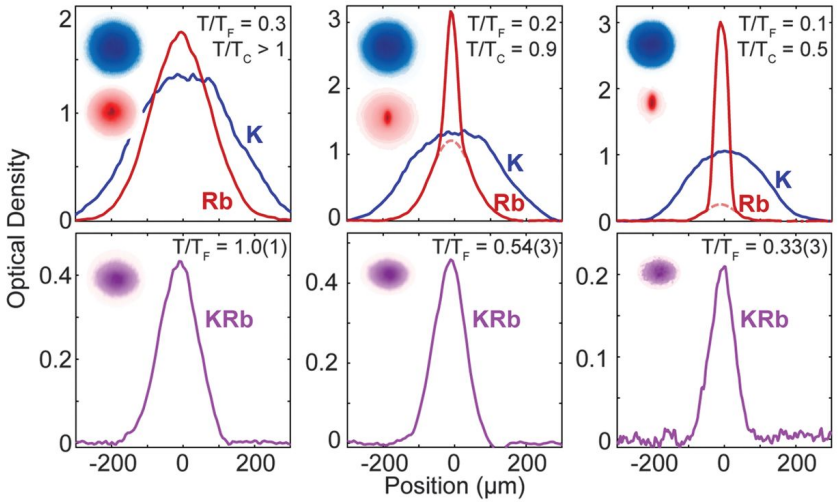

Figure 4.1: Atom conditions for molecule association. Density distributions of K and Rb atoms (top row) and corresponding molecule distribution. The Rb thermal fraction is indicated with dashed lines. When the K atoms are the majority species, a Rb BEC can be very efficiently converted into molecules despite the poor density overlap (right column), creating the most degenerate molecule conditions. Reproduced from Ref. [61].

T (nK)	N_{Rb}	T/T_c	N_{K}	T/T_F	N_{KRb}	T/T_F
230	6×10^5	> 1	1.2×10^6	0.3	1×10^5	1.0(1)
110	2×10^5	0.9	1×10^6	0.2	5×10^4	0.54(3)
50	7×10^4	0.5	5×10^5	0.1	3×10^4	0.33(3)

Table 4.1: Atom and molecule numbers and temperatures corresponding to Fig. 4.1. Reproduced from Ref. [61].

the Rb atoms are purely thermal (leftmost panel), the atomic density distributions are relatively well overlapped. Here, we produce as many as 10^5 KRb molecules, although the conversion fraction of the total Rb number is only about 15%. The coldest and most degenerate molecular samples, by contrast, are produced from a Rb BEC (rightmost panel); though the Rb distribution is sharply localized inside the broad K distribution, the conversion of Rb can approach 50%.

The Feshbach molecule conditions depend on the density overlap and phase space density of the constituent atoms. In previous studies on ^{40}K and ^{87}Rb mixtures, the conversion efficiency and final phase space density increased as the K T/T_F decreased [109, 73]. For molecules confined in 3D optical lattices, where the wavefunction overlap between atoms remains high throughout association, the association efficiency can approach unity on sites containing exactly one atom of each species [56, 110, 111]. When the majority species is bosonic [112, 73], the conversion efficiency of the minority species declines below the critical temperature T_c of the majority, where a Bose-Einstein condensate (BEC) is formed and the density overlap is reduced.

We operate in the opposite regime, where the Rb atoms in the BEC are a small minority. Though the overall density overlap is very low, the local density of K is high enough for efficient pairing with condensed Rb atoms. A recent experiment demonstrating the formation of degenerate NaK molecules found optimal conversion in the BEC in the case when the two atomic species had nearly equal peak densities, and confirmed the result that degenerate molecules could be associated from degenerate atomic gases [113]. In our experiment, high K phase-space density aids the formation of degenerate molecules by sympathetically cooling the KRb* through elastic collisions, as explored in the next section. Using a small Rb number also reduces the rate of lossy three-body recombination with KRb* molecules. Near the Feshbach resonance, free K and Rb atoms are indistinguishable from the weakly bound molecular constituents, leading to fermionic suppression of inelastic collisions of KRb* with K and bosonic enhancement of those with Rb [114, 115]. In order to minimize inelastic Rb-KRb* losses, the initial Rb number is chosen so that Rb is no longer condensed after molecule production.

We measure the ground state molecule momentum distribution in time of flight expansion

to characterize the degenerate gas (Fig. 4.2). The density distribution for a classical (Maxwell-Boltzmann) gas, integrated along the imaging axis, is Gaussian:

$$n(\tau) = n_0 e^{-\frac{x^2}{2\sigma_x^2} - \frac{y^2}{2\sigma_y^2}} \tag{4.1}$$

where x, y are the axes perpendicular to the imaging axis and n_0 is the peak density. $\sigma_{x,y}$ are widths that depend on the time of flight τ:

$$\sigma(\tau) = \sigma_0\sqrt{1+\omega^2 t^2} = \frac{\sqrt{1+\omega^2\tau^2}}{\omega}\sqrt{\frac{k_B T}{m}} \tag{4.2}$$

σ_0 is the *in situ* width of the cloud, ω is the trap frequency along the axis σ is measured, m is the mass, T is the temperature, and k_B is the Boltzmann constant. Degenerate Fermi gases have a different density distribution, which depends on the Fermi temperature T_F [116]:

$$n(\tau) = n_0 \frac{\mathrm{Li}_2\left(-\zeta \exp\left[-\frac{x^2}{2\sigma_x^2} - \frac{y^2}{2\sigma_y^2}\right]\right)}{\mathrm{Li}_2(-\zeta)} \tag{4.3}$$

Li_i is the polylogarithm function of order i and $\zeta = e^{\mu/k_B T}$ is the fugacity, where μ is the chemical potential. ζ is connected to T/T_F in 3D by the relation

$$\frac{T}{T_F} = \frac{1}{\left(-6\mathrm{Li}_3[-\zeta]\right)^3} \tag{4.4}$$

By fitting to Eq. 4.3, using $\sigma_{x,y}$ and n_0 as fitting parameters, we can extract T/T_F[1] .

We fit the density distribution shown in Fig. 4.2 to both the classical and Fermi-Dirac distributions. The classical fit overestimates the molecule density at low momentum and underestimates the width; this is a consequence of the Pauli exclusion principle, which prevents identical fermions from occupying the same quantum state [117]. The Fermi-Dirac distribution, by contrast, fits the measured density well. We extract $T/T_F = 0.31(2)$ from the fit. Comparing the fit residuals for each of these distributions (bottom panel), we see "oscillations" on the classical distribution previously measured for the first degenerate Fermi gas of atoms [42]. In the high momentum region of the gas, where the average occupation of each quantum state is small, the momentum distribution of the degenerate Fermi gas should look essentially classical. We fit only the high-momentum

[1] I had trouble inverting this equation numerically for $T/T_F \ll 1$, so here is a Mathematica line that works:
`ζ = E^q /.FindRoot[x == (-6 PolyLog[3, -E^q])^-1/3,{q,0}]`

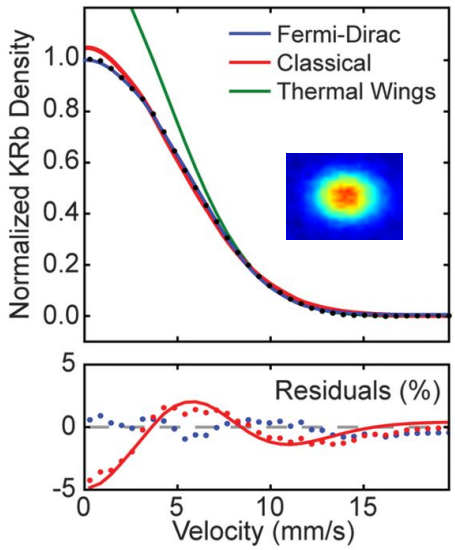

Figure 4.2: Momentum profile of a degenerate Fermi gas of KRb molecules. Classical fits to the entire distribution (red) and wings of the distribution (green) capture the density of high-momentum particles but overestimate the density at low momentum. This is the signature of Pauli exclusion in a degenerate gas. Fitting with a Fermi-Dirac distribution (blue) gives $T/T_F = 0.31(2)$. **Inset:** Averaged image of degenerate KRb. Adapted from Ref. [61].

region to a classical distribution (Fig. 4.2, green curve) and accurately extract the temperature of the molecules, although the fit again overestimates the density at low momentum.

In 3D, the Fermi temperature is

$$T_F = \frac{\hbar\overline{\omega}}{k_B}(6N)^{1/3} \tag{4.5}$$

where $\overline{\omega} = (\omega_x\,\omega_y\,\omega_z)^{1/3}$ is the harmonic mean trap frequency. Referring to Table 4.1, the KRb number is reduced by a factor of 16 compared to the K number and the trap frequencies are lower by a factor of 0.79. If the temperature is maintained during association, we therefore expect the molecular T/T_F to be 3.2 times larger than the atomic T/T_F. We measure fractional increases between 2.5 and 3.5 at all initial temperatures (Tab. 4.1), consistent with this estimate. The KRb phase space density may be slightly higher than predicted from uniform conversion over all K atoms because the Rb BEC is localized to a low-momentum region of the K at the center of the trap.

4.3 Feshbach Molecule Thermalization

In the formation of degenerate atomic gases, collisions between atoms are essential for maintaining thermal equilibrium. Bosonic Feshbach molecules formed in Fermi–Fermi mixtures are observed to reach thermal equilibrium due to strong elastic interactions and fermionic suppression of inelastic processes [118, 119, 120, 121, 122]. For heteronuclear molecules produced from Bose–Fermi mixtures, the situation is more complex. Inelastic boson–molecule collisions play a larger role [67, 115, 123] and atom–molecule elastic scattering has not been previously measured. Characterizing elastic and inelastic processes in these systems is essential for understanding thermalization dynamics and optimizing the production of a low-entropy sample.

We made the following series of measurements to identify the effect of atom-molecule interactions on the molecule phase space density and thermalization. After forming molecules, the peak density of K is approximately 10 times larger than that of Rb, so thermalization of KRb* is expected to occur predominantly through collisions with K. We measure elastic K–KRb* scattering as a function of the magnetic field B by two related methods.

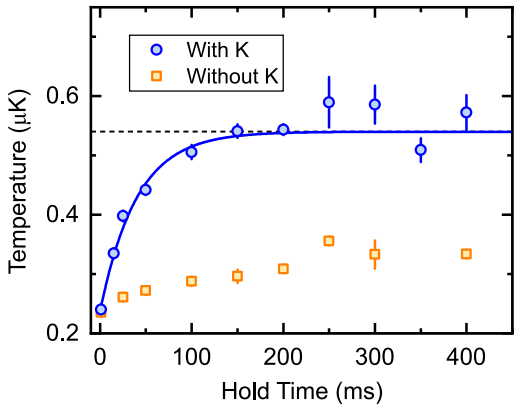

Figure 4.3: Feshbach molecule thermalization with K atoms. When the atoms are heated using near-resonant optical pulses to 540 nK (dashed black line), the Feshbach molecules increase to the same temperature (blue curve). Without atoms, the heating rate is much slower and no thermalization is observed over the lifetime of the molecules (orange points).

First, to confirm qualitatively that K–KRb* collisions are occurring, we measure cross-species thermalization. We prepare a mixture of K and KRb* at a temperature of 220 nK and $B = 546.5$ G, just below the interspecies resonance. We remove Rb atoms using resonant optical pulses. To create a temperature imbalance between K and KRb*, we heat the atoms using off-resonant optical pulses to 540 nK. By monitoring the temperature evolution of the KRb* with and without K atoms present, we observe the effects of thermalization (Fig. 4.3). KRb* molecules alone exhibit a small, linear temperature increase. With K present, however, they rapidly equilibrate to the atomic temperature with an exponential time constant of 35 ms.

4.3.1 K-KRb* Scattering Length

We make a quantitative measurement of the elastic cross section for K–KRb* scattering, denoted $a_{\text{K-KRb*}}$, by measuring the damping of KRb* center-of-mass oscillations due to collisions with K. To perform the measurement, we first use STIRAP to produce ground-state KRb at $B = 545.5$ G and remove all of the Rb atoms and a fraction of the K atoms using a combination of microwave pulses and light resonant with the atomic transition. A second STIRAP sequence transfers the molecules back to the Feshbach state, producing a sample of 2×10^4 KRb* at $T = 300$

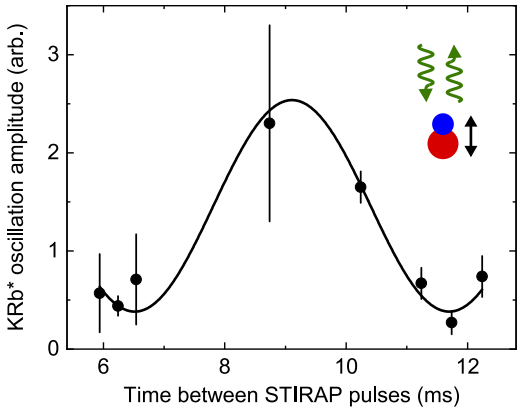

Figure 4.4: Using STIRAP to excite molecule oscillations. The oscillation amplitude of Feshbach molecules depends on the time delay between the association and dissociation STIRAP pulses. The period of the amplitude vs. delay time corresponds to the optical trap period of 1/(190 Hz) for ground-state KRb.

nK and 1.5×10^5 K at $T = 600$ nK.

We excite KRb* oscillations by varying the time delay between the two STIRAP sequences. During each sequence, the molecules absorb and emit photons of $\lambda_d = 690$ nm and $\lambda_u = 970$ nm along the direction of STIRAP beam propagation ($\mathbf{y}$), imparting a recoil momentum equal to the momentum difference between the photons:

$$p_{\text{rec}} = h\left(\frac{1}{\lambda_d} - \frac{1}{\lambda_u}\right) \tag{4.6}$$

After the first STIRAP sequence, which converts KRb* to KRb, the recoil causes the molecules to oscillate in the optical trap. The trap frequency is $\omega_y = 2\pi \times 190$ Hz for KRb, corresponding to a period of 5.3 ms. The second STIRAP sequence, converting KRb back to KRb*, imparts an opposite momentum kick. Therefore, if the two STIRAP pulses occur sequentially with no time delay, the molecules do not oscillate. If, however, the pulses are delayed in time by half the trap period, the momentum kicks add constructively and the oscillation amplitude is increased. We vary the delay time between the pulses and measure the expected dependence of the oscillation amplitude (Fig. 4.4).

We use this technique to excite an oscillation of KRb* and measure the thermalization rate by

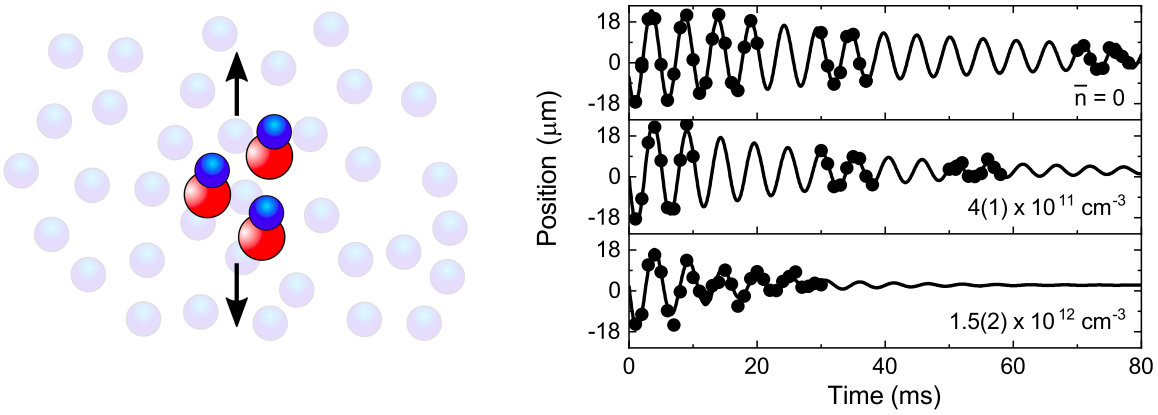

Figure 4.5: Elastic collisions between K atoms and KRb* molecules. We excite KRb* oscillations using STIRAP at varying K densities and measure the exponential damping rate to extract the elastic collision cross section. Adapted from Ref. [62].

varying the background K density (Fig. 4.5). As the density is increased at fixed B, the oscillations damp more quickly. In the absence of K, the oscillations are damped with time constant τ_a due to small anharmonicity in the trapping potential. To correct the measured damping time constant τ_m for this effect we subtract τ_a

$$\frac{1}{\tau} = \frac{1}{\tau_m} - \frac{1}{\tau_a} \tag{4.7}$$

to obtain $1/\tau$, the rate of damping due to elastic collisions, which is proportional to the elastic collision rate Γ. We relate Γ and τ using the methods of Refs. [124]. For more details about this calculation, see the Supplementary Material to Ref. [62].

Γ is related to the elastic cross section σ_{el} by $\Gamma = \overline{n}\sigma_{el}v$, where $\overline{n}$ is the overlap density between K and KRb*

$$\overline{n} = \left(\frac{1}{N_{\mathrm{K}}} + \frac{1}{N_{\mathrm{KRb^*}}}\right) \int n_{\mathrm{K}} n_{\mathrm{KRb^*}}\, d^3x \tag{4.8}$$

and v is the relative velocity between K and KRb*, averaged over the joint distribution [124, 125]:

$$v = \sqrt{\frac{8k_{\mathrm{B}}}{\pi}\left(\frac{T_{\mathrm{K}}}{m_{\mathrm{K}}} + \frac{T_{\mathrm{KRb^*}}}{m_{\mathrm{KRb}}}\right)} \tag{4.9}$$

We convert the cross section σ_{el} to scattering length $|a_{\text{K-KRb*}}|$ using

$$\sigma_{el} = \frac{4\pi a_{\text{K-KRb*}}^2}{1 + k_{\mathrm{th}}^2 a_{\text{K-KRb*}}^2} \tag{4.10}$$

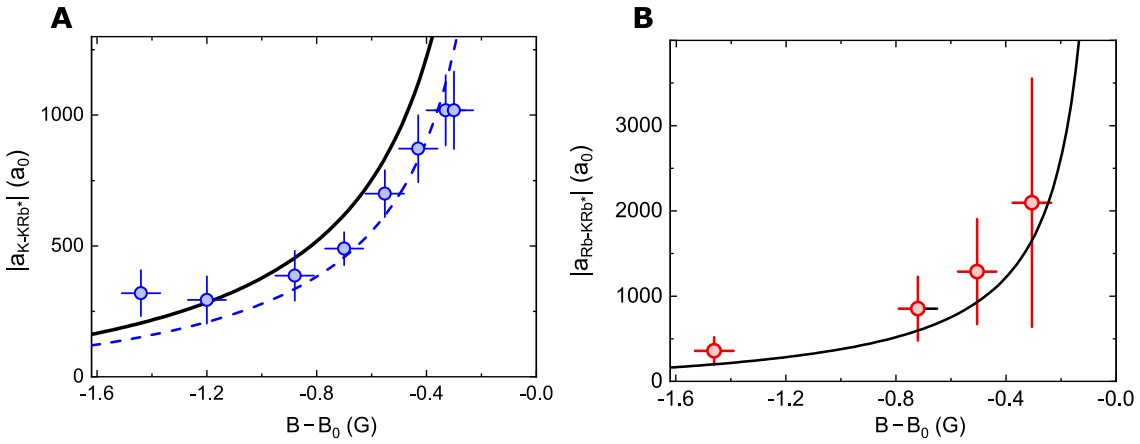

Figure 4.6: Atom-molecule scattering lengths, with the atom-atom scattering length ($a_{\text{K-Rb}}$) plotted as solid black lines **(a)** $a_{\text{K-KRb}^*}$ is smaller than $a_{\text{K-Rb}}$ by a factor of 0.74(5). **(b)** $a_{\text{Rb-KRb}^*}$ is similar to $a_{\text{K-Rb}}$, but the Rb density is relatively low so these collisions do not contribute many elastic collisions during the Feshbach ramp. Adapted from Ref. [62].

where $k_{\text{th}} = \sqrt{2\mu k_B T/\hbar^2}$ is the thermal collision wavevector, and μ is the K–KRb* reduced mass [74]. Figure 4.6 shows the measured scattering lengths for both K-KRb* and Rb-KRb* collisions as a function of magnetic field B. Since Feshbach molecules are very weakly bound, we expect these scattering lengths to be similar to the K-Rb scattering length; theory predicts a scaling of $a_{\text{K-KRb}^*} = 1.09\, a_{\text{K-Rb}}$ given the K-Rb mass ratio [126]. We measure a slightly lower scattering length of $a_{\text{K-KRb}^*} = 0.74(5)\, a_{\text{K-Rb}}$, though the trend of both $a_{\text{K-KRb}^*}$ and $a_{\text{Rb-KRb}^*}$ is in qualitative agreement with $a_{\text{K-Rb}}$.

Using $\sigma_{el}(B)$, we can estimate the number of elastic collisions experienced by each KRb* molecule during Feshbach association. To associate KRb* from the atomic mixture, the magnetic field is ramped from 555 G to 545.5 G in 5 ms, through the interspecies resonance at $B_0 = 546.6$ G, corresponding to a ramp rate of 1.9 G/ms. The average number of elastic collisions per molecule is $\overline{\Gamma}\,\Delta t = \overline{n}\,\overline{\sigma}_{el} v \times \Delta t$, where Δt is the ramp time on the molecular side of the Feshbach resonance, ΔB is the difference between the final magnetic field and B_0, and $\overline{\sigma}_{el}$ is the time-averaged elastic cross section:

$$\overline{\sigma}_{el} = \frac{1}{\Delta B} \int_{545.5\text{ G}}^{B_0} \sigma_{el}(B)\, dB \tag{4.11}$$

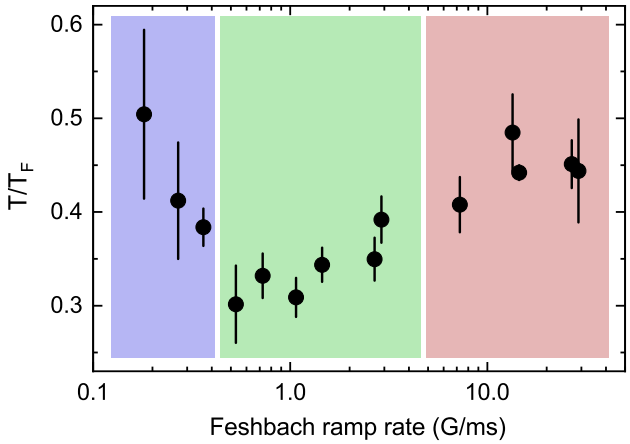

Figure 4.7: Molecule degeneracy vs. Feshbach ramp rate. For a fixed change in magnetic field from above to below resonance, the final T/T_F of the molecules depends on the field ramp speed. When the ramp speed is too slow (blue), lossy two-body collisions between Feshbach molecules increase the T/T_F. When the ramp speed is too fast (red), not enough elastic collisions between Feshbach molecules and atoms occur to cool and thermalize the molecules. Adapted from Ref [62].

We find that each molecule experiences about 6 collisions with K atoms, enabling thermalization.

The ratio of elastic and inelastic collisions depends on the Feshbach ramp rate. During magnetoassociation there is a competition between thermalization, which favors slower ramp rates, and inelastic losses, which are minimized with faster ramp rates. By varying the ramp time for fixed initial and final magnetic fields, we observe a strong dependence on the molecule T/T_F (Fig. 4.7). For intermediate ramp rates of 0.5–3 G/ms, T/T_F reaches a minimum at 0.3. At very slow ramp rates (< 0.5 G/ms), we observe substantial loss from inelastic processes, resulting in a sharp increase in the molecular T/T_F. We also observe a gradual rise in T/T_F as the ramp time becomes much shorter than the trap oscillation period, while the molecule number remains constant, suggesting that during fast ramps too few elastic collisions occur for complete thermalization.

4.4 Two-Body Loss

KRb molecules experience two-body loss due to reactive collisions, which cause the density to decay as the molecules are held in the trap (Fig. 4.8). The average density in 3D, in terms of

the particle number N, the temperature T, and the trap frequencies ω_i, is

$$\begin{aligned} n &= \frac{N}{8\pi^{3/2}\sigma_x\sigma_y\sigma_z} \\ &= \frac{\omega_x\,\omega_y\,\omega_z}{8\pi^{3/2}} N \left(\frac{k_B T}{m}\right)^{-3/2} \end{aligned} \tag{4.12}$$

The temperature is time-dependent because of one-body heating from the optical traps and two-body loss that modifies the average energy distribution. Differentiating Eq. 4.12, we find the following differential equation for the density decay:

$$\frac{dn}{dt} = -\beta n^2 - \frac{3}{2}\frac{n}{T}\frac{dT}{dt} \tag{4.13}$$

where we have described the two-body number loss with

$$\frac{dN}{dt} = -\frac{\beta}{V}N^2 \tag{4.14}$$

β is the two-body loss rate coefficient and $V = 8\pi^{3/2}\sigma_x\sigma_y\sigma_z$ is the effective volume of the trapped gas. The time- and density-dependence of the temperature, calculated in Ref. [46], is

$$\frac{dT}{dt} = h + \frac{\beta n T}{12} \tag{4.15}$$

For our experimental parameters, the one-body heating h typically exceeds the second term after only a short hold time. Therefore, following Ref. [21], we assume linear heating: $T(t) \approx T_0 + ht$. We measure the heating dynamics and confirm that they are approximately linear.

With linear heating, the differential equation describing the density becomes

$$\frac{dn}{dt} = -b(T_0 + ht)n^2 - \frac{3}{2}\frac{hn}{T_0 + ht} \tag{4.16}$$

where we have rewritten $\beta = bT$. This equation has an analytic solution:

$$n(t) = \frac{h n_0 T_0^{3/2}}{T(t)\left(h\sqrt{T(t)} + 2bn_0 T_0^{3/2}(T(t) - \sqrt{T(t)T_0})\right)} \tag{4.17}$$

where n_0 is the initial density. In the case when $h = 0$, this simplifies to

$$n(t) = \frac{n_0}{1 + bT_0 n_0 t} \tag{4.18}$$

We independently measure the density and temperature at each time t, and obtain T_0 and h from a linear fit to the temperature evolution. We then use these quantities as inputs to Eq. 4.17 and fit the density evolution to obtain b and n_0.

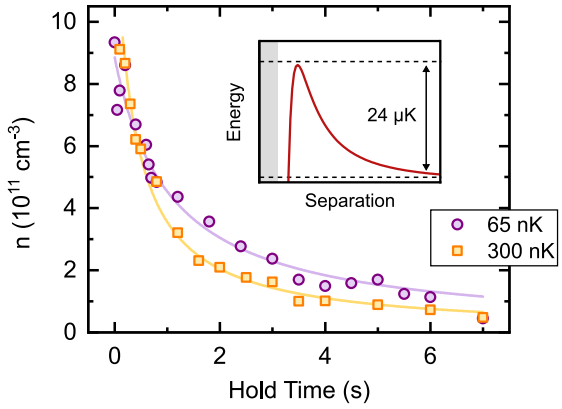

Figure 4.8: Temperature dependence of two-body loss. Density decay of KRb at $T = 65, 300$ nK. The two-body loss rate coefficient β scales linearly with T for thermal gases. **Inset:** Colliding molecules must tunnel through the p-wave centrifugal barrier to short range, where we assume they are lost with unit probability. Adapted from Ref. [61].

4.4.1 Temperature Dependence

The intermolecular potential for colliding molecules in zero electric field is

$$V(r) = \frac{\hbar^2 L(L+1)}{2\mu r^2} - \frac{C_6}{r^6} \tag{4.19}$$

where the first term is the centrifugal potential and the second term is the van der Waals potential. KRb molecules are fermions, which means at ultracold temperatures they primarily collide with the lowest odd partial wave, $L = 1$. This forms an effective barrier with a height of 24 μK (shown in the inset to Fig. 4.8), much higher than the thermal energy. When molecules tunnel through the barrier, they are lost with near-unit probability to chemical reactions. Given the functional form of the barrier, β is predicted to scale proportionally to T; this motivates writing the loss rate coefficient as $\beta = bT$, where $b = 0.8(1) \times 10^{-5}$ cm^3 K^{-1} s^{-1} [23]. b was previously measured and was found to be constant up to 900 nK for thermal KRb [21]. A simple semiclassical derivation of the temperature scaling of β is presented in Appendix B. Figure 4.8 shows representative density decay curves at 65 and 300 nK, displaying a marked density difference at late times.

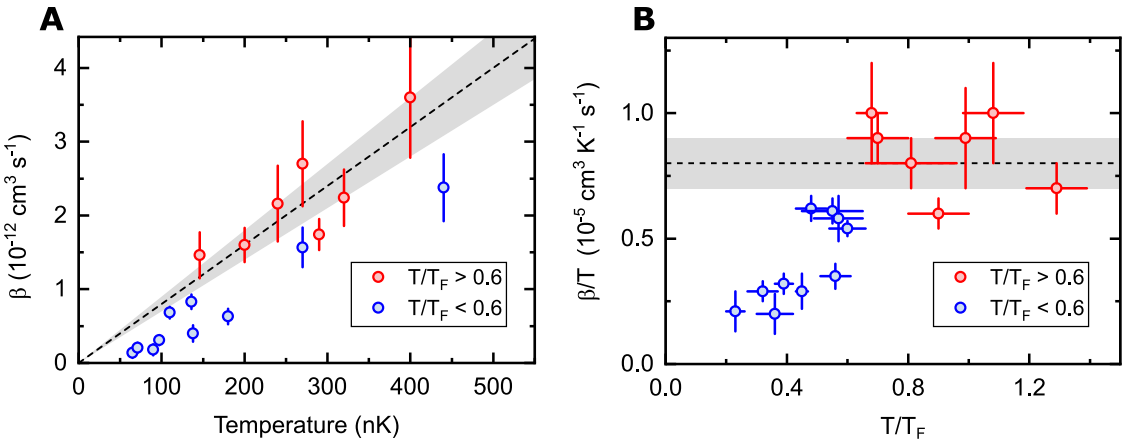

Figure 4.9: Dependence of two-body loss on temperature and T/T_F. **(a)** We expect $\beta/T = 0.8(1) \times 10^{-5}$ cm^3 K^{-1} s^{-1}, shown as a shaded region. Degenerate molecules, with $T/T_F < 0.6$, have lower β than expected at all temperatures. **(b)** Rearranging the points by T/T_F, we observe smaller β/T at lower T/T_F. Adapted from Ref. [61].

4.4.2 Suppressed Loss Below T_F

We measure b at molecule temperatures ranging from 60 to 450 nK, and plot $\beta = bT_0$ (Fig. 4.9a). At certain temperatures, the loss rate coefficient is consistent with predictions, while at other temperatures the rate is substantially smaller. Coloring the points according to T/T_F, we see that the loss rate for degenerate molecules ($T/T_F < 0.6$) is suppressed relative to thermal molecules. We also plot b, ordering the points by T/T_F rather than temperature (Fig. 4.9b). As T/T_F decreases, so does the loss rate. b reaches a minimum of $0.21(8) \times 10^{-5}$ cm^3 K^{-1} s^{-1}, four times lower than the predicted value and the values measured for thermal molecules.

We have written $\beta \propto T$, which is valid for $T/T_F \gg 1$. More fundamentally, however, β is proportional to the average collision energy E [23]. For ultracold fermions, where energy levels up to the Fermi energy E_F are populated even at $T = 0$, the collision energy and β saturate at non-zero values. Rather than $\beta/T \to 0$ at low temperatures, as we have measured, we would expect $\beta/T \to \infty$. We reanalyzed the data in Fig. 4.9 making the replacement $T \to E/k_B$ and found that the loss suppression was even more pronounced.

The fact that the loss suppression depends on degeneracy rather than temperature suggests

that quantum statistics are involved. The scaling of b with T/T_F looks qualitatively similar to the suppression of s-wave elastic collision cross sections due to Pauli blocking, previously measured with dipolar fermions [127] and fermionic mixtures [128]. For elastic collisions, the suppression in a degenerate gas arises because most states below E_F are occupied, restricting the number of states available for particles to scatter into. For inelastic collisions, by contrast, the colliding molecules are ejected from the trap and therefore the state distribution of the remaining molecules should not play a role.

In Ref. [61], we hypothesized that the loss suppression was due to reductions in density fluctuations, previously measured in atomic gases [129, 130] and discussed in detail in the following chapter (based on Ref. [62]). In regions of a degenerate Fermi gas, the particle number variance approaches zero linearly with T/T_F, a phenomenon called "anti-bunching". This effect leads to anti-correlations in the positions of degenerate fermions; since two molecules must collide to react, we suggested that the reaction rate should decrease proportionally to the fluctuations. However, our collaborators in the Rey, Greene, and Zhou groups performed calculations showing that this intuitive argument was incorrect, and that the reaction rate scales with the collision energy even for $T/T_F \ll 1$ [131, 132]. The loss suppression remains a mystery, although recent experiments showing the creation of degenerate fermionic NaK molecules [113, 133] may allow testing this effect in a different species with equivalent statistics.

Chapter 5

Density Fluctuations in a Degenerate Fermi Gas

In the previous chapter, we measured that Feshbach molecules reach thermal equilibrium through elastic collisions with atoms. Here, we probe the quantum statistical properties of the resulting degenerate molecular gases by measuring the local suppression of density fluctuations in both Feshbach and ground state KRb. This chapter is based on Ref. [62] and is a follow-up study to Ref. [61], where we first demonstrated degenerate molecules.

5.1 Introduction

Quantum statistics play a key role in the behavior of ultracold atoms and molecules, even when the particles are non-interacting. In degenerate Fermi gases of identical particles, the Pauli exclusion principle prevents multiple occupancy of each quantum state. This effect leads to suppressed number fluctuations in the occupation of each state compared to a classical gas (degenerate Bose gases have correspondingly enhanced fluctuations), and has been previously used to characterize degeneracy and phase transitions in atomic gases [134, 135, 129, 130, 136, 137].

Here we measure suppressed fluctuations for the first time in ultracold molecules. In our previous work, we measured the temperature and T/T_F of molecular samples by fitting the momentum distribution after free expansion [61]. Compared to previous works with fermionic atoms, one important consideration for thermometry of ground-state molecules is the effect of STIRAP, which uniformly introduces a small number of holes in the KRb state distribution while preserving the shape of the expanded cloud. By measuring number fluctuations, we are able to directly ac-

cess the state occupancy and probe degenerate molecules on a microscopic scale. We find that for Feshbach molecules (KRb*), the fluctuation thermometry produces consistent results with expansion thermometry, confirming that the molecules reach thermal equilibrium due to collisions with K atoms. For ground state molecules (KRb), we observe increased fluctuations, suggesting that STIRAP produces a slightly out-of-equilibrium state distribution.

We are indebted to Refs. [129, 130] for the experimental methods and theory background that we followed in conducting these experiments. See also the related theses Refs. [138, 139, 140] for full derivations of the fluctuation statistics for Bose and Fermi gases, and in particular for the connections to the fluctuation-dissipation theorem and extensions to interacting particles.

5.2 Density Fluctuations in Degenerate Gases

We probe the state occupation of degenerate atomic and molecular gases by measuring number fluctuations. If we subdivide a gas of particles into small volumes and count the particle number in one volume over many experimental realizations, we would measure a mean number $\overline{N}$ and number variance σ_N^2. For a classical gas, as a consequence of the Poissonian distribution of energy state occupation, these two quantities are equal: $\sigma_N^2/\overline{N} = 1$. For a degenerate Fermi gas, however, the fluctuations are suppressed below the classical value due to the Pauli exclusion principle. In the limit of $T/T_F = 0$, each state below the Fermi energy is occupied by exactly one particle; therefore, the variance of any collection of states is zero.

For trapped fermions, the number variance depends on position. We use the local density approximation and define the chemical potential locally at position $\mathbf{r}$ as

$$\mu(\mathbf{r}) = \mu - V(\mathbf{r}) \tag{5.1}$$

where $V(\mathbf{r})$ is the potential due to the optical trap. We can then define the fugacity locally as well:

$$\zeta(\mathbf{r}) = e^{\mu(\mathbf{r})/k_B T} \equiv \zeta\, e^{-V(\mathbf{r})/k_B T} \tag{5.2}$$

ζ is defined as the peak fugacity, occurring at the center of the trap where we define $V(0) = 0$ as the potential minimum. After time of flight expansion the position of each particle is determined by

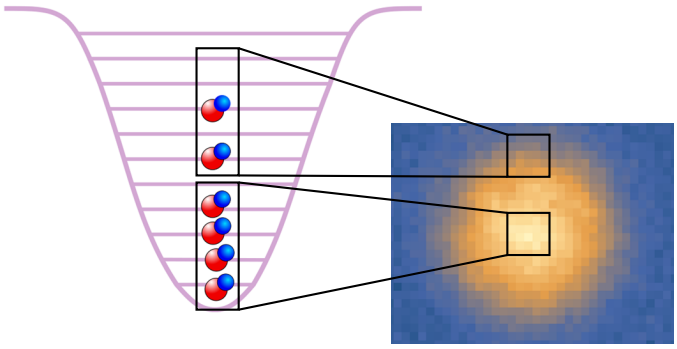

Figure 5.1: Momentum state occupation in degenerate Fermi gases. The occupation probability approaches unity for low-momentum states in a degenerate gas, corresponding to the center of the particle distribution after time of flight expansion. The occupation of high-momentum states, however, still behaves classically.

its *in situ* position and momentum. In the particular case of harmonic trapping, $\zeta(\mathbf{r})$ is conserved up to a rescaling of the position coordinates by the factor $\sqrt{1+\omega_i^2\tau^2}$, where ω_i is the trapping frequency along the ith coordinate and τ is the time of flight [129, 116].

In terms of the fugacity, the density fluctuations in a 3D Fermi gas are

$$\frac{\sigma_N^2}{\overline{N}} = \frac{\mathrm{Li}_{1/2}(-\zeta e^{-V(\mathbf{r})/k_BT})}{\mathrm{Li}_{3/2}(-\zeta e^{-V(\mathbf{r})/k_BT})} \tag{5.3}$$

where Li_n is the polylogarithm function of order n. The fluctuations are minimized where $V(\mathbf{r})$ is minimized, corresponding to the center of the trap *in situ* or to low-momentum states in expansion. In absorption imaging, the 3D atom and molecule density is integrated along the imaging axis, producing 2D images. This modifies the form of the fluctuations:

$$\frac{\sigma_N^2}{\overline{N}} = \frac{\mathrm{Li}_{1}(-\zeta e^{-V(x,z)/k_BT})}{\mathrm{Li}_{2}(-\zeta e^{-V(x,z)/k_BT})} \tag{5.4}$$

x, z are the radial coordinates of the optical trap, perpendicular to the imaging axis y.

The basic principle is illustrated in Fig. 5.1. For low-momentum states, where the occupancy is highest, fluctuations are suppressed. The opposite is true for high-momentum states. By imaging particles in time of flight, we probe the entire momentum distribution and expect to see spatial

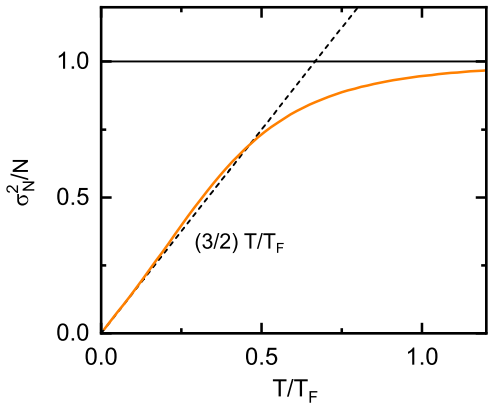

Figure 5.2: Density fluctuations in 3D as a function of T/T_F. At high T/T_F, $\sigma_N^2/\overline{N} \to 1$, the value given by Poissonian statistics. At low T/T_F, $\sigma_N^2/\overline{N} \to (3/2)T/T_F$ (dashed line).

dependence of fluctuations. The peak fugacity ζ is related to T/T_F by

$$\frac{T}{T_F} = \frac{1}{(-6\mathrm{Li}_3[-\zeta])^3} \tag{5.5}$$

Figure 5.2 shows the number fluctuations as a function of T/T_F. At very low temperatures, where $T/T_\mathrm{F} \ll 1$, nearly all states below the Fermi energy are singly occupied and the peak variance is suppressed below the mean by the factor $(3/2)\,T/T_\mathrm{F}$ [129]. At high temperatures, this quantity approaches 1.

5.3 Imaging Number Fluctuations

We make measurements of number fluctuations using absorption imaging, where the absorption of an optical probe beam by the atoms or molecules is measured to determine the optical density. Each image consists of three frames taken in order, called "shadow", "light", and "dark." On the shadow frame, the particles are present and absorb probe light at their position in space. On the light frame, the molecules are gone, and the camera images only the probe light. On the dark frame, there is no probe, so the camera images stray light and internal readout noise. We denote the photon numbers on a given pixel on these three frames P_s, P_l, and P_d.

The optical density on each pixel is

$$OD = \ln\left(\frac{P_l - P_d}{P_s - P_d}\right) + \frac{P_l - P_s}{P_{\text{sat}}^{\text{eff}}} \tag{5.6}$$

$P_{\text{sat}}^{\text{eff}} = tI_{\text{sat}}^{\text{eff}}/(hc/\lambda)$ is the effective saturation intensity for the imaging system, in units of photon number, for probe time t and imaging wavelength λ. The OD is related to the atom density n and number N as

$$OD = \sigma_{\text{eff}}\, n = \frac{\sigma_{\text{eff}}}{A} N \tag{5.7}$$

A is the effective area of each pixel at the location of the atoms, related to the pixel size on the camera by the squared magnification of the imaging system, and σ_{eff} is the effective absorption cross section.

5.3.1 Saturation Intensity

We use effective parameters $I_{\text{sat}}^{\text{eff}}$ and σ_{eff}, which are related to their bare atomic counterparts by the parameter α: $I_{\text{sat}}^{\text{eff}} = \alpha I_{\text{sat}}$ and $\sigma^{\text{eff}} = \sigma_0/\alpha$ [141]. α quantifies the effects of imperfect polarization and imaging laser linewidth. For instance, if the polarization is rotated from the polarization that drives a particular atomic transition, the measured photon number on the camera will be higher than the photon number of the correct polarization at the position of the atoms. To convert the OD directly to atom number the only unknown parameter is α.

We measure α by two complementary methods. First, by directly measuring the probe polarization and linewidth, we find that the maximum physical absorption cross section is reduced by a factor $\alpha = 1.66$. Second, we follow the procedure described in Ref. [142] to extract α using measurements on the atoms:

(1) Take a series of absorption images with approximately constant atom number and temperature, varying the probe intensity over a factor of ten between images

(2) Extract the atom number from the OD using Eq. 5.6, varying α (or equivalently $P_{\text{sat}}^{\text{eff}}$)

(3) Choose the α that minimizes the variation of atom number with intensity

By this method, we extract $\alpha = 1.7(1)$, consistent with the direct measurement of the imaging light. We fix $\alpha = 1.66$ for the following.

5.3.2 Correcting the Optical Density Variance

The variance of the optical density (σ^2_{OD}) contains contributions not only from atom number variance (σ^2_N) but also spurious variance due to photon number shot noise (σ^2_I). These quantities are related as

$$\sigma^2_{OD} = \left(\frac{\sigma_{\text{eff}}}{A}\right)^2 \sigma^2_N + \sigma^2_I \tag{5.8}$$

We can explicitly compute the imaging noise using Eq. 5.6. We set $P_d = 0$, since the counts on each dark frame are almost entirely due to a static thermal background and readout noise:

$$\begin{aligned} \sigma^2_I &= \left(\frac{\partial OD}{\partial P_s}\right)^2_{P_d=0} \sigma^2_{P_s} + \left(\frac{\partial OD}{\partial P_l}\right)^2_{P_d=0} \sigma^2_{P_l} + \left(\frac{\partial OD}{\partial P_d}\right)^2_{P_d=0} \sigma^2_{P_d} \\ &= \left(\frac{1}{P_s} + \frac{1}{P^{\text{eff}}_{\text{sat}}}\right)^2 \sigma^2_{P_s} + \left(\frac{1}{P_l} + \frac{1}{P^{\text{eff}}_{\text{sat}}}\right)^2 \sigma^2_{P_l} + \left(\frac{P_l - P_s}{P_l P_s}\right)^2 \sigma^2_{P_d} \end{aligned} \tag{5.9}$$

We expect the photon number noise to have a Poissonian distribution, meaning the mean is equal to the variance ($\sigma^2_N = \overline{N}$). To measure this, we take a set of images without atoms, each consisting of a shadow and light frame. We subtract the photon number on the shadow and light frames to obtain the photon number difference on each pixel, and then compute the variance for each pixel across the set of images. A histogram of the variance versus the mean photon number, with the variance divided by two to account for the uncorrelated noise on the two frames, is shown in Fig. 5.3. In making this measurement, we must subtract the noise added by the quantum efficiency of the camera, which is the probability of an incident photon being converted into a camera count. This is modeled as a binomial process with probability 85%, based on the manufacturer specifications. We measure $\sigma^2_N/\overline{N} = 0.98$, very similar to the expected value.

The camera adds readout noise to each frame, with variance denoted σ^2_r in units of photon number. We directly measure this readout noise by taking images with no light present and comparing the photon number between the same pixel on consecutive frames. The noise is two counts per pixel (Fig. 5.4a), which is the specified readout noise for our camera. To account for

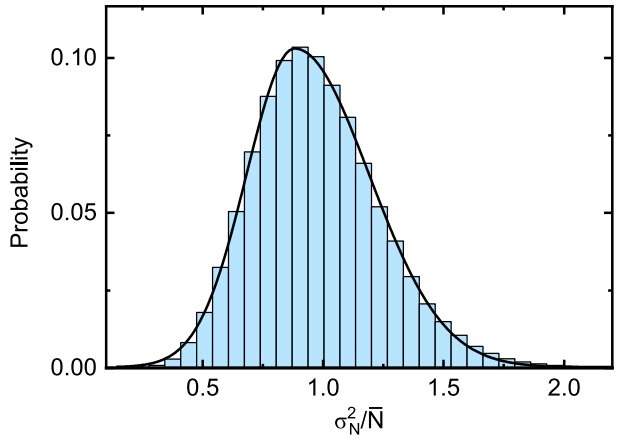

Figure 5.3: Photon number statistics. Distribution of photon number variance and mean per pixel, after accounting for the specified quantum efficiency of the camera. We measure a mean of $\sigma_N^2/\overline{N} = 0.98$, very close to the expected value of 1.

the photon noise distribution and the readout noise, we make the substitutions $\sigma^2_{P_{s/l}} \to P_{s/l} + \sigma_r^2$ and $\sigma^2_{P_d} \to \sigma_r^2$:

$$\begin{aligned}\sigma_I^2 &= \left(\frac{1}{P_s} + \frac{1}{P_{\text{sat}}^{\text{eff}}}\right)^2 (P_s + \sigma_r^2) + \left(\frac{1}{P_l} + \frac{1}{P_{\text{sat}}^{\text{eff}}}\right)^2 (P_l + \sigma_r^2) + \left(\frac{1}{P_s} - \frac{1}{P_l}\right)^2 \sigma_r^2 \\ &\approx \frac{1}{P_s} + \frac{1}{P_l} + \frac{2\sigma_r^2}{P_s^2} + \frac{2\sigma_r^2}{P_l^2} + \frac{4}{P_{\text{sat}}^{\text{eff}}} + \frac{P_l + P_s}{(P_{\text{sat}}^{\text{eff}})^2}\end{aligned} \tag{5.10}$$

The last approximation relies on two assumptions: first, that the probe is weak relative to the saturation intensity ($P_{s/l} \ll P_{\text{sat}}^{\text{eff}}$), and second, that the readout noise is small relative to the photon noise ($\sigma_r^2 \ll P_{s/l}$). We operate with relatively weak probe power ($P_{l/s} \approx 0.2 P_{\text{sat}}^{\text{eff}}$) and directly measure that the variance on the dark frame is two orders of magnitude smaller than on the light frame, indicating that both inequalities are satisfied. By subtracting Eq. 5.10 from the total measured OD variance, the contribution from fluctuating atom number can be isolated (Eq. 5.8). Without this correction, we measure a background variance of several atoms per pixel, with a spatial profile roughly inversely proportional to the probe intensity (Fig. 5.4b, yellow curve). By subtracting the calculated imaging noise (green curve), the corrected variance is near zero on each pixel (red curve). The mean effective atom number (blue curve) is zero because the noise is randomly distributed around zero.

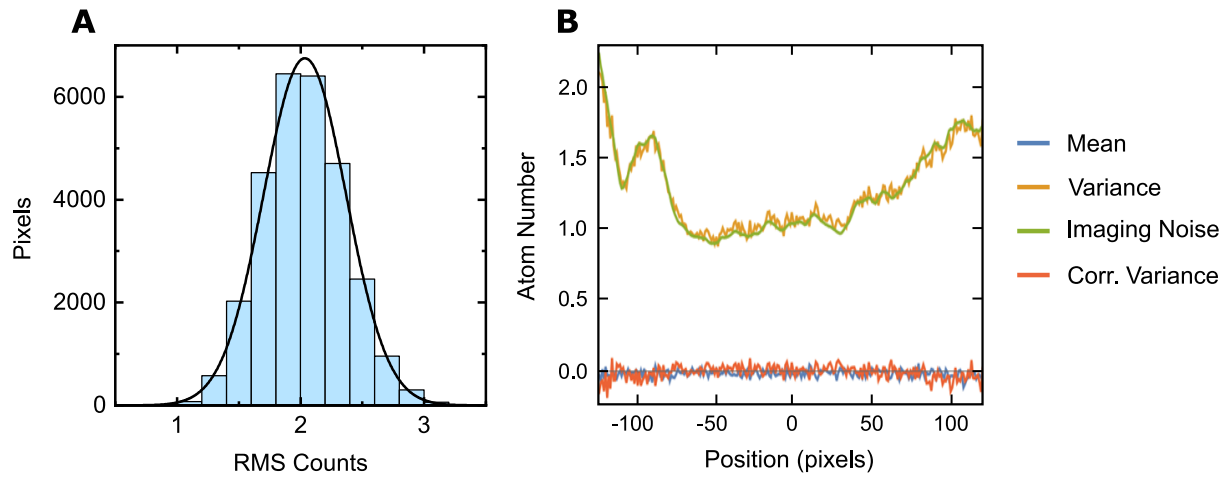

Figure 5.4: Subtracting imaging noise from number fluctuations. **(a)** The camera adds readout noise of two counts per pixel, as specified. **(b)** By accounting for the spurious atom number fluctuations introduced by photon number fluctuations (orange and green curves), we nearly eliminate the atom number variance measured on images with no atoms (red curve).

5.3.3 Image Binning and Resolution

In the measurement of number fluctuations, each image is divided into many smaller bins, corresponding to an integer number of CCD pixels. Since real imaging systems have finite resolution, the absorption signal from a single particle contributes to the signal measured on multiple adjacent bins. This effect tends to reduce the effective number variance on each bin, since holes in the particle distribution that fluctuate shot-to-shot are averaged across neighboring bins. As an extreme example, consider the case where the resolution is the size of the cloud, so that the positions of each particle cannot be resolved. The particle number variance on each pixel would then be equal to the variance of the total number divided by the number of pixels, and would have no relationship to the actual fluctuations in state occupation. A similar effect can occur due to particle motion during the imaging pulse; however, this effect is negligible for the probe time (10 μs) and particle mass in this experiment.

We could choose to use bin sizes much larger than the imaging resolution, which would make this "blurring" of the fluctuations negligible. However, using larger bins reduces the total number of bins obtained from each image and makes it more difficult to accumulate statistics. The alternative route of improving the imaging resolution has the downside of reducing the depth of field, which is related to the resolution r and imaging wavelength λ as

$$\mathrm{DOF} \approx \frac{2r^2}{\lambda} \tag{5.11}$$

A shallow depth of field broadens the absorption signal from atoms displaced from the focal plane. At the imaging resolution of approximately 2.5 μm, the depth of field is 16 μm.

Rather than change the imaging resolution, we correct the measured variance to account for the resolution and depth of field. We quantify the reduction of the fluctuations $\sigma_N^2/\overline{N}$ by reanalyzing images of non-degenerate K ($T/T_F > 0.6$) using bin widths ranging from 1.29–14.19 μm (Fig. 5.5). For a non-degenerate cloud the expected slope is determined by Poissonian statistics: $\sigma_N^2/\overline{N} = 1$. Over the range of bin widths, the slope is found to increase from 0.18 to 0.84, with the trend indicating saturation at $\sigma_N^2/\overline{N} = 1$. The small size of the cloud prevents the use of larger

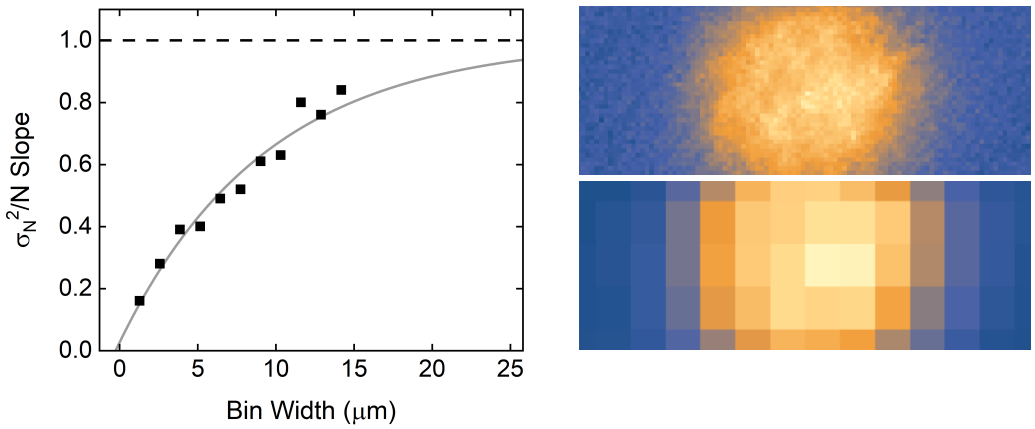

Figure 5.5: The measured number fluctuations depend on the image bin width relative to the imaging resolution. We analyze images of non-degenerate K atoms and plot the fluctuations as a function of the binning. $\sigma_N^2/\overline{N}$ approaches 1 (dashed line) as the width is increased. We operate at a bin width of 6.45 μm relative to the resolution of approximately 2.5 μm, necessitating a scaling of the measured variance by the factor 2.2. Two images with different bin sizes are shown on the right. Adapted from Ref. [62].

bin widths for this measurement, but the slope saturating near 20-25 μm would be consistent with previous experiments that observed saturation at approximately 10 times the resolution [129, 136]. We chose to operate at a bin width of 6.45 μm, equal to five camera pixels, where we measured $\sigma_N^2/\overline{N} = 0.45(4)$. We scaled up the measured variances by a factor of 2.2 to recover the actual particle number variance.

We additionally perform a simulation to verify the experimental results. Using the atom and molecule temperatures recorded in experiment, we generate simulated absorption images by random sampling from the Maxwell-Boltzmann momentum distribution. To approximate resolution and depth of field effects, we treat the absorption signal from each particle as having a Gaussian waist determined by the imaging resolution, and propagate the signal to the camera. We then bin and analyze the data equivalently to the experimental data and average over many images. We extract a slope of 0.4 from the simulation, consistent with the experimental measurement.

5.4 Fluctuation Measurements

We perform measurements of number fluctuations on K, KRb*, and KRb after 6 ms of free expansion. In order to accurately count the molecule number and eliminate added fluctuations from the lower KRb* imaging cross section, we adiabatically dissociate KRb* during expansion with a 2.5 G/ms ramp of B before imaging [143]. Sub-Poissonian number fluctuations have not been previously observed in molecules, making characterization of the imaging system and of the data analysis procedure essential. We use measurements on degenerate and non-degenerate K atoms to benchmark the experimental methods against previous studies on atomic Fermi gases [129, 130].

For each species, a set of 100–125 absorption images are taken. We subdivide the images into bins and fit each to the Fermi–Dirac momentum distribution. We post-select images to reduce shot-to-shot variation by automatically discarding outliers in total number and temperature, and do not manually exclude any images. Only images with total particle number within $\pm 15\%$ of the median number are retained, leaving between 50–60 images of each species for analysis. We subtract the fitted profile of each image from the raw optical density profile to normalize against

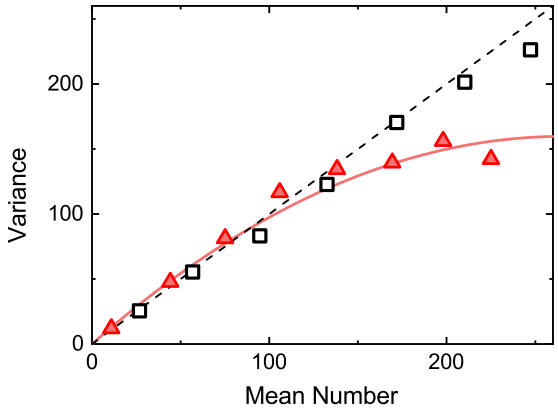

Figure 5.6: Number fluctuations for thermal K atoms (squares) and degenerate KRb molecules (triangles), averaged over bins with similar mean numbers. The dashed line indicates $\sigma_N^2/\overline{N} = 1$, the expected result for classical particles, and the solid curve is a guide to the eye. Low-momentum states containing high molecule numbers demonstrate suppression of the number variance due to Pauli exclusion. The solid line is a quadratic guide to the eye. Reproduced from Ref. [62].

total particle number fluctuations, which would otherwise be the dominant contribution to the variance. With this method, we are essentially measuring only number fluctuations on top of a perfect Fermi-Dirac distribution.

5.4.1 Degenerate KRb and Non-Degenerate K

Figure 5.6 shows the dependence of number variance on mean number for degenerate KRb and non-degenerate K. Each point on the figure represents an average over bins with similar mean number. If there were no number fluctuations, this would correspond to averaging over bins in a concentric ring of fixed radius on each image (Fig. 5.1). In the non-degenerate case, $\sigma_N^2/\overline{N} = 1$ across the entire sample, the result expected from Poissonian statistics. This validates the variance scaling factor we computed in the previous section. By contrast, the degenerate KRb exhibits non-linear scaling of fluctuations, which separate into two distinct regimes. At the edge of the cloud, corresponding to bins with the lowest mean molecule number, the fluctuations are Poissonian due to high availability of unfilled states near the Fermi surface. At the center of the cloud, corresponding to bins with the highest mean molecule number, the fluctuations are sub-Poissonian since most

states are filled.

5.4.2 Degenerate K, KRb*, and KRb

We proceeded to measure density fluctuations in degenerate gases of K, KRb*, and KRb. In previous experiments on degenerate KRb, typical K conditions were 5×10^5 atoms at $T/T_F = 0.1$ [61]. Such samples are too dense to measure particle number with the accuracy needed for this experiment. Therefore, the K conditions used for the fluctuation measurement are less degenerate than those used to create molecules. To create appropriate samples for the fluctuation measurement, we remove Rb atoms, prepare a spin mixture of K in the $|F, m_F\rangle = |9/2, -9/2\rangle$ and $|9/2, -7/2\rangle$ hyperfine states, and hold the mixture for three seconds to allow thermal equilibration. Varying the optical trap depth and the fraction of K in each spin state allows control over the final atom conditions. Typical K conditions for the measurement on degenerate atoms are 1×10^5 atoms at $T/T_F = 0.2$; for the measurement on non-degenerate atoms, typical conditions are 5×10^4 atoms at $T/T_F > 0.6$. Typical molecule conditions are 6×10^4 of KRb* and KRb at $T/T_F = 0.45$.

Figure 5.7a shows profiles of the mean and variance for each species. The suppression is largest at the center of the gas and is reduced approaching the edges, due to the spatial profile of the trapping potential. We fit the spatial profile of $\overline{N}$ to Eq. 4.3 and of $\sigma_N^2/\overline{N}$ to Eq. 5.4. By these fits we obtain independent measures of T/T_F, which are compared in Fig. 5.7b. Over a factor of two in T/T_F, we find decent agreement. Though fits to $\overline{N}$ on KRb* and KRb produce the same T/T_F, KRb exhibits higher number fluctuations.

5.5 Effects of STIRAP

We attribute the increased fluctuations of ground state KRb to STIRAP. STIRAP is used twice in measurements on KRb, first to associate KRb* into KRb and second to dissociate KRb immdiately prior to imaging. We consider the effects of association and dissociation separately in the following two subsections.

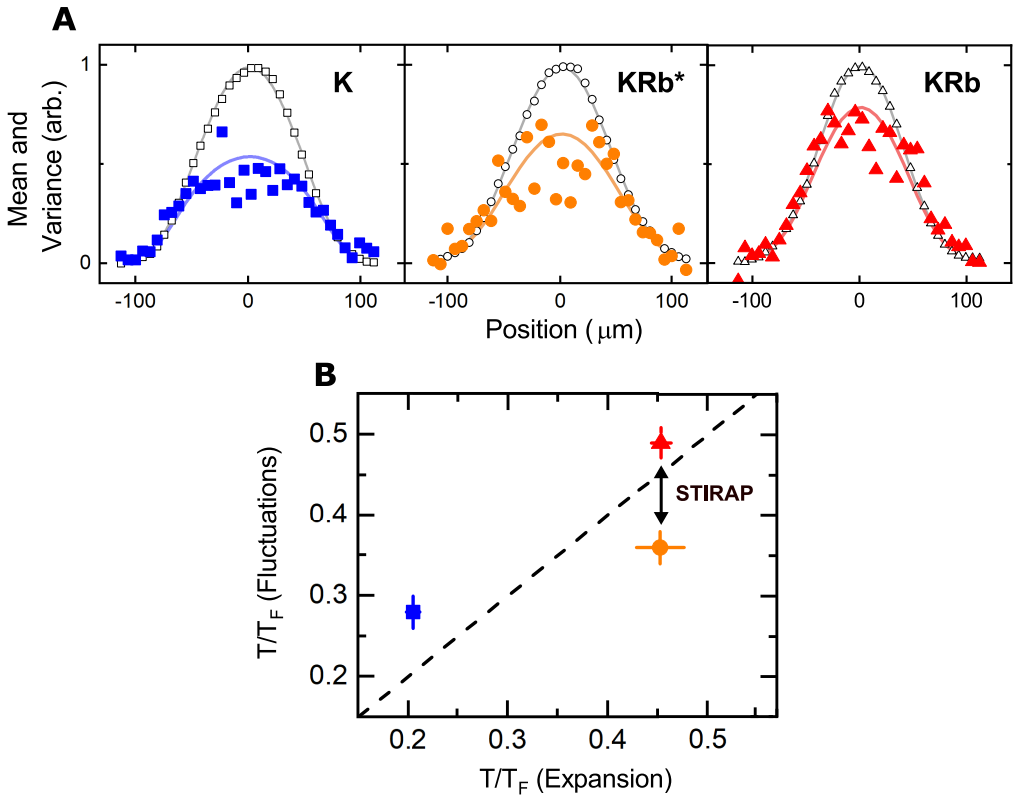

Figure 5.7: Spatial distribution of number fluctuations in degenerate K, KRb*, and KRb. **(a)** Mean (open symbols) and variance (solid symbols) profiles. The number fluctuations relative to the mean number are lowest for low-momentum states at the center of the time-of-flight distributions. Solid lines are fits of the mean and variance to the Fermi-Dirac distribution (Eq. 4.3) and Eq. 5.4, respectively, used to independently determine the T/T_F. **(b)** Comparing the T/T_F extracted by both fitting methods shows reasonable agreement. The fluctuations measured in KRb are increased relative to KRb* due to STIRAP. Adapted from Ref. [62].

5.5.1 Association

The measurement of number fluctuations probes the occupation of states in the Fermi gas. When STIRAP is used to associate KRb* into KRb, if the conversion does not have unit efficiency, additional holes will be introduced into the distribution. The occupancy of the lowest-energy state in a Fermi gas is given by the Fermi-Dirac distribution

$$f(\epsilon = 0) = \frac{1}{e^{-\beta\mu} + 1}, \tag{5.12}$$

where $f(\epsilon)$ is the occupation of states with energy ϵ, $\beta = 1/kT$ and μ is the chemical potential, and the product $\beta\mu$ is the logarithm of the peak fugacity ζ.

In the previous chapter, we measured that KRb* is in thermal equilibrium after Feshbach association. Therefore, it has a peak occupancy determined only by the fugacity: $f(\epsilon = 0, \zeta)$. After STIRAP, with conversion probability p, the peak occupancy is modified to be $pf(0, \zeta)$, assuming no elastic collisions leading to rethermalization in the KRb gas. Even in the absence of thermalization, for high STIRAP efficiency KRb has a distribution near an equilibrium Fermi-Dirac distribution. We can relate the modified peak occupancy to a modified fugacity ζ' by making the equivalence

$$pf(0, \zeta) = f(0, \zeta') \tag{5.13}$$

which we can solve for ζ' to extract an effective T/T_F after STIRAP association.

Figure 5.8 shows the effect on T/T_F of STIRAP with conversion efficiencies between 85% and 100%. For the conditions reported in Ref. [61], $T/T_F = 0.3$ and $p = 0.9$, the peak state occupancy is equivalent to molecules in thermal equilibrium with $T/T_F = 0.37$. The fractional effect of STIRAP on T/T_F is smallest for high initial T/T_F, since the occupancy is already low. For highly degenerate gases, by contrast, the occupancy saturates at the STIRAP efficiency. To prepare a degenerate KRb gas with high peak occupancy, therefore, it is critical to have high STIRAP efficiency or to have thermalization occurring in the gas.

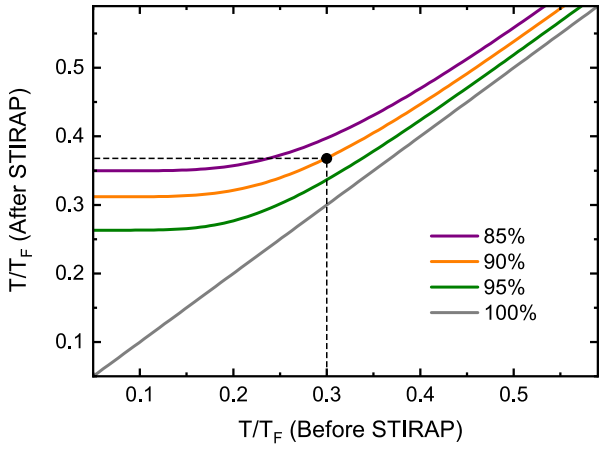

Figure 5.8: Modifying T/T_F to account for STIRAP. Since STIRAP has sub-unity efficiency, it introduces holes in the momentum distribution not captured by fits to the entire distribution. The measured value of $T/T_F = 0.3$ from Ref. [61], given the STIRAP efficiency of 90%, corresponds to the same peak state occupancy of thermalized molecules at $T/T_F = 0.37$. Adapted from Ref. [62].

5.5.2 Dissociation

When the KRb molecules are dissociated, STIRAP introduces random holes in the momentum distribution that increase the variance. Unlike the "real" fluctuations introduced during association, which correspond to reduced state occupancy for measurements on KRb, the dissociation process does not affect the physical KRb distribution and essentially represents an imaging artifact. We quantify and correct for fluctuations added in dissociation using a simple statistical model.

In any given bin for a set of images, the peak variance suppression has the form

$$\frac{\sigma_N^2}{\overline{N}} = \frac{\mathrm{Li}_1(-\zeta)}{\mathrm{Li}_2(-\zeta)} \equiv \eta \tag{5.14}$$

Each bin comprises N_k single-particle states. The probability of occupying each state is given by the Fermi-Dirac occupation number f_k. Since the occupation of each state is independent, the distribution of total particle number in the bin is the sum of independent binomial random variables over all k states contained in the bin:

$$N \sim \sum_k \mathrm{Bin}(1, f_k), \tag{5.15}$$

where $\mathrm{Bin}(m,p)$ is the binomial distribution with m trials, each with p probability of success. Assuming that all of the f_k are equal, which is valid in the limit of small bin size, this simplifies to

$$N \sim \mathrm{Bin}(N_k, f_k) \tag{5.16}$$

In a bin with mean particle number $\overline{N}$ and variance σ_N^2, the values of N_k, f_k can be written in terms of $\overline{N}, \sigma_N^2$ using the mean and variance of the binomial distribution:

$$\begin{aligned} \overline{N} &= N_k f_k \\ \sigma_N^2 &= N_k f_k (1 - f_k) \end{aligned} \tag{5.17}$$

Substituting and simplifying:

$$\begin{aligned} N &\sim \mathrm{Bin}(N_k, f_k) \\ &= \mathrm{Bin}\left(\frac{\overline{N}^2}{\overline{N} - \sigma_N^2}, \frac{\overline{N} - \sigma_N^2}{\overline{N}}\right) \\ &= \mathrm{Bin}\left(\frac{\overline{N}}{1-\eta}, 1 - \eta\right) \end{aligned} \tag{5.18}$$

After applying STIRAP, modeled as a binomial process that reduces the probability of measuring a molecule in each state by the factor p, the modified distribution is

$$N' \sim \mathrm{Bin}\left(\frac{\overline{N}}{1-\eta}, p(1-\eta)\right) \tag{5.19}$$

The modified ratio of mean and variance after STIRAP is therefore

$$\frac{\sigma_{N'}^2}{\overline{N'}} = 1 - p(1-\eta) \tag{5.20}$$

We can check the limiting behaviors: for $p = 1$, corresponding to perfectly efficient STIRAP, $\sigma_{N'}^2/\overline{N'} = \eta$ and the fluctuations are not modified. As $p \to 0$, however, $\sigma_{N'}^2/\overline{N'} \to 1$, which is the expected result for a binomial distribution with small success probability (and which is equal to the same quantity for a Poissonian distribution).

Using Eq. 5.20 in combination with the STIRAP efficiency p, the fluctuations after dissociation ($\sigma_{N'}^2/\overline{N'}$) can be used to calculate η, which can then be used to calculate ζ prior to dissociation by inverting Eq. 5.14. Accounting for the added variance reduces the measured T/T_F for KRb,

shown on Fig. 5.7b, from 0.49(2) to 0.44(2). The arrow drawn between KRb* and KRb indicates the sum of fluctuations added during association and dissociation, neither of which we correct for on the figure.

In this chapter, we have measured sub-Poissonian density fluctuations in degenerate Feshbach and ground-state molecules. Building on the results of the previous chapter, these measurements provide independent thermometry and a consistent picture of Feshbach molecules in thermal equilibrium, with the STIRAP process slightly modifying the equilibrium distribution.

Chapter 6

Direct Evaporation in Two Dimensions

We previously produced degenerate molecules by associating degenerate atomic gases [61]. While the Feshbach molecules reached thermal equilibrium via collisions with background K atoms, lossy collisions prevented the ground state molecules from equilibrating [62]. In this section, I describe how we use confinement in an optical lattice and apply external electric fields to generate conditions where molecules interact primarily through repulsive dipolar collisions, enabling direct evaporation below the Fermi temperature. The following is based on Ref. [63].

6.1 Introduction

Realizing quantum many-body phases with ultracold molecules requires low temperatures, comparable to the interaction strength between molecules. Direct evaporation of atomic gases, where collisions between atoms maintain thermal equilibrium as the trapping potential is reduced, is routinely used to reach quantum degeneracy. On this experiment, for instance, Rb is evaporated in an optical trap and sympathetically cools K in order to produce a degenerate mixture. When ultracold molecules collide at short range, however, their complex internal structure leads to rapid chemical or photoassociative loss and prevents thermalization [21, 46, 47, 31].

In an external electric field, polar molecules develop induced dipole moments which lead to strong long-range interactions. Dipolar interactions are anisotropic, and can be attractive or repulsive depending on the orientation of two colliding dipoles. By confining the molecules to two dimensions (2D) in an optical lattice, we eliminate the attractive region of the potential and

stabilize the molecules against reactive loss. The dipolar cross section permits efficient evaporation, as previously measured in magnetic atoms [44]. Below the Fermi temperature, we observe a non-classical momentum distribution, indicating the molecules are entering the quantum degenerate regime. This work follows several previous theory proposals [144, 145, 146].

6.2 Counting Layers

To prepare molecules in quasi-2D, we load atoms into a lattice from 3D optical traps. This means the particles occupy a distribution of layers, with the particle number on each layer reflecting the distribution in the optical traps. We measure the total molecule number N, which is the sum of the number on each layer:

$$N = \sum_i N_i \tag{6.1}$$

In this chapter, we consider two properties of the molecules: the T/T_F, and the two-body loss rate β. To extract each of these quantities, which depend on the layer populations N_i, we must use a unique approach for interpreting measurements on the total number N.

In 2D, the Fermi temperature T_F on a layer with N_i molecules is

$$T_F^i = \frac{\hbar\bar{\omega}^{1/2}}{k_B}(2N_i)^{1/2} \tag{6.2}$$

where $\bar{\omega} = (\omega_x\omega_z)^{1/2}$ is the harmonic mean of the trap frequencies providing radial confinement. We assume each lattice layer has approximately the same temperature T, since the atoms are initially thermalized prior to molecular association. In terms of N, we denote the average T_F per molecule

$$T_F = \langle T_F^i \rangle = \frac{1}{N}\sum_i N_i T_F^i \equiv \frac{\hbar\bar{\omega}^{1/2}}{k_B}\left(\frac{2N}{\alpha}\right)^{1/2} \tag{6.3}$$

where α is a constant we call the "layer number," which depends on the layer populations. For instance, if the lattice contained exactly three layers of equal population (as in Chapter 8), the number per layer would be $N_i = N/3$ and therefore $\alpha = 3$. From Eq. 6.3, we have

$$\alpha = \frac{N}{\langle\sqrt{N_i}\rangle^2} \tag{6.4}$$

Therefore, if the layer populations relative to the total number are known, the average T/T_F can be extracted from N. Note that the average T/T_F is always larger than the peak T/T_F if the layer populations are not equal. For the remainder of this work, any reference to T/T_F means the average over the measured layer distribution.

For two-body loss, the loss dynamics on each layer are described by the differential equation

$$\frac{dn_i}{dt} = -\beta n_i^2 \tag{6.5}$$

where n_i is the average density on the ith layer, related to N_i by

$$n_i = \frac{N_i}{4\pi\sigma_x\sigma_z} \tag{6.6}$$

where $\sigma_{x,z}$ are the Gaussian cloud widths in the plane of the lattice. Compared to density decay in 3D, where we add an additional term to account for changes in temperature (Eq. 4.13), we do not measure heating or cooling from reactive loss in 2D, as predicted [146]. Assuming the temperature is the same on each layer, β is also layer-independent. Similarly to above, we want to find a layer number τ where, measuring only the dynamics of the total density n

$$\frac{d(n/\tau)}{dt} = -\beta\left(\frac{n}{\tau}\right)^2 \tag{6.7}$$

we can extract the physical β. Given a layer distribution n_i, we simulate the time evolution of the total density n using the solution to Eq. 6.5 and summing over all layers:

$$n(t) = \sum_i \frac{n_i^0}{1 + n_i^0\beta t} \tag{6.8}$$

where n_i^0 is the density of layer i at $t = 0$. We then find τ by using the solution to Eq. 6.7 and making the equivalence

$$n(t) = \sum_i \frac{n_i^0}{1 + n_i^0\beta t} = \frac{n^0}{1 + n^0\beta t/\tau} \tag{6.9}$$

τ is essentially a constant fit parameter that relates β governing the real dynamics (Eq. 6.5) to the dynamics in the case where each layer has equal population (Eq. 6.7). In general, the fit τ depends on the total time over which the dynamics are observed. It also differs from the other quantity parameterizing layer number, α.

6.2.1 Matter Wave Focusing

Both τ and α can be calculated from the layer distribution N_i. However, since the layer separation is 540 nm and our optical resolution is several μm, each layer cannot be imaged individually. In Chapter 8, we use electric field gradients to directly measure N_i; here, prior to our work on stabilizing the phase of the lattice, we used more indirect methods.

One simple way to measure the layer distribution without phase stabilization still involves an electric field gradient. We assume the density distribution of the molecules in the lattice is approximately Gaussian with width σ_y, i.e.

$$N_i \approx \frac{N}{\sqrt{2\pi}\sigma_y} e^{-y_i^2/2\sigma_y} \tag{6.10}$$

In an applied gradient $\partial_y|\mathbf{E}|$, at a field where the frequency sensitivity of a rotational transition is s, the frequency shift of a molecule at position y_i is $\nu_i = y_i\, s\, \partial_y|\mathbf{E}|$. In the limit where the broadening due to the gradient is much larger than the spectral width of the microwave pulse used to probe the transition, the rotational lineshape is simply Gaussian with scaled frequency width $\sigma_\nu = \sigma_y\, s\, \partial_y|\mathbf{E}|$. By measuring σ_ν in a known gradient we can infer σ_y.

We would like to measure N_i on each individual layer without assuming a particular distribution. We use a method called "matter wave focusing," illustrated schematically in Fig. 6.1a [147, 148, 149]. Initially, the particles are confined along y, parallel to gravity, in two traps: the lattice, which has a layer spacing a and a trap frequency ω_L, and the optical dipole trap (ODT), which has a trap frequency ω_y. When the lattice is removed, the particles are accelerated towards the center of the ODT and gain momentum according to their initial displacement. Following an evolution time of one-quarter the trap period, the ODT is removed and the particles expand in time-of-flight, so that the initial position distribution is effectively magnified by the expansion.

In phase space (Fig. 6.1b), two lattice layers are initially separated by a, with the harmonic length inside each layer being

$$\Delta y = \sqrt{\frac{\hbar}{2m\omega_L}} \tag{6.11}$$

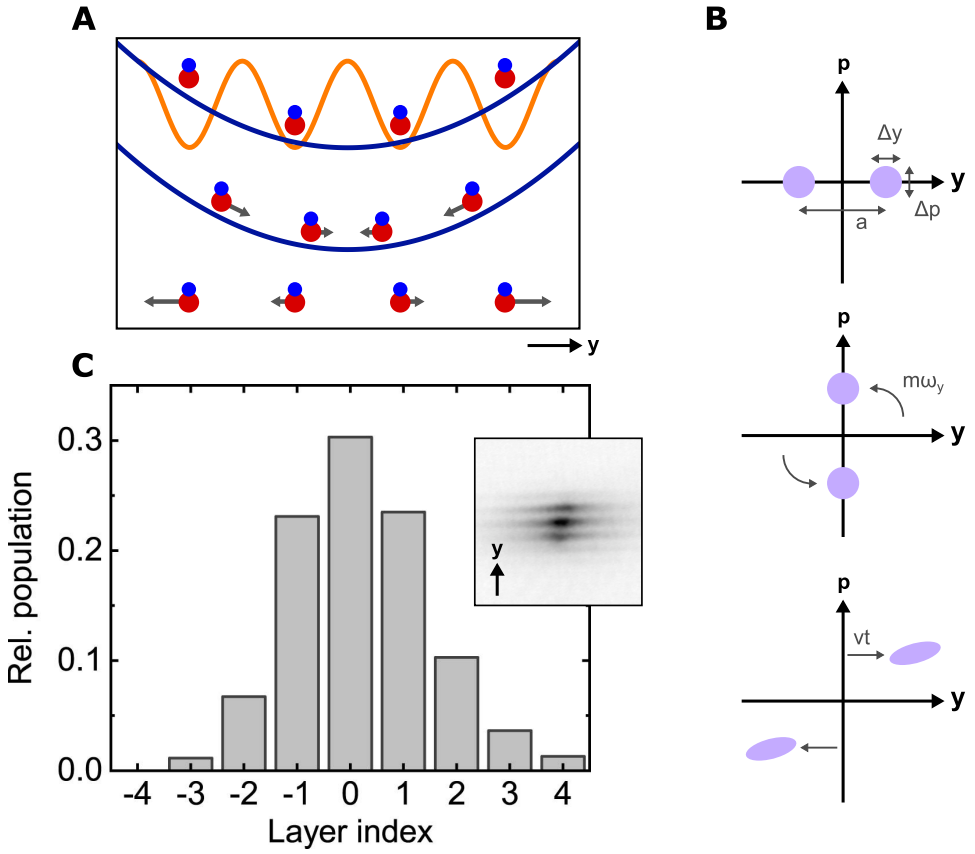

Figure 6.1: Matter wave focusing for layer counting. **(a)** Molecules are initially separated by 540 nm in the combined trap formed by the lattice (orange) and ODT (blue). When the lattice is ramped off, the molecules move towards the center of the ODT and gain momentum corresponding to their initial displacement from the trap center. In time of flight, the initial position distribution is magnified. **(b)** Phase-space picture of the matter wave focusing for two lattice layers. **(c)** Layer occupation measured with matter wave focusing. **Inset:** Averaged Rb distribution corresponding to the experimental conditions. Adapted from Ref. [63].

and the conjugate momentum

$$\Delta p = \sqrt{\frac{\hbar m \omega_L}{2}} \tag{6.12}$$

The time evolution in the ODT is equivalent to a 90° rotation in phase space, corresponding to the transformation $p = m\omega_y y$. A time of flight t makes the transformation $y(t) = y(0) + (p/m)t$. With these relations, we can calculate the visibility $\mathcal{V}$ of the lattice layers, defined as the ratio of the separation of two layers to the width of each layer:

$$\mathcal{V} = \frac{(m\omega_y)\, a\, t}{\sqrt{\frac{\Delta p^2}{(m\omega_y)^2} + (m\omega_y)^2 \Delta y^2 t^2}} \overset{t\to\infty}{=} \frac{a}{\Delta y} \tag{6.13}$$

The first term in the denominator is the initial width after rotation but before expansion, and the second term is the shearing of the distribution due to the momentum width of each layer. $\mathcal{V}$ is limited to the ratio of the layer separation and the harmonic length, and the spacing between layers can be magnified arbitrarily by increasing the time-of-flight. For our parameters, $a/\Delta y \approx 9$, although the contrast we achieve experimentally is still limited by t.

We use matter wave focusing to measure the Rb distribution prior to molecule association. Since Rb is partially condensed and is the minority species, it occupies a smaller spatial extent than K. We therefore assume that the molecule distribution approximately matches the Rb distribution and that the association efficiency is approximately uniform across the Rb cloud. We prepare Rb atoms in the optical lattice with the same number and temperature as for molecule association, and repeat the matter wave focusing technique 33 times. Since the phase of the lattice is not stabilized relative to the optical trap or to the imaging system, we align the fringes visible on each image by hand to produce an average image (inset, Fig. 6.1c). About 30% of the Rb is condensed, which appears as a higher-density region in the center of the cloud. The relative populations on each layer are shown in Fig. 6.1c, peaking at 31% of the total number in the central layer. For this distribution, we calculate layer numbers $\alpha = 5(1)$ for T/T_F and $\tau = 8(1)$ for β, where the uncertainties account for possible non-uniform conversion over the Rb distribution and the fluctuating condensate fraction. The molecules occupy many fewer layers here than in subsequent measurements where the lattice is loaded directly from the optical trap (Fig. 8.4); this is because

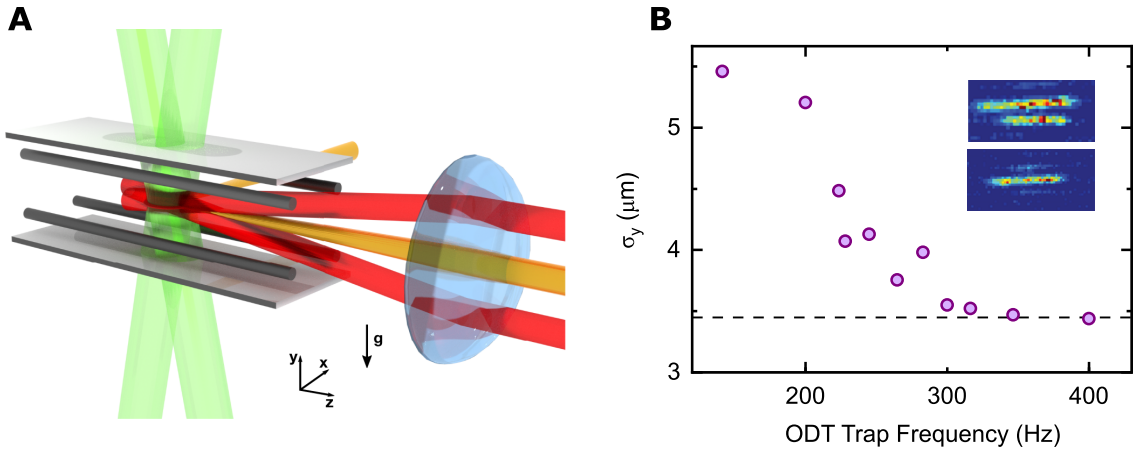

Figure 6.2: Experimental configuration and LSL loading. **(a)** Three optical traps confine the molecules inside the electrode assembly (gray): the vertical lattice (green), with a layer spacing of 540 nm, is loaded from the LSL (red) and the ODT (orange). **(b)** By increasing the ODT frequency in the **y**-axis, a single LSL layer can be loaded, with an imaged width corresponding to the dashed line. **Insets:** Images of atoms loaded into one and two LSL layers. Adapted from Ref. [63].

we tightly confine the atoms in an intermediate optical trap, the "large-spacing lattice," described in the next section.

6.3 Sample Preparation

We create 2D samples of molecules using a series of optical traps, shown in Fig 6.2a. The K and Rb atoms are initially loaded into the ODT, with trap frequencies $(\omega_x, \omega_y, \omega_z) = 2\pi \times (40, 180, 40)$ Hz for Rb. The direction of tight confinement, **y**, is oriented parallel to gravity. We then transfer the atoms to a single layer of the large-spacing lattice (LSL), which has a layer spacing of 8 μm. Following transfer, we reduce the ODT power, forming a combined trap with frequencies $(\omega_x, \omega_y, \omega_z) = 2\pi \times (25, 600, 25)$ Hz. The typical atomic conditions are 4.1×10^5 K and 7.0×10^4 Rb at a temperature of $T = 115(10)$ nK. We load the atoms into the vertical lattice, which has a layer spacing of 540 nm, populating between 5 and 15 layers depending on the confinement strength in the LSL. By varying the lattice power we set $\omega_y/2\pi = 2 - 17$ kHz, and adjust the ODT power to maintain radial trap frequencies of 40 Hz at all ω_y. The atoms are then associated into molecules, with a conversion efficiency of about 30% of Rb, resulting in 20,000 molecules at $T = 250$ nK and

$T/T_F = 1.5 - 3$ depending on the layer populations. Using the techniques described in Chapter 3, we associate molecules at either $|\mathbf{E}| = 0$ or 4.5 kV/cm with similar efficiency.

6.3.1 Large-Spacing Lattice

The LSL is generated by two parallel beams that are focused onto the position of the atoms (Fig. 6.2a). The focusing lens doubles as the collection lens for imaging. For a focal distance of d (15 cm, in our experiment), and parallel beams spaced by s (about 2 cm), the layer spacing is

$$a_{\mathrm{LSL}} = \frac{\lambda}{2\sin\theta} \tag{6.14}$$

where $\theta = \tan^{-1}(s/2d)$ is the half-angle between the beams after the lens. By varying s, we can adjust a_{LSL} from $5 - 16$ μm. Figure 6.2b describes the loading from the ODT into the LSL. As the ODT power is increased, the measured width along $\mathbf{y}$ decreases, until it saturates and a single LSL layer is loaded. Because the LSL spacing is relatively large compared to the imaging resolution, the population of molecules or atoms in each layer can be directly imaged, as shown in the inset.

6.4 Dipolar Suppression of Two-Body Loss

The density of the molecules evolves according to a two-body loss rate equation, with rate coefficient β (Eq. 6.7). The interaction Hamiltonian for molecules separated by distance r is

$$\hat{H}(r) = \frac{\hbar^2 L(L+1)}{2\mu r^2} - \frac{C_6}{r^6} + \frac{d^2(1 - 3\cos^2\theta)}{r^3} \tag{6.15}$$

where L is the partial wave of the collision channel, μ is the reduced mass, $C_6 \approx 16\,100$ a.u. [150], d is the magnitude of the dipole moment, and θ is the angle between the intermolecular axis and the dipole moment. The first term is the centrifugal barrier; for identical fermions such as KRb, collisions occur only in channels with odd L. At ultracold temperatures, collisions predominantly occur in the p-wave channel ($L = 1$). The second term is the isotropic van der Waals potential, arising due to dipolar couplings to excited electronic states. The third term is the dipole-dipole interaction between molecules with induced dipole moments oriented by an external electric field,

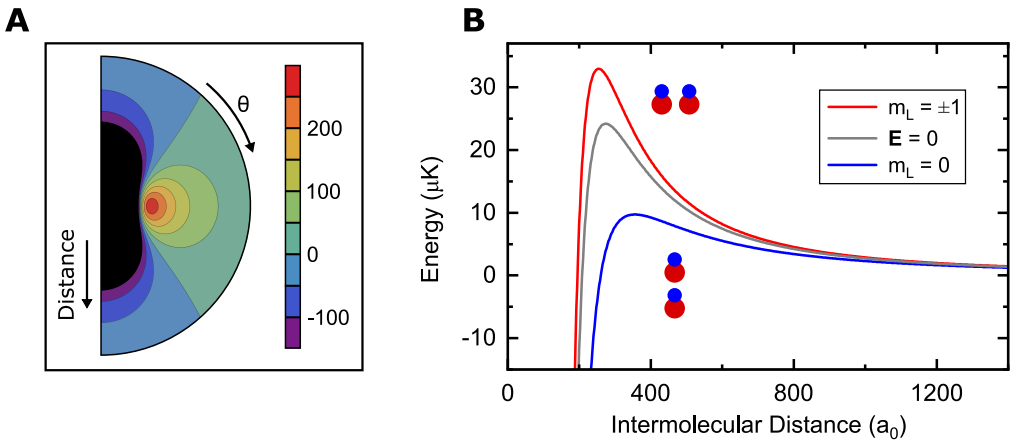

Figure 6.3: Dipole-dipole interaction energies for colliding molecules. **(a)** Total energy at $d = 0.2$ D and $L = 1$ as a function of molecule separation and θ, in units of μK. The radius of the plot corresponds to a separation of 500 a_0. **(b)** Intermolecular potentials for $m_L = 0$ (blue) and $m_L = \pm 1$ (red) collisions, which are attractive and repulsive, respectively, at $d = 0.1$ D. The bare p-wave barrier, in the absence of dipolar interactions, is shown in gray.

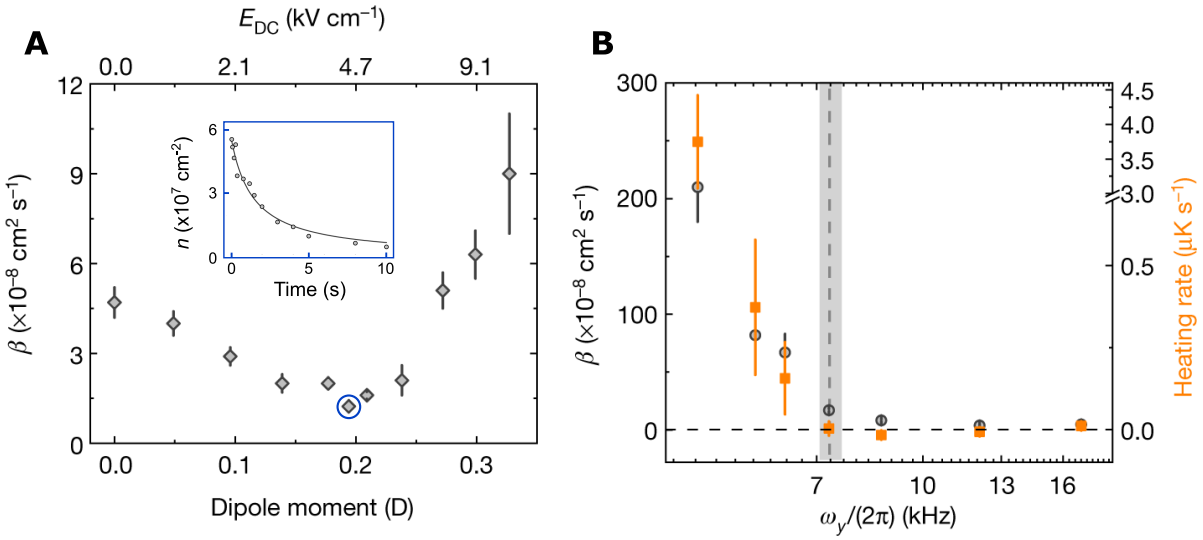

Figure 6.4: Two-body loss suppression and 2D/3D crossover. **(a)** The two-body loss rate β is minimized at 0.2 D, or 4.5 kV/cm. **Inset:** Density loss at 0.2 D, corresponding to the circled point. **(b)** Crossover of β and heating rate vs. lattice frequency, at $|\mathbf{E}| = 5$ kV/cm. The vertical line indicates the transition from 3D to quasi-2D, at $\hbar\omega_y \approx k_B T$. Adapted from Ref. [63].

as discussed in Chapter 3. Figure 6.3a shows the total interaction energy as a function of separation and angle.

With $|\mathbf{E}| = 0$, the loss rate coefficient β at fixed temperature is determined by the tunneling rate through the p-wave centrifugal barrier [21, 23]. At non-zero $|\mathbf{E}|$, however, dipolar interactions modify the intermolecular barrier and change β (Fig. 6.3b). For $L = 1$, collisions can occur with $m_L = 0$, corresponding to attractive head-to-tail collisions, or $m_L = \pm 1$, corresponding to repulsive side-by-side collisions. While m_L is conserved during collisions, the dipolar interactions mix higher partial waves L, which modifies the intermolecular potential. The potential energy curves for $m_L = 0, \pm 1$, along with the bare p-wave barrier, are shown in Fig. 6.3b. In 3D, where molecules may approach with any orientation, the loss rate increases as d^6 for $d > 0.1$ D [46, 151]. If instead the molecules are confined to approach perpendicularly relative to the dipole moment ($m_L = \pm 1$), the dipolar repulsion can suppress the reaction rate.

We orient the electric field along $\mathbf{y}$, perpendicular to the lattice layers, and measure β as a function of d (Fig. 6.4a). For $d < 0.2$, the dipolar interactions decrease β, which is reduced by a

factor of five relative to $d = 0$ at $d = 0.2$ D ($|\mathbf{E}| = 4.7$ kV/cm). At large dipole moments, the properties depend on the confinement frequency. The two relevant length scales are the dipolar length

$$a_{\mathrm{dd}} = \frac{\mu d^2}{\hbar^2} = 38 \text{ nm} \tag{6.16}$$

and the harmonic length

$$a_{\mathrm{ho}} = \sqrt{\frac{\hbar}{2m\omega_y}} = 50 \text{ nm} \tag{6.17}$$

at $d = 0.2$ D and $\omega_y = 17$ kHz. For $a_{\mathrm{dd}} \gg a_{\mathrm{ho}}$, the system is fully 2D and β monotonically decreases with increasing d [88, 144, 106]. For $a_{\mathrm{dd}} \lesssim a_{\mathrm{ho}}$, however, the system is in the quasi-2D regime, meaning interactions mix partial waves L during collisions. For $m_L = \pm 1$, the averaged dipolar interaction for collisions with $L = 1$ is repulsive but becomes attractive for higher L [46]. This effect leads to an increase in β for $d > 0.2$ D (Fig. 6.4a).

At higher temperatures, where $k_B T > \hbar\omega_y$, molecules occupy excited lattice bands and can collide in the $m_L = 0$ channel. Increasing the temperature or decreasing the lattice trap frequency modifies the band populations and effectively transitions the system from 2D to 3D. With the temperature fixed at $k_B T/\hbar \approx 7$ kHz (indicated by a gray line on Fig. 6.4b), we measure β and the molecule heating rate at $\omega_y = 2$-17 kHz. Both quantities saturate above 7 kHz but rise sharply at small ω_y, indicating the 2D-3D crossover. The β increase from excited band populations was previously measured in KRb in Ref. [48]. The heating is due to anti-evaporation: in 3D, molecules are predominantly lost from the highest-density region of the trap, causing an increase in the average energy per particle and apparent heating [46]. In 2D, by contrast, loss does not change the average energy [146], and no heating is observed.

6.5 Cross-Dimensional Thermalization

Repulsive dipolar interactions not only suppress inelastic collisions but also enhance elastic collisions. We use cross-dimensional thermalization to measure the elastic collision rate as a function of dipole moment. The molecules are initially in thermal equilibrium. We diabatically increase ω_z

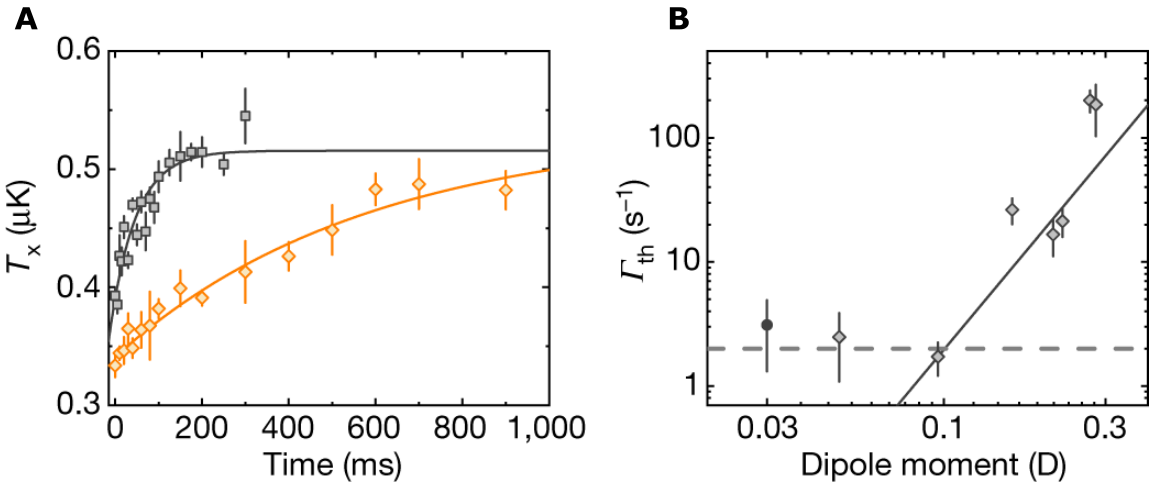

Figure 6.5: Cross-dimensional thermalization in quasi-2D. **(a)** Thermalization dynamics at 0.1 D (orange) and 0.21 D (black). **(b)** Thermalization rate vs. dipole moment, with a power-law fit (solid line). The solid point represents 0 D, displayed at non-zero dipole moment for clarity. The dashed line represents the apparent thermalization rate due to trap anharmonicity, and the solid line is proportional to $d^{3.3}$, the measured scaling with dipole moment. Figure from Ref. [63].

to increase the energy along the **z** axis, and monitor the temperature evolution along **x**. As the molecules collide, energy is redistributed between **z** and **x**. At dipole moments of $d = 0.1$ and $d = 0.21$ D, the thermalization timescales differ by a factor of ten (Fig. 6.5a).

We extract the thermalization rate Γ_{th} by fitting the temperature increase along **x** to an exponential curve. Figure 6.5b shows Γ_{th} as a function of dipole moment. Above $d = 0.1$ D, the rate increases as $d^{3.3(1.0)}$, consistent with theoretical predictions of d^4 scaling [151]. Below $d = 0.1$ D, we measure apparent thermalization due to trap anharmonicity, which limits the minimum measurable Γ_{th}. The maximum Γ_{th} we observe exceed the radial trapping frequency of 40 Hz, a regime where hydrodynamic effects could be observed in future experiments [152].

Theoretical models predict $\gamma = 8$ collisions are necessary for thermalization in 2D, considering the differential cross section of fermionic polar molecules [146]. At $d = 0.2$ D, where the loss rate is minimized, we extract the elastic collision rate from the relation $\Gamma_{\text{el}} = \gamma\Gamma_{\text{th}} = 168(48)\ \text{s}^{-1}$. The maximum inelastic collision rate is $\Gamma_{\text{in}} = \beta n_0$, where n_0 is the initial density. Putting these together, we find an elastic-to-inelastic collision ratio of $\Gamma_{\text{el}}/\Gamma_{\text{in}} = 200(60)$, showing that elastic

collisions dominate.

6.6 Direct Evaporation to Degeneracy

A high ratio between elastic and inelastic collisions enables direct evaporation using dipolar interactions. We quantify the efficiency of evaporation using the molecule number N and temperature T. From Eq. 6.3, $T_F \propto N^{1/2}$. Therefore, to increase phase-space density and decrease T/T_F, an evaporation trajectory must satisfy

$$S_{\text{evap}} = \frac{\Delta \log N}{\Delta \log T} < 2 \tag{6.18}$$

where S is the slope of the change in N and T, on logarithmic scales. A trajectory with $S = 2$ has constant T/T_F.

6.6.1 Combined Electro-Optical Trap Potential

To evaporate the molecules, we lower the trap depth to remove the hottest particles, and the remaining particles rethermalize via dipolar interactions to a lower temperature. To modify the trap depth, we add electric field curvature using the electrodes. The electric field distribution depends sensitively on the ratio of voltages on the rod and plate electrodes. If these voltages are in the ratio of approximately 0.4225, the electric field distribution is maximally homogeneous and the trapping potential derives solely from the optical trap (Fig. 6.6a, left). However, if the rod/plate ratio is increased, the electrodes add an anti-trapping curvature and the total trap depth is lowered (Fig 6.6a, right).

We quantify the electric field curvature by measuring the trap frequency ω_x as a function of rod/plate ratio at $|\mathbf{E}| = 5$ kV/cm (Fig. 6.6b). By controlling the voltage ratio, we vary $\omega_x/2\pi$ from 30-47 Hz and change the trap depth by more than an order of magnitude. The measurements agree well with the results of finite element simulation of the electric field curvature (Fig. 6.6b, dashed line). We explored evaporation using an electric field gradient, instead of a curvature, but we never achieved efficient evaporation with this method for unknown reasons.

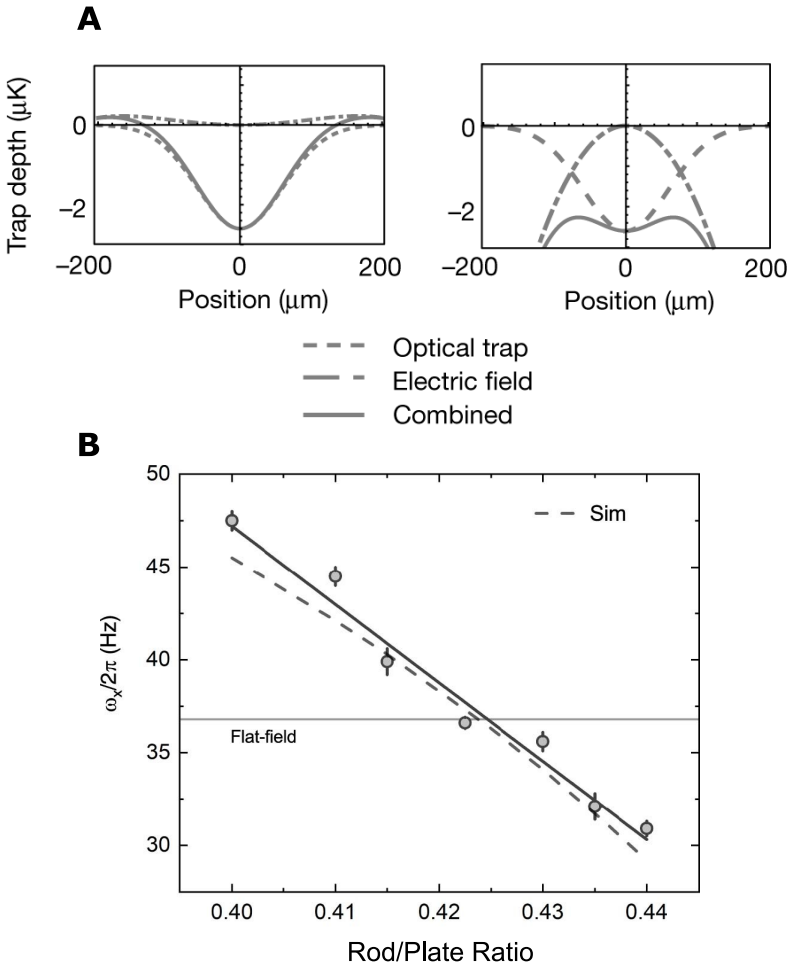

Figure 6.6: Lowering the trap potential using electric field curvature. **(a)** Combined electro-optical trap potential at the beginning (left) and end (right) of evaporation. The trap depth is lowered by a factor of ten using electric field anti-curvature. **(b)** Measured radial trap frequency as a function of rod/plate voltage ratio. The solid line is a linear fit and the dashed line is the simulated trend in trap frequency. The solid line, marked "flat field," corresponds to the left panel in (a). Adapted from Ref. [63].

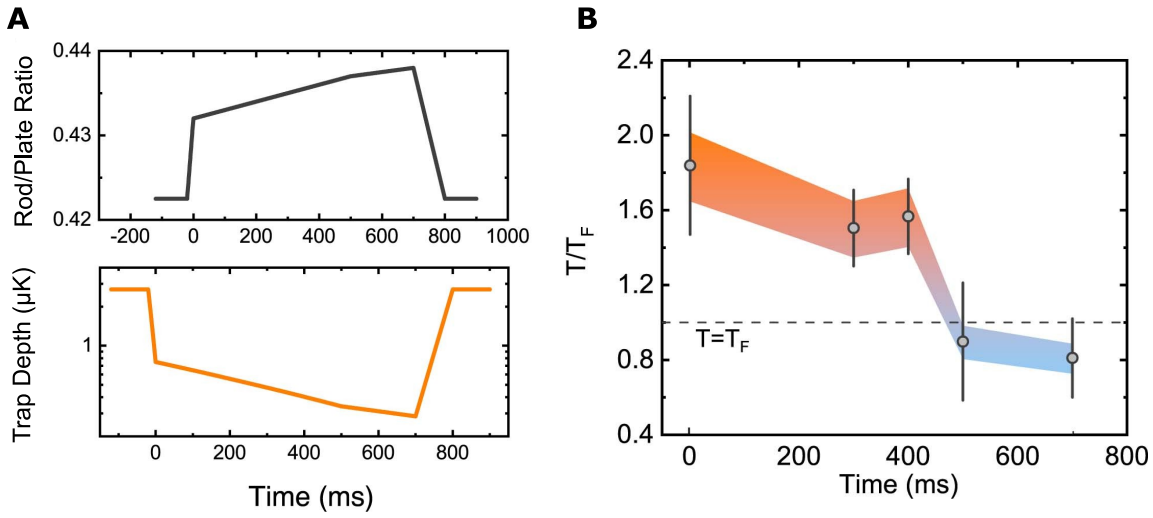

Figure 6.7: Evaporation trajectory. **(a)** Rod/plate voltage ratio and corresponding trap depth during evaporation. The trap is always recompressed to the original depth prior to measuring the molecule temperature. **(b)** Evolution of T/T_F during evaporation. Adapted from Ref. [63].

6.6.2 Results

We evaporate molecules starting from initial conditions of 7000 molecules in $\alpha = 5(1)$ layers, at a temperature of 170 nK and $T/T_F = 1.5(1)$. We associate the molecules at either $|\mathbf{E}| = 0$ or 4.5 kV/cm, and ramp the field to a target electric field for evaporation. To measure an evaporation trajectory, we lower the trap depth over hundreds of ms using the electric field curvature. Figure 6.7a shows the rod/plate voltage ratio and corresponding trap depth for an evaporation trajectory at $|\mathbf{E}| = 6.5$ kV/cm. After a variable evaporation time, we measure the molecule number and temperature by raising the trap depth to the original value and dissociating the molecules at the initial electric field. Recompressing the trap removes systematic effects from adiabatic decompression, where the molecule temperature changes adiabatically as the trap frequency is lowered without any molecule loss; unlike evaporation, this mechanism does not increase phase-space density because T_F decreases along with the trap frequencies. We extract the temperature by releasing the molecules from the optical trap and fitting the radial profile in time of flight. The time evolution of T/T_F for the trajectories shown (Fig. 6.7b) indicates that direct evaporation achieves $T/T_F < 1$.

The efficiency of evaporation depends on the elastic and inelastic collision rates and consequently on the dipole moment. We measure S_{evap} at six different electric fields, optimizing the evaporation trajectory at each field by scanning the evolution in time of the trap depth (Fig. 6.8). The most efficient evaporation is achieved at $d = 0.25$ D, where $S_{\mathrm{evap}} = 1.06(15)$ (Fig. 6.8a). Above $d = 0.15$ D, we find evaporation trajectories that increase phase-space density, while evaporation is inefficient at smaller dipole moments. (Fig. 6.8b). The best evaporation results we achieved were $N = 1.7(1) \times 10^3$ at $T/T_F = 0.6(2)$.

The onset of quantum degeneracy is observed in the momentum distribution of the molecules. We average 20 images before and after evaporation to compare each condition, with $T/T_F = 2.0(1)$ and 0.81(15), respectively (Fig. 6.8c). At low temperatures, the occupation of low-momentum states in a Fermi gas is smaller than that of a classical or Bose gas, since Pauli exclusion dictates that each state can be occupied by a maximum of one molecule. When the molecules expand in time of flight, the momentum distribution is mapped onto position. For a degenerate Fermi gas, we therefore expect to measure lower molecule density near the center of the cloud relative to a classical (Gaussian) distribution.

Figure 6.8d shows the integrated momentum profiles for the images in Fig. 6.8c, before and after evaporation. We fit each profile by two methods: first, with the Fermi-Dirac distribution to the entire profile, and second, with a Gaussian to the outer (high-momentum) wings of the profile. The Fermi-Dirac and Gaussian distributions correspond for high-momentum states since the average occupancy is low. Before evaporation, when the temperature is well above T_F, the molecule profile is fit well by both distributions. After evaporation, however, the Gaussian distribution overestimates the density at low momentum while the Fermi-Dirac distribution produces an accurate fit. The deviation from classical thermodynamics indicates the onset of degeneracy.

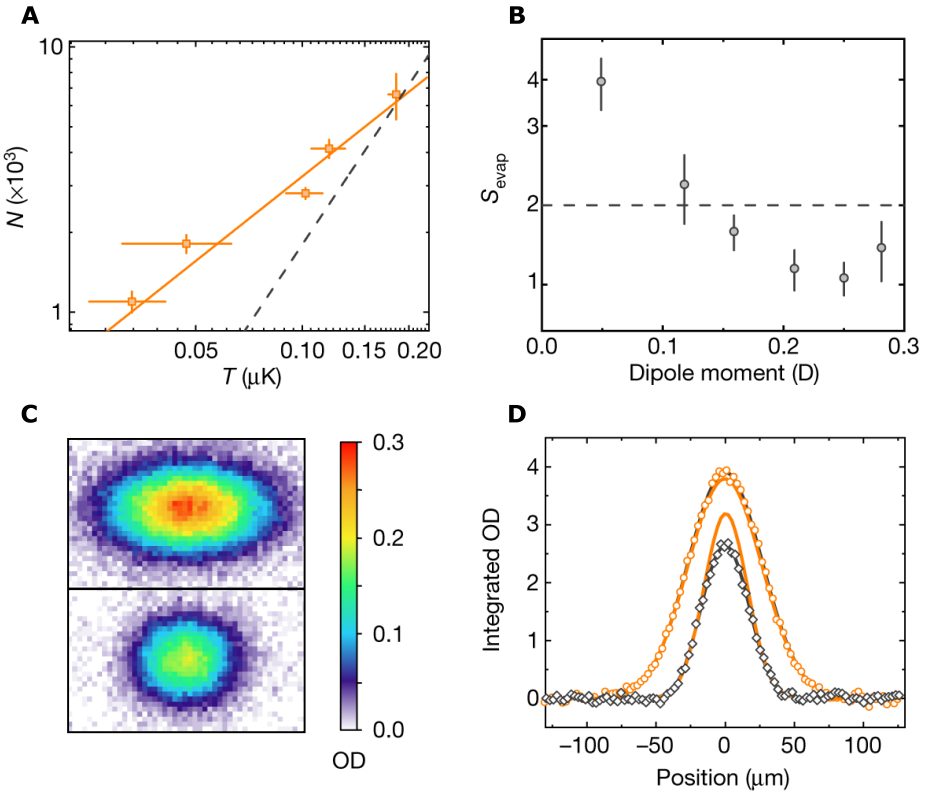

Figure 6.8: Evaporation results. **(a)** Number and temperature evolution during evaporation. We measure $S_{\text{evap}} = 1.06(15)$, corresponding to decreasing T/T_F. The dashed line represents a trajectory with constant T/T_F ($S_{\text{evap}} = 2$). **(b)** Evaporation slopes vs. dipole moment. Optimal evaporation is achieved between 0.2-0.25 D. **(c)** OD images of molecules before (top) and after (bottom) evaporation. **(d)** Integrated optical density profiles at $T/T_F = 2.0(1)$ (orange points) and $T/T_F = 0.81(15)$ (gray points). The solid lines are Gaussian fits to the wings of the clouds, which overestimate the density at low momentum for the low-temperature gas due to the Fermi-Dirac momentum distribution. Adapted from Ref. [63].

Chapter 7

Resonant Shielding of Collisions

In the previous chapter, we induced repulsive dipolar interactions between KRb molecules using an applied electric field and two-dimensional (2D) confinement. At particular electric fields, it was predicted that resonant dipolar coupling between degenerate pairs of rotational states would strongly modify the intermolecular potentials in 3D as well [153, 154]. In this section, I describe this "resonant shielding" effect, which can be used to suppress two-body loss and enhance the ratio of elastic to inelastic collisions.

Our research on this topic proceeded in two stages, described in the following sections. First [64], with the molecules confined in 2D, we measured the spatial anisotropy of resonant shielding and confirmed that reactive loss was suppressed for all orientations of colliding dipoles. It followed that the shielding should remain effective in 3D, which we confirmed in Ref. [65]. We also explored the elastic collisions between molecules, which displayed anisotropy characteristic of dipole-dipole interactions, and used elastic collisions to directly evaporate the molecules.

7.1 Introduction

For molecules trapped in 3D, dipolar interactions are predicted to generate effects including Fermi surface deformation [104], collisional hydrodynamics [155], ordered phases [156], and superfluidity [105]. Two related problems present a barrier to observing these effects: high thermal energies, relative to the interaction energy scales, and rapid loss. In contrast to dipolar atoms, both reactive and nominally non-reactive molecules undergo two-body loss on timescales of seconds. The

small ratio of elastic to inelastic collisions prevents the use of evaporation to lower the temperature. Inducing a dipole moment of magnitude d using external electric fields typically exacerbates this problem, since the inelastic cross section scales as d^6 compared to d^4 for the elastic cross section [46, 151]. While we have created degenerate KRb molecules in 3D at zero field (with the as-yet-unexplained side effect of reduced loss rates at degeneracy) [61], and demonstrated the suppression of loss in a restricted geometry [63], a stable 3D molecular gas with dipolar interactions was still lacking.

Here we explore resonant shielding of lossy collisions using large DC electric fields in 3D, and create a system of collisionally stable, interacting molecules. We also demonstrate direct evaporation near resonance, providing a promising path towards degeneracy. A similar shielding mechanism uses microwave fields to couple rotational states [157, 158]; in NaK molecules, a recent experiment demonstrated direct evaporation to quantum degeneracy using this method [133].

7.2 Shielding Resonance

Shielding resonances occur between pairs of molecules, which we label by combined rotational state: for example, $|N, m_N\rangle\,|N', m'_N\rangle$ represents the combined state of two molecules in the indicated rotational states, separated in space. The energy of these combined states varies with electric field, as shown in Fig. 7.1a. $|1,0\rangle\,|1,0\rangle$ is degenerate with two other pairs of states at experimentally-accessible electric fields: $|0,0\rangle\,|2,\pm1\rangle$ at $|\mathbf{E}| = 11.7$ kV/cm, and $|0,0\rangle\,|2,0\rangle$ at $|\mathbf{E}| = 12.51$ kV/cm, denoted $|\mathbf{E}_s|$. Many other crossings occur at higher fields.

Near $|\mathbf{E}_s|$, resonant couplings between combined states modify the intermolecular potential [153, 154, 159, 160]. This effect can be visualized as a simple avoided crossing, depending on the electric field and the strength of the coupling between input and output rotational states (Fig. 7.1b). When the molecules are separated by a large distance, such that the dipolar interaction energy is small compared to the bare rotational energy, the energies of the combined states cross. As the molecules approach, however, the dipolar coupling opens an avoided crossing. For the initial state $|1,0\rangle\,|1,0\rangle$ at a field slightly above $|\mathbf{E}_s|$, as shown in Fig. 7.1b, the energy increases for smaller

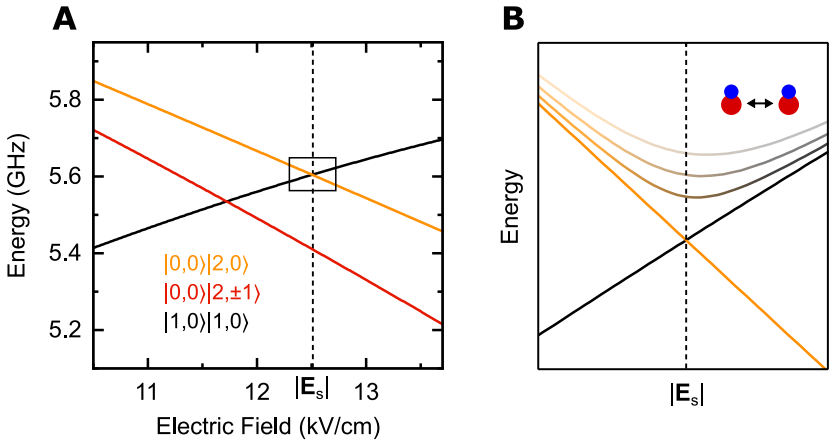

Figure 7.1: Resonant shielding in KRb. **(a)** The energy of rotational state pairs $|1,0\rangle\,|1,0\rangle$ and $|0,0\rangle\,|2,0\rangle$ cross at $|\mathbf{E}_s| = 12.51$ kV/cm, experiencing a strong coupling due to dipolar interactions. **(b)** Around $|\mathbf{E}_s|$, interactions between pairs of molecules open an avoided crossing between the degenerate states. Above $|\mathbf{E}_s|$ the energy of state $|1,0\rangle\,|1,0\rangle$ (solid black line) is raised as the two molecules approach each other (ascending lines). This creates an repulsive potential barrier. Below $|\mathbf{E}_s|$, the energy is lowered as the molecules approach, forming an attractive potential. Inspired by a similar figure in Ref. [64].

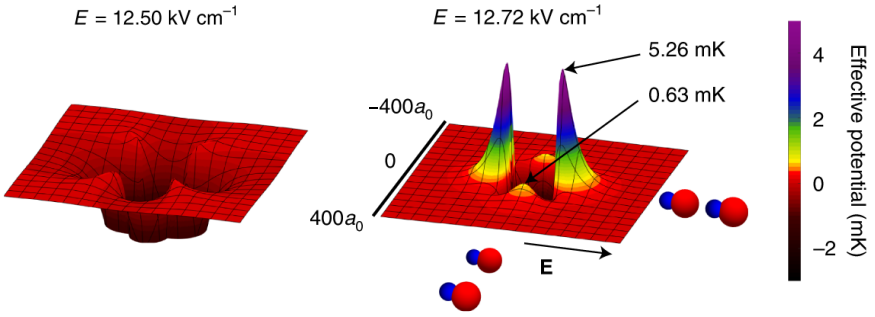

Figure 7.2: Calculated adiabatic potential energies for two molecules in $|1,0\rangle|1,0\rangle$ approaching with different relative orientations. Above the resonance (right panel), large potential barriers are created for both head-to-tail and side-by-side collisions, in contrast to off-resonant interactions between induced dipoles (Fig. 6.3). Below the resonance (left panel), resonant interactions create attractive potentials. Figure from from Ref. [65].

intermolecular separations and therefore creates an effective potential barrier.

Unlike the situation away from resonance, where the potential can be either attractive or repulsive depending on the relative angle of colliding dipoles (Fig. 6.3), the energy gap near resonance scales only with the magnitude of the dipolar coupling. In Ref. [64] we explored the dipolar anisotropy in both the resonant and off-resonant cases by confining the molecules in 2D. Figure 7.2 shows the adiabatic intermolecular potentials as a function of orientation and distance, calculated by our colleagues in the Quéméner group using the methods of Ref. [154]. For both head-to-tail and side-by-side orientations above the resonance (right panel), a repulsive barrier as large as 5 mK is present. Below the resonance, the avoided crossing lowers the energy of $|1,0\rangle|1,0\rangle$, creating an attractive potential (left panel).

When molecules collide near resonance, three outcomes can occur. First, the molecules may scatter elastically off of the potential barrier, remaining in their original rotational states. Second, the molecules may tunnel through the barrier to short range and undergo a chemical reaction. Third, the molecules may resonantly exchange rotational states, for example colliding in state $|1,0\rangle|1,0\rangle$ and exiting in state $|0,0\rangle|2,0\rangle$. This process, which is similar to two-particle coherent exchange occurring at Feshbach and Forster resonances [161, 162], only occurs in a very narrow range of electric fields around resonance. In Chapter 8, we measure exchange between states

$|0,0\rangle\,|1,0\rangle$ and $|1,0\rangle\,|0,0\rangle$, which unlike this process is resonant at constant electric fields of any magnitude. Collisions resulting in reactions and exchange, called "quenching" and "inelastic" in Ref. [154], both manifest as loss in our experiment because molecules in minority spin states are rapidly lost to s-wave collisions [21]; we therefore refer to all collisions causing loss as "inelastic." We measure the properties of both the elastic and inelastic collisions in the following.

7.2.1 Simple Model for Resonant Shielding

The shielding mechanism can be described using a simple model, explained in much more detail in the Supplementary Information to Ref. [65]. We consider two-particle states of the form

$$|\psi\rangle = |L, m_L\rangle\,|N, m_N\rangle\,|N', m'_N\rangle \tag{7.1}$$

where the first ket is the partial wave of the collision. In general, dipolar interactions mix higher L partial waves at small intermolecular separations, but ultracold fermions primarily collide with $L = 1$ at large distances. The notation for the pair of rotational states should be understood to mean the symmetric combination of $|N, m_N\rangle\,, |N', m'_N\rangle$, in order to establish overall antisymmetry. For two states $|\psi_1\rangle$ and $|\psi_2\rangle$, the diagonal elements of the interaction matrix are $E_i(r) = \langle\psi_i|\hat{H}(r,\theta)|\psi_i\rangle$, where r is the intermolecular separation and

$$\hat{H}(r,\theta) = \hat{H}_0 + \hat{H}_I(r) + \hat{V}(r,\theta) \tag{7.2}$$

$\hat{H}_0$ represents the energy of the single-particle states in the absence of interactions, $\hat{H}_I(r)$ represents the isotropic interactions, and $\hat{V}(r,\theta)$ represents the dipole-dipole interactions, which have angular dependence

$$\begin{aligned} \hat{H}_0 &= \hat{H}_R + \hat{H}_D + \hat{H}'_R + \hat{H}'_D \\ \hat{H}_I(r) &= \frac{C_2}{r^2} - \frac{C_6}{r^6} \\ \hat{V}(r,\theta) &= \hat{d}\hat{d}'\,\frac{1 - 3\cos^2\theta}{r^3} \end{aligned} \tag{7.3}$$

$\hat{H}_R, \hat{H}'_R$ and $\hat{H}_D, \hat{H}'_D$ are the rotational and dipole-electric field Hamiltonians acting on each of the two molecules represented by $|\psi_i\rangle$, defined in Eq. 3.6. $\hat{d}$ and $\hat{d}'$ are the dipole operators, and C_2 and

C_6 are the isotropic centrifugal and van der Waals coefficients, respectively, which depend in general on L and N, m_N. Since the rotational state wavefunctions are orthogonal, the off-diagonal elements only have contributions from the dipole-dipole interaction: $\Omega(r) = \langle\psi_i|\hat{V}(r,\theta)|\psi_j\rangle$. Combining all of this, the shielding potentials for a single partial wave can be obtained by diagonalizing:

$$\hat{H}(r) = \begin{pmatrix} E_1(r) & \Omega(r) \\ \Omega(r) & E_2(r) \end{pmatrix} \tag{7.4}$$

When $E_1 = E_2$, as at the shielding resonance, the avoided crossing opens an energy gap of 2Ω, which scales as $\Omega \sim r^{-3}$. See Ref. [65] for a full derivation of this simplified model and plots of the potential energy curves.

7.3 Two-Body Loss

We probe the shielding potentials by measuring two-body loss rates at different electric fields near the resonance. We associate molecules in rotational state $|0,0\rangle$ at $|\mathbf{E}| = 4.5$ kV/cm and transfer the molecules to $|1,0\rangle$. We then ramp the electric field to the target electric field for the loss measurement in 60 ms, hold for a variable time, ramp back to 4.5 kV/cm, and dissociate the molecules to measure the density and temperature. The trap frequencies for $|1,0\rangle$ in the optical dipole trap (ODT) are $(\omega_x, \omega_y, \omega_z) = 2\pi \times (45, 250, 40)$ Hz. Prior to the hold time at the target field, the inital conditions are $N = 1.5 \times 10^4$ and $T = 330$ nK, which correspond to a density of $n = 2.5 \times 10^{11}$ cm^{-3}. Since the thermal energy is much larger than the trap frequencies, the molecules are in a 3D geometry.

In 3D, the density loss takes the form:

$$\frac{dn}{dt} = -\beta n^2 - \frac{3}{2}\frac{n}{T}\frac{dT}{dt} \tag{7.5}$$

The first term, with loss rate coefficient β, represents lossy two-body collisions. The second term represents changes in n due to heating [46], which may occur due to single-particle effects like off-resonant heating in the trap or two-particle effects such as anti-evaporation (see Chapter 4).

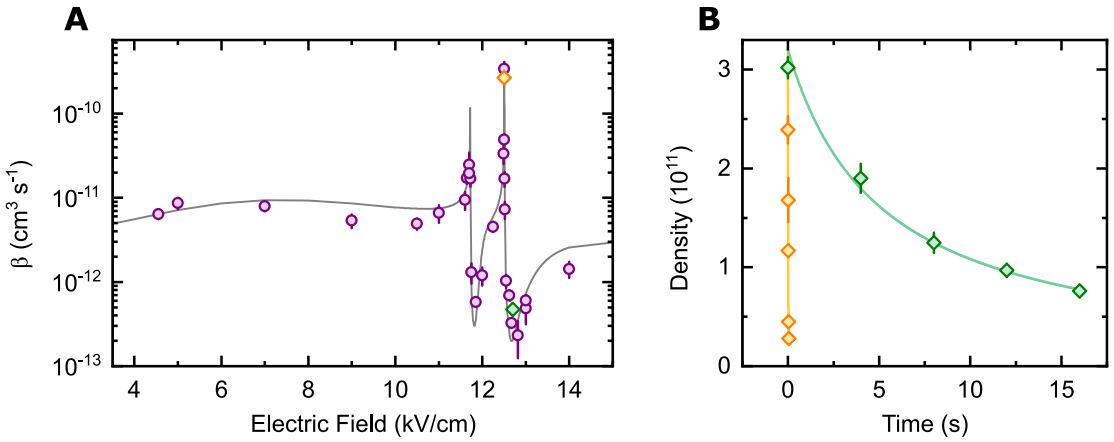

Figure 7.3: Electric field dependence of two-body loss in 3D. **(a)** Measured β for $|1,0\rangle$ molecules. Two resonances are observed, corresponding to different pairs of degenerate rotational states. Far below the resonances, β increases as the dipole moment increases. The solid line is a theoretical prediction with no free parameters. **(b)** Two-body loss dynamics at $|\mathbf{E}| = 12.50$ and 12.52 kV/cm, just above and below $|\mathbf{E}_s|$. We observe a strong enhancement and suppression of loss, respectively. Below the resonance (orange curve) the molecule density essentially vanishes after 50 ms, compared to over 15 s above the resonance (green curve). Adapted from Ref. [65].

We fit the time evolution of density and temperature to the solution to Eq. 7.5 to extract β as a function of $|\mathbf{E}|$.

We measure β at electric fields between 4.5-14 kV/cm (Fig. 7.3a). Our measurements agree very well with theoretical predictions using no free parameters [154], shown as a solid line. In particular, we see two features where the loss rate is strongly modulated, corresponding to resonances with output states $|0,0\rangle\,|2,0\rangle$ and $|0,0\rangle\,|2,\pm1\rangle$. At the fields $|\mathbf{E}| = 12.50$ and 12.72 kV/cm, separated by only 220 V/cm, the loss rates differ by three orders of magnitude (Fig. 7.3b). Below the resonance, molecules experiencing an attractive potential are depleted within 50 ms. Above the resonance, however, the shielding potential extends the molecule lifetime past 15 s, a factor of 30 reduction in the loss rate below the background value. Using the shielding resonance, we have realized a long-lived gas of molecules with dipolar interactions in 3D.

7.4 Dipolar Elastic Collisions

Dipole moments mediate elastic collisions between molecules. The rate of elastic collisions is given by

$$\Gamma_{\mathrm{el}} = nv\sigma_{\mathrm{el}}(\theta) \tag{7.6}$$

where n is the density, $\sigma_{\mathrm{el}}(\theta)$ is the elastic cross section for collisions oriented at θ with respect to the dipole moment, and v is the averaged relative collisional velocity between pairs of molecules. In the case of an out-of-equilibrium gas, where each trap axis has a different effective temperature (or average energy), v is given by

$$v = \sqrt{\frac{16k_B\pi(T_x + T_y + T_z)}{3\pi^2 m}} \tag{7.7}$$

At low temperatures, the average of $\sigma_{\mathrm{el}}(\theta)$ over all angles reaches a universal value

$$\sigma_{\mathrm{el}} = \langle\sigma_{\mathrm{el}}(\theta)\rangle = \frac{32\pi}{15}a_d^2 \tag{7.8}$$

a_d is a length scale quantifying the dipolar interactions, $a_d = \mu d^2/\hbar^2$, where d is the dipole moment and μ is the reduced mass [163].

When the molecules are out of equilibrium, elastic collisions redistribute energy between the axes and bring the system to thermal equilibrium. Due to the anisotropy of the dipolar cross section, two molecules approaching along one axis preferentially scatter out along the same axis, a process that does not contribute to thermalization [146]. This means the rate of thermalization Γ_{th} is slower than the elastic collision rate; we relate these quantities by the parameter $N_{\mathrm{coll}}(\theta)$:

$$\Gamma_{\mathrm{th}} = \frac{\Gamma_{\mathrm{el}}}{N_{\mathrm{coll}}(\theta)} = \frac{n\sigma_{\mathrm{el}}v}{N_{\mathrm{coll}}(\theta)} \tag{7.9}$$

N_{coll} can be interpreted as the number of collisions needed to scatter between axes. $N_{\mathrm{coll}} = 2.7$ and 4.1 for ultracold bosons [164] and fermions [42], which collide predominantly in the s- and p-wave channels at low temperatures. For simplicity, we incorporate all of the angular dependence in N_{coll} and use the universal value for the cross section at $d = -0.08$ D, $\sigma_{\mathrm{el}} = 2.8 \times 10^{-12}$ cm^2.

In principle, in the vicinity of the resonance the dipolar coupling modifies the elastic cross section from the universal value. However, this modification is small at $|\mathbf{E}_s|$ [154].

We describe the time evolution of the molecule density and temperature by a set of coupled differential equations:

$$\begin{aligned}
\dot{n} &= -K_L(T_y + 2T_x)n^2 - \frac{n}{T_y}\dot{T}_y - \frac{n}{T_x}\dot{T}_x \\
\dot{T}_y &= \frac{n}{4}K_L(-T_y + 2T_x)T_y - \frac{2\Gamma_{\text{th}}}{3}(T_y - T_x) + c_y \\
\dot{T}_x &= \frac{n}{4}K_L T_y T_x + \frac{\Gamma_{\text{th}}}{3}(T_y - T_x) + c_x
\end{aligned} \tag{7.10}$$

K_L is the two-body loss rate coefficient, related to β as $\beta = 3K_L T$, where T is the temperature in thermal equilibrium. c_x and c_y are rates capturing all of the one-body background heating, including off-resonant heating from the optical traps. n depends on temperature-dependent two-body loss as well as the decrease of density with increased temperature at fixed particle number. $T_{x,y}$ depend on one-body heating, thermalization between axes, and anti-evaporation, a process where low-energy molecules are lost preferentially in 3D and the average energy correspondingly rises. We have made two assumptions that will be discussed more in the following subsections: first, the radial temperatures are equal ($T_x = T_z$), and second, K_L does not vary with dipole angle.

7.4.1 Cross-Dimensional Thermalization

As in 2D (Fig. 6.5), we use cross-dimensional thermalization (CDT) to measure elastic collisions between molecules. We prepare the molecules at $|\mathbf{E}| = 12.72$, with the field oriented at $\theta = 0°$ with respect to the $\mathbf{y}$ axis (Fig. 7.4c). The field is rotated to the target angle θ in 60 ms. Starting from thermal equilibrium at $T = 300$ nK, we parametrically heat the molecules along $\mathbf{y}$ by modulating the optical trap power for 50-100 ms, increasing the temperature to 800 nK. By measuring the time evolution of T_x, T_y, and n and fitting to Eq. 7.10, we can extract $N_{\text{coll}}(\theta)$.

Figures 7.4a and 7.4b show T_x and T_y at hold times of 0-10 s after heating for $\theta = 45°$ and 90°. The qualitative behavior is very different: at 45°, the temperatures converge to within 50 nK, while at 90°, the temperatures approach only at early times while the molecule density is

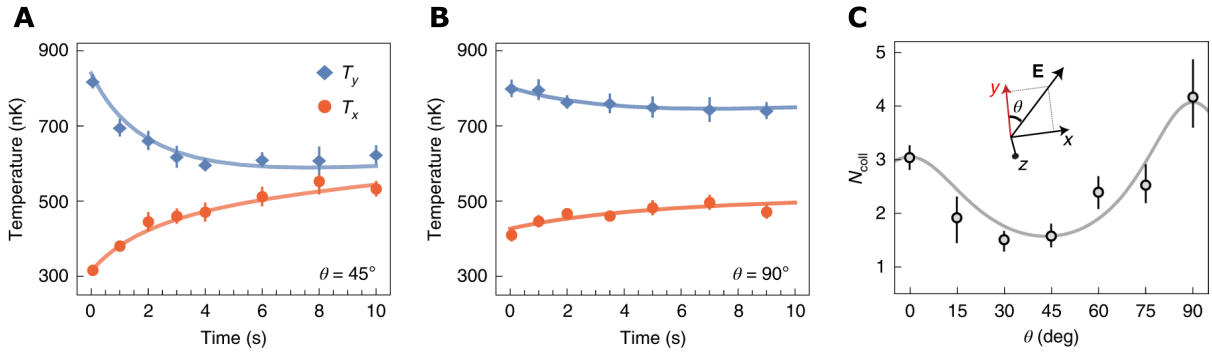

Figure 7.4: Cross-dimensional thermalization in 3D. **(a)** At 45°, the heated and unheated axes approach temperature equilibrium due to elastic collisions. **(b)** At 90°, by contrast, the temperature do not converge. **(c)** Varying the dipole angle with respect to the heated axis changes N_{coll}. This directly shows the anisotropy of dipolar interactions. Figure from Ref. [65].

highest but remain separated by 250 nK. We measure N_{coll} for each θ and find strong dependence (Fig. 7.4c), with N_{coll} varying from $1.6^{+0.2}_{-0.1}$ to $4.1^{+0.9}_{-0.6}$ for the two angles shown in (a) and (b). Our colleagues in the Bohn group analytically calculated N_{coll} in the limit of small excitation, which gave the expression

$$N_{\mathrm{coll}}(\theta) \approx \frac{97.4}{45 + 4\cos(2\theta) - 17\cos(4\theta)} \tag{7.11}$$

We find close agreement with this prediction. More details about the calculation can be found in the supplementary information to Ref. [65] and in Refs. [165, 166].

For fitting the data and extracting N_{coll}, we make the assumption $T_x = T_z$ at all hold times (Eq. 7.10). This is because our imaging system is oriented along **z**. However, the rethermalization rates from **y** to **x** and from **y** to **z** may differ due to the asymmetry of the dipole angle with respect to these axes. At $\theta = 90°$, this assumption is correct because of rotational symmetry in the **x**-**z** plane; at $\theta = 45°$, the rate of energy transfer to **x** is faster than to **z**. Since $T_z < T_x$ in this situation, we overestimate the average velocity v and therefore overestimate N_{coll}.

The shielding potential barrier is anisotropic (Fig. 7.2), so we expect that the loss coefficient K_L may have angular dependence. We measure K_L at each θ and find a small anti-correlation with N_{coll} (Fig. 7.5). K_L is maximized around 45°, although the total variation is only about 30%. At $\theta \approx 55°$, the dipolar coupling and repulsive barrier vanish (Fig. 7.2); while each collision involves

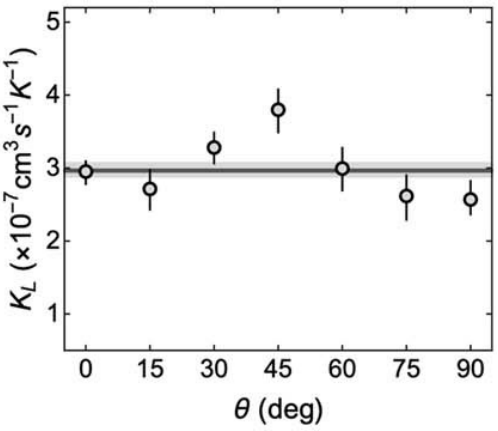

Figure 7.5: Two-body loss vs. dipole angle. K_L is weakly anti-correlated with N_{coll}, possibly due to the lower potential barrier for collisions oriented near 45° (Fig. 7.2). Fixing K_L to its mean value (black line) for all angles does not significantly change the measured N_{coll}. Figure from Ref. [65].

a distribution of angles given by L, m_L, leading to an overall repulsive potential, the averaged potential is lowest around this angle and may contribute to the increased loss rate. Fitting every angle with K_L fixed to its average value, indicated on Fig. 7.5, does not qualitatively change the measured N_{coll}.

7.4.2 Density Correction

CDT is measured at various θ at $|\mathbf{E}| = 12.72$ kV/cm. To measure the temperature and density, we dissociate the molecules using STIRAP at $|\mathbf{E}| = 4.5$ kV/cm and $\theta = 0°$, ramping from the CDT field configuration in 60 ms. The trap frequencies experienced by the molecules depend on $|\mathbf{E}|$, due to field-dependent ac polarizability [167], and on θ, due to curvature introduced by rotating the electric field away from $\mathbf{y}$, the axis of symmetry (Fig. 3.5). We must correct the measured density (n^m) and temperatures ($T^m_{x,y}$) at the dissociation field to get the real density (n) and temperatures ($T_{x,y}$) during the hold time.

To make this correction, we measure $\omega_{x,y,z}(\theta)$, the trap frequencies along all three axes, at seven angles between 0° and 90°, and find variation of nearly 20% at extreme angles. We also measure $\omega^0_{x,y}$, the trap frequencies at the dissociation field. Since the field ramp is slow with

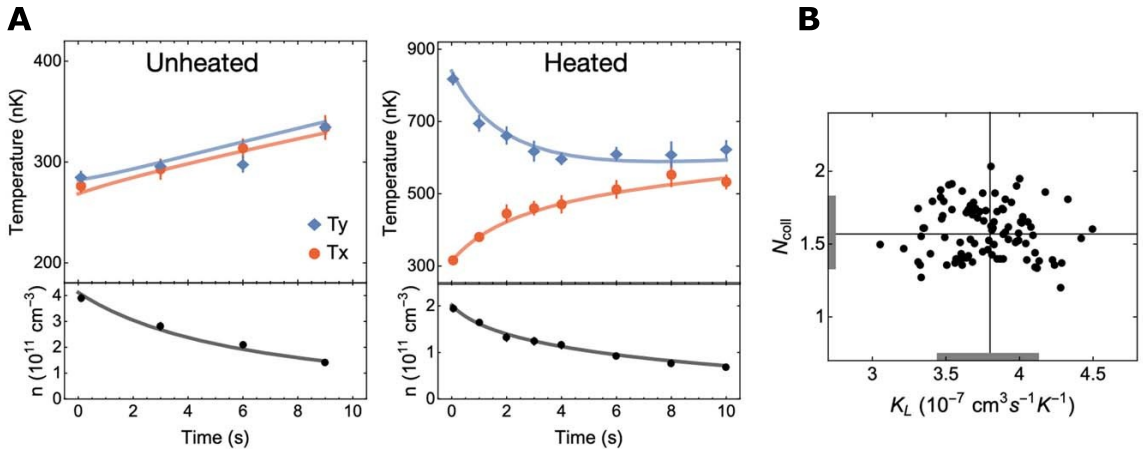

Figure 7.6: Bootstrap fitting of cross-dimensional thermalization. **(a)** We simultaneously fit the temperatures of the **y** and **x** axes and the densities of the molecules with and without parametric heating to Eq. 7.10. **(b)** Bootstrap fit results for N_{coll} and K_L, using 100 iterations. Gray bars show the 68% confidence intervals of the fits. N_{coll} and K_L are only weakly correlated. Figure from Ref. [65].

respect to the oscillation period in the optical trap, we assume that the molecules are decompressed adiabatically during the ramp and make the following corrections

$$\begin{aligned} T_i &= \left(\frac{\omega_i(\theta)}{\omega_i^0}\right) T_i^m(\theta) \\ n &= \left(\frac{\overline{\omega}(\theta)}{\overline{\omega}^0}\right)^{3/2} n^m(\theta) \end{aligned} \tag{7.12}$$

where $\overline{\omega}$ represents the harmonic mean trap frequency.

7.4.3 Bootstrap Fitting

For each θ, we measure the quantities n, T_x, and T_y between 0-10 s hold time in two different conditions: with and without parametric heating along **y**. Data for $\theta = 45°$ is shown in Fig. 7.6a. We simultaneously fit the data sets to Eq. 7.10 to extract ten fit parameters: $N_{\text{coll}}, K_L, c_x, c_y$, and the initial densities and temperatures in both the heated and unheated data sets.

The thermalization model does not have an explicit solution, so we fit the data numerically and use the bootstrap method to estimate the error on the parameters. At each hold time and for both the heated and unheated conditions, we fit n, T_x, T_y using time of flight expansion (Fig. 7.6a).

For j times in the heated condition and m times in the unheated condition, we get $N = 3(j + m)$ total data points, with mean values $\vec{x} = \{x_1, x_2, ..., x_N\}$ and standard errors $\vec{\sigma}_x = \{\sigma_{x_1}, \sigma_{x_2}, ..., \sigma_{x_N}\}$. The set of ten fit parameters in Eq. 7.10 that minimizes χ^2, given $\vec{x}$ and $\vec{\sigma}_x$, is denoted $\vec{p}(\vec{x}, \vec{\sigma}_x) = \{p_1, ...p_{10}\}$.

In bootstrap resampling, we estimate the error of each element of $\vec{p}$ by generating and fitting a large number of synthetic data sets. We sample M sets of data points $\vec{x}^j$ from the multivariate normal distribution $\mathcal{N}(\vec{x}, \vec{\sigma}_x)$, and fit each $\vec{x}^j$ to produce $\vec{p}^j(\vec{x}^j, \vec{\sigma}_x)$. The mean and standard error of parameter p_i are then

$$\begin{aligned} \overline{p}_i &= \frac{1}{M}\sum_{j=1}^{M} p_i^j \\ \sigma_{\overline{p}_i} &= \sqrt{\frac{1}{M}\sum_{j=1}^{M}(p_i^j - \overline{p}_i)^2} \end{aligned} \tag{7.13}$$

Figure 7.6b shows fit results for parameters N_{coll} and K_L, with $M = 100$ samples from the data shown in Fig. 7.6a. The gray bars denote the 68% confidence interval of the fits ($\sigma_{\overline{p}_i}$). Because every parameter is fit simultaneously, we can compute the correlation coefficient for each pair of parameters. In Fig. 7.6b, the correlation between N_{coll} and K_L is -0.26, so these parameters are only weakly correlated.

7.5 Evaporative Cooling in 3D

Away from the shielding resonances, the dipolar potential has repulsive and attractive regions. Combined with the fermionic p-wave barrier, which is isotropic and repulsive, the ratio between elastic and inelastic collisions for molecules is smaller than two [154]. Since it takes several elastic collisions to thermalize (Fig. 7.4), direct evaporation from molecule-molecule collisions is impossible. Around the shielding resonances, the potential barrier varies rapidly. At the point where the two-body loss is smallest, above the resonance, the elastic/inelastic ratio $\gamma = 17.8$ (Fig. 7.7). Based on the measured β (Fig. 7.3), we estimate $\gamma = n\sigma_{\text{el}}v/\beta n_0 = 12(1)$ for our experimental conditions. While this is smaller than the ratio of 200(60) we achieve in 2D (Chapter 6), we proceeded to

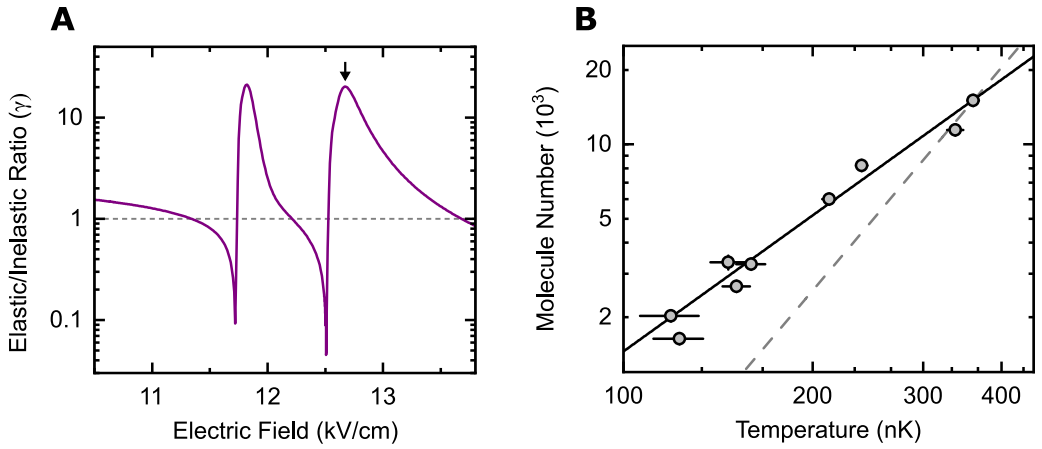

Figure 7.7: Direct evaporation in 3D. **(a)** The ratio of elastic to inelastic collisions reaches a maximum of 19 above the shielding resonance. **(b)** We measure an evaporation slope of $S_{\text{evap}} = 1.84(9)$ (black line), well below the slope of constant phase-space density ($S_{\text{evap}} = 3$, dashed line). Adapted from Ref. [65].

measure evaporation.

In 3D, the Fermi temperature $T_F \propto N^{1/3}$. Similarly to 2D, to decrease T/T_F an evaporation trajectory must satisfy

$$S_{\text{evap}} = \frac{\Delta \log N}{\Delta \log T} < 3 \tag{7.14}$$

where S is the slope of the change in N and T, on logarithmic scales. A trajectory with $S = 3$ has constant T/T_F, indicated by a dashed line on Fig. 7.7b. We prepare 1.5×10^4 molecules at $T = 330$ nK at $|\mathbf{E}| = 12.72$ kV/cm and $\theta = 0°$. By lowering the depth of the optical trap, we remove high-energy molecules and the remaining molecules thermalize through elastic collisions. We measure $S_{\text{evap}} = 1.84(9)$, corresponding to a decrease of T/T_F from 2.3(1) to 1.4(2) over the trajectory.

In previous works [61, 62], we reported molecules at $T/T_F = 0.3$ from direct association of degenerate atomic gases, substantially colder than here. Several technical limitations prevented reaching similar conditions or colder in this work. First, it should be noted that in prior works the molecules were not in thermal equilibrium due to losses during STIRAP [62]. Second, we previously associated molecules at zero field in state $|0, 0\rangle$, where the STIRAP process is most efficient; here

we associate directly at 4.5 kV/cm and transfer to state $|1,0\rangle$, which reduced the overall molecule number by about 30%. Most importantly, to make measurements around the shielding resonances we adiabatically ramp the field up and down from 4.5 kV/cm in hundreds of milliseconds, during which two-body loss further lowers the number. Using the techniques of Chapter 2 to associate molecules directly at the shielding resonance, which we developed after this work, we would expect to achieve more efficient evaporation and colder temperatures.

In molecules with larger dipole moments, $\gamma > 1000$ could be obtained at lower electric fields, potentially enabling low loss and very efficient evaporation [160]. Though KRb has less favorable properties for reaching high phase-space density, we have demonstrated a general approach for controlling resonant dipolar interactions using electric fields and tuning the collisional properties of polar molecules.

Chapter 8

Dipolar Exchange

In our previous measurements on two-dimensional systems [63, 64], we measured properties averaged over all molecules on all layers. For instance, in Ref. [63], we corrected the measured T/T_F and two-body loss coefficients for the layer occupations, which we measured by indirect means such as expansion in a harmonic trap. Here we demonstrate layer-resolved state preparation and imaging using an applied electric field gradient, directly addressing the molecules on each layer. This method is inspired by previous works with atoms [168, 169, 170], where magnetic field gradients were used instead. We eliminate the differential polarizability between rotational states and maximize the coherence time by rotating the electric field relative to the light polarization. Molecules in adjacent layers interact via dipolar exchange of rotational angular momentum; by adjusting the interaction strength between spatially separated molecules, we regulate the local chemical reaction rate and study the dependence on frequency detuning between layers. This section is based on results reported in Ref. [66].

8.1 Introduction

In reduced dimensionality, the sign and magnitude of interactions between molecules depend on the orientation of the dipole moments with respect to the external confinement. Within two-dimensional (2D) layers, for example, the averaged interactions between molecules can be varied continuously from attractive to repulsive by rotating the dipoles into and out of the plane. Molecules in an isolated 2D layer are predicted to exhibit diverse quantum phenomena determined by the

dipole angle and other parameters including electric field and rotational state. These include complex ground state phases such as superfluids and topological insulators [171, 172, 173, 174, 175, 53, 176, 177], collective excitations in the hydrodynamic regime [152], and interaction-enhanced rotational coherence and dynamical generation of spin squeezing [178]. Molecules prepared in multiple 2D layers may pair and form states with long-range order [179, 180, 181, 182]. Addressing individual lattice layers would allow initialization of varied configurations to realize these models: single layers, where molecules are isolated against out-of-plane interactions, and minimal systems with interlayer interactions such as bilayers and trilayers (two and three adjacent layers, respectively).

Recent experimental progress with molecules in 2D has included reaching quantum degeneracy using direct evaporation [63] or pairing in a degenerate atomic gas [183], performing optical microscopy of single lattice sites [55], and lengthening the coherence time of rotational superpositions [184, 20]. When translational motion is allowed within layers, as is the case for confinement in a 1D optical lattice, molecules approaching at short range undergo lossy chemical reactions [96, 185, 36, 37, 34]. These losses can be mitigated by orienting the dipole moments perpendicular to the layer [88, 46, 48, 63, 186] or engineering rotational state couplings [64, 65, 157, 154, 158] to generate a repulsive collisional barrier. A major missing capability is the ability to prepare molecules in different internal states and control multiple layers individually, which is essential for tuning dipolar interactions in reduced dimensionality.

8.2 Layer Selection

To study dynamics in single layer and multilayer configurations, we developed a technique for addressing individual lattice layers. Inspired by previous works with atoms [168, 169, 170], we apply an electric field gradient parallel to the direction of tight confinement to shift rotational transitions between lattice layers (Fig. 8.1). The electric field dependence of rotational state energies enables microwave addressing of individual lattice layers. In terms of the layer spacing a, a field gradient $\partial_y |\mathbf{E}|$ shifts the transition between states with differential dipole moment $\widetilde{d}$ on adjacent layers by

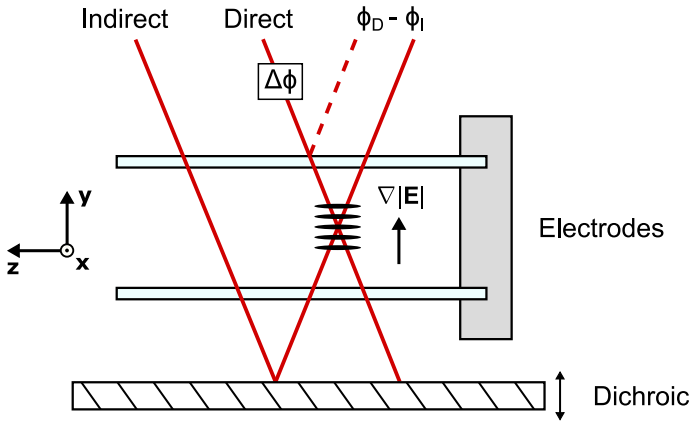

Figure 8.1: Phase stabilization diagram. The two lattice beams (red) interfere at the location of the atoms, with the indirect beam first reflecting off of the dichroic (striped). The phase of the direct beam can be modulated to adjust the lattice phase. The electrodes (light blue) are rigidly connected by a ceramic mount (gray), and generate an electric field gradient at the molecule position. Both the electrodes and dichroic vibrate with respect to a space-fixed position. Adapted from Ref. [66].

the frequency

$$\Delta = \partial_y |\mathbf{E}| \cdot a \cdot \widetilde{d}/h \tag{8.1}$$

There are two primary technical challenges for layer selection, which it took us several attempts over two years to solve: stabilizing the lattice phase with respect to the electric field, and eliminating tilts in the lattice angle relative to the field gradient.

8.2.1 Phase Stabilization

Our lattice is generated by interfering two beams, called "direct" and "indirect" (Fig. 8.1). The beams enter the chamber at an angle of 12° from the **y** axis, and the indirect beam reflects off of a dichroic mirror below the chamber prior to intersecting the direct beam at the position of the atoms. Both beams are derived from a common source immediately prior to entering the experimental apparatus, and therefore initially have a static phase difference; the phase of the direct beam can be shifted by a variable amount $\Delta\phi$ by adjusting its path length using a mirror mounted on a piezoelectric actuator (Fig. 8.2a). The maximum throw of the piezo is 3.5 μm, corresponding to a path length change of 7 μm $\approx 13\,a$.

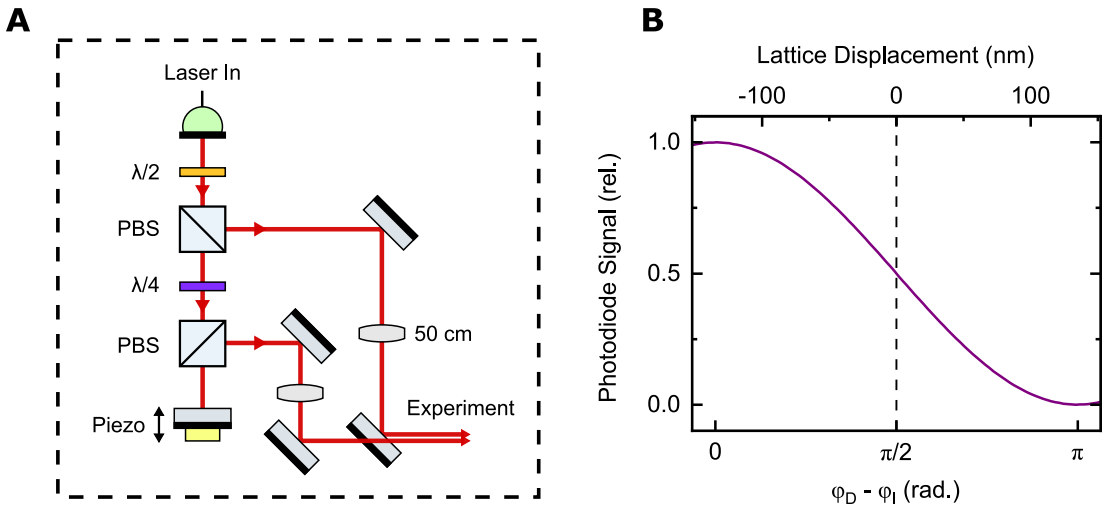

Figure 8.2: Lattice phase stabilization. **(a)** Simplified experimental schematic for the direct and indirect lattice beams. The path length of the direct beam is modulated using a mirror mounted on a piezo. **(b)** Measured photodiode voltage vs. phase difference between direct and indirect beams. By varying the setpoint we can displace lattice layers by up to 270 nm.

During the experiment, the dichroic and electrodes move relative to each other and relative to the optical breadboard where the lattice beams originate. Since the electrodes generate the field gradient for layer selection, it is essential to stabilize the position of the lattice layers to the electrodes and to cancel shifts due to the motion of the dichroic. To measure the position of the dichroic during the experimental sequence, we retroreflect a laser off of the dichroic and monitor the phase shift. We find that it has a fundamental mechanical frequency of 350 Hz, a time constant for vibration damping of 150 ms, and moves several times the lattice spacing a during the experimental sequence. The primary sources of noise are the moving cart and fans on cameras and power supplies.

When the dichroic moves relative to the electrodes by a substantial fraction of a, each lattice layer experiences a random electric field shot-to-shot and layer selection is impossible. Therefore, feedback is necessary for stabilizing the relative position. We use a photodiode to measure $\phi_D - \phi_I$, the phase difference between the indirect beam after the dichroic and a weak reflection of the direct beam from the upper electrode plate (Fig. 8.1). Neutral density filters are used to equalize the power of the two reflections, and both reflections are coupled into a fiber before the photodiode to ensure near-perfect mode matching and full fringe contrast. By feeding back to $\Delta\phi$ to fix $\phi_D - \phi_I$, we fix the lattice phase with respect to the electrodes. Since the intensity of the lattice beams is stabilized, the measured voltage on the photodiode indicates the phase difference between the beams (Fig. 8.2b). We typically operate at a setpoint of half of the full-scale voltage, but we can vary the vertical displacement of the lattice by up to the layer spacing a by changing the voltage setpoint.

8.2.2 Lattice Tilt Angle

To control single lattice layers, the microwave pulse used for addressing rotational transitions must be resonant with every molecule on one layer and off-resonant with all other layers. This condition can be expressed in terms of three energy scales. First, the mean rotational transition shift between adjacent layers is Δ (Eq. 8.1). Second, the spectral width of a microwave pulse, σ_F,

is determined by the Fourier limit, where for a rectangular (constant power) pulse of duration T

$$\sigma_F \approx \frac{0.8}{T} \tag{8.2}$$

Finally, if there is a radial electric field gradient $\partial_r|\mathbf{E}|$, perpendicular to $\mathbf{y}$, molecules displaced from the center of the trap will experience a transition frequency shift proportional to the gradient times the displacement. For layer selection, we must have:

$$\Delta > \sigma_F > \left(\partial_r|\mathbf{E}| \cdot \widetilde{d}/h\right) \cdot l_r \tag{8.3}$$

where l_r is the radial width of the cloud. If the first inequality is not satisfied, the pulse is broad enough to affect molecules on multiple layers; if the second is not, the pulse is too narrow to transfer all molecules on one layer.

In a layer selection gradient of $\partial_y|\mathbf{E}|$, if the lattice is tilted by an angle θ out of the **x**-**z** plane, an effective radial gradient with magnitude $\partial_r|\mathbf{E}| = \partial_y|\mathbf{E}|\sin\theta$ is created since the **y** position varies across the layer (Fig. 8.3a). Even small tilt angles can generate large effective gradients due to the large radial extent of the molecular cloud. With the typical layer selection gradient of 6.4 kV/cm^2 and a = 540 nm, Δ = 14 kHz. At a tilt of only $\theta = 0.5°$, the detuning over $\pm 2\sigma$ of the molecular distribution (about 60 μm) is equal to Δ. Due to the symmetry of the electrodes (Fig. 3.4), gradients along **x** can be eliminated using the rod voltages but gradients along **z** cannot. The only experimental method for changing the effective **z** gradient is varying the lattice angle by changing the inclination of the direct and indirect beams as they enter the vacuum chamber (Fig. 8.1).

We use spectroscopy on the $|0,0\rangle \rightarrow |1,0\rangle$ rotational transition to measure and correct the lattice angle relative to the electrodes. If a narrow pulse is applied, with a Fourier width much smaller than the broadening across one layer, a small fraction of the molecules on one layer will be transferred. The position of these molecules will vary with the microwave detuning; by measuring the slope of the position vs. detuning, we can estimate the gradient. Figure 8.3b shows the position of the transferred molecules over 50 kHz detuning. The gray lines indicate four layers, with identical slopes and spaced equally by Δ.

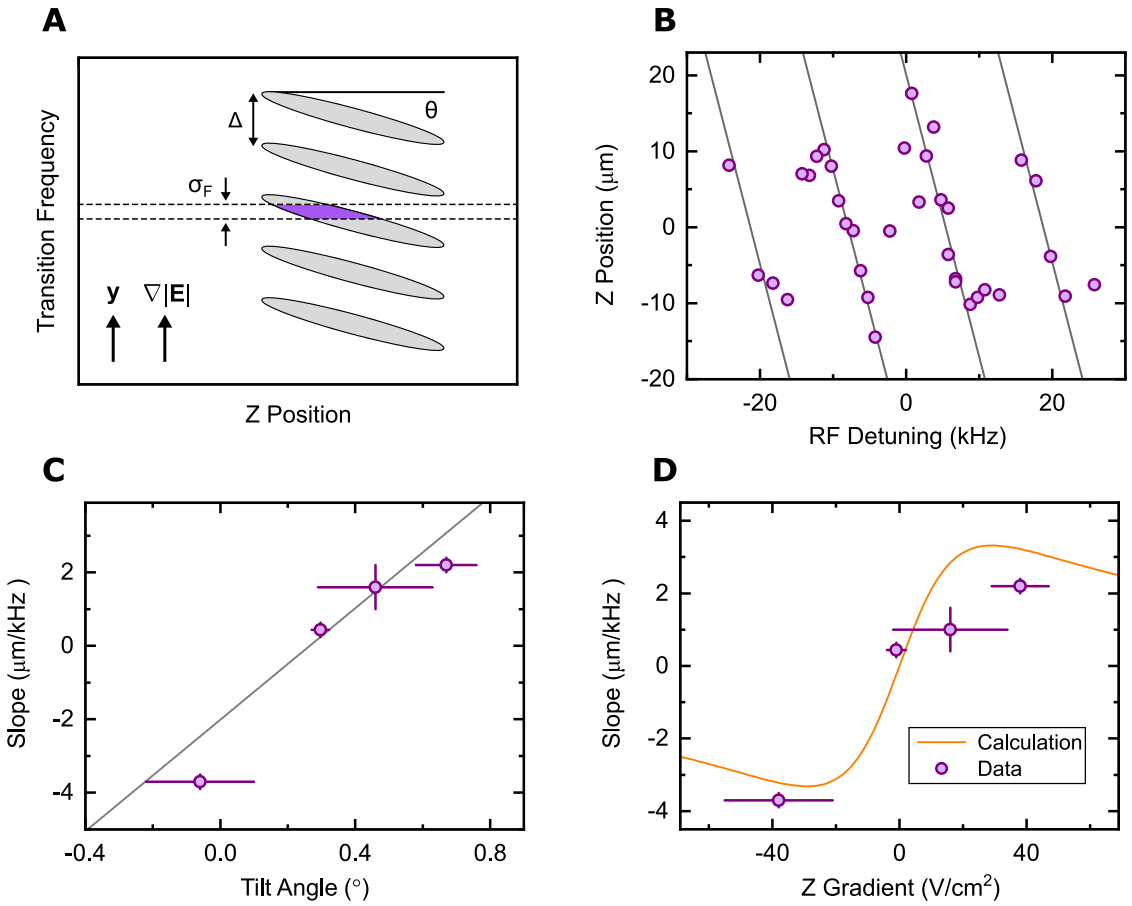

Figure 8.3: Spectroscopic measurement of lattice tilt angle. **(a)** In a gradient $\partial_y|\mathbf{E}|$, a lattice tilt angle θ creates an effective **z** gradient. A narrow pulse will only transfer a fraction of molecules from one layer, with the **z** position of the transferred molecules depending on the pulse frequency. **(b)** Measuring the position shift vs. detuning for four lattice layers, indicated by gray lines. **(c)** Slope of position vs. detuning at four different lattice angles. As the lattice is tilted, the effective gradient varies. **(d)** Extracting the **z** gradient using the measured slope. The data is consistent with the calculated trend.

We measure the slope for four different lattice angles (Fig. 8.3c). Using Kapitza-Dirac diffraction of a BEC in the optical lattice, where the atoms are diffracted in the direction perpendicular to the layers [187], the angle of the lattice relative to the imaging system can be measured. We also use a simple model to calculate the expected slope per gradient. In the limit of an infinitely narrow pulse, the slope of the mean position $\langle z \rangle$ vs. frequency ν is

$$\frac{d\langle z \rangle}{d\nu} = \frac{h}{\widetilde{d}} \cdot \frac{1}{\partial_z |\mathbf{E}|} \tag{8.4}$$

To account for the pulse width, we consider a Gaussian distribution of molecules along $\mathbf{z}$, $n(z)$, where the width of this distribution is determined by the temperature and trap frequencies used in making the measurement. We compute $\langle z \rangle$, weighting by $p_{\sigma_F}(\nu_0, \nu)$, the probability of excitation for a molecule with resonant frequency ν_0 by a pulse of frequency ν and width σ_F:

$$\frac{d\langle z \rangle}{d\nu} = \frac{d}{d\nu} \int z\, n(z)\, p_{\sigma_F}(\nu_0, \nu)\, dz \tag{8.5}$$

where the position- and gradient-dependent resonant frequency is

$$\nu_0 = z \cdot \left(\partial_z |\mathbf{E}| \cdot \frac{\widetilde{d}}{h} \right) \tag{8.6}$$

For our parameters, the calculated and measured slopes are shown in Fig. 8.3d. The lone fitting parameter is a constant offset to the gradient—or equivalently, lattice angle—since the absolute angle of the lattice is unknown. We leave the lattice at the angle where the gradient is minimized.

8.2.3 Results

With the phase stabilization and lattice angle optimized, we apply a gradient of $\partial_y |\mathbf{E}| = 6.4$ kV/cm^2 and scan the microwave detuning over the full distribution of the molecules in the optical lattice (Fig. 8.4a). Thirteen separate layers are visible, with an interlayer spacing of $\Delta = 14$ kHz. Fitting the layer populations with a Gaussian envelope, we find a width of $\sigma = 57$ kHz, corresponding to 4.1 layers or 2.2 μm. Even though each individual layer is too small to image directly, we can track the central position of the transferred molecules over the full distribution

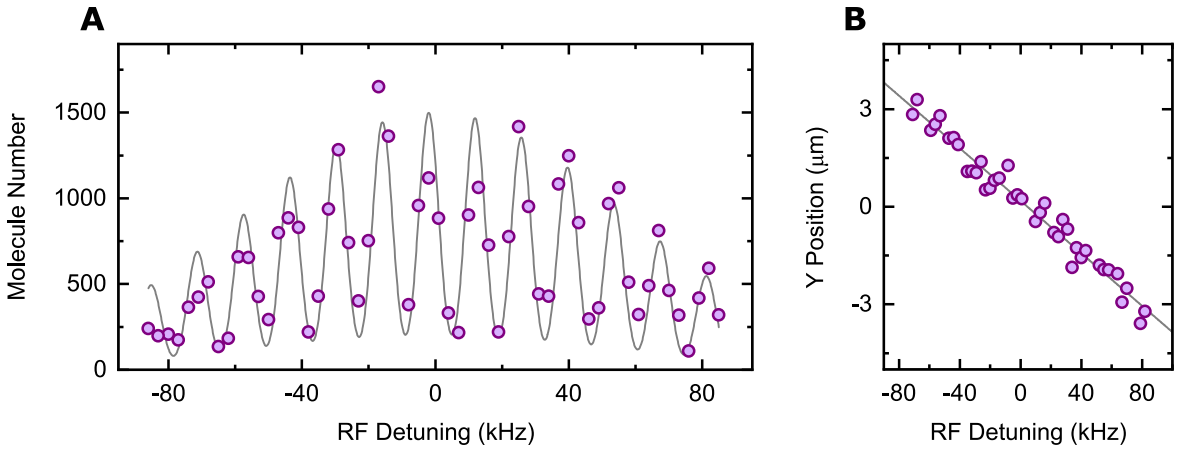

Figure 8.4: Measuring the molecule distribution using layer selection. **(a)** Full molecule distribution in the optical lattice. **(b)** Due to the electric field gradient, only molecules at a particular **y** position are transferred by the layer selection pulse.

(Fig. 8.4b). The slope is 0.040(12) μm/kHz, corresponding to a gradient of 6250(190) V/cm^2, consistent with the calculated value.

In resolving individual lattice layers, this electric field imaging technique exceeds the capability of optical imaging, which is limited to a resolution of approximately $\lambda/2\mathrm{NA}$, where λ is the imaging wavelength and NA is the numerical aperture of the imaging system. Due to the electrode geometry (Fig. 3.4), our NA for imaging parallel to the lattice layers is less than 0.35, limiting the resolution to 1.1 $\mu\mathrm{m} = 2a$. A number of experiments use high-NA microscope objectives for imaging single lattice sites containing atoms or molecules [188, 169, 55], but the depth of field in the imaging direction is much smaller than the radial extent of our lattice layers. Our method, which uses electric and microwave fields with which only molecules in a small region of space are resonant, is conceptually similar to recent experiments that use two optical fields to probe sub-μm regions of atomic gases in lattices [189, 190]. However, those experiments directly measure the atomic wavefunction, while our experiment only probes the molecular density; the frequency width of the measured layers (Fig. 8.4a) represents a combination of the inhomogeneous broadening and the pulse width rather than the harmonic length.

To quantify the relationship between the interlayer separation, the pulse width, and the

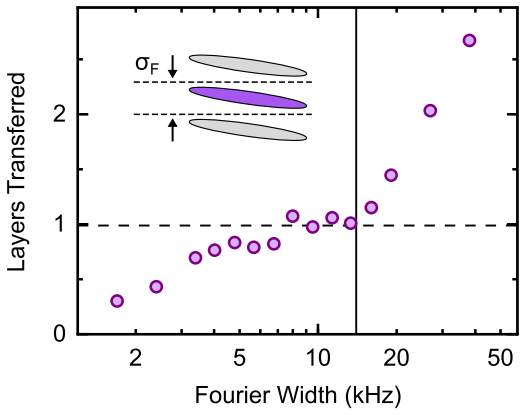

Figure 8.5: Optimizing pulse width for layer selection. For pulses narrower than the broadening across one layer, fewer than one layer is transferred. Above Δ (solid line), the frequency spacing between layers, more than one layer is transferred. For a range of intermediate pulse widths, exactly one layer is transferred (dashed line, also shown in the inset).

broadening across each layer (Eq. 8.3), we scan the pulse width on the layer selection (Fig. 8.5). To normalize against molecule number fluctuations, we first select three adjacent layers of approximately equal population and remove the other layers (see next section). We center a microwave pulse with variable Fourier width σ_F on the middle layer and monitor the transferred fraction, so that one-third transfer of the total molecule number equates to one layer. We identify three distinct regions of pulse power. For very narrow pulses, the broadening exceeds the pulse width and only a fraction of the middle layer is transferred. For very broad pulses, exceeding the interlayer detuning Δ, more than one layer is transferred. In an intermediate regime, between 6-12 kHz, exactly one layer is transferred (as shown in the inset of Fig. 8.5). We operate in this range for layer selection, at a typical width of $\sigma_F = 10$ kHz.

8.3 State Preparation and Electric Field Microscopy

The following sections describe the procedures and results from Ref. [66]. At a bias electric field of $|\mathbf{E}| = 1$ kV/cm, we associate KRb in a 1D optical lattice to form a stack of 2D layers, with an interlayer spacing $a = 540$ nm [63]. KRb is formed in the rotational ground state $|0, 0\rangle \equiv |0\rangle$, where $|N\rangle$ denotes the state with electric field-dressed rotational quantum number N and zero

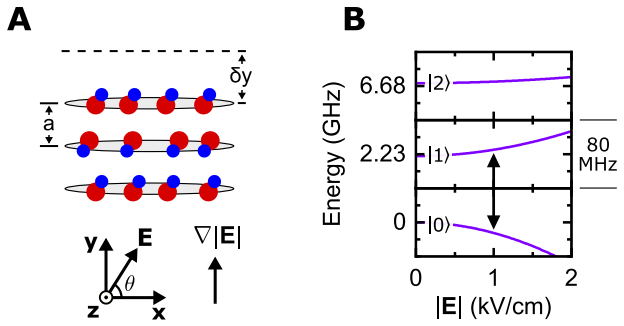

Figure 8.6: Experimental configuration for layer selection and spin exchange. **(a)** Molecules occupy two-dimensional layers in the **x**-**z** plane, separated by layer spacing a. The bias electric field $\mathbf{E}$ is oriented at an angle θ in the **x**-**y** plane, with an electric field gradient $\nabla|\mathbf{E}|$ parallel to **y**. The lattice layers are displaced relative to the electrodes generating $\mathbf{E}$ by a distance δy. **(b)** KRb rotational structure. The arrow indicates the layer selection transition. Reproduced from Ref. [66].

angular momentum projection ($m_N = 0$) onto the quantization axis specified by $\mathbf{E}$. The harmonic trapping frequencies for $|0\rangle$ in the combined trap are $(\omega_x, \omega_y, \omega_z) = 2\pi \times (42, 17\,000, 48)$ Hz. The molecules are pinned along **y**, parallel to gravity, but are free to move radially (**x**-**z** plane, Fig. 8.6a). In terms of the Boltzmann constant k_B and the reduced Planck constant $\hbar = h/2\pi$, for the typical temperature $T = 350$ nK, $k_B T = 0.4\,\hbar\omega_y$ and so the molecules predominantly occupy the lowest lattice band. Due to the thermal extent of the atomic clouds along **y** prior to loading the optical lattice, the initial molecule distribution spans approximately 12 lattice layers, with a peak of about 1500 molecules per layer. Compared with our previous work in 2D [63], where an auxiliary optical trap was used to compress KRb into few lattice layers to increase peak density, we deliberately prepare a broad distribution of molecules to minimize population differences among the central layers prior to layer addressing.

To orient the induced dipole moments of the molecules, we rotate $\mathbf{E}$ by a variable angle θ, where $\theta = 0°$ corresponds to $\mathbf{E} \parallel \mathbf{x}$ (Fig. 8.6a). An electric field gradient $\nabla|\mathbf{E}|$ can be applied along **y**, parallel to the direction of tight confinement in the optical lattice. Each rotational state $|N\rangle$ develops an induced dipole moment d_N parallel to $\mathbf{E}$, the magnitude of which depends on $|\mathbf{E}|$, leading to a state-dependent energy shift of $-d_N|\mathbf{E}|$ (Fig. 8.6b). At $|\mathbf{E}| = 1$ kV/cm, where all of the subsequent measurements are performed, the sensitivity of the $|0\rangle \rightarrow |1\rangle$ transition to $|\mathbf{E}|$ is

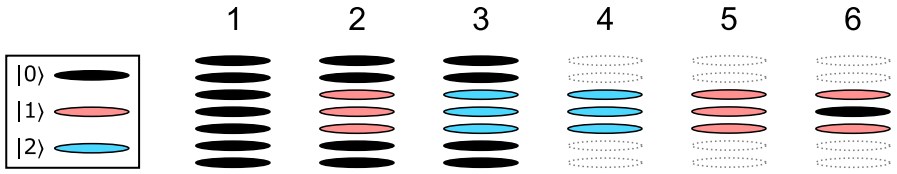

Figure 8.7: Pulse sequence for layer selection. Reproduced from Ref. [66].

$\widetilde{d} = d_0 - d_1 = h \cdot 40$ kHz/(V/cm). In a gradient of $\partial_y |\mathbf{E}| = 6.4$ kV/cm^2, the interlayer spacing a corresponds to $\Delta = 14$ kHz.

We perform layer-selective addressing of the $|0\rangle \rightarrow |1\rangle$ transition using the procedures described in the previous sections. We also have the capability to apply global microwave pulses (addressing all molecules, irrespective of $\partial_y |\mathbf{E}|$) on the $|0\rangle \rightarrow |1\rangle$ and $|1\rangle \rightarrow |2\rangle$ transitions, as well as to globally remove $|0\rangle$ and $|1\rangle$ molecules with optical pulses of STIRAP light. From an initial condition of many occupied $|0\rangle$ layers, we use sequences of these microwave and optical pulses to prepare arbitrary layer configurations containing states $|0\rangle$, $|1\rangle$, and $|2\rangle$, including isolated 2D layers. To illustrate this procedure, the following sequence is used to prepare a central $|0\rangle$ layer with only nearest-neighbor $|1\rangle$ layers:

(1) Initial condition: many occupied layers in state $|0\rangle$

(2) Three subsequent layer-selective $|0\rangle \rightarrow |1\rangle$ pulses, detuned by $0, \pm 14$ kHz from the resonant frequency of the central layer, to transfer three layers to $|1\rangle$

(3) Global $|1\rangle \rightarrow |2\rangle$ pulse, to transfer the three selected layers to $|2\rangle$

(4) Global STIRAP pulse, to remove the remaining molecules in $|0\rangle$

(5) Global $|1\rangle \rightarrow |2\rangle$ pulse, to return layers to $|1\rangle$

(6) Layer-selective $|0\rangle \rightarrow |1\rangle$ pulse, to transfer the central layer to $|0\rangle$

We find experimentally that the STIRAP pulse removes both $|0\rangle$ and $|1\rangle$ molecules but not $|2\rangle$, necessitating the involvement of $|2\rangle$ in layer selection. A similar procedure allows imaging the

populations in both rotational states $|0\rangle$ and $|1\rangle$ on a single experimental shot (Chapter 2). We use this method in the subsequent measurements to normalize the molecule number in each state against the total molecule number, reducing sensitivity to overall number fluctuations.

To demonstrate layer selection and removal, we prepare three adjacent layers in $|1\rangle$ and scan the frequency of an additional layer-selective $|0\rangle \rightarrow |1\rangle$ pulse while applying a gradient $\partial_y |\mathbf{E}| = 6.4(2)$ kV/cm^2. By monitoring the population transferred to $|0\rangle$ as a function of frequency, we probe the initial $|1\rangle$ distribution (Fig. 8.8a). We measure about 1200 molecules in each occupied layer, with adjacent layers detuned by 14 kHz. No molecules are transferred from outside the trilayer, nor at detunings halfway between occupied layers, confirming that the pulses are selectively addressing individual layers.

By varying the layer displacement δy and tracking the layer selection transition frequency, $|\mathbf{E}(y)|$ can be extracted with high spatial resolution, far below the interlayer spacing of 540 nm or the imaging diffraction limit. To characterize this technique, we probe the layer selection gradient. At each of eight different δy, spanning 360 nm (corresponding to a lattice phase shift of 240°), we measure the central frequency for layer selection (Fig. 8.8b). Fitting the frequency shift as a function of δy, we extract $\partial_y |\mathbf{E}| = 5.8(3)$ kV/cm^2, with a maximum offset between δy and the line of best fit of only 20 nm. These measurements demonstrate subwavelength detection of molecule distributions using electric field gradients and high-precision electric field microscopy on nm spatial scales.

8.4 Rotational Coherence in a Single Layer

Using layer-selective addressing, we next optimize the rotational coherence in a single layer. Long-lived coherence is essential for realizing strong dipolar interactions [175, 178]. However, inhomogeneous broadening from electric field gradients and optical trapping potentials tends to limit coherence. We eliminate electric field gradients along $\mathbf{x}$ by adding a small additional gradient with the electrodes, and along $\mathbf{z}$ by tilting the lattice (Fig. 8.3). The primary remaining source of inhomogeneity is the optical trapping potential.

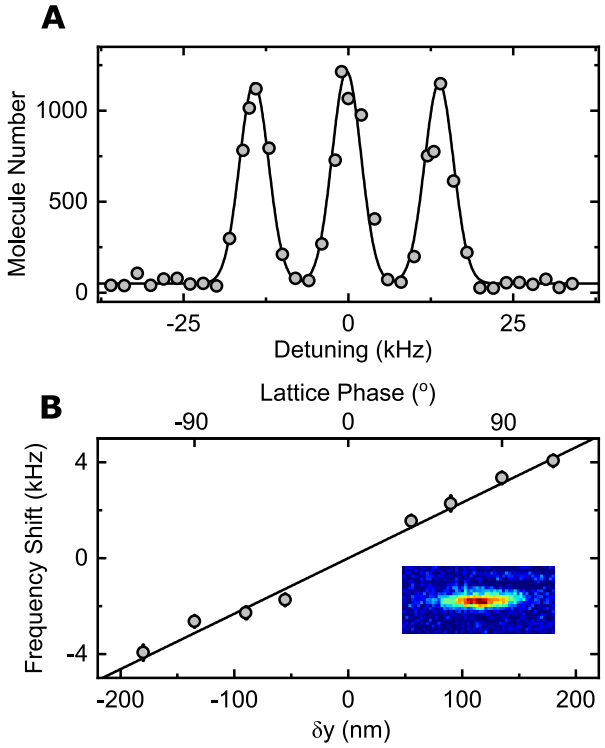

Figure 8.8: Trilayer selection and electric field microscopy. **(a)** Frequency spectrum of a trilayer at $\partial_y |\mathbf{E}| = 6.4(2)$ kV/cm^2. Only three adjacent lattice layers are populated. **(b)** Center frequency shift of layer selection vs. δy. Displacements smaller than 20 nm are measured. **Inset:** Absorption image of a single layer. Reproduced from Ref. [66].

8.4.1 Optimizing Magic Angle

In an optical trap of local intensity $I(\mathbf{r})$, the potential is $U(\mathbf{r}) = -\alpha I(\mathbf{r})$, where α is the atomic or molecular polarizability. The rotational states of diatomic molecules with $N > 0$ are spherically anisotropic (Eq. 3.4); therefore, α depends on rotational state and also on the orientation of the light polarization ϵ relative to the quantization axis, which here is aligned with $\mathbf{E}$ [167]. In our apparatus, the optical lattice polarization $\boldsymbol{\epsilon}$ is fixed parallel to $\mathbf{x}$, so this angle coincides with the rotation angle θ of $\mathbf{E}$ (Fig. 8.6a). Since the optical trap intensity varies over the radial extent of each layer, the differential polarizability between states $|0\rangle$ and $|1\rangle$ contributes a position-dependent frequency shift. At $\theta = 90°$, the transition frequency varies by several kHz across the layer for our molecule temperature and trapping parameters.

In terms of θ, the polarizabilities of $|0\rangle$ and $|1\rangle$ are

$$\begin{aligned} \alpha_0 &= \frac{1}{3}(\alpha_\parallel + 2\alpha_\perp) \\ \alpha_1 &= \frac{\alpha_\parallel + 4\alpha_\perp}{5}\sin^2\theta + \frac{3\alpha_\parallel + 2\alpha_\perp}{5}\cos^2\theta \end{aligned} \tag{8.7}$$

where $\alpha_\parallel$ and $\alpha_\perp$ are parallel and perpendicular components of the total polarizability with respect to the quantization axis [184]. At the "magic angle" where $\cos^2\theta = 1/3$, or $\theta \approx 54.7°$, $\alpha_0 = \alpha_1$. Here, the differential ac polarizability between all rotational states with $m_N = 0$ vanishes. In general α_1 contains additional contributions due to mixing with the rotational states $|1, \pm 1\rangle$, but these states are detuned by more than 10 MHz from $|0\rangle$ at 1 kV/cm and so the effect is negligible.

To achieve state-insensitive trapping, we hold the molecules in the optical lattice alone and rotate the electric field to minimize the differential polarizability (Fig. 8.9a). At each calculated field angle, we measure the $|0\rangle \to |1\rangle$ transition frequency at three optical lattice intensities. The change in frequency $\Delta\nu$ as a function of intensity is the differential polarizability $\Delta\alpha/h = (\alpha_0 - \alpha_1)/h$ (Fig. 8.9b). Using $\alpha_\parallel$, $\alpha_\perp = h \cdot 120$, 20 kHz/(kW/cm^2) [167], we calculate $\Delta\alpha/h$ and find good agreement with the measured values. There is systematic uncertainty on both the lattice intensity and field angle, so in practice we work at the calculated angle of 54°, where we measure the minimum differential polarizability. For Ref. [66], which was written before these polarizability

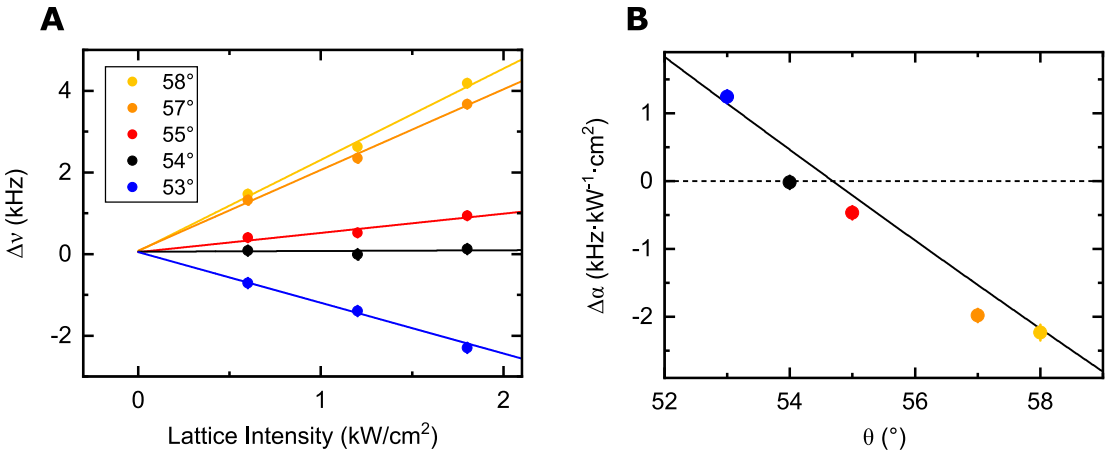

Figure 8.9: Locating the electric field "magic angle." **(a)** The $|0\rangle \rightarrow |1\rangle$ transition frequency vs. lattice intensity is measured at various electric field angles relative to the lattice polarization. **(b)** Polarizability vs. angle, compared with a theory prediction (solid black line, Refs. [167, 184])

measurements, we used a similar technique but only optimized the angle to within 3° of the true magic angle. At this angle, which we denote θ_m, $\Delta\alpha$ is predicted to be reduced by a factor of seven relative to 90°.

8.4.2 Measuring Single-Layer Coherence

We measure the Ramsey coherence of a single 2D layer with $\partial_y |\mathbf{E}| = 0$ at both $\theta = 90°$ and $\theta = \theta_m$. For both angles, the ODT polarization is set to the magic angle with respect to $\mathbf{E}$. Figure 8.10a shows the calculated optical potentials for states $|0\rangle$ and $|1\rangle$; at θ_m, the differential polarizability vanishes. Using a single layer removes possible systematics such as dipolar interactions between layers, stray electric field gradients along $\mathbf{y}$, and layer-to-layer optical trap intensity variation. To measure the coherence decay, we prepare a single layer of molecules, use a $\pi/2$ pulse to initialize all molecules on the layer in an equal superposition of $|0\rangle$ and $|1\rangle$, hold for a variable evolution time, apply a second $\pi/2$ pulse, and simultaneously measure the population in both states.

At short Ramsey evolution times t (Fig. 8.10b), we fit the fraction f of molecules in state $|0\rangle$ to the functional form

$$f(t) = \frac{1}{2} + \frac{e^{-t^2/\tau^2}}{2} \cos(2\pi\nu t + \phi) \tag{8.8}$$

where ν is the precession frequency, ϕ is a fixed phase, and τ is the coherence time. For t longer than about 600 μs, however, variation in $|\mathbf{E}|$ changes ν slightly between experimental runs. We therefore compute the contrast $\mathcal{C}(t)$ based on the observed variance of the rotational state populations: at a fixed t, we randomize the relative phase of the two Ramsey $\pi/2$ pulses, and measure f. We repeat this process between 10 and 20 times and calculate $\sigma_f(t)$, the standard deviation of f. $\sigma_f(t)$ decreases at large t as the molecules decohere. At $t \gg \tau$, $\sigma_f(t)$ is non-zero even in the absence of coherence because of imaging noise. Denoting these residual number fluctuations σ_0, the contrast is calculated by the expression

$$\mathcal{C}(t) = 2\sqrt{2}\sqrt{\sigma_f^2(t) - \sigma_0^2} \tag{8.9}$$

where the prefactor is the calculated standard deviation of f for $\mathcal{C} = 1$ (that is, $\mathcal{C}$ at $t = 0$), in the absence of imaging noise. We verify this factor by measuring $\mathcal{C}$ at $t = 21$ μs, much shorter than the decoherence time τ, and find $\mathcal{C} = 1.02(8)$. By fitting $\mathcal{C}(t)$ to the form e^{-t^2/τ^2}, we can extract τ (Fig. 8.10c).

For $\theta = 90°$, we measure $\tau = 310(30)$ μs (Fig. 8.10b, top). At $\theta = \theta_m$, little contrast decay is observed over 600 μs (Fig. 8.10, bottom). We measure $\tau = 1450(80)$ μs (Fig. 8.10c), a factor of five improvement over $\theta = 90°$ and exceeding the longest bulk coherence time previously observed for KRb [184]. Factors that may limit the maximum achieved coherence include any remaining differential ac polarizability, residual electric field gradients, and intralayer dipolar interactions. With ms-scale coherence times and realistic experimental parameters, KRb is predicted to dynamically generate spin-squeezed states in 2D [178].

8.4.3 Modeling Coherence Time

We perform a simple simulation to estimate the decoherence rate of Ramsey oscillations due to the differential polarizability between states $|0\rangle$ and $|1\rangle$. With $|\mathbf{E}| = 1$ kV/cm and $\theta = 90°$ (Fig. 8.10a, upper panel), the polarizabilities of $|0\rangle$ and $|1\rangle$ differ by approximately 20% at 1064 nm. Since the optical trap intensity varies over the molecule distribution, separated molecules undergo Ramsey precession at slightly different frequencies, causing dephasing.

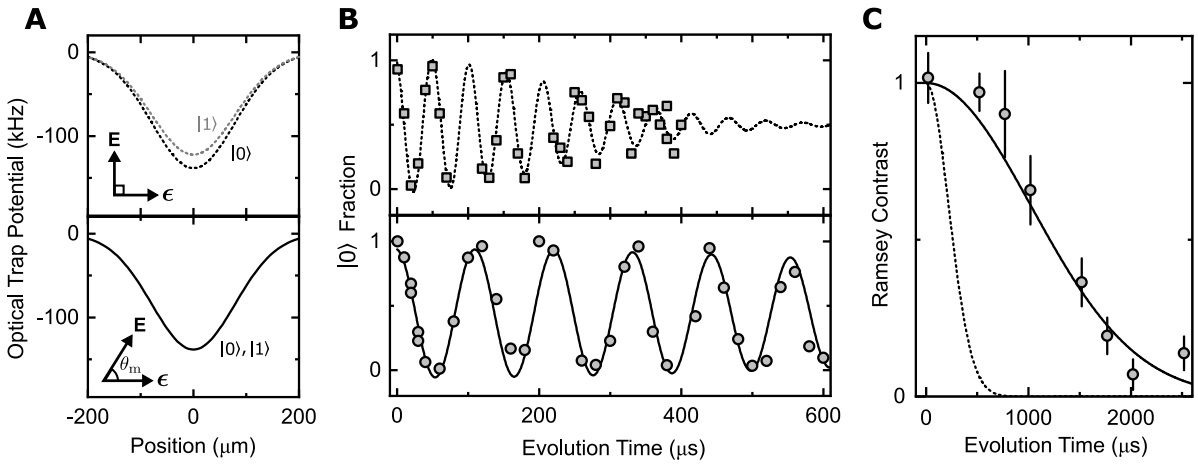

Figure 8.10: Increasing rotational coherence time by rotating **E**. **(a)** Calculated optical trap potentials for states $|0\rangle$ and $|1\rangle$ in the ODT and optical lattice. The differential polarizability between rotational states depends on the angle θ between **E** and the optical lattice polarization $\boldsymbol{\epsilon}$, and vanishes at $\theta_m \approx 54.7°$. **(b)** Ramsey oscillations of a single layer of molecules at $\theta = 90°$ (top, dashed line) and $\theta = \theta_m$ (bottom, solid line). **(c)** Contrast of Ramsey fringes at long evolution times. The coherence time at $\theta = \theta_m$ (points, solid line) is increased by a factor of 5 compared to $\theta = 90°$ (dashed line). Reproduced from Ref. [66].

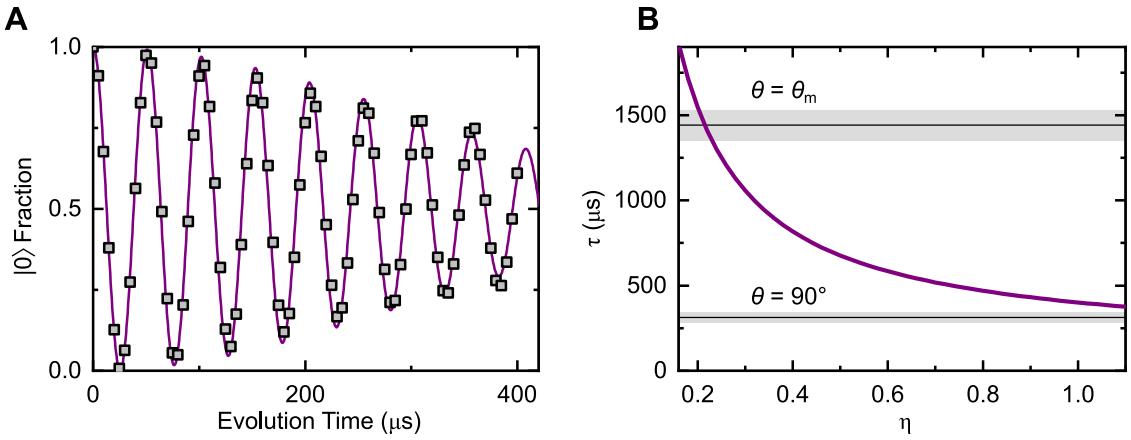

Figure 8.11: Simulating decoherence from differential polarizability. **(a)** Ramsey oscillations at $\eta = 1$ ($\theta = 90°$). The points are simulation results and the solid line is a fit to a Gaussian envelope. **(b)** Coherence time vs. differential polarizability. The shaded areas represent experimental results at $\theta = 90°$ and $\theta = \theta_m$. Reproduced from Ref. [66].

To simulate this effect, we initialize a 2D distribution of molecules using the temperature and radial trap frequencies corresponding to the experimental conditions. Each molecule is assigned a position-dependent frequency shift $\Delta\nu = \eta\,\Delta\alpha\,I(x,z)$, where $\Delta\alpha$ is the differential polarizability and $I(x,z)$ is the optical lattice intensity at the molecule position. η is a scaling factor on $\Delta\alpha$, accounting for changes in the polarizabilities as a function of the relative angle θ between the electric field and the optical lattice polarization: for example, at $\theta = 90°$, $\eta = 1$, while at $\theta = \theta_m$ (where the polarizabilities of both states match), $\eta \approx 0$. The total Ramsey oscillation signal, which models the experimental measurement, is obtained by summing the signal from each molecule. By fitting the decay envelope of the simulated signal to Eq. 8.8 (Fig. 8.11a), the effective decoherence rate can be extracted as a function of η (Fig. 8.11b).

For $\eta = 1$, the simulation predicts a decoherence time of 400 μs, compared to the measured value of 310(30) μs (Fig. 8.10b, upper panel). In general, the simulation results represent an upper bound on τ, since other mechanisms such as electric field gradients and molecule-molecule interactions may contribute to decoherence. Due to molecular motion during the evolution time, each molecule actually experiences a time-varying frequency shift, instead of the static shift simu-

lated here. However, since the maximum Ramsey evolution time in experiment (2.5 ms) is small compared to the period of oscillation in the optical trap (20 ms), we neglect this effect.

At θ_m we measure $\tau = 1450(80)$ μs (Fig. 8.10c), corresponding to $\eta \approx 0.2$ in the simulation (Fig. 8.11b), or a factor of five reduction in $\Delta\alpha$. By further reducing the differential polarizability, as shown in Fig. 8.9, τ was extended to 4.7(5) ms, corresponding to $\eta = 0.06$. τ is likely limited in part by gradients and interactions at long times.

For high-fidelity layer selection, it was essential to eliminate the tilt of the lattice with respect to the electric field gradient (Fig. 8.3). We vary the gradient $\partial_y|\mathbf{E}|$ and measure the Ramsey coherence time to quantify the frequency broadening due to the residual tilt angle. At gradients of $\partial_y|\mathbf{E}| = 0$, 2, and 6 kV/cm^2 the coherence time at $\theta = 90°$ is 310(30), 286(28), and 270(33) μs, respectively. The coherence time does not change substantially with the addition of a gradient, indicating that the broadening at the layer selection gradient is much smaller than the broadening from the differential polarizability.

8.5 Spin Exchange

The capability to prepare arbitrary layer configurations enables the realization of novel interacting systems. We study a system where the rate of chemical reactions on a single 2D layer can be controlled with the presence of adjacent layers by varying the strength of dipolar spin exchange interactions [191, 49]. The dynamics of molecules on multiple layers depends on a number of processes (Fig. 8.12). In a single layer, molecules undergo two-body chemical reactions according to the rate equation

$$\frac{dN}{dt} = -\beta N^2 \tag{8.10}$$

where N is the molecule number and β is the two-body rate coefficient. KRb is fermionic, so ultracold molecules in the same internal state undergo reactions in the p-wave channel, with rate coefficient β_p. Molecules in different rotational states are distinguishable and therefore react in the s-wave channel, with rate coefficient β_s, which is typically orders of magnitude higher than β_p due

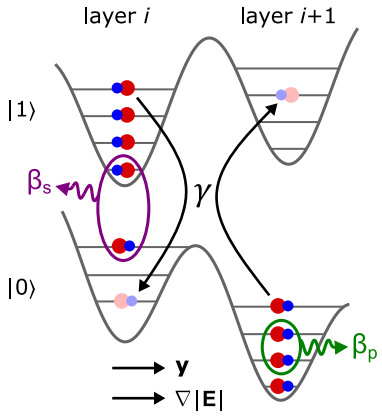

Figure 8.12: Interaction and loss dynamics for molecules in 2D. In a single layer, molecules in the same and in different rotational states undergo two-body loss with rate coefficients β_p and β_s, respectively. Molecules in different rotational states in adjacent layers may also exchange rotational states with rate γ, potentially changing harmonic oscillator modes during the exchange. Reproduced from Ref. [66].

to the absence of a centrifugal barrier [23, 96]. Typically, Eq. 8.10 is formulated in terms of the density since the two-body loss rate $\beta_p n$ scales with density and temperature rather than number. In terms of the temperature T, the rate coefficient $\beta_p \propto T$ (see Chapter 4 and Appendix B) and the density $n \propto T^{-d/2}$, where d is the dimensionality. This means that the product $\beta_p n$ is independent of temperature in 2D, and therefore the two-body loss can be expressed equivalently in terms of number and density since those quantities are proportional. β_s does not scale linearly with T, so the loss rate is not strictly constant with T, but β_s far exceeds the other rate coefficients β_s and γ and therefore the dynamics are not sensitive to its exact value.

Molecules in separate layers in different rotational states may also exchange rotational angular momenta via long-range dipolar interactions [49], changing harmonic oscillator modes in the process (represented by γ on Fig. 8.12). Spin exchange can only occur between states of opposite parity, meaning that $|0\rangle \rightarrow |1\rangle$ exchange is allowed and $|0\rangle \rightarrow |2\rangle$ exchange is forbidden at $|\mathbf{E}| = 0$. Applying an electric field induces rotational state mixing, but this effect only slightly weakens the above selection rules at $|\mathbf{E}| = 1$ kV/cm. Elastic collisions within layers can also redistribute molecules among harmonic modes, but the ratio of elastic to inelastic collisions is predicted to

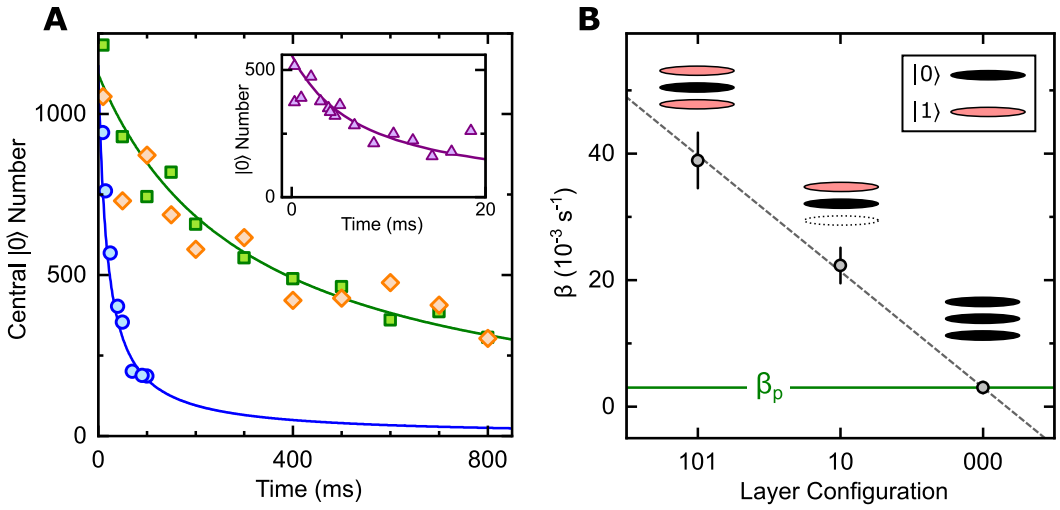

Figure 8.13: Rotational state and density dependence of spin exchange. **(a)** Central layer $|0\rangle$ molecule number vs. time for 000 (β_p, green squares), 101 (blue circles), and 202 (orange diamonds) trilayers. The solid lines are fits to the two-body loss rate equation. **Inset:** Loss for an equal mixture of molecules in states $|0\rangle$ and $|1\rangle$ (β_s). **(b)** Density dependence of spin exchange. β fit to the loss of $|0\rangle$ from layer configurations 000, 10, and 101 scales linearly with the number of adjacent layers containing $|1\rangle$. The solid green line indicates β_p. Reproduced from Ref. [66].

be smaller than one for these experimental parameters due to the small induced dipole moments [88, 63]. As such, we neglect this effect.

Spin exchange facilitates the mixing of rotational state populations between initially spin-polarized layers, causing molecules undergoing exchange to be rapidly lost with rate coefficient β_s [191]. In order to distinguish exchange from chemical reactions, we first measure the rate coefficients β_p and β_s at the temperature $T = 334(30)$ nK, with $\nabla |\mathbf{E}| = 0$. Throughout the following, we describe bilayer and trilayer configurations according to the rotational states present in layers containing molecules: for example, "202" refers to a central layer containing only molecules of state $|0\rangle$ with adjacent $|2\rangle$ layers above and below, and all other layers unoccupied. To extract β_p, which in general depends on rotational state due to variation in the intermolecular potentials [167], we prepare spin-polarized 000 (Fig. 8.13a, green squares), 111, and 222 trilayers and fit the number decay to the two-body loss rate equation. For $|0\rangle$ and $|1\rangle$, $\beta_p = 2.99(17) \times 10^{-3}$ s^{-1}. For $|2\rangle$, the loss rate is reduced to $\beta_p = 1.78(24) \times 10^{-3}$ s^{-1}. To extract β_s, we prepare a 111 trilayer,

and apply a $\pi/2$ pulse to form an equal superposition of $|0\rangle$ and $|1\rangle$, which decoheres completely within several milliseconds (Fig. 8.13a, inset). We measure $\beta_s = 2.0(3) \times 10^{-1}$ s^{-1}, nearly two orders of magnitude larger than β_p, as has been previously observed [96].

8.5.1 Density and State Dependence on Resonance

The interplay of exchange and loss is evident in layer configurations where multiple rotational states are present. In a 202 trilayer, where selection rules disallow spin exchange, the loss rate of $|0\rangle$ molecules from the central layer matches β_p (Fig. 8.13a, orange diamonds). By contrast, for a 101 trilayer, the effective two-body loss rate increases by more than a factor of 10 (Fig. 8.13a, blue circles). The spin exchange rate depends on the density of molecules in adjacent layers, which is analogous to the dependence of the chemical reaction rate on the local molecule density. We demonstrate this effect by preparing 000, 10, and 101 layer configurations, and fitting the decay of $|0\rangle$ molecules in the central layer to the two-body loss rate equation. The fit β scales linearly with the number of adjacent $|1\rangle$ layers (Fig. 8.13b). These results show the dependence of spin exchange on density and rotational state, and demonstrate tuning of the chemical reaction rate using experimental control of the layer configuration.

8.5.2 Detuning Dependence

To extract the spin exchange rate quantitatively, we describe N_i^σ, the molecule number in layer i and in rotational state $|\sigma\rangle$, by a set of coupled differential equations including the aforementioned loss and exchange processes:

$$\frac{dN_i^\sigma}{dt} = -\beta_p N_i^\sigma N_i^\sigma - \beta_s N_i^\sigma N_i^{\sigma'} + \gamma \sum_{k=i\pm1} \left(N_i^{\sigma'} N_k^\sigma - N_i^\sigma N_k^{\sigma'} \right) \tag{8.11}$$

$\sigma \neq \sigma'$ are the two rotational states participating in the dynamics. The first two terms represent intralayer two-body loss, with rates β_p and β_s for spin-polarized and spin-mixed molecules, respectively. The third term represents spin exchange, which depends on the molecule populations in different rotational states in adjacent layers, occurring with rate constant γ (Fig. 8.12). γ is an

effective parameter describing the spin exchange, averaged over all molecules and over the full duration of the measurement. We extract the parameter errors by the bootstrap method, equivalently to Eq. 7.10.

Since spin exchange is a resonant process, adding an energy offset between adjacent layers suppresses its rate. To probe the energy spectrum of exchange, we add a variable gradient $\partial_y |\mathbf{E}|$ (Fig. 8.12). The total change in electric potential energy when molecules in adjacent layers exchange rotational states is $h\Delta$ (Eq. 8.1), which is equivalent to the shift in microwave transition energy between adjacent layers (Fig. 8.8b). For states $|0\rangle$ and $|1\rangle$, $\Delta = 14$ kHz at $\partial_y |\mathbf{E}| = 6.4$ kV/cm, the gradient used for layer selection.

We measure the spin exchange rate γ as a function of Δ in 101 and 202 trilayer configurations (Fig. 8.14a), with $\theta = 90°$ and at $T = 334(30)$ nK. For 202, the measured γ is consistent with zero spin exchange and does not depend on Δ. For 101, however, the peak exchange rate is $\gamma = 7.0(6) \times 10^{-3}$ s^{-1}, more than two times β_p. Strikingly, γ remains non-zero for large Δ, with a Lorentzian fit to $\gamma(\Delta)$ having a full width at half maximum (FWHM) of 6.4(6) kHz. This energy scale vastly exceeds the dipolar interaction energy between two molecules: at a separation of 540 nm, the rate of spin exchange between molecules in $|0\rangle$ and $|1\rangle$ is only 100 Hz [49].

Thermal energy contributes to the broad linewidth. To compensate Δ and conserve energy during spin exchange, molecules must change harmonic modes (Fig. 8.12), the initial occupation of which is determined by the temperature. Qualitatively, this mechanism gives insight into the scaling of γ with T and Δ. At low temperatures, no spin exchange can occur when Δ greatly exceeds the thermal energy. For small Δ, however, the spin exchange rate is enhanced because of the high average occupation and strong dipolar coupling of low-lying harmonic modes. At high temperatures, the situation is reversed: high-lying modes are occupied, allowing exchange even at large Δ, but the peak exchange rate on resonance is suppressed. These effects suggest that increasing the temperature should broaden the spin exchange linewidth.

To quantify the temperature dependence, we repeat the measurement of $\gamma(\Delta)$ with a 101 trilayer at four temperatures between 370-650 nK (Fig. 8.14b). We set $\theta = \theta_m$ in order to eliminate

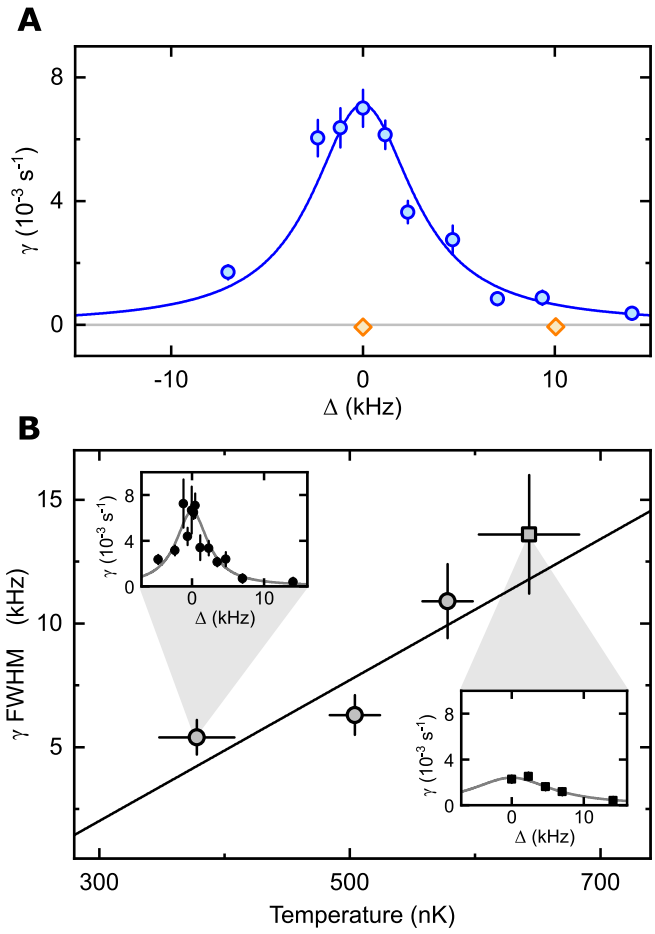

Figure 8.14: Dependence of spin exchange rate on interlayer detuning Δ, rotational state, and temperature. **(a)** Spin exchange rate vs. Δ, with $\theta = 90°$ and $T = 334(30)$ nK, for 101 (blue circles) and 202 (orange diamonds) trilayers. The solid line is a Lorentzian fit to extract the FWHM. The point displayed at $\Delta = 0$ kHz is the weighted average of measurements at $\Delta = 0$ and ± 0.12 kHz. **(b)** Temperature dependence of spin exchange linewidth, with $\theta = \theta_m$. The solid line is a linear fit for the temperature range shown. **Insets**: γ vs. Δ at $T = 378(30)$ nK (circles, upper) and $T = 643(40)$ nK (squares, lower). Reproduced from Ref. [66].

possible broadening due to varying trap potentials between rotational states (Fig. 8.11b). Here the strength of dipolar interactions between harmonic modes is slightly altered because the dipole moments are rotated relative to the plane of motion. At the lowest temperature we measure a FWHM of 5.4(7) kHz, only slightly narrower than at $\theta = 90°$. At the highest temperature, by contrast, the peak γ is reduced and the FWHM more than doubles to 13.6(2.4) kHz. We attribute this broadening to the thermal energy using a two-particle model, described in the next section. In addition to thermal energy, effects that may contribute to broadening include many-body interactions, where multiple molecules participate jointly in the spin exchange process, and intralayer dipole-dipole interactions. Both of these mechanisms should only weakly affect the temperature scaling due to the relatively low molecule density and small dipole moments at $|\mathbf{E}| =$ 1 kV/cm.

8.5.3 Theory Results

To provide physical insight into the temperature dependence, we use a simple two-particle model of molecules in adjacent layers interacting via dipolar spin exchange. This model was developed by Thomas Bilitewski and Ana Maria Rey, our theory collaborators at JILA. I summarize the results here, and the full model can be found in the Supplementary Materials to Ref. [66].

We use Fermi's Golden Rule (FGR) to estimate the spin exchange rate. For simplicity, we assume isotropic trap frequencies in the **x-z** directions, $\omega = \omega_x = \omega_y = 45$ Hz, and $\omega_y =$ 17 kHz. We also assume zero differential polarizability between $|0\rangle$ and $|1\rangle$. We label the two particles undergoing exchange 1 and 2. Before exchange, particle i occupies the harmonic mode $\vec{n}_i = (n_i^x, n_i^y, n_i^z)$, and after exchange it occupies the mode $\vec{m}_i = (m_i^x, m_i^y, m_i^z)$. The total change in energy during spin exchange ΔE, accounting for the detuning Δ (sorry for the notation, but there is a global shortage of deltas), is:

$$\frac{\Delta E}{h} = \Delta + \sum_{i=1,2} \omega\left(n_i^x - m_i^x\right) + \omega\left(n_i^z - m_i^z\right) + \omega_y\left(n_i^y - m_i^y\right) \tag{8.12}$$

The FGR then gives the following expression for the rate of particles leaving initial states $\vec{n}_i$:

$$k(\vec{n}_1, \vec{n}_2) = \pi \sum_{\vec{m}_1, \vec{m}_2} \left| V_{\vec{n}_1, \vec{n}_2}^{\vec{m}_1, \vec{m}_2} \right|^2 \delta(\Delta E) \tag{8.13}$$

where V is the matrix element of the dipolar interaction between the initial and final states. This is the sum over every possible energy-conserving exchange pathway. To extract the total exchange rate K, we weight by the thermal occupation of initial states, denoted ρ

$$K = \sum_{\vec{n}_1, \vec{n}_2} \rho(\vec{n}_1, \vec{n}_2) k(\vec{n}_1, \vec{n}_2) \tag{8.14}$$

To compare to the experimental parameter γ, we additionally sum over the layer above and below the central layer of interest, which have detunings Δ with opposite sign. This treatment makes several simplifying assumptions, including neglecting off-resonant couplings, intralayer interactions, and particle losses, but provides a qualitative picture of the scaling of spin exchange with temperature and Δ.

Figure 8.15 shows the FGR predictions for the FWHM of $\gamma(\Delta)$ and the peak spin exchange rate as a function of temperature, in comparison to experimental measurements. We calculate that the linewidths increase (Fig. 8.15a) and the peak rates decrease (Fig. 8.15b) with increasing temperature, in qualitative agreement with the trends observed in experiment. In the quantum degenerate regime, the linewidth is predicted to saturate near the Fermi energy E_F. This result indicates that the resonance width of the exchange is determined by the average energy of the molecules, and would presumably continue to narrow in a bosonic gas. The overall exchange rate is predicted to increase significantly at low temperatures, saturating above $\gamma = 100 \times 10^{-3}$ s^{-1}, more than 15 times the peak rates we observe at higher temperature.

In this chapter, we have demonstrated experimental control over spin exchange and chemical reactions in two-dimensional systems of ultracold molecules, enabled by subwavelength addressing of individual lattice layers. These results provide a general method for layer-resolved state preparation and imaging of polar molecules, facilitating the study of many-body phases and non-equilibrium dynamics in long-range interacting systems with reduced dimensionality.

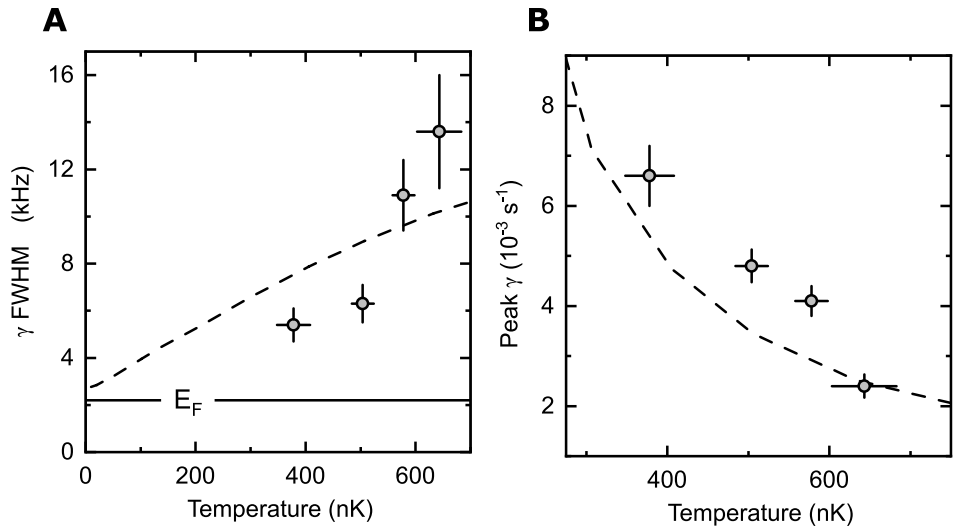

Figure 8.15: Two-body model of spin exchange. **(a)** FWHM of $\gamma(\Delta)$ as a function of temperature. The dashed line is the theory calculation, the points are experimental data, and the solid line represents the Fermi energy E_F. **(b)** Comparison of peak γ between experiment (points) and theory (line) as a function of temperature. Reproduced from Ref. [66].

Chapter 9

Conclusion

On any given day over the past four years, we ran the experiment about two hundred times and formed about twenty thousand KRb molecules each time. Accounting for weekends, holidays, conferences, and the lasers breaking, we worked about three hundred days per year. This means we made approximately five billion KRb molecules[1] during my time at JILA, which seems like a good place to conclude.

In this thesis, I have described our work on controlling losses and interactions between ultracold KRb molecules. We first produced degenerate molecules in 3D and studied the thermalization with the background atomic mixture. In 2D, though the molecules were initially formed above the Fermi temperature, we applied an electric field and induced dipolar interactions to enable evaporation to degeneracy. By tuning resonant interactions between rotational states, we suppressed reactive loss and realized a stable, polar molecular quantum gas. Finally, we used electric fields for microscopic control of the density and internal state. Our results represent progress towards using KRb to study open problems in many-body physics and towards realizing the incredible promise of ultracold molecules.

In the next section I outline several possible future experiments, in particular those enabled by our work. Included are the theoretical proposals Refs. [178] and [192], which we co-authored as "experimental consultants."

[1] 10^{-14} mol, for chemists.

9.1 Outlook

In Ref. [66], we demonstrated preparation of single 2D layers of molecules. Combined with the conditions of Ref. [63], we could produce isolated layers containing on the order of one thousand degenerate molecules. In these conditions, dipolar interactions between molecules are predicted to shift rotational transition energies by kHz [193]. Similarly to previous measurements on magnetic atoms [194], the interactions would depend on density, dipole orientation, electric field, and other parameters under experimental control. Resolving these shifts may involve dynamical decoupling, similar to that demonstrated in Fig. 3.11 for measuring electric field noise, to isolate the interaction-dependent frequency shift from contributions due to fluctuating electric field and differential polarizability. Preliminary results on the dipolar frequency shift are already arriving thanks to the efforts of the other KRb members.

Collective behaviors can emerge from dipolar interactions in 2D. Compared to particles localized in sites of an optical lattice, the distribution in energy of molecule-molecule interactions in a 2D harmonic trap is relatively narrow [178], particularly for $T < T_F$. If position-dependent shifts due to optical trap intensity are eliminated, as we demonstrated in Figs. 8.9 and 8.10, every particle would have a similar coupling to the other trapped particles and there would be little single-particle dephasing. Interactions should lead to enhanced Ramsey coherence due to "spin locking," extending far beyond the single-particle coherence time [195]. These conditions should also lead to dynamical generation of spin squeezed states, entangled states where the spin variance is decreased below the classical limit along one quadrature, providing metrological benefits [178]. Spin squeezing experiments would require careful measurement of particle number to establish that the spin noise is non-classical; the methods described in Chapter 5 to account for imaging noise and added variance due to STIRAP may be useful here for precise measurement of number fluctuations. Though spin squeezing is unlikely to lead to improved electric field sensing with KRb molecules, studies of fundamental physics with ultracold molecules could benefit from similar techniques.

Chapter 8, where we prepared controllable layer configurations of molecules, lists several

theory proposals involving paired states spanning lattice layers [179, 180, 181, 182]. A technical difficulty for realizing these proposals is the high temperature relative to the interaction strength; for instance, the peak interaction strength for layers separated by 532 nm is 100 Hz [49], compared to the Fermi temperature of $k_B T_F/h \approx 2$ kHz in 2D. One strategy for increasing the interaction strength is using shorter-wavelength light to generate the optical lattice, decreasing the interlayer spacing a and increasing the interactions as a^{-3}. Unfortunately, the excited energy levels of KRb are dense above our current wavelength of 1064 nm [196], so shorter wavelengths may lead to heating and loss. Reference [192] offers an alternative approach for generating bilayer systems within single lattice layers using optical fields or a combination of microwave fields and electric field gradients. Effective layer separations smaller than 100 nm could potentially be realized using these methods, generating interactions stronger than 10 kHz and much larger than the thermal energies.

The experiments described above could be realized at current temperatures and densities and represent promising future directions. Ultracold molecules offer many exciting challenges and opportunities, and it has been a pleasure to be a part of the KRb experiment. I am looking forward to seeing what the future holds, over the next five billion molecules and beyond.

Bibliography

[1] John L. Bohn, Ana Maria Rey, and Jun Ye. Cold molecules: Progress in quantum engineering of chemistry and quantum matter. Science, 357(6355):1002–1010, 2017.

[2] Lincoln D Carr, David DeMille, Roman V Krems, and Jun Ye. Cold and ultracold molecules: science, technology and applications. New Journal of Physics, 11(5):055049, May 2009.

[3] A. Micheli, G. K. Brennen, and P. Zoller. A toolbox for lattice-spin models with polar molecules. Nat. Phys., 2(5):341–347, 2006.

[4] M. A. Baranov, M. Dalmonte, G. Pupillo, and P. Zoller. Condensed matter theory of dipolar quantum gases. Chem. Rev., 112(9):5012–5061, 2012.

[5] M. S. Safronova, D. Budker, D. DeMille, Derek F. Jackson Kimball, A. Derevianko, and Charles W. Clark. Search for new physics with atoms and molecules. Rev. Mod. Phys., 90:025008, Jun 2018.

[6] S. F. Yelin, K. Kirby, and Robin Côté. Schemes for robust quantum computation with polar molecules. Phys. Rev. A, 74:050301, Nov 2006.

[7] Matthew T. Hummon, Mark Yeo, Benjamin K. Stuhl, Alejandra L. Collopy, Yong Xia, and Jun Ye. 2D magneto-optical trapping of diatomic molecules. Phys. Rev. Lett., 110:143001, Apr 2013.

[8] J. F. Barry, D. J. McCarron, E. B. Norrgard, M. H. Steinecker, and D. DeMille. Magneto-optical trapping of a diatomic molecule. Nature, 512(7514):286–289, Aug 2014.

[9] Loïc Anderegg, Benjamin L. Augenbraun, Yicheng Bao, Sean Burchesky, Lawrence W. Cheuk, Wolfgang Ketterle, and John M. Doyle. Laser cooling of optically trapped molecules. Nature Physics, 14(9):890–893, Sep 2018.

[10] Shiqian Ding, Yewei Wu, Ian A. Finneran, Justin J. Burau, and Jun Ye. Sub-Doppler cooling and compressed trapping of YO molecules at μK temperatures. Phys. Rev. X, 10:021049, Jun 2020.

[11] Nathaniel B Vilas, Christian Hallas, Loïc Anderegg, Paige Robichaud, Andrew Winnicki, Debayan Mitra, and John M Doyle. Magneto-optical trapping and sub-Doppler cooling of a polyatomic molecule. arXiv:2112.08349, 2021.

[12] Yewei Wu, Justin J. Burau, Kameron Mehling, Jun Ye, and Shiqian Ding. High phase-space density of laser-cooled molecules in an optical lattice. Phys. Rev. Lett., 127:263201, Dec 2021.

[13] Thorsten Köhler, Krzysztof Góral, and Paul S. Julienne. Production of cold molecules via magnetically tunable Feshbach resonances. Rev. Mod. Phys., 78:1311–1361, Dec 2006.

[14] K.-K. Ni, S. Ospelkaus, M. H. G. de Miranda, A. Pe'er, B. Neyenhuis, J. J. Zirbel, S. Kotochigova, P. S. Julienne, D. S. Jin, and J. Ye. A high phase-space-density gas of polar molecules. Science, 322(5899):231–235, 2008.

[15] Tetsu Takekoshi, Lukas Reichsöllner, Andreas Schindewolf, Jeremy M. Hutson, C. Ruth Le Sueur, Olivier Dulieu, Francesca Ferlaino, Rudolf Grimm, and Hanns-Christoph Nägerl. Ultracold dense samples of dipolar RbCs molecules in the rovibrational and hyperfine ground state. Phys. Rev. Lett., 113:205301, Nov 2014.

[16] Peter K. Molony, Philip D. Gregory, Zhonghua Ji, Bo Lu, Michael P. Köppinger, C. Ruth Le Sueur, Caroline L. Blackley, Jeremy M. Hutson, and Simon L. Cornish. Creation of ultracold $^{87}Rb^{133}Cs$ molecules in the rovibrational ground state. Phys. Rev. Lett., 113:255301, Dec 2014.

[17] Jee Woo Park, Sebastian A. Will, and Martin W. Zwierlein. Ultracold dipolar gas of fermionic $^{23}Na^{40}K$ molecules in their absolute ground state. Phys. Rev. Lett., 114:205302, May 2015.

[18] Mingyang Guo, Bing Zhu, Bo Lu, Xin Ye, Fudong Wang, Romain Vexiau, Nadia Bouloufa-Maafa, Goulven Quéméner, Olivier Dulieu, and Dajun Wang. Creation of an ultracold gas of ground-state dipolar $^{23}Na^{87}Rb$ molecules. Phys. Rev. Lett., 116:205303, May 2016.

[19] Timur M. Rvachov, Hyungmok Son, Ariel T. Sommer, Sepehr Ebadi, Juliana J. Park, Martin W. Zwierlein, Wolfgang Ketterle, and Alan O. Jamison. Long-lived ultracold molecules with electric and magnetic dipole moments. Phys. Rev. Lett., 119:143001, Oct 2017.

[20] Frauke Seeßelberg, Xin-Yu Luo, Ming Li, Roman Bause, Svetlana Kotochigova, Immanuel Bloch, and Christoph Gohle. Extending rotational coherence of interacting polar molecules in a spin-decoupled magic trap. Phys. Rev. Lett., 121:253401, Dec 2018.

[21] S. Ospelkaus, K.-K. Ni, D. Wang, M. H. G. de Miranda, B. Neyenhuis, G. Quéméner, P. S. Julienne, J. L. Bohn, D. S. Jin, and J. Ye. Quantum-state controlled chemical reactions of ultracold potassium-rubidium molecules. Science, 327(5967):853–857, 2010.

[22] Zbigniew Idziaszek and Paul S. Julienne. Universal rate constants for reactive collisions of ultracold molecules. Phys. Rev. Lett., 104:113202, Mar 2010.

[23] Zbigniew Idziaszek, Goulven Quéméner, John L. Bohn, and Paul S. Julienne. Simple quantum model of ultracold polar molecule collisions. Phys. Rev. A, 82:020703, Aug 2010.

[24] Jason N. Byrd, John A. Montgomery, and Robin Côté. Structure and thermochemistry of K_2Rb, KRb_2, and K_2Rb_2. Phys. Rev. A, 82:010502, Jul 2010.

[25] Piotr S. Żuchowski and Jeremy M. Hutson. Reactions of ultracold alkali-metal dimers. Phys. Rev. A, 81:060703, Jun 2010.

[26] M. Aymar and O. Dulieu. Calculation of accurate permanent dipole moments of the lowest $^{1,3}\sum$ states of heteronuclear alkali dimers using extended basis sets. The Journal of Chemical Physics, 122(20):204302, 2005.

[27] Kai K. Voges, Philipp Gersema, Mara Meyer zum Alten Borgloh, Torben A. Schulze, Torsten Hartmann, Alessandro Zenesini, and Silke Ospelkaus. Ultracold gas of bosonic ^{23}Na^{39}K ground-state molecules. Phys. Rev. Lett., 125:083401, Aug 2020.

[28] Lawrence W. Cheuk, Loïc Anderegg, Yicheng Bao, Sean Burchesky, Scarlett S. Yu, Wolfgang Ketterle, Kang-Kuen Ni, and John M. Doyle. Observation of collisions between two ultracold ground-state CaF molecules. Phys. Rev. Lett., 125:043401, Jul 2020.

[29] Xin Ye, Mingyang Guo, Maykel L. González-Martínez, Goulven Quéméner, and Dajun Wang. Collisions of ultracold ^{23}Na^{87}Rb molecules with controlled chemical reactivities. Science Advances, 4(1):eaaq0083, 2018.

[30] Michael Mayle, Goulven Quéméner, Brandon P. Ruzic, and John L. Bohn. Scattering of ultracold molecules in the highly resonant regime. Phys. Rev. A, 87:012709, Jan 2013.

[31] Philip D. Gregory, Matthew D. Frye, Jacob A. Blackmore, Elizabeth M. Bridge, Rahul Sawant, Jeremy M. Hutson, and Simon L. Cornish. Sticky collisions of ultracold RbCs molecules. Nature Communications, 10(1):3104, Jul 2019.

[32] Arthur Christianen, Martin W. Zwierlein, Gerrit C. Groenenboom, and Tijs Karman. Photoinduced two-body loss of ultracold molecules. Phys. Rev. Lett., 123:123402, Sep 2019.

[33] Arthur Christianen, Tijs Karman, and Gerrit C. Groenenboom. Quasiclassical method for calculating the density of states of ultracold collision complexes. Phys. Rev. A, 100:032708, Sep 2019.

[34] Philip D. Gregory, Jacob A. Blackmore, Sarah L. Bromley, and Simon L. Cornish. Loss of ultracold ^{87}Rb^{133}Cs molecules via optical excitation of long-lived two-body collision complexes. Phys. Rev. Lett., 124:163402, Apr 2020.

[35] Yu Liu, Ming-Guang Hu, Matthew A. Nichols, David D. Grimes, Tijs Karman, Hua Guo, and Kang-Kuen Ni. Photo-excitation of long-lived transient intermediates in ultracold reactions. Nature Physics, 16(11):1132–1136, Nov 2020.

[36] Roman Bause, Andreas Schindewolf, Renhao Tao, Marcel Duda, Xing-Yan Chen, Goulven Quéméner, Tijs Karman, Arthur Christianen, Immanuel Bloch, and Xin-Yu Luo. Collisions of ultracold molecules in bright and dark optical dipole traps. Phys. Rev. Research, 3:033013, Jul 2021.

[37] Philipp Gersema, Kai K. Voges, Mara Meyer zum Alten Borgloh, Leon Koch, Torsten Hartmann, Alessandro Zenesini, Silke Ospelkaus, Junyu Lin, Junyu He, and Dajun Wang. Probing photoinduced two-body loss of ultracold nonreactive bosonic ^{23}Na^{87}Rb and ^{23}Na^{39}K molecules. Phys. Rev. Lett., 127:163401, Oct 2021.

[38] Arthur Christianen, Gerrit C. Groenenboom, and Tijs Karman. Lossy quantum defect theory of ultracold molecular collisions. Phys. Rev. A, 104:043327, Oct 2021.

[39] M. H. Anderson, J. R. Ensher, M. R. Matthews, C. E. Wieman, and E. A. Cornell. Observation of Bose-Einstein condensation in a dilute atomic vapor. Science, 269(5221):198–201, 1995.

[40] B. DeMarco and D. S. Jin. Onset of Fermi degeneracy in a trapped atomic gas. Science, 285(5434):1703–1706, 1999.

[41] Stefano Giorgini, Lev P. Pitaevskii, and Sandro Stringari. Theory of ultracold atomic Fermi gases. Rev. Mod. Phys., 80:1215–1274, Oct 2008.

[42] B. DeMarco, J. L. Bohn, J. P. Burke, M. Holland, and D. S. Jin. Measurement of p-wave threshold law using evaporatively cooled fermionic atoms. Phys. Rev. Lett., 82:4208–4211, May 1999.

[43] Lindsay Sonderhouse, Christian Sanner, Ross B. Hutson, Akihisa Goban, Thomas Bilitewski, Lingfeng Yan, William R. Milner, Ana M. Rey, and Jun Ye. Thermodynamics of a deeply degenerate SU(N)-symmetric Fermi gas. Nature Physics, 16(12):1216–1221, Dec 2020.

[44] K. Aikawa, A. Frisch, M. Mark, S. Baier, R. Grimm, and F. Ferlaino. Reaching Fermi degeneracy via universal dipolar scattering. Phys. Rev. Lett., 112:010404, Jan 2014.

[45] Mingwu Lu, Nathaniel Q. Burdick, and Benjamin L. Lev. Quantum degenerate dipolar Fermi gas. Phys. Rev. Lett., 108:215301, May 2012.

[46] K.-K. Ni, S. Ospelkaus, D. Wang, G. Quéméner, B. Neyenhuis, M. H. G. de Miranda, J. L. Bohn, J. Ye, and D. S. Jin. Dipolar collisions of polar molecules in the quantum regime. Nature, 464(7293):1324–1328, Apr 2010.

[47] Mingyang Guo, Xin Ye, Junyu He, Maykel L. González-Martínez, Romain Vexiau, Goulven Quéméner, and Dajun Wang. Dipolar collisions of ultracold ground-state bosonic molecules. Phys. Rev. X, 8:041044, Dec 2018.

[48] M. H. G. de Miranda, A. Chotia, B. Neyenhuis, D. Wang, G. Quéméner, S. Ospelkaus, J. L. Bohn, J. Ye, and D. S. Jin. Controlling the quantum stereodynamics of ultracold bimolecular reactions. Nature Physics, 7(6):502–507, Jun 2011.

[49] Bo Yan, Steven A. Moses, Bryce Gadway, Jacob P. Covey, Kaden R. A. Hazzard, Ana Maria Rey, Deborah S. Jin, and Jun Ye. Observation of dipolar spin-exchange interactions with lattice-confined polar molecules. Nature, 501:521–525, 2013.

[50] Rudolf Grimm, Matthias Weidemüller, and Yurii B. Ovchinnikov. Optical dipole traps for neutral atoms. volume 42 of Advances In Atomic, Molecular, and Optical Physics, pages 95–170. Academic Press, 2000.

[51] Amodsen Chotia, Brian Neyenhuis, Steven A. Moses, Bo Yan, Jacob P. Covey, Michael Foss-Feig, Ana Maria Rey, Deborah S. Jin, and Jun Ye. Long-lived dipolar molecules and Feshbach molecules in a 3D optical lattice. Phys. Rev. Lett., 108:080405, Feb 2012.

[52] Alexey V. Gorshkov, Salvatore R. Manmana, Gang Chen, Jun Ye, Eugene Demler, Mikhail D. Lukin, and Ana Maria Rey. Tunable superfluidity and quantum magnetism with ultracold polar molecules. Phys. Rev. Lett., 107:115301, Sep 2011.

[53] Sergey V. Syzranov, Michael L. Wall, Victor Gurarie, and Ana Maria Rey. Spin-orbital dynamics in a system of polar molecules. Nat. Commun., 5:5391, 2014.

[54] M. P. Kwasigroch and N. R. Cooper. Bose-Einstein condensation and many-body localization of rotational excitations of polar molecules following a microwave pulse. Phys. Rev. A, 90:021605, Aug 2014.

[55] Jason S. Rosenberg, Lysander Christakis, Elmer Guardado-Sanchez, Zoe Z. Yan, and Waseem S. Bakr. Observation of the Hanbury Brown and Twiss effect with ultracold molecules. arXiv:2111.09426, 2021.

[56] Steven A. Moses, Jacob P. Covey, Matthew T. Miecnikowski, Bo Yan, Bryce Gadway, Jun Ye, and Deborah S. Jin. Creation of a low-entropy quantum gas of polar molecules in an optical lattice. Science, 350(6261):659–662, 2015.

[57] L. R. Liu, J. D. Hood, Y. Yu, J. T. Zhang, N. R. Hutzler, T. Rosenband, and K.-K. Ni. Building one molecule from a reservoir of two atoms. Science, 360(6391):900–903, 2018.

[58] William B. Cairncross, Jessie T. Zhang, Lewis R. B. Picard, Yichao Yu, Kenneth Wang, and Kang-Kuen Ni. Assembly of a rovibrational ground state molecule in an optical tweezer. Phys. Rev. Lett., 126:123402, Mar 2021.

[59] Loïc Anderegg, Lawrence W. Cheuk, Yicheng Bao, Sean Burchesky, Wolfgang Ketterle, Kang-Kuen Ni, and John M. Doyle. An optical tweezer array of ultracold molecules. Science, 365(6458):1156–1158, 2019.

[60] Jessie T Zhang, Lewis RB Picard, William B Cairncross, Kenneth Wang, Yichao Yu, Fang Fang, and Kang-Kuen Ni. An optical tweezer array of ground-state polar molecules. arXiv:2112.00991, 2021.

[61] Luigi De Marco, Giacomo Valtolina, Kyle Matsuda, William G. Tobias, Jacob P. Covey, and Jun Ye. A degenerate Fermi gas of polar molecules. Science, 363(6429):853–856, 2019.

[62] William G. Tobias, Kyle Matsuda, Giacomo Valtolina, Luigi De Marco, Jun-Ru Li, and Jun Ye. Thermalization and sub-Poissonian density fluctuations in a degenerate molecular Fermi gas. Phys. Rev. Lett., 124:033401, Jan 2020.

[63] Giacomo Valtolina, Kyle Matsuda, William G. Tobias, Jun-Ru Li, Luigi De Marco, and Jun Ye. Dipolar evaporation of reactive molecules to below the Fermi temperature. Nature, 588(7837):239–243, Dec 2020.

[64] Kyle Matsuda, Luigi De Marco, Jun-Ru Li, William G. Tobias, Giacomo Valtolina, Goulven Quéméner, and Jun Ye. Resonant collisional shielding of reactive molecules using electric fields. Science, 370(6522):1324–1327, 2020.

[65] Jun-Ru Li, William G. Tobias, Kyle Matsuda, Calder Miller, Giacomo Valtolina, Luigi De Marco, Reuben R. W. Wang, Lucas Lassablière, Goulven Quéméner, John L. Bohn, and Jun Ye. Tuning of dipolar interactions and evaporative cooling in a three-dimensional molecular quantum gas. Nature Physics, 17(10):1144–1148, Oct 2021.

[66] William G. Tobias, Kyle Matsuda, Jun-Ru Li, Calder Miller, Annette N. Carroll, Thomas Bilitewski, Ana Maria Rey, and Jun Ye. Reactions between layer-resolved molecules mediated by dipolar spin exchange. Science, 375(6586):1299–1303, 2022.

[67] J. Zirbel. Ultracold Fermionic Feshbach Molecules. PhD thesis, University of Colorado, Boulder, 2008.

[68] K.-K. Ni. A Quantum Gas of Polar Molecules. PhD thesis, University of Colorado, Boulder, 2009.

[69] Marcio de Miranda. Control of dipolar collisions in the quantum regime. PhD thesis, University of Colorado, Boulder, 2010.

[70] Brian Neyenhuis. Ultracold polar KRb molecules in optical lattices. PhD thesis, University of Colorado, Boulder, 2012.

[71] Steven Moses. A quantum gas of polar molecules in an optical lattice. PhD thesis, University of Colorado, Boulder, CO, Apr 2016.

[72] Jacob Covey. Enhanced optical and electric manipulation of a quantum gas of KRb molecules. PhD thesis, University of Colorado, Boulder, Jul 2017.

[73] J. J. Zirbel, K.-K. Ni, S. Ospelkaus, T. L. Nicholson, M. L. Olsen, P. S. Julienne, C. E. Wieman, J. Ye, and D. S. Jin. Heteronuclear molecules in an optical dipole trap. Phys. Rev. A, 78:013416, Jul 2008.

[74] Cheng Chin, Rudolf Grimm, Paul Julienne, and Eite Tiesinga. Feshbach resonances in ultracold gases. Rev. Mod. Phys., 82:1225–1286, Apr 2010.

[75] K. Bergmann, H. Theuer, and B. W. Shore. Coherent population transfer among quantum states of atoms and molecules. Rev. Mod. Phys., 70:1003–1025, Jul 1998.

[76] Rio Fernandes, D., Sievers, F., Kretzschmar, N., Wu, S., Salomon, C., and Chevy, F. Sub-Doppler laser cooling of fermionic ^{40}K atoms in three-dimensional gray optical molasses. EPL, 100(6):63001, 2012.

[77] A. Burchianti, G. Valtolina, J. A. Seman, E. Pace, M. De Pas, M. Inguscio, M. Zaccanti, and G. Roati. Efficient all-optical production of large ^{6}Li quantum gases using D_1 gray-molasses cooling. Phys. Rev. A, 90:043408, Oct 2014.

[78] Sara Rosi, Alessia Burchianti, Stefano Conclave, Devang S. Naik, Giacomo Roati, Chiara Fort, and Francesco Minardi. Λ-enhanced grey molasses on the D_2 transition of rubidium-87 atoms. Scientific Reports, 8(1):1301, Jan 2018.

[79] M Weidemüller, T Esslinger, M. A Ol'shanii, A Hemmerich, and T. W Hänsch. A novel scheme for efficient cooling below the photon recoil limit. Europhysics Letters (EPL), 27(2):109–114, Jul 1994.

[80] G Grynberg and J.-Y Courtois. Proposal for a magneto-optical lattice for trapping atoms in nearly-dark states. Europhysics Letters (EPL), 27(1):41–46, Jul 1994.

[81] J. Dalibard and C. Cohen-Tannoudji. Laser cooling below the Doppler limit by polarization gradients: simple theoretical models. J. Opt. Soc. Am. B, 6(11):2023–2045, Nov 1989.

[82] Andrew T. Grier, Igor Ferrier-Barbut, Benno S. Rem, Marion Delehaye, Lev Khaykovich, Frédéric Chevy, and Christophe Salomon. Λ-enhanced sub-Doppler cooling of lithium atoms in D_1 gray molasses. Phys. Rev. A, 87:063411, Jun 2013.

[83] A. Aspect, E. Arimondo, R. Kaiser, N. Vansteenkiste, and C. Cohen-Tannoudji. Laser cooling below the one-photon recoil energy by velocity-selective coherent population trapping. Phys. Rev. Lett., 61:826–829, Aug 1988.

[84] Daniel Steck. Rubidium 87 D line data. Available at `https://steck.us/alkalidata/rubidium87numbers.1.6.pdf` (Accessed 2022/01/11).

[85] Tobias Tiecke. Properties of potassium. Available at `https://www.tobiastiecke.nl/archive/PotassiumProperties.pdf` (Accessed 2022/01/11).

[86] Gary C. Bjorklund. Frequency-modulation spectroscopy: a new method for measuring weak absorptions and dispersions. Opt. Lett., 5(1):15–17, Jan 1980.

[87] S. Kotochigova, P. S. Julienne, and E. Tiesinga. Ab initio calculation of the KRb dipole moments. Phys. Rev. A, 68:022501, Aug 2003.

[88] Goulven Quéméner and John L. Bohn. Electric field suppression of ultracold confined chemical reactions. Phys. Rev. A, 81:060701, Jun 2010.

[89] R. W. P. Drever, J. L. Hall, F. V. Kowalski, J. Hough, G. M. Ford, A. J. Munley, and H. Ward. Laser phase and frequency stabilization using an optical resonator. Applied Physics B, 31(2):97–105, Jun 1983.

[90] Yunping Yang, Demetri Psaltis, Marc Luennemann, Dirk Berben, Ulrich Hartwig, and Karsten Buse. Photorefractive properties of lithium niobate crystals doped with manganese. J. Opt. Soc. Am. B, 20(7):1491–1502, Jul 2003.

[91] Walther Gerlach and Otto Stern. Das magnetische moment des silberatoms. Zeitschrift für Physik, 9(1):353–355, Dec 1922.

[92] T. Sleator, T. Pfau, V. Balykin, O. Carnal, and J. Mlynek. Experimental demonstration of the optical Stern-Gerlach effect. Phys. Rev. Lett., 68:1996–1999, Mar 1992.

[93] Simon Stellmer, Rudolf Grimm, and Florian Schreck. Detection and manipulation of nuclear spin states in fermionic strontium. Phys. Rev. A, 84:043611, Oct 2011.

[94] Beatriz Cordero, Verónica Gómez, Ana E. Platero-Prats, Marc Revés, Jorge Echeverría, Eduard Cremades, Flavia Barragán, and Santiago Alvarez. Covalent radii revisited. Dalton Trans., pages 2832–2838, 2008.

[95] J. Aldegunde, Ben A. Rivington, Piotr S. Żuchowski, and Jeremy M. Hutson. Hyperfine energy levels of alkali-metal dimers: Ground-state polar molecules in electric and magnetic fields. Phys. Rev. A, 78:033434, Sep 2008.

[96] S. Ospelkaus, K.-K. Ni, G. Quéméner, B. Neyenhuis, D. Wang, M. H. G. de Miranda, J. L. Bohn, J. Ye, and D. S. Jin. Controlling the hyperfine state of rovibronic ground-state polar molecules. Phys. Rev. Lett., 104:030402, Jan 2010.

[97] Jamie Shaw. External electric fields: A new tool for controlling ultracold polar molecules. Undergraduate Honors Thesis, University of Colorado, 2015.

[98] William G. Duff. Designing Electronic Systems for EMC: Grounding for the Control of EMI. SciTech Publishing, North Carolina, 2011.

[99] Analog Devices. The 20-bit dac is the easiest part of a 1-ppm-accurate precision voltage source. Available at `https://www.analog.com/en/analog-dialogue/articles/20-bit-dac-and-accurate-precision-voltage-source.html` (Accessed 2022/01/27).

[100] Jonas Bylander, Simon Gustavsson, Fei Yan, Fumiki Yoshihara, Khalil Harrabi, George Fitch, David G. Cory, Yasunobu Nakamura, Jaw-Shen Tsai, and William D. Oliver. Noise spectroscopy through dynamical decoupling with a superconducting flux qubit. Nature Physics, 7(7):565–570, Jul 2011.

[101] M. Bishof, X. Zhang, M. J. Martin, and Jun Ye. Optical spectrum analyzer with quantum-limited noise floor. Phys. Rev. Lett., 111:093604, Aug 2013.

[102] M. Martin. Quantum Metrology and Many-Body Physics: Pushing the Frontier of the Optical Lattice Clock. PhD thesis, University of Colorado, Boulder, CO 80309-0440, Apr 2013.

[103] E. L. Hahn. Spin echoes. Phys. Rev., 80:580–594, Nov 1950.

[104] K. Aikawa, S. Baier, A. Frisch, M. Mark, C. Ravensbergen, and F. Ferlaino. Observation of Fermi surface deformation in a dipolar quantum gas. Science, 345(6203):1484–1487, 2014.

[105] Bo Liu, Xiaopeng Li, Lan Yin, and W. Vincent Liu. Weyl superfluidity in a three-dimensional dipolar Fermi gas. Phys. Rev. Lett., 114:045302, Jan 2015.

[106] Goulven Quéméner, John L. Bohn, Alexander Petrov, and Svetlana Kotochigova. Universalities in ultracold reactions of alkali-metal polar molecules. Phys. Rev. A, 84:062703, Dec 2011.

[107] S. Truppe, H. J. Williams, M. Hambach, L. Caldwell, N. J. Fitch, E. A. Hinds, B. E. Sauer, and M. R. Tarbutt. Molecules cooled below the Doppler limit. Nature Physics, 13(12):1173–1176, Dec 2017.

[108] Hyungmok Son, Juliana J. Park, Wolfgang Ketterle, and Alan O. Jamison. Collisional cooling of ultracold molecules. Nature, 580(7802):197–200, Apr 2020.

[109] Tyler D. Cumby, Ruth A. Shewmon, Ming-Guang Hu, John D. Perreault, and Deborah S. Jin. Feshbach-molecule formation in a Bose-Fermi mixture. Phys. Rev. A, 87:012703, Jan 2013.

[110] Jacob P. Covey, Steven A. Moses, Martin Gärttner, Arghavan Safavi-Naini, Matthew T. Miecnikowski, Zhengkun Fu, Johannes Schachenmayer, Paul S. Julienne, Ana Maria Rey, Deborah S. Jin, and Jun Ye. Doublon dynamics and polar molecule production in an optical lattice. Nature Communications, 7(1):11279, Apr 2016.

[111] Lukas Reichsöllner, Andreas Schindewolf, Tetsu Takekoshi, Rudolf Grimm, and Hanns-Christoph Nägerl. Quantum engineering of a low-entropy gas of heteronuclear bosonic molecules in an optical lattice. Phys. Rev. Lett., 118:073201, Feb 2017.

[112] S. B. Papp and C. E. Wieman. Observation of heteronuclear Feshbach molecules from a ^{85}Rb $-^{87}$ Rb gas. Phys. Rev. Lett., 97:180404, Oct 2006.

[113] Marcel Duda, Xing-Yan Chen, Andreas Schindewolf, Roman Bause, Jonas von Milczewski, Richard Schmidt, Immanuel Bloch, and Xin-Yu Luo. Transition from a polaronic condensate to a degenerate Fermi gas of heteronuclear molecules. arXiv:2111.04301, 2021.

[114] J. J. Zirbel, K.-K. Ni, S. Ospelkaus, J. P. D'Incao, C. E. Wieman, J. Ye, and D. S. Jin. Collisional stability of fermionic Feshbach molecules. Phys. Rev. Lett., 100:143201, Apr 2008.

[115] Ruth S. Bloom, Ming-Guang Hu, Tyler D. Cumby, and Deborah S. Jin. Tests of universal three-body physics in an ultracold Bose-Fermi mixture. Phys. Rev. Lett., 111:105301, Sep 2013.

[116] Wolfgang Ketterle and Martin W. Zwierlein. Making, probing and understanding ultracold Fermi gases. Ultracold Fermi Gases, Proceedings of the International School of Physics "Enrico Fermi", June 2006.

[117] Andrew G. Truscott, Kevin E. Strecker, William I. McAlexander, Guthrie B. Partridge, and Randall G. Hulet. Observation of Fermi pressure in a gas of trapped atoms. Science, 291(5513):2570–2572, 2001.

[118] Markus Greiner, Cindy A. Regal, and Deborah S. Jin. Emergence of a molecular Bose-Einstein condensate from a Fermi gas. Nature, 426(6966):537–540, 2003.

[119] C. A. Regal, M. Greiner, and D. S. Jin. Lifetime of molecule-atom mixtures near a Feshbach resonance in ^{40}K. Phys. Rev. Lett., 92:083201, Feb 2004.

[120] S. Jochim, M. Bartenstein, A. Altmeyer, G. Hendl, C. Chin, J. Hecker Denschlag, and R. Grimm. Pure gas of optically trapped molecules created from fermionic atoms. Phys. Rev. Lett., 91:240402, Dec 2003.

[121] M. W. Zwierlein, C. A. Stan, C. H. Schunck, S. M. F. Raupach, A. J. Kerman, and W. Ketterle. Condensation of pairs of fermionic atoms near a Feshbach resonance. Phys. Rev. Lett., 92:120403, Mar 2004.

[122] M. Jag, M. Cetina, R. S. Lous, R. Grimm, J. Levinsen, and D. S. Petrov. Lifetime of Feshbach dimers in a Fermi-Fermi mixture of ^{6}Li and ^{40}K. Phys. Rev. A, 94:062706, Dec 2016.

[123] Jacob Johansen, B. J. DeSalvo, Krutik Patel, and Cheng Chin. Testing universality of Efimov physics across broad and narrow Feshbach resonances. Nat. Phys., 13:731, 2017.

[124] G. Ferrari, M. Inguscio, W. Jastrzebski, G. Modugno, G. Roati, and A. Simoni. Collisional properties of ultracold K-Rb mixtures. Phys. Rev. Lett., 89:053202, Jul 2002.

[125] F. Ferlaino, R. J. Brecha, P. Hannaford, F. Riboli, G. Roati, G. Modugno, and M. Inguscio. Dipolar oscillations in a quantum degenerate Fermi-Bose atomic mixture. Journal of Optics B: Quantum and Semiclassical Optics, 5(2):S3–S8, Apr 2003.

[126] D. S. Petrov. Three-body problem in Fermi gases with short-range interparticle interaction. Phys. Rev. A, 67:010703, Jan 2003.

[127] K. Aikawa, A. Frisch, M. Mark, S. Baier, R. Grimm, J. L. Bohn, D. S. Jin, G. M. Bruun, and F. Ferlaino. Anisotropic relaxation dynamics in a dipolar Fermi gas driven out of equilibrium. Phys. Rev. Lett., 113:263201, Dec 2014.

[128] B. DeMarco, S. B. Papp, and D. S. Jin. Pauli blocking of collisions in a quantum degenerate atomic Fermi gas. Phys. Rev. Lett., 86:5409–5412, Jun 2001.

[129] Christian Sanner, Edward J. Su, Aviv Keshet, Ralf Gommers, Yong-il Shin, Wujie Huang, and Wolfgang Ketterle. Suppression of density fluctuations in a quantum degenerate Fermi gas. Phys. Rev. Lett., 105:040402, Jul 2010.

[130] Torben Müller, Bruno Zimmermann, Jakob Meineke, Jean-Philippe Brantut, Tilman Esslinger, and Henning Moritz. Local observation of antibunching in a trapped Fermi gas. Phys. Rev. Lett., 105:040401, Jul 2010.

[131] Mingyuan He, Chenwei Lv, Hai-Qing Lin, and Qi Zhou. Universal relations for ultracold reactive molecules. Science Advances, 6(51):eabd4699, 2020.

[132] Peiru He, Thomas Bilitewski, Chris H. Greene, and Ana Maria Rey. Exploring chemical reactions in a quantum degenerate gas of polar molecules via complex formation. Phys. Rev. A, 102:063322, Dec 2020.

[133] Andreas Schindewolf, Roman Bause, Xing-Yan Chen, Marcel Duda, Tijs Karman, Immanuel Bloch, and Xin-Yu Luo. Evaporation of microwave-shielded polar molecules to quantum degeneracy. arXiv:2201.05143, 2022.

[134] J. Esteve, J.-B. Trebbia, T. Schumm, A. Aspect, C. I. Westbrook, and I. Bouchoule. Observations of density fluctuations in an elongated Bose gas: Ideal gas and quasicondensate regimes. Phys. Rev. Lett., 96:130403, Apr 2006.

[135] Nathan Gemelke, Xibo Zhang, Chen-Lung Hung, and Cheng Chin. In situ observation of incompressible Mott-insulating domains in ultracold atomic gases. Nature, 460(7258):995–998, 2009.

[136] A. Amico, F. Scazza, G. Valtolina, P. E. S. Tavares, W. Ketterle, M. Inguscio, G. Roati, and M. Zaccanti. Time-resolved observation of competing attractive and repulsive short-range correlations in strongly interacting Fermi gases. Phys. Rev. Lett., 121:253602, Dec 2018.

[137] Ahmed Omran, Martin Boll, Timon A. Hilker, Katharina Kleinlein, Guillaume Salomon, Immanuel Bloch, and Christian Gross. Microscopic observation of Pauli blocking in degenerate fermionic lattice gases. Phys. Rev. Lett., 115:263001, Dec 2015.

[138] Christian Sanner. Fluctuations in Quantum Degenerate Fermi Gases. PhD thesis, MIT, Cambridge, Dec 2012.

[139] Torben Müller. Microscopic probing and manipulation of ultracold fermions. PhD thesis, ETH Zurich, Zurich, 2011.

[140] Jan Jakob Meineke. Fluctuations and correlations in ultracold Fermi gases. PhD thesis, ETH Zurich, Zurich, 2011.

[141] Klaus Hueck, Niclas Luick, Lennart Sobirey, Jonas Siegl, Thomas Lompe, Henning Moritz, Logan W. Clark, and Cheng Chin. Calibrating high intensity absorption imaging of ultracold atoms. Opt. Express, 25(8):8670–8679, Apr 2017.

[142] G. Reinaudi, T. Lahaye, Z. Wang, and D. Guéry-Odelin. Strong saturation absorption imaging of dense clouds of ultracold atoms. Opt. Lett., 32(21):3143–3145, Nov 2007.

[143] T. Mukaiyama, J. R. Abo-Shaeer, K. Xu, J. K. Chin, and W. Ketterle. Dissociation and decay of ultracold sodium molecules. Phys. Rev. Lett., 92:180402, May 2004.

[144] Goulven Quéméner and John L. Bohn. Dynamics of ultracold molecules in confined geometry and electric field. Phys. Rev. A, 83:012705, Jan 2011.

[145] Andrea Micheli, Zbigniew Idziaszek, Guido Pupillo, Mikhail A. Baranov, Peter Zoller, and Paul S. Julienne. Universal rates for reactive ultracold polar molecules in reduced dimensions. Phys. Rev. Lett., 105:073202, Aug 2010.

[146] Bihui Zhu, Goulven Quéméner, Ana M. Rey, and Murray J. Holland. Evaporative cooling of reactive polar molecules confined in a two-dimensional geometry. Phys. Rev. A, 88:063405, Dec 2013.

[147] I. Shvarchuck, Ch. Buggle, D. S. Petrov, K. Dieckmann, M. Zielonkowski, M. Kemmann, T. G. Tiecke, W. von Klitzing, G. V. Shlyapnikov, and J. T. M. Walraven. Bose-Einstein condensation into nonequilibrium states studied by condensate focusing. Phys. Rev. Lett., 89:270404, Dec 2002.

[148] P. A. Murthy, D. Kedar, T. Lompe, M. Neidig, M. G. Ries, A. N. Wenz, G. Zürn, and S. Jochim. Matter-wave Fourier optics with a strongly interacting two-dimensional Fermi gas. Phys. Rev. A, 90:043611, Oct 2014.

[149] Klaus Hueck, Niclas Luick, Lennart Sobirey, Jonas Siegl, Thomas Lompe, and Henning Moritz. Two-dimensional homogeneous Fermi gases. Phys. Rev. Lett., 120:060402, Feb 2018.

[150] Svetlana Kotochigova. Dispersion interactions and reactive collisions of ultracold polar molecules. New Journal of Physics, 12(7):073041, jul 2010.

[151] Goulven Quéméner and John L. Bohn. Strong dependence of ultracold chemical rates on electric dipole moments. Phys. Rev. A, 81:022702, Feb 2010.

[152] Mehrtash Babadi and Eugene Demler. Collective excitations of quasi-two-dimensional trapped dipolar fermions: Transition from collisionless to hydrodynamic regime. Phys. Rev. A, 86:063638, Dec 2012.

[153] Alexander V. Avdeenkov, Masatoshi Kajita, and John L. Bohn. Suppression of inelastic collisions of polar $^1\Sigma$ state molecules in an electrostatic field. Phys. Rev. A, 73:022707, Feb 2006.

[154] Gaoren Wang and Goulven Quéméner. Tuning ultracold collisions of excited rotational dipolar molecules. New J. Phys., 17(3):035015, mar 2015.

[155] Vladimir Veljić, Antun Balaž, and Axel Pelster. Time-of-flight expansion of trapped dipolar Fermi gases: From the collisionless to the hydrodynamic regime. Phys. Rev. A, 95:053635, May 2017.

[156] Benjamin M. Fregoso and Eduardo Fradkin. Ferronematic ground state of the dilute dipolar Fermi gas. Phys. Rev. Lett., 103:205301, Nov 2009.

[157] Loïc Anderegg, Sean Burchesky, Yicheng Bao, Scarlett S. Yu, Tijs Karman, Eunmi Chae, Kang-Kuen Ni, Wolfgang Ketterle, and John M. Doyle. Observation of microwave shielding of ultracold molecules. Science, 373(6556):779–782, 2021.

[158] Tijs Karman and Jeremy M. Hutson. Microwave shielding of ultracold polar molecules. Phys. Rev. Lett., 121:163401, Oct 2018.

[159] Goulven Quéméner and John L. Bohn. Shielding $^2\Sigma$ ultracold dipolar molecular collisions with electric fields. Phys. Rev. A, 93:012704, Jan 2016.

[160] Maykel L. González-Martínez, John L. Bohn, and Goulven Quéméner. Adimensional theory of shielding in ultracold collisions of dipolar rotors. Phys. Rev. A, 96:032718, Sep 2017.

[161] M. L. Olsen, J. D. Perreault, T. D. Cumby, and D. S. Jin. Coherent atom-molecule oscillations in a Bose-Fermi mixture. Phys. Rev. A, 80:030701, Sep 2009.

[162] Sylvain Ravets, Henning Labuhn, Daniel Barredo, Lucas Béguin, Thierry Lahaye, and Antoine Browaeys. Coherent dipole–dipole coupling between two single Rydberg atoms at an electrically-tuned Förster resonance. Nature Physics, 10(12):914–917, Dec 2014.

[163] J L Bohn, M Cavagnero, and C Ticknor. Quasi-universal dipolar scattering in cold and ultracold gases. New Journal of Physics, 11(5):055039, may 2009.

[164] C. R. Monroe, E. A. Cornell, C. A. Sackett, C. J. Myatt, and C. E. Wieman. Measurement of Cs-Cs elastic scattering at T = 30 μk. Phys. Rev. Lett., 70:414–417, Jan 1993.

[165] Reuben R. W. Wang and John L. Bohn. Anisotropic thermalization of dilute dipolar gases. Phys. Rev. A, 103:063320, Jun 2021.

[166] Reuben R. W. Wang, Andrew G. Sykes, and John L. Bohn. Linear response of a periodically driven thermal dipolar gas. Phys. Rev. A, 102:033336, Sep 2020.

[167] Svetlana Kotochigova and David DeMille. Electric-field-dependent dynamic polarizability and state-insensitive conditions for optical trapping of diatomic polar molecules. Phys. Rev. A, 82:063421, Dec 2010.

[168] Michał Karski, Leonid Förster, Jai-Min Choi, Andreas Steffen, Noomen Belmechri, Wolfgang Alt, Dieter Meschede, and Artur Widera. Imprinting patterns of neutral atoms in an optical lattice using magnetic resonance techniques. New J. Phys., 12(6):065027, jun 2010.

[169] Jacob F. Sherson, Christof Weitenberg, Manuel Endres, Marc Cheneau, Immanuel Bloch, and Stefan Kuhr. Single-atom-resolved fluorescence imaging of an atomic Mott insulator. Nature, 467(7311):68–72, Sep 2010.

[170] G. J. A. Edge, R. Anderson, D. Jervis, D. C. McKay, R. Day, S. Trotzky, and J. H. Thywissen. Imaging and addressing of individual fermionic atoms in an optical lattice. Phys. Rev. A, 92:063406, Dec 2015.

[171] N. Y. Yao, A. V. Gorshkov, C. R. Laumann, A. M. Läuchli, J. Ye, and M. D. Lukin. Realizing fractional Chern insulators in dipolar spin systems. Phys. Rev. Lett., 110:185302, Apr 2013.

[172] Alexey V. Gorshkov, Salvatore R. Manmana, Gang Chen, Eugene Demler, Mikhail D. Lukin, and Ana Maria Rey. Quantum magnetism with polar alkali-metal dimers. Phys. Rev. A, 84:033619, Sep 2011.

[173] Salvatore R. Manmana, E. M. Stoudenmire, Kaden R. A. Hazzard, Ana Maria Rey, and Alexey V. Gorshkov. Topological phases in ultracold polar-molecule quantum magnets. Phys. Rev. B, 87:081106, Feb 2013.

[174] N. Y. Yao, M. P. Zaletel, D. M. Stamper-Kurn, and A. Vishwanath. A quantum dipolar spin liquid. Nat. Phys., 14(4):405–410, 2018.

[175] D. Peter, S. Müller, S. Wessel, and H. P. Büchler. Anomalous behavior of spin systems with dipolar interactions. Phys. Rev. Lett., 109:025303, Jul 2012.

[176] N. R. Cooper and G. V. Shlyapnikov. Stable topological superfluid phase of ultracold polar fermionic molecules. Phys. Rev. Lett., 103:155302, Oct 2009.

[177] J. Levinsen, N. R. Cooper, and G. V. Shlyapnikov. Topological $p_x + ip_y$ superfluid phase of fermionic polar molecules. Phys. Rev. A, 84:013603, Jul 2011.

[178] Thomas Bilitewski, Luigi De Marco, Jun-Ru Li, Kyle Matsuda, William G. Tobias, Giacomo Valtolina, Jun Ye, and Ana Maria Rey. Dynamical generation of spin squeezing in ultracold dipolar molecules. Phys. Rev. Lett., 126:113401, Mar 2021.

[179] Daw-Wei Wang, Mikhail D. Lukin, and Eugene Demler. Quantum fluids of self-assembled chains of polar molecules. Phys. Rev. Lett., 97:180413, Nov 2006.

[180] Andrew C. Potter, Erez Berg, Daw-Wei Wang, Bertrand I. Halperin, and Eugene Demler. Superfluidity and dimerization in a multilayered system of fermionic polar molecules. Phys. Rev. Lett., 105:220406, Nov 2010.

[181] A. Pikovski, M. Klawunn, G. V. Shlyapnikov, and L. Santos. Interlayer superfluidity in bilayer systems of fermionic polar molecules. Phys. Rev. Lett., 105:215302, Nov 2010.

[182] N. T. Zinner, B. Wunsch, D. Pekker, and D.-W. Wang. BCS-BEC crossover in bilayers of cold fermionic polar molecules. Phys. Rev. A, 85:013603, Jan 2012.

[183] Zhendong Zhang, Liangchao Chen, Kai-Xuan Yao, and Cheng Chin. Transition from an atomic to a molecular Bose–Einstein condensate. Nature, 592(7856):708–711, Apr 2021.

[184] B. Neyenhuis, B. Yan, S. A. Moses, J. P. Covey, A. Chotia, A. Petrov, S. Kotochigova, J. Ye, and D. S. Jin. Anisotropic polarizability of ultracold polar ^{40}K^{87}Rb molecules. Phys. Rev. Lett., 109:230403, Dec 2012.

[185] M.-G. Hu, Y. Liu, D. D. Grimes, Y.-W. Lin, A. H. Gheorghe, R. Vexiau, N. Bouloufa-Maafa, O. Dulieu, T. Rosenband, and K.-K. Ni. Direct observation of bimolecular reactions of ultracold KRb molecules. Science, 366(6469):1111–1115, 2019.

[186] A. Frisch, M. Mark, K. Aikawa, S. Baier, R. Grimm, A. Petrov, S. Kotochigova, G. Quéméner, M. Lepers, O. Dulieu, and F. Ferlaino. Ultracold dipolar molecules composed of strongly magnetic atoms. Phys. Rev. Lett., 115:203201, Nov 2015.

[187] Phillip L. Gould, George A. Ruff, and David E. Pritchard. Diffraction of atoms by light: The near-resonant Kapitza-Dirac effect. Phys. Rev. Lett., 56:827–830, Feb 1986.

[188] Waseem S. Bakr, Jonathon I. Gillen, Amy Peng, Simon Fölling, and Markus Greiner. A quantum gas microscope for detecting single atoms in a Hubbard-regime optical lattice. Nature, 462(7269):74–77, Nov 2009.

[189] Mickey McDonald, Jonathan Trisnadi, Kai-Xuan Yao, and Cheng Chin. Superresolution microscopy of cold atoms in an optical lattice. Phys. Rev. X, 9:021001, Apr 2019.

[190] S. Subhankar, Y. Wang, T-C. Tsui, S. L. Rolston, and J. V. Porto. Nanoscale atomic density microscopy. Phys. Rev. X, 9:021002, Apr 2019.

[191] A. Pikovski, M. Klawunn, A. Recati, and L. Santos. Nonlocal state swapping of polar molecules in bilayers. Phys. Rev. A, 84:061605, Dec 2011.

[192] Andreas Kruckenhauser, Lukas M. Sieberer, Luigi De Marco, Jun-Ru Li, Kyle Matsuda, William G. Tobias, Giacomo Valtolina, Jun Ye, Ana Maria Rey, Mikhail A. Baranov, and Peter Zoller. Quantum many-body physics with ultracold polar molecules: Nanostructured potential barriers and interactions. Phys. Rev. A, 102:023320, Aug 2020.

[193] Kaden R. A. Hazzard, Alexey V. Gorshkov, and Ana Maria Rey. Spectroscopy of dipolar fermions in layered two-dimensional and three-dimensional lattices. Phys. Rev. A, 84:033608, Sep 2011.

[194] Y.-Q. Zou, B. Bakkali-Hassani, C. Maury, É. Le Cerf, S. Nascimbene, J. Dalibard, and J. Beugnon. Magnetic dipolar interaction between hyperfine clock states in a planar alkali Bose gas. Phys. Rev. Lett., 125:233604, Dec 2020.

[195] C. Deutsch, F. Ramirez-Martinez, C. Lacroûte, F. Reinhard, T. Schneider, J. N. Fuchs, F. Piéchon, F. Laloë, J. Reichel, and P. Rosenbusch. Spin self-rephasing and very long coherence times in a trapped atomic ensemble. Phys. Rev. Lett., 105:020401, Jul 2010.

[196] R. Vexiau, D. Borsalino, M. Lepers, A. Orbán, M. Aymar, O. Dulieu, and N. Bouloufa-Maafa. Dynamic dipole polarizabilities of heteronuclear alkali dimers: optical response, trapping and control of ultracold molecules. International Reviews in Physical Chemistry, 36(4):709–750, 2017.

[197] C. D. Motchenbacher and J. A. Connelly. Low-Noise Electronic System Design. Wiley-Interscience, New Jersey, 1993.

[198] Texas Instruments. Application note: Noise analysis in operational amplifier circuits. Available at `https://www.ti.com/lit/an/slva043b/slva043b.pdf` (Accessed 2022/01/26).

[199] H. Nyquist. Thermal agitation of electric charge in conductors. Phys. Rev., 32:110–113, Jul 1928.

[200] Eugene P. Wigner. On the behavior of cross sections near thresholds. Phys. Rev., 73:1002–1009, May 1948.

[201] Rudolph E. Langer. On the connection formulas and the solutions of the wave equation. Phys. Rev., 51:669–676, Apr 1937.

Appendix A

High Voltage Noise Floor

The feedback loop for controlling the high voltage is described in Chapter 3. Here, we analyze part of the feedback circuit to identify the noise sources. We consider two sections of the circuit: first, the voltage reference and DAC, which generate the stable control voltage, and second, the high voltage divider and loop filter, which stabilize the output voltage relative to the control voltage. The circuit diagrams shown in the following sections are specific to our experiment, although the basic design for the divider and loop filter may be generally applicable to experiments with precision control of high voltage. Many of the noise analysis techniques described here come from Refs. [197] and [198]. The next four sections are organized as follows:

A.1: Description of noise mechanisms, including Johnson-Nyquist noise, RC filter noise, and amplifier noise.

A.2: Noise analysis of the voltage reference and DAC circuit.

A.3: Noise analysis of the divider and feedback circuit.

A.4: Summary of the total noise in the system with real component values, and perspectives on reducing the noise. Top-level results from the previous two sections are summarized here.

A.1 Noise Sources

There are two primary noise sources in this circuit: the Johnson-Nyquist noise intrinsic to resistors, and amplifier noise. For the following, we denote current, voltage, and total noise as i,

v, and e_j respectively, where (j) is the label on the circuit diagram at the point where the noise is measured. These quantities in general depend on frequency. The total voltage noise of two sources with noise e_i, e_j is

$$(e_i + e_j)^2 = e_i^2 + e_j^2 + c \times (2e_i e_j) \tag{A.1}$$

The factor on the cross term, c, quantifies the correlation between the noise sources. For uncorrelated sources, such as Johnson noise from two resistors, $c = 0$ since the time average of the last term is zero. For completely in-phase and out-of-phase noise, respectively, $c = \pm 1$.

In terms of the temperature T and the Boltzmann constant k_B, the voltage spectral density of Johnson-Nyquist noise in a resistor of value R is [199]

$$v_J(R) = \sqrt{4k_B T R} \approx 0.13\sqrt{R} \left[\frac{\text{nV}}{\sqrt{\text{Hz}}}\right] \tag{A.2}$$

at $T = 293$ K and is constant for all frequencies. In the case where a resistor and capacitor form a low pass filter, as in Fig. A.1, the Johnson noise is reduced by the gain of the filter $g(\omega, R, C)$:

$$v_J(R, C, \omega)^2 = 4k_B T R \times g(\omega, R, C)^2 = \frac{4k_B T R}{1 + (\omega R C)^2} \tag{A.3}$$

Integrating over all frequencies to obtain the total noise $V_J(R, C)$:

$$\begin{aligned} V_J(R, C)^2 &= \int_0^\infty v_J(R, C, \omega)^2 d\omega \\ &= 4k_B T R \int_0^\infty g(\omega, R, C)^2 d_\omega \\ &= \int_0^\infty \frac{4k_B T R}{1 + (\omega R C)^2} d\omega \\ &= \frac{kT}{C} \end{aligned} \tag{A.4}$$

The total noise does not depend on the resistance, because as the resistance is increased—increasing the Johnson noise—the frequency corner of the filter moves to lower frequency to compensate. At room temperature, for capacitance measured in μF:

$$V_J(C) \approx \frac{64}{\sqrt{C}} \,[\text{nV}] \tag{A.5}$$

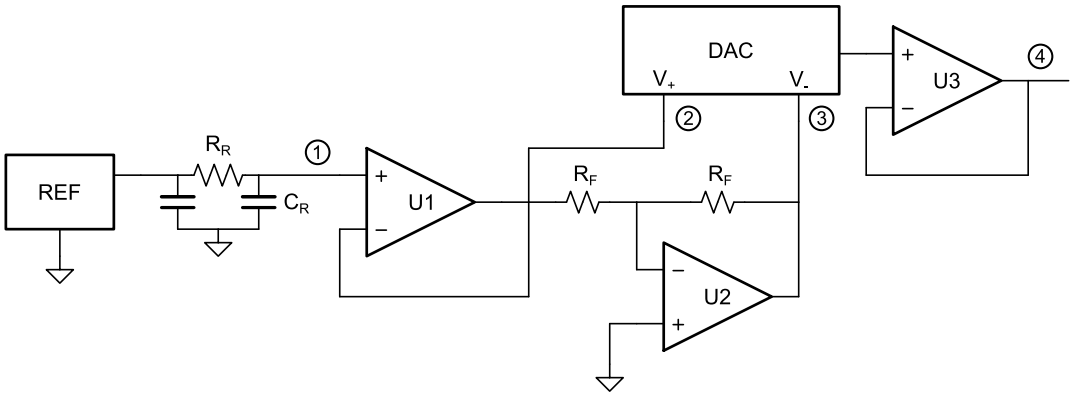

Figure A.1: Circuit diagram for the programmable precision DAC. The reference voltage is filtered (R_R, C_R), buffered (U1) and inverted (U2) to provide positive and negative voltage sources (V_+, V_-) for the DAC. The DAC output is buffered by U3.

Operational amplifiers have two additional noise mechanisms: output voltage noise, which acts as a random noise source on the amplifier output, and input current noise, which acts as random current fluctuations on both inputs and generates a voltage on input resistors.

A.2 Voltage Reference and DAC

We generate high-precision programmable voltages using a voltage reference and DAC (Fig. A.1). The voltage output from the reference passes through a low pass filter with component values R_R and C_R at point (1) and is buffered by U1 to generate the positive reference voltage V_+ at point (2). V_+ is inverted using U2, with feedback resistors R_F, to generate the negative reference V_- at point (3), with $V_+ = -V_-$. These reference voltages enter the DAC. For an n-bit DAC with R-2R architecture, the output voltage is

$$V_{DAC} = A(V_+ - V_-) + V_- = V_+(2A - 1) \tag{A.6}$$

where $A = d/(2^n - 1)$ and d is the DAC value, an integer between 0 and $2^n - 1$.

The noise at point (1) is the sum of the filtered reference noise v_R and the capacitive noise from the low pass filter:

$$e_1^2 = v_R^2 + \int_0^\omega v_J (R_R)^2 g(\omega, R, C)^2 \tag{A.7}$$

For fixed-voltage references, as here, the low pass filter component values will typically be large enough to neglect the capacitive noise. For example, for our values $R_R = 1$ MΩ and $C_R = 10$ μF, the total integrated noise is only 20 nV, half of which is contained in the frequency band below $f_{3\mathrm{dB}} = 1/2\pi R_R C_R \approx 16$ mHz. This is much lower than v_R integrated below 10 Hz for even the best references. For the same reason, we neglect input current noise across R_R from U1.

At point (2), V_+, the reference noise is summed with the output noise of U1:

$$e_2^2 = e_1^2 + v_{\mathrm{U1}}^2 \approx v_R^2 + v_{\mathrm{U1}}^2 \tag{A.8}$$

At point (3), additional noise is added due to the intrinsic output noise of U2, current noise across R_F, and Johnson noise from both feedback resistors. Since in our design U1 and U2 are the same model, the magnitude of the voltage and current noise on the amplifiers is the same:

$$e_3^2 = v_R^2 + 2v_{\mathrm{U1}}^2 + i_1^2 R_F^2 + 2v_J(R_F)^2 \tag{A.9}$$

Using Eq. A.6, we can see that the DAC output noise interpolates between e_2 and e_3, the noise on each reference voltage, depending on the output voltage. On the DAC output, correlations in the noise are relevant, since V_+ and V_- are derived from the same reference, low-pass filter, and buffer. Rearranging Eq. A.6 and substituting in noise terms e_2, e_3 to find the total noise at point (4), with the addition of the intrinsic DAC noise v_{DAC} and the noise from the buffer amplifier U3:

$$e_4^2 = v_{\mathrm{U3}}^2 + v_{\mathrm{DAC}}^2 + (Ae_2 + (1-A)e_3)^2 \equiv v_D^2 \tag{A.10}$$

v_D represents the total noise from the reference-DAC system.

In the case $A = 0.5$, corresponding to zero output voltage:

$$e_4^2 = v_{\mathrm{U3}}^2 + \frac{1}{4}(e_2 + e_3)^2 \tag{A.11}$$

The noise terms v_R, v_{U1} are shared between e_1 and e_2, but are of opposite phase since U2 is inverting. For example, if the reference voltage increases, V_+ increases and V_- decreases by equal amounts, leaving the output voltage $V_{DAC} = (V_+ + V_-)/2$ unchanged. Accounting for these correlations:

$$e_4^2 = v_{\mathrm{U3}}^2 + v_{\mathrm{U1}}^2 + i_1^2 R_F^2 + 2v_J(R_F)^2 \tag{A.12}$$

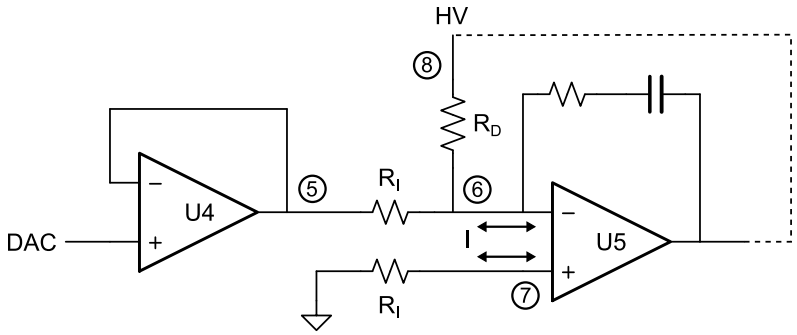

Figure A.2: Circuit diagram for high voltage feedback control. The buffered control voltage from the DAC (5) is stabilized relative to the high voltage (8) divided by a factor R_D/R_I (6).

All six electrodes have an independent DAC but share V_+ and V_-. To calculate the effect of the correlations on the electric field, the DAC value (and corresponding A) for each electrode must be taken into account, as well as the change in electric field per change in voltage for each electrode in a given field configuration. A calculation of this type is used in Chapter 3 to quantify the electrode noise.

A.3 High Voltage Divider and Loop Filter

Figure A.2 shows the circuit used for stabilizing the high voltage. The control signal is generated by a DAC and buffered by U4, generating voltage V_5 at the point marked (5). The high voltage (V_8) enters the circuit at point (8), and is divided down by the resistive divider comprising "input" and "divider" resistors R_I, R_D, where $R_I \ll R_D$. The non-inverting input of U5 at point (7) is connected to ground through R_I. The dashed line schematically indicates feedback minimizing $V_7 - V_6$, the voltage difference across the op-amp input. Several PI gain stages and the high voltage power supply after U5 are omitted for simplicity; see Fig. 3.6 for a complete block diagram and Ref. [97] for complete schematics, the modifications to which are described here and in Chapter 3.

V_6, the voltage at the inverting input of U5, is related to the DAC and HV voltages by

$$V_6 = V_5 \frac{R_D}{R_I + R_D} + V_8 \frac{R_I}{R_I + R_D} \tag{A.13}$$

Since $V_7 = 0$ and $V_6 = V_7$ when the feedback loop is closed, this implies

$$-V_5 \frac{R_D}{R_I + R_D} = V_8 \frac{R_I}{R_I + R_D} \tag{A.14}$$

Simplifying, using $R_I \ll R_D$:

$$V_8 = -V_5 \frac{R_D}{R_I} \tag{A.15}$$

In other words, the DAC voltage is inverted and amplified by the ratio of the resistors to generate the high voltage setpoint.

At point (7), the total noise comes from the Johnson noise on R_I and the current noise across R_I:

$$e_7^2 = v_J(R_I)^2 + i_5^2 R_I^2 \tag{A.16}$$

At point (5), the total noise comes from the amplifier voltage noise v_{U4} and the DAC noise v_D from the previous section:

$$e_5^2 = v_{\mathrm{U4}}^2 + v_{\mathrm{D}}^2 \tag{A.17}$$

At point (6), the noise has contributions from e_5, the Johnson noise on R_I and R_D, and the current noise on R_I. Using Eq. A.13 and the fact that the noise sources are uncorrelated, the noise is:

$$e_6^2 = e_5^2 + i_5^2 R_I^2 + v_J(R_I)^2 \left(\frac{R_D}{R_I + R_D}\right)^2 + v_J(R_D)^2 \left(\frac{R_I}{R_I + R_D}\right)^2 \tag{A.18}$$

Again using $R_I \ll R_D$:

$$\begin{aligned} e_6^2 &= e_5^2 + i_5^2 R_I^2 + 4k_B T R_I + 4k_B T \frac{R_I^2}{R_D} \\ &= e_5^2 + i_5^2 R_I^2 + v_J(R_I)^2 \end{aligned} \tag{A.19}$$

The noise on the high voltage, which is the quantity of interest, is the combination of the noise at the amplifier inputs times the amplification factor (Eq. A.15):

$$e_8^2 = \frac{R_D^2}{R_I^2}\left(v_{\mathrm{U4}}^2 + v_D^2 + 2i_5^2 R_I^2 + 2v_J(R_I)^2\right) \tag{A.20}$$

Any noise on the high voltage power supply that is not cancelled by feedback (for example, at frequencies above the servo bandwidth) will also be added on the output. Substituting the

DAC/reference noise from Eq. A.10:

$$e_8^2 = \frac{R_D^2}{R_I^2}\left(v_{\mathrm{U4}}^2 + v_{\mathrm{U3}}^2 + (Ae_2 + (1-A)e_3)^2 + 2i_5^2R_I^2 + 2v_J(R_I)^2\right) \tag{A.21}$$

A.4 Real Values and Outlook

In this section, I first calculate the total noise in the electrode control system and describe some possible improvements. Second, I discuss processes that lead to long-term drift and give typical values for the drift with temperature.

A.4.1 AC Noise (> 0.1 Hz)

For detailed measurements of the actual noise spectrum and comparisons to measurements of the electric field, see Chapter 3. Table A.1 contains the real component values for the circuits shown in Figs. A.1 and A.2. For component U4, we replaced the former part (model OP97) with an AD8675 to reduce the noise voltage density from 17 to 3 nV/$\sqrt{\mathrm{Hz}}$. Table A.2 summarizes the relationship between the sources contributing to the total noise and gives an expression for the noise at each labeled point in the figures. The number to note here is the amplification factor of $R_D/R_I = 2000$; this means that any voltage noise after the divider is amplified by this factor onto the high voltage.

Table A.3 shows the noise figures for each component as well at the total noise density at several points in the circuit. We have directly measured the noise at several places; these measurements are indicated in bold. Both low-frequency integrated noise and high-frequency noise density are shown in the table. In integrated circuits, the noise profile often scales as *1/f* (where f is the frequency of noise) below about 10 Hz, then saturates at a constant value [198]. The LF column captures the total *1/f* noise and the HF column shows the typical broadband noise density. At higher frequencies, comparable to the amplifier bandwidth, the noise is further reduced. We neglect this effect, however, because the low-pass filter on the output of the high voltage power supplies reduces noise above about 10 kHz (Fig. 3.8). Here are several comments about the important results in Table A.3:

Component	Value/Model
REF	LTC6655
R_R	1 MΩ
C_R	10 μF
U1, U2	ADA4625-2
R_F	5 kΩ (Vishay DSMZ)
DAC	EVAL-AD5791
U3, U4, U5	AD8675
R_I	7.5 kΩ (Vishay Z201)
R_D	15 MΩ = 30×500 kΩ (Vishay Z206)
R_D/R_I	2000

Table A.1: Component values for the high voltage reference and feedback circuits.

Point	Total Noise	Equation
(1)	$e_1^2 = v_R^2$	A.7
(2)	$e_2^2 = e_1^2 + v_{\mathrm{U1}}^2$	A.8
(3)	$e_3^2 = e_2^2 + v_{\mathrm{U2}}^2 + i_1^2 R_F^2 + 2v_J(R_F)^2$	A.9
(4)	$e_4^2 = v_{\mathrm{DAC}}^2 + v_{\mathrm{U3}}^2 + (Ae_2 + (1-A)e_3)^2$	A.10
(5)	$e_5^2 = e_4^2 + v_{\mathrm{U4}}^2$	A.17
(6)	$e_6^2 = e_5^2 + i_5^2 R_I^2 + v_J(R_I)^2$	A.19
(7)	$e_7^2 = v_J(R_I)^2 + i_5^2 R_I^2$	A.16
(8)	$e_8^2 = (R_D^2/R_I^2)\left(e_6^2 + e_7^2\right)$	A.20

Table A.2: Summary of sources contributing to high voltage noise. Each entry represents a point labeled on Fig. A.1 and A.2, with equations indicating the derivation in the text.

Label	Description/Model	HF (nV/$\sqrt{\text{Hz}}$)	LF
v_R	**LTC6655 + RC Filter**	**<7**	
$v_{\text{U1}}, v_{\text{U2}}$	ADA4625-2 (Voltage)	3.3	0.15 $\mu\text{V}_{\text{p-p}}$ (0.1-10 Hz)
$i_1 R_F$	ADA4625-2 (Current)	<0.01 (4.5 fA · 5 kΩ)	
$v_J(R_F)$	Johnson Noise, 5 kΩ	9	
v_{DAC}	EVAL-AD5791	7.5	1.1 $\mu\text{V}_{\text{p-p}}$ (0.1-10 Hz)
$v_{\text{U3}}, v_{\text{U4}}$	AD8675 (Voltage)	2.8	0.1 $\mu\text{V}_{\text{p-p}}$ (0.1-10 Hz)
$i_5 R_I$	AD8675 (Current)	2.3 (0.3 pA · 7.5 kΩ)	
$v_J(R_I)$	Johnson Noise, 7.5 kΩ	11	
e_2	**+5V Reference**	**8**	**0.25 μV_{rms} (0.1-12 Hz)**
e_3	**-5V Reference**	**32**	**0.3 μV_{rms} (0.1-12 Hz)**
e_4	Total, After DAC Buffer	19	1.2 $\mu\text{V}_{\text{p-p}}$ (0.1-10 Hz)
$e_8/2000$	Total, After Divider	25	1.2 $\mu\text{V}_{\text{p-p}}$ (0.1-10 Hz)
e_8	Total, High Voltage	51×10^3	2.5 $\text{mV}_{\text{p-p}}$ (0.1-10 Hz)

Table A.3: Specified and measured rms voltage noise for noise sources listed in Table A.2. High-frequency (HF) noise refers to average or typical broadband noise density above about 10 Hz. Low-frequency (LF) noise is shown where available and refers to integrated noise in the frequency band specified. Bold entries are measured; all other entries are either specified by the component manufacturer or calculated based on noise specifications, measurements, and the equations in Table A.2. The first block of entries are component-level noise sources, such as the current noise for a particular op-amp and resistor pair in the circuit. The second block is the measured noise of the voltage references V_+, V_- for the DAC. The third block is the total voltage noise after the DAC, after the DAC and the HV divider circuit, and after the amplification to high voltage. These values use the measured e_2, e_3 from the previous block, assuming $A = 0.5$ (zero output voltage, Eq. A.6) and neglecting any correlations between e_2 and e_3.

- The low frequency noise is dominated by the DAC (v_{DAC})
- The measured noise on V_+ (e_2) is the expected value; however, the noise on V_- (e_3) is about twice as high as expected, after accounting for the contributions from the inverting amplifier and feedback resistors
- The reference (v_R) does not contribute strongly to the total noise after the DAC (e_4); instead, the primary contributions are from the negative input to the DAC (e_3), the DAC itself (v_{DAC}), and the Johnson noise on the two feedback resistors ($v_J(R_F)$)
- The reference and DAC (e_4) contribute one-half of the total noise after the divider ($e_8/2000$), with the remainder of the noise primarily coming from Johnson noise on input resistors R_I
- The total noise on the DAC, divider, and HV is calculated assuming $A = 0.5$, or zero output voltage, and no correlation between V_+ and V_- (noise terms e_2, e_3)
- The divider ratio ($R_D/R_I = 2000$) is a scaling factor on the total high voltage noise e_8

There are several alterations (some easy, some difficult) that could be made to improve the performance of the electric field control. Since the divider ratio is a multiplicative factor on all noise sources, reducing it would lead to a proportional reduction in the noise. The DACs are currently configured to output between -5 and 5 V, and the ratio of electric field to DAC voltage V_{DAC} and electrode voltage V_{HV} is:

$$\frac{V_{\mathrm{DAC}}}{E} = \left(\frac{R_I}{R_D}\right)\frac{V_{\mathrm{HV}}}{E} \approx 0.15\left[\frac{\mathrm{V}}{\mathrm{kV/cm}}\right] \tag{A.22}$$

Therefore, changes in the divider ratio will limit the maximum electric field. The current maximum field is **32 kV/cm**. The electric fields for in the experiments described in this thesis are: **1 kV/cm**, a low electric field where layer selection can still be performed [66]; **4.5 kV/cm**, where 2D evaporation of molecules is most efficient [63]; and **12.7 kV/cm**, where resonant shielding protects molecules against reactive collisions [64, 65]. We could reduce the divider ratio by up to a factor of 2.5 while still being able to access the shielding field. To change the divider ratio, we can

either increase R_I or decrease R_D. Increasing R_I leads to higher Johnson and current noise after the divider, but may be simpler since it only requires changing two components. R_D is a network of resistors in series [97, 72], so it may be possible to decrease it by connecting the input from the electrode to a different point in the network or shorting over some fraction of the resistors. In this case, a higher voltage would be dropped over each resistor and properties such as the voltage and power coefficients of resistance might present issues.

Here is a non-exhaustive list of ways to reduce the noise, with the calculated output noise (in $\mu\text{V}/\sqrt{\text{Hz}}$) in parentheses

- Current noise level (51)
- Fix negative voltage reference (40)
    - Reduce R_F to 1 kΩ (38)
- Remove R_I on the non-inverting input of U5 (45)
- Increase R_I by a factor of 2.5 (26)
- Decrease R_D by a factor of 2.5 (20)

The indented point would have to be done together with fixing the negative voltage reference since that is the dominant noise source. Using these methods, it seems possible to reduce the high-frequency noise by a factor of three.

A.4.2 Long-Term Drift

In addition to the frequency noise, several elements of the circuit may be susceptible to drift with time or temperature. On U5, voltage offsets due to the input bias current (common-mode input current on the inverting and non-inverting inputs) should be cancelled since each input has a matched resistor R_I. However, input offset currents (differential input currents between the inputs) will cause voltage offsets. The typical value for the input offset current is 0.1 nA, equal to 0.75 μV

IC Model	Typical TC (μV/°C)	Maximum TC (μV/°C)
LTC6655	5	10
EVAL-AD5791	0.2	0.25
ADA4625-2	0.2	1.2
AD8675	0.2	0.6
HV, DAC = 0V	$< 1.6 \times 10^3$	$< 5.3 \times 10^3$
HV, DAC = $\pm$5V	$< 11 \times 10^3$	$< 25 \times 10^3$

Table A.4: Typical and maximum temperature coefficients of the integrated circuits in the electric field control loop. The values in the bottom two rows are maximum total drifts obtained by adding the above drifts for each IC in Figs. A.1 and A.2, assuming completely correlated drift, multiplied by the high voltage division factor of 2000. Total temperature coefficients for two different DAC values are shown to illustrate the effect of correlated voltage reference drifts.

over $R_I = 7500\ \Omega$. U5 has a typical offset voltage (voltage difference between the inputs) of 10 μV. Scaling by R_D/R_I, the typical offset on the high voltage is more than 20 mV. The long-term drift of these offsets is not specified, but it could lead to small changes in the high voltage output over months.

Table A.4 shows typical and maximum temperature coefficients for the integrated circuits used in the electric field control loop. The voltage reference has the largest temperature coefficient, but as discussed above (Eq. A.6), for DAC outputs near zero the reference does not affect the output value. The expected total coefficient ranges from several mV/°C to tens of mV/°C (depending on the DAC output), on top of voltages of 0-4000 V. The lab temperature is stabilized to about 0.5 °C within one day and 1-2 °C day-to-day, so these temperature coefficients can certainly contribute shifts at the ppm level. The exact conversion between voltage drifts and electric field drifts will depend on the specific electrode configuration.

Temperature changes in resistors R_D, R_I, and R_F would also result in changes to the output voltage. We use Vishay Z-Foil resistors for all of these components, which have a temperature coefficient of resistance of only 0.05 ppm/°C. In order to ensure that the voltage and power coefficients of resistance for the high voltage divider are negligible, we use 30 separate Z206 resistors for R_D,

which are each effectively six individual resistors packaged together. This ensures that the voltage drop and power dissipated in each resistor remains small even for large voltages.

Appendix B

WKB Approximation for Two-Body Loss Temperature Dependence

In terms of the molecule density n, the two-body density loss rate (in the absence of single particle loss or heating) is

$$\frac{dn}{dt} = -\beta n^2 \tag{B.1}$$

where β is the two-body loss rate coefficient. The general expression for the collision rate is

$$\Gamma = n\sigma_{\text{in}} \langle v \rangle \tag{B.2}$$

where σ_{in} is the inelastic cross section and $\langle v \rangle$ is the mean thermal velocity. Since βn is the rate of two-body collisions, we associate $\beta = \sigma_{\text{in}} \langle v \rangle$. The inelastic cross section at collision energy E of indistinguishable particles of reduced mass μ is

$$\sigma_{\text{in}} = \frac{\hbar^2 \pi}{\mu E} \left| T^{\text{in}} \right|^2 \tag{B.3}$$

where T^{in} is the transition matrix, which depends in general on the molecular states involved in the reaction [151]. In terms of L, the partial wave of the collision, threshold law scaling gives $\left|T^{\text{in}}\right|^2 \propto E^{L+1/2}$ [200]. Combining this with the energy scaling of the relative velocity, $v \propto \sqrt{E}$, we therefore have $\sigma_{\text{in}} \propto E^{L-1/2}$ and $\beta \propto E^L$. For indistinguishable fermions like KRb, which collide predominantly in the p-wave channel ($L = 1$), this implies that the two-body loss rate scales linearly with temperature, as has been measured previously [21].

Here we present a simple semi-classical calculation based on the WKB method to derive the temperature scaling of the loss rate at small collision energies. The radial potential, given by the

sum of the isotropic centrifugal and van der Waals terms, is

$$V(r) = \frac{\hbar^2 L(L+1)}{2\mu r^2} - \frac{C_6}{r^6} \tag{B.4}$$

For $L \geq 1$, the centrifugal term creates a barrier to molecules approaching at close range and undergoing a chemical reaction (Fig. B.1a). We assume that molecules tunneling through this barrier are lost with unit probability, an approximation based on experiment-theory comparison [23]. $\left|T^{\text{in}}\right|^2$ therefore represents the probability of a molecule tunneling through the barrier and reacting at short range.

In the WKB approximation, the tunneling probability is

$$\left|T^{\text{in}}\right|^2 = \exp\left(-2\int_{r_i}^{r_o} k(r)dr\right) \tag{B.5}$$

where r_i, r_o are the inner and outer classical turning points, and $k(r)$ is the momentum of the particle in the classically forbidden region:

$$k(r) = \sqrt{\frac{2\mu[V(r) - E]}{\hbar^2}} \tag{B.6}$$

The inner turning point r_i depends on the C_6 coefficient: for simplicity, we for now set $C_6 = 0$, and fix r_i as a constant. The physical justification for this approximation is that the inner side of the potential barrier falls off fast enough that r_i does not depend strongly on E, in contrast to r_o. We also make the Langer correction to the centrifugal potential in order to perform WKB in spherical coordinates [201]. This is the replacement $L(L+1) \to (L+1/2)^2$:

$$V(r) = \frac{\hbar^2 (L+1/2)^2}{2\mu r^2} \equiv \frac{A}{r^2} \tag{B.7}$$

Substituting this modified potential into Eq. B.6, and defining $B \equiv \sqrt{2\mu/\hbar^2}$, we expand in powers of E:

$$\begin{aligned} k(r) &= B\sqrt{V(r) - E} \\ &= B\sqrt{\frac{A}{r^2} - E} \\ &\approx B\left(\sqrt{\frac{A}{r^2}} - \frac{E}{2}\sqrt{\frac{r^2}{A}} + \mathcal{O}(E^2)\right) \end{aligned} \tag{B.8}$$

This expansion is justified because $E \ll V(r)$ for nearly all of the trajectory (except for short distances near the turning points, which is a general issue with the WKB method). The typical thermal energy is $E \approx 200$ nK and the potential has the maximum value of $V(r) = 24$ μK, a difference of two orders of magnitude.

Substituting this into Eq. B.5 and performing the integral:

$$\begin{aligned}
\left|T^{\text{in}}\right|^2 &= \exp\left(-2\int_{r_i}^{r_o} k(r)dr\right) \\
&= \exp\left(-2\int_{r_i}^{r_o} B\left(\sqrt{\frac{A}{r^2}} - \frac{E}{2}\sqrt{\frac{r^2}{A}}\right)dr\right) \\
&= \left(\frac{r_o}{r_i}\right)^{-2B\sqrt{A}} \exp\left(\frac{BE\left(r_o^2 - r_i^2\right)}{2\sqrt{A}}\right) \\
&\approx \left(\frac{r_o}{r_i}\right)^{-2B\sqrt{A}} \left(1 + \frac{BE\left(r_o^2 - r_i^2\right)}{2\sqrt{A}} + \mathcal{O}(E^2)\right)
\end{aligned} \tag{B.9}$$

We again use $E \ll A/r^2$ and set the exponential equal to one, keeping only the prefactor. Equating the collision energy to the potential energy at r_o, we have:

$$r_o = \sqrt{\frac{A}{E}} \tag{B.10}$$

Substituting for A and B, this recovers the following expression for the tunneling probability:

$$\left|T^{\text{in}}\right|^2 \propto E^{L+1/2} \tag{B.11}$$

We numerically calculate the WKB transmission probability without any of the above approximations, keeping the C_6 coefficient and not expanding in small $E/V(r)$ (Fig. B.1b). We use parameters corresponding to KRb: $L = 1$, $\mu = 127/2$ amu, and $C_6 = 16133$ a.u. [150]. In the experimental range of collision energies, between $T = 10$-1000 nK ($E = 3k_BT/2$ in three dimensions, where k_B is the Boltzmann constant), the calculated transmission probability scales nearly exactly with $T^{3/2}$ and therefore gives $\beta \propto T$ (Eq. B.3).

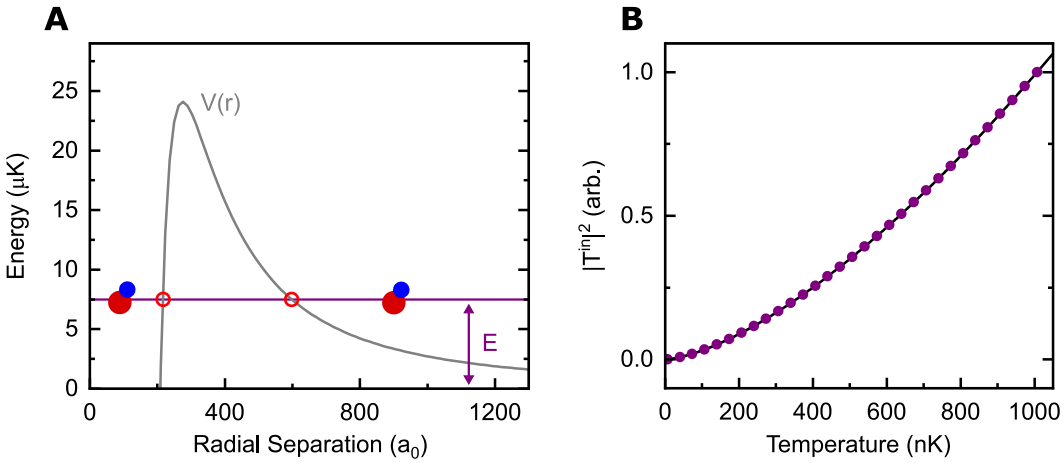

Figure B.1: Using the WKB approximation to find the temperature scaling of two-body loss. **(a)** Potential barrier $V(r)$ with contributions from the centrifugal and van der Waals terms. The incoming molecule must tunnel to short range to react. The inner and outer turning points (r_i, r_o) for collision energy E are highlighted with red circles. The collision energy shown is 10-40 times higher than typical temperatures. **(b)** Calculated tunneling probability vs. temperature for KRb, in arbitrary units. The probability scales as $T^{3/2}$ (solid line).